

Predicting microstructural pattern formation using stabilized spectral homogenization

Thesis by
Vidyasagar

In Partial Fulfillment of the Requirements for the
Degree of
Doctor of Philosophy (Ph.D.) in Aeronautics

The logo for the California Institute of Technology (Caltech), featuring the word "Caltech" in a bold, orange, sans-serif font.

CALIFORNIA INSTITUTE OF TECHNOLOGY
Pasadena, California

2019
Defended 7 September 2018

© 2019

Vidyasagar

ORCID: 0000-0003-0262-5429

All rights reserved except where otherwise noted.

ACKNOWLEDGEMENTS

I would like to express my strong heartfelt gratitude to my adviser, mentor, teacher, and friend Prof. Dennis M. Kochmann. It has been a very enlightening journey, from first encountering his work on material instabilities as a young undergraduate in London, to joining his group at Caltech, and then following him on a sojourn to Switzerland. This work would not have been possible without his brilliant ideas, patient responses, and understanding nature.

Next I would like to extend my appreciation to my thesis committee. I am extremely honored to have had meetings and discussions with Prof. Bhattacharya and Prof. Ortiz. Prof. Ravi always been there for support and encouragement, from the very first time I visited Caltech.

I would also like to express immense gratitude to the wonderful Mechanics and Materials family, who made my time at Caltech and ETH Zürich memorable. My seniors Neel Nadkarni, Ishan Tembhekar, Yingrui Chang, Stan Wojnar, and Alex Zelhofer passed on to me the knowledge and foundation upon which this work is built. My group members Abbas Tutcuoglu, Carlos Portela, Greg Phlipot, Wei-Lin Tan, Sid Kumar, Basti Krödel, Romik Khajehtourian, Claire Lestringant, Bastian Telgen, and Raphael Glaesener made every day I spent with them a bright one. Our administrative staff, Denise Ruiz in Pasadena, and Maria Trodella in Zürich, deserve special mentions for their unwavering patience, kindness and life advice.

My friends at Caltech have been crucial sources of strength throughout this journey. They gave me much needed motivation to spend time outside work – be it on weekend brunches, hiking trips, or Vegas adventures. I particularly thank Matt Leibowitz, Christophe Leclerc, Nelson Yanes, Cecilia Huertas, Will Schill, Kavya Sudhir, Jaeyun Moon, Danilo Kusanovic, Chandru Dhandapani, Joel Lawson, Louisa Avellar, Dingyi Sun, Trenton Kirchdoerfer and Serena Ferraro. I am also indebted to Laura Flower Kim and Daniel Yoder of the International Office at Caltech (ISP), who made life significantly easier. I thank Christine Ramirez and Profs. McKeon and Meiron for their help with the academic process at GALCIT.

Finally, I would like to thank my family for their unwavering support. Their patience and encouragement allowed me to pull through this Ph.D., especially during times of hardship. I dedicate this work to my mother Indira Ananthan, little sister Utthra Ananthan, and father V.V. Ananthan.

ABSTRACT

Instability-induced patterns are ubiquitous in nature, from phase transformations and ferroelectric switching to spinodal decomposition and cellular organization. While the mathematical basis for pattern formation has been well-established, autonomous numerical prediction of complex pattern formation has remained an open challenge. This work aims to simulate realistic pattern evolution in material systems exhibiting non-(quasi)convex energy landscapes. These simulations are performed using fast Fourier spectral techniques, developed for high-resolution numerical homogenization. In a departure from previous efforts, compositions of standard FFT-based spectral techniques with finite-difference schemes are used to overcome ringing artifacts while adding grid-dependent implicit regularization.

The resulting spectral homogenization strategies are first validated using benchmark energy minimization examples involving non-convex energy landscapes. The first investigation involves the St. Venant-Kirchhoff model, and is followed by a novel phase transformation model and finally a finite-strain single-slip crystal plasticity model. In all these examples, numerical approximations of energy envelopes, computed through homogenization, are compared to laminate constructions and, where available, analytical quasiconvex hulls.

Subsequently, as an extension of single-slip plasticity, a finite-strain viscoplastic formulation for hexagonal-closed-packed magnesium is presented. Microscale intragranular inelastic behavior is captured through high-fidelity simulations, providing insight into the micromechanical deformation and failure mechanisms in magnesium. Studies of numerical homogenization in polycrystals, with varying numbers of grains and textures, are also performed to quantify convergence statistics for the macroscopic viscoplastic response.

In order to simulate the kinetics of pattern evolution, stabilized spectral techniques are utilized to solve phase-field equations. As an example of conservative gradient-flow kinetics, phase separation by anisotropic spinodal decomposition is shown to result in cellular structures with tunable elastic properties and promise for metamaterial design. Finally, as an example of non-conservative kinetics, the study of domain wall motion in polycrystalline ferroelectric ceramics predicts electromechanical hysteresis behavior under large bias fields. A first-principles approach using DFT-informed model constants is outlined for lead zirconate titanate, producing results showing convincing qualitative agreement with in-house experiments. Overall, these examples demonstrate the promise of the stabilized spectral scheme in predicting pattern evolution as well as effective homogenized response in systems with non-quasiconvex energy landscapes.

PUBLISHED CONTENT AND CONTRIBUTIONS

Vidyasagar, A., Tan, W. L., Kochmann, D. M. 2017. Predicting the effective response of bulk polycrystalline ferroelectric ceramics via improved spectral phase field methods. *Journal of the Mechanics and Physics of Solids* 106, 113-151.

URL: <https://doi.org/10.1016/j.jmps.2017.05.017>

A. V. developed and implemented numerical schemes. W.-L. T. set up and performed experiments under supervision of D. M. K.

Vidyasagar, A., Tutcuoglu, A., Kochmann, D. M. 2018. Deformation patterning in finite-strain crystal plasticity by spectral homogenization with application to magnesium. *Computer Methods in Applied Mechanics and Engineering*, 335, pp.584-609.

URL: <https://doi.org/10.1016/j.cma.2018.03.003>

A. V. and A. T. jointly developed the numerical methods under the guidance of D. M. K.

Vidyasagar, A., Krödel, S., Kochmann, D. M. 2018. Microstructural patterns with tunable mechanical anisotropy obtained by simulating anisotropic spinodal decomposition. *Proceedings of the Royal Society A: Mathematical, Physical and Engineering Sciences* 474, 20180535.

URL: <https://doi.org/10.1098/rspa.2018.0535>

A. V. and S. K. jointly developed the numerical methods under the guidance of D. M. K.

TABLE OF CONTENTS

Acknowledgements	iii
Abstract	iv
Published Content and Contributions	v
Table of Contents	vi
List of Illustrations	viii
List of Tables	xv
Chapter I: Introduction	1
1.1 Patterns Across Scales In Nature	1
1.2 Energy Relaxation and Microstructures	4
1.3 Dissipation and Kinetic Models	11
1.4 Outline	13
Chapter II: Development of Spectral Homogenization Schemes	14
2.1 Introduction to Computational Homogenization	14
2.2 Fast Fourier Spectral Methods	16
2.3 Iterative Spectral Methods	18
2.4 Ringing Artifacts	21
2.5 Finite-Difference Corrections for Spectral Differentiation	23
2.6 Special Considerations for Non-Convex Problems	28
Chapter III: Numerical Solutions to Non-Convex Problems	31
3.1 Introduction	31
3.2 The St. Venant-Kirchoff Model	31
3.3 Generalized Finite-Strain Phase Transition Model	35
3.4 Single-Slip in Single- and Bi-Crystals	42
3.5 Conclusion	53
Chapter IV: Deformation Patterns and Crystal Visco-Plasticity in Magnesium Polycrystals	56
4.1 Introduction	56
4.2 Constitutive Model: Finite-Strain Crystal Plasticity in Magnesium	58
4.3 Material Constants for the Mg Constitutive Model	60
4.4 Numerical Solution Strategy – Explicit Updates	60
4.5 Plasticity in Polycrystalline Magnesium	62
4.6 Conclusions	70
Chapter V: Patterns and Elastic Surface Evolution During Anisotropic Spinodal Decomposition	71
5.1 Introduction	71
5.2 Constitutive Model and Kinetics	73
5.3 Numerical Solution Strategy	75
5.4 Elastic Surface Calculation	77
5.5 Pattern Formation Process	78
5.6 Conclusion	88
Chapter VI: Kinetics of Domain Patterns in Ferroelectrics	93

6.1 Introduction	93
6.2 Ferroelectric Constitutive Model	95
6.3 Material Constants for BaTiO ₃ and PZT	100
6.4 Boundary Value Problem at the RVE Level	100
6.5 Simulations of Domain Patterns Evolution and Experimental Validation	106
6.6 Conclusions	112
Chapter VII: Conclusions	114
7.1 Summary	114
7.2 Outlook & Future Directions	115
Bibliography	118

LIST OF ILLUSTRATIONS

<i>Number</i>	<i>Page</i>
1.1 Multi-scale nature of patterns in a butterfly wing that lead to structural iridescence (Thomé et al., 2014). <i>Reproduced with permission.</i>	1
1.2 A series of natural patterns in mechanics that form from disordered initial states: (a) cross-hatched dislocation patterns in an Al bicrystal at the interface (Kuo et al., 2003), (b) twinning laminate structures in Cu-Ni (Abeyaratne et al., 1996), (c) labyrinth-type patterns in a fatigued Cu single crystal (Jin and Winter, 1984), (d) martensitic phase transformation domain patterns (Bhattacharya and James, 2005). <i>Reproduced with permission.</i>	2
1.3 Micrograph of striped domain patterns forming within grains of ferroelectric PZT polycrystal during fatigue cycling. <i>Courtesy of Wei-Lin Tan, Caltech.</i>	3
1.4 Loss of convexity of the condensed energy $W(\gamma)$ with decreasing μ , for $\lambda = 1$	6
1.5 Examples of loss of convexity in systems exhibiting pattern formation.	6
1.6 $QW(\mathbf{F})$ for phase transitions with $W(\mathbf{F}) = \min(W^1(\mathbf{F}), W^2(\mathbf{F}))$. Spontaneous breakdown of the homogeneous blue and red phases at a deformation gradient state corresponding to the quasiconvex envelope results in (non-unique) pattern formation.	8
1.7 An overview of the variety of dislocation slip and twinning modes in magnesium.	12
2.1 An FFT-based interpolation of a rectangular function $f(x) = \text{rect}(\frac{1}{3}, \frac{2}{3})$ (a) results in oscillatory approximations with the Gibbs phenomenon. Here, the slopes are shown in black at the grid points, and this directly results in the oscillations of the derivative $f'(x)$, shown in (b), which is computed using the wave vector multiplied by the Fourier transform of $f(x)$	22
2.2 Spectral derivative of the double step function using first- and fourth-order finite-difference correction, compared with classical FFT, and analytical solution (Vidyasagar et al., 2017).	26
2.3 Spectral derivative of the half-sine function using first- and fourth-order finite-difference correction, compared with classical FFT, and analytical solution (Vidyasagar et al., 2017).	27
2.4 (a) Finite-difference approximation indicates loss of accuracy when the mesh convergence is computed. The plot shows error-norm against number of grid-points n . (Vidyasagar et al., 2017) (b) The convergence orders plotted against the number of grid-points (Vidyasagar et al., 2017).	28

2.5	Stress distribution $\frac{\sigma_{11}}{\mu_{\text{mat}}}$ (a) the standard iterative spectral method (b) fourth-order finite-difference corrections and (c) first-order corrections (Vidyasagar et al., 2017).	28
3.1	Loss of convexity of the condensed energy $W(\gamma)$ as the shear modulus μ decreases, for $\lambda = 1$.	33
3.2	The calculated numerical hull shown in (a) shown near the origin in (b). Corresponding microstructural patterns are shown in sequence in (c) during the loading process through the deformation gradient component F_{11} .	34
3.3	The numerically calculated hulls at $\gamma = -0.25$ shown for different degrees of non-convexity with given parameters $\lambda = 1$ from (a) $\mu = 0.001$ and (b) $\mu = 0.01$.	35
3.4	The largest patterns formed using first-order central difference approximation demonstrate complexity of pattern formation, with each component of deformation showing different patterns that are compatible.	35
3.5	Plot of F^* from (3.18) for the biaxial loading defined by (3.30) with $\mu = 1$ and $\kappa = 3$ for various values of k_T from 0.001 to 0.05.	40
3.6	The calculated numerical hull is shown in (a). The corresponding microstructural patterns are shown in the volume fractions (b) & deformation gradient component F_{12} (c) during the loading process.	41
3.7	The calculated numerical hull is shown in (a) for the three-well case. The corresponding microstructural patterns are shown in the volume fractions (b) & deformation gradient component F_{21} (c) during the loading process.	43
3.8	The calculated numerical hull is shown in (a) for the three-well case where the extremal wells lie below the middle-well. The corresponding microstructural patterns are shown in the volume fractions (b) & deformation gradient component F_{21} (c) during the loading process.	44
3.9	Loss of convexity of the condensed energy $A^*(\lambda)$ as the hardening parameter H decreases (Vidyasagar et al., 2018).	46
3.10	Approximation of the quasiconvex envelope obtained by spectral homogenization without finite-different approximation: the average energy of the RVE is compared to the non-convex condensed energy with (a) showing a magnification of (b); (c) shows the microstructural slip activity within the RVE at stages A through G along the loading path as indicated in (b) (Vidyasagar et al., 2018).	48
3.11	Approximation of the quasiconvex envelope obtained by spectral homogenization with the twelfth-order finite-difference approximation: the average energy of the RVE is compared to the non-convex condensed energy with (a) showing a magnification of (b); (c) shows the microstructural slip activity within the RVE at stages A through G along the loading path as indicated in (b) (Vidyasagar et al., 2018).	49

3.12	Laminate patterns for the simple shear test case at $\lambda = 0.208$ obtained from (a) numerical simulations using the above spectral homogenization framework and (b) the equivalent sharp-interface description. (c) shows the local energy density distribution of the numerical solution in (a), which shows concentrated energy within interfaces (Vidyasagar et al., 2018).	51
3.13	Influence of the slip system orientation φ on the non-convex, condensed energy landscape of a single-crystal, with all shown energies exhibiting non-convexity at different range of values for the shear parameter λ (Vidyasagar et al., 2018).	53
3.14	Laminate pattern formation in bicrystals at an applied shear strain of $\lambda = 0.03$: (a) the geometric arrangement of the two grains within the bicrystal RVE along with the definition of angles φ_1 and φ_2 in the blue and red grains, respectively. Results are shown for (b) $\varphi_1 = -\pi/3$ and $\varphi_2 = -\pi/4$, (c) $\varphi_1 = -\pi/3$ and $\varphi_2 = -\pi/6$, and (d) $\varphi_1 = -\pi/3$ and $\varphi_2 = -\pi/12$ (Vidyasagar et al., 2018).	54
4.1	An overview of the variety of dislocation slip and twinning modes in magnesium (Vidyasagar et al., 2018).	61
4.2	(a) Effective stress-strain response of a simple shear test of an RVE containing 100 grains whose orientations are shown in the pole figure (b). (c) State of the RVE at an applied average shear strain of $F_{12}^0 = \lambda = 0.09$. RVEs are shown in the deformed configuration, whereas the bounding box indicates the undeformed shape. Plots illustrate the grain shapes and components of the first Piola-Kirchhoff stress tensor \mathbf{P} as well as the distribution of prismatic slip and of the total volume fraction of all extension-twinned regions. The shown stress distributions are in units of GPa (Vidyasagar et al., 2018).	64
4.3	Using the same grain geometry as in Fig. 4.2(a), an investigation is performed on how the effective stress-strain response in (a) changes with increasing grain misorientation, as shown by the pole figures in (b). Increasing the spread of the texture allows more easy-slip and -twin systems to become active across a larger number of grains, resulting in significant softening even at low strains. (c) The resulting shear stress distribution illustrates stronger stress differences and concentrations with increasing misorientation. The shown stress distributions are in units of GPa (Vidyasagar et al., 2018).	65
4.4	Polycrystalline case (E) of the simple shear experiment (see the pole figure in Fig. 4.3): shown is the shear stress distribution (in GPa) with all displacements magnified by a factor of 10 for better visibility. Several of the grains display laminate-like patterns, as may be expected due to the non-quasiconvexity in finite-strain crystal plasticity, as discussed above (Vidyasagar et al., 2018).	66

4.5	Influence of permuting the grain orientations within an RVE with fixed grain geometry: stress-strain behavior shown in terms of mean and standard deviation of ten RVE realizations with different permutations of grain-orientation assignments for RVEs containing 20, 50, 100, and 1000 grains. Grain orientations are taken from the pole shown in (b); the given components of the first Piola-Kirchhoff stress tensor include (a) tensile, (c) shear, and (d) compressive stresses. Mean stresses are shown as thick lines and standard deviations as shaded color regions (Vidyasagar et al., 2018).	67
4.6	Polycrystalline RVEs with (a) 20, (b) 50, (c) 100, and (d) 1000 grains. The left half of each graphic illustrates the grain size and arrangement, whereas the right half shows the tensile/compressive stress distribution at a representative load of $\lambda = 0.01$ (Vidyasagar et al., 2018).	68
4.7	Illustration of the stress-strain response for simple shear loading ($F_{12}^0 = \alpha$) showing convergence with increasing order of the finite-difference approximation to the standard Fourier spectral scheme (Vidyasagar et al., 2018).	69
4.8	Illustration of the local stress fields and inelastic activity within the same RVE, obtained with different orders of the finite-difference approximation, shown at the maximum shear strain shown in Fig. 4.7 (Vidyasagar et al., 2018).	70
5.1	Depiction of a possible choice of the m_α unit vectors to obtain facets on the associated normal planes.	75
5.2	Periodic structures obtained from the anisotropic spinodal decomposition process for (a) an isotropic medium (no preferred orientations), (b) cubic symmetry with six energetically favorable directions along the coordinate axes, (c) a columnar structure with four energetically favorable in-plane directions, and (d) a lamellar structure with a single energetically favorable orientation. Results are shown at two different times t_1 and t_2 , where t_2 indicates the final, equilibrated state, whereas t_1 is the state of fastest energy decrease, which occurs at approximately half of the energy relaxation time. For all anisotropic structures $a_i = 0.3$ with an average relative density of $\langle \varphi \rangle = 0.5$.	80
5.3	Periodic structures with cubic symmetry (case (b) in Fig. 5.2) shown for varying degrees of anisotropy a and relative density $\langle \varphi \rangle$: (a) $\langle \varphi \rangle = 0.2$, $a = 0.3$, (b) $\langle \varphi \rangle = 0.7$, $a = 0.3$, (c) $\langle \varphi \rangle = 0.5$, $a = 0.15$, (d) $\langle \varphi \rangle = 0.5$, $a = 0.4$.	81

5.4	Kinetics of the spinodal decomposition process measured by the evolution of the total energy E and of the total mobility Λ . Isotropic surface energy leads to the interfacial energy (a) and mobility (c), whereas cubic symmetry with $a = 0.15$ generates the interfacial energy (b) and mobility (d). In all plots the shown curves are for $\langle\varphi\rangle = 0.3$ (green, dotted), $\langle\varphi\rangle = 0.4$ (red, dashed), and $\langle\varphi\rangle = 0.5$ (blue, solid). The interfacial energies, mobility and time scales have been normalized by their respective maximum. For (c) and (d) the maximum of the isotropic mobility function is used. An exemplary microstructure evolution is shown in (e) for the three times labeled A through C in (a).	82
5.5	Contour plots of the solid-void interfaces (visualized at constant $\varphi = 0.5$) and the interfacial shape distribution as a function of the principal curvatures (κ_1, κ_2) of (a) isotropic, (b) cubic, (c) columnar, and (d) lamellar microstructures.	84
5.6	Distribution of the von Mises stress σ_m for an applied average strain ε_0 in the e_3 -direction (i.e., $\langle\varepsilon_{33}\rangle = \varepsilon_0$ and $\langle\varepsilon_{ij}\rangle = 0$ else) for (a) isotropic, (b) columnar and (c) lamellar microstructures. Analogously, the von Mises stress distribution is shown for an applied average strain in the e_1 -direction (i.e., $\langle\varepsilon_{11}\rangle = \varepsilon_0$ and $\langle\varepsilon_{ij}\rangle = 0$ else) for (d) isotropic, (e) columnar and (f) lamellar microstructures. Stresses are normalised by the peak stress among (a)-(f).	85
5.7	Surface plots of the directional surface energy density $\gamma(\mathbf{n})$ from Eq. (5.4) and the corresponding homogenised directional normalized Young's modulus $E(\mathbf{d})$ from Eq. (5.19) for (a,d) cubic (b,e) columnar and (c,f) lamellar microstructures, as seen in Fig. 5.2.	86
5.8	Directional Poisson's ratio for isotropic (green, solid), cubic (red, small dashed), columnar (black, dotted), and lamellar structures (blue, dashed). (a) shows Poisson's ratio in the e_1 - e_2 -plane, and (b) shows Poisson's ratio in the e_1 - e_3 -plane. The direction \mathbf{n} in the definition of Poisson's ratio, cf. Eq. (5.20), lies in the plane and is always perpendicular to the stretch direction \mathbf{d} (see the inset schematic).	87
5.9	Relative Young's modulus of four different microstructures vs. relative densities $\langle\varphi\rangle$, where solid lines indicate the mean modulus and shaded envelopes show the maximum/minimum directional variations of Young's modulus across all 3D directions. Shown are results for (a) isotropic microstructures, (b) cubic microstructures, (c) columnar microstructures, and (d) lamellar microstructures. In (b)-(d) solid black lines represent a low degree of anisotropy ($a = 0.15$) and red dashed lines high degree of anisotropy ($a = 0.4$). Also included is the Voigt upper bound.	89

5.10	Microstructures obtained from non-orthogonal m_i -vectors: (a) sharp angles with the four directions $[\pm \frac{1}{\sqrt{5}}, 0, \pm \frac{2}{\sqrt{5}}]$, (b) trigonal system with six preferential directions $[0, \frac{1}{\sqrt{3}}, \frac{2}{\sqrt{3}}]$, $[\pm \frac{1}{2}, -\frac{1}{2\sqrt{3}}, \sqrt{\frac{2}{3}}]$, $[\frac{1}{\sqrt{3}}, 0, -\frac{\sqrt{2}}{\sqrt{3}}]$, $[-\frac{1}{2\sqrt{3}}, \pm \frac{1}{2}, \sqrt{\frac{2}{3}}]$. (c) and (d) show the corresponding normalized $\gamma(\mathbf{n})$ surfaces and the normalized directional Young's moduli. (e), (f) and (g) show Poisson's ratio for the two microstructures in all three orthogonal planes.	90
5.11	Spinodal microstructures printed at the macroscale with 5mm thickness and RVE width 120 mm. Original work.	91
5.12	Spinodal microstructures printed at the nanoscale with 10nm thickness and RVE width 120 μm . <i>Original joint work, courtesy of Carlos Portela, Greer Group, Caltech.</i>	91
5.13	Spinodal microstructures from Fig. 5.11 after heat treatment, colored by oxide layers.	92
6.1	Visualization of the non-convex energy potential (in 2D) for both ferroelectrics. . . .	98
6.2	Domain formation in a 3D BaTiO ₃ single-crystal with domain walls visualized by color-coding the shear stress σ_{12} (starting from initial random polarizations, the system is relaxed (Vidyasagar et al., 2017).	107
6.3	The formation of domain structures from an initially random polarization distribution in a BaTiO ₃ polycrystal: (a) polarization component p_2 (normalized by the saturated polarization p_s), (b) grain distribution, (c) shear stresses, and (d) magnification of the shear stress distribution with polarizations highlighted by the vector field. (Vidyasagar et al., 2017)	107
6.4	Electrical hysteresis and butterfly curve for BaTiO ₃ polycrystals with increasing levels of grain misorientation for a total of 50 grains with random orientations deviating by the shown maximum degrees from the electric loading axis (50 grains were chosen ensure a sufficiently large representation while being able to capture domain patterns) (Vidyasagar et al., 2017).	109
6.5	Illustration of laminate patterns arising in BaTiO ₃ polycrystals of high crystal misorientation; shown is the (normalized) vertical polarization component p_2/p_s (50 grains with random orientation deviating by the shown maximum degrees from the electric loading axis) (Vidyasagar et al., 2017).	110
6.6	Local distribution of (normalized) polarization and von Mises stress in an RVE of polycrystalline PZT throughout the electric hysteresis (Vidyasagar et al., 2017). . . .	111
6.7	Sketch of the experimental setup used to measure the average electric displacement and the (surface) strain hystereses in polycrystalline PZT samples (Vidyasagar et al., 2017).	111

6.8	Comparison between simulated and experimental hystereses (simulations used the same periodic polycrystal with 50 grains with Gaussian orientation distribution with mean 0° and standard deviation 20.42°). Note that for both curves simulated and experimental data were normalized with respect to their own values of e_c , p_s , and $\varepsilon_{\text{crit}}$, as explained in Section 6.5 (Vidyasagar et al., 2017).	113
-----	---	-----

LIST OF TABLES

<i>Number</i>	<i>Page</i>
4.1 Material parameters are adopted from Chang and Kochmann (2015) who obtained their constants by fitting to experimental results of Kelley and Hosford (1968) for individually activated slip and twin systems, together with simulation parameters.	60
6.1 Material parameters for BaTiO ₃ , adopted from Zhang and Bhattacharya (2005a), as well as simulation parameters used in numerical examples.	101
6.2 Material parameters for PZT, adopted in modified form from Völker et al. (2011), as well as simulation parameters used in numerical examples.	101

Chapter 1

INTRODUCTION

1.1 Patterns Across Scales In Nature

Patterns are characterized by periodicity and order, and pattern formation is a recurrent theme throughout nature. The autonomous formation and evolution of patterns can be experimentally observed in a variety of physical, chemical, and biological systems. Often, such patterns cascade and interact across spatial and temporal scales, and are closely associated with instabilities in the systems where they manifest.

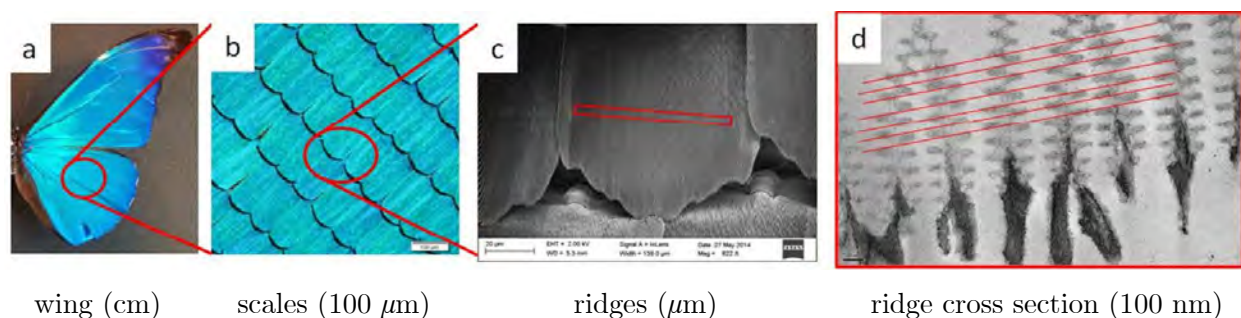


Figure 1.1: Multi-scale nature of patterns in a butterfly wing that lead to structural iridescence (Thomé et al., 2014). *Reproduced with permission.*

The visually appealing patterns that form in biological systems demonstrate the influence of structures, at lower spatial scale, on macroscopic properties. Spiral microstructures in Mantis shrimp shells and lamellar microstructures in butterfly wings both illustrate structure across scales, and arise from spinodal phase separation (Dufresne et al., 2009) and differential growth-induced instabilities (Javili et al., 2015; Kinoshita, 2013). The helicoidal biocomposite structure present in the claw of the Mantis shrimp enhances toughness required for high-velocity strikes when hunting for prey (Yaraghi et al., 2016). In Figure 1.1, various patterns in a *Morpho Rhetenor* butterfly wing are shown at different scales, forming a hierarchy which results in structural coloration (Thomé et al., 2014; Giraldo and Stavenga, 2016). Recent efforts have aimed to mimic this behavior in micro-architected systems (Huang et al., 2006; Zhang et al., 2013; Sellers et al., 2017).

Examples of natural pattern formation, of interest in mechanics, include nanoscale lamellar patterns during deformation twinning (Christian and Mahajan, 1995; Abeyaratne et al., 1996), dislocation-walls in crystal plasticity (Ortiz and Repetto, 1999; Kochmann and Hackl, 2010), martensitic phase transformations (Chu and James, 1995; Bhattacharya, 2003), dendritic hexagonal

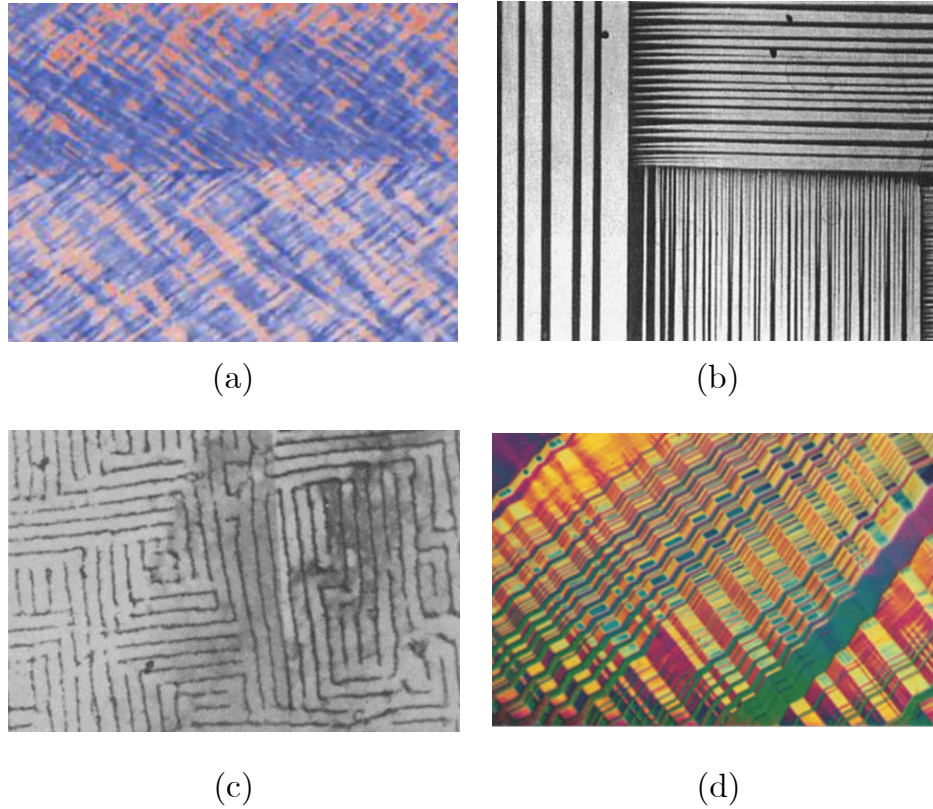


Figure 1.2: A series of natural patterns in mechanics that form from disordered initial states: (a) cross-hatched dislocation patterns in an Al bicrystal at the interface (Kuo et al., 2003), (b) twinning laminate structures in Cu-Ni (Abeyaratne et al., 1996), (c) labyrinth-type patterns in a fatigued Cu single crystal (Jin and Winter, 1984), (d) martensitic phase transformation domain patterns (Bhattacharya and James, 2005). *Reproduced with permission.*

structures in snowflake formation (Demange et al., 2017), and cellular structures through spinodal decomposition (Stanich et al., 2013). Such patterns also form in engineered systems such as periodic metamaterials which exploit multi-stability (Overvelde et al., 2012; Goncu et al., 2011; Frazier and Kochmann, 2017).

Figure 1.2 provides an illustrative overview of examples where ordered heterogeneous microstructures form from either homogeneous or disordered initial states. The patterns are not unique, exhibit great geometric intricacy, and are all attributed to inherent instabilities (Ball, 1976; Ball and James, 1987; Bhattacharya et al., 1999) which arise as a result of non-convexity in the potential energy landscapes of their respective systems.

Phenomena as different as wrinkling in thin nematic elastomer sheets (Plucinsky and Bhattacharya, 2017) and domain pattern formation in martensite (Bhattacharya, 2003) share common underlying principles. They result in energy *relaxation* and stabilize their respective systems. Re-

laxation in this instance refers to the spontaneous collapse of homogeneous non-convex systems as a means of reducing the potential energy – by modifying microstructural character using fluctuations and oscillations (Ball, 1976; Ball and James, 1987; Fonseca and Leoni, 2001). In systems that span several spatial scales, lower-scale patterns and microstructures stabilize microscopic energy landscapes – strongly influencing the macroscopic homogenized response.

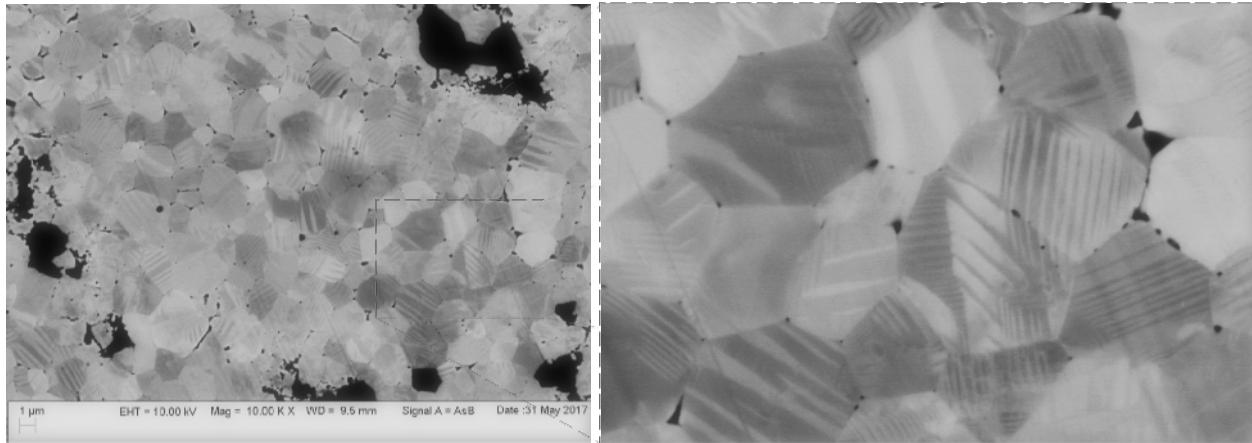


Figure 1.3: Micrograph of striped domain patterns forming within grains of ferroelectric PZT polycrystal during fatigue cycling. *Courtesy of Wei-Lin Tan, Caltech.*

Experimentally, pattern formation has been investigated through application of external mechanical, thermal, or electric fields to non-convex material systems. Examples of particular significance to this thesis include domain pattern evolution in ferroelectrics (Merz, 1956; Gao et al., 2013; Chaplya and Carman, 2002b; Wojnar et al., 2014), martensitic phase transformation (Bhattacharya, 2003), spinodal decomposition during dealloying (Erlebacher et al., 2001; Geslin et al., 2015), and dislocation-induced microstructure formation (Jin and Winter, 1984; Kuo et al., 2003). For polycrystalline materials undergoing mechanical loading, texture, anisotropy, and inhomogeneity resulting from microstructure formation influence yield strength, toughness, Young’s modulus, and mechanical damping coefficient. These mechanical fields are often strongly coupled to electric potentials and temperature. For example, in ferroelectrics, applied electric fields induce strains and applied stresses induce potential differences (Wojnar et al., 2014). Experiments show lamellar polarization domain formation in polycrystals, and resulting macroscale electric field-induced mechanical strains (Merz, 1956). Figure 1.3 illustrates unidirectional patterns within grains, exhibiting correlation with damage initiation sites. Engineering resilient and tunable ferroelectric composites requires a deeper understanding of underlying damage mechanisms during cyclic electromechanical loading.

The interplay between the laws of thermodynamics and non-equilibrium kinetics provides a path to autonomously predict the pattern formation process. In the following section, the

origin of instabilities and non-convexity will be explained in detail together with the mathematical preliminaries required for further investigation. Subsequently, an overview of previous numerical approaches taken towards predictive modeling will be provided.

1.2 Energy Relaxation and Microstructures

Fine-scale oscillations which develop into complex geometric patterns have their origin in non-(quasi)convex energetic potentials (Ericksen, 1975; Ball and James, 1987; Chipot and Kinderlehrer, 1988; Bhattacharya et al., 1999; Govindjee et al., 2003). These arise as energy-infimizing sequences, allowing for energy relaxation by way of effective *quasiconvexification* of the potential energy landscape (Dacorogna, 1989; Ball and James, 1987).

The classical variational framework developed by Truesdell and Noll (1965), describing the quasi-static boundary value problem in finite strains, is of primary importance to this discussion. A deformation map φ relates the deformed configuration $\mathbf{x} = \varphi(\mathbf{X})$, as a function of the undeformed positions \mathbf{X} within a volume Ω , such that it minimizes the overall total potential energy functional,

$$\mathcal{I}[\varphi] = \int_{\Omega} W(\nabla\varphi) dV - \ell(\varphi), \quad (1.1)$$

where $W(\nabla\varphi)$ denotes the stored energy density and $\ell(\varphi)$ the potential of externally applied fields. In the case of linearized kinematics, the functional depends on the displacement field \mathbf{u} and the infinitesimal strain tensor $\boldsymbol{\varepsilon} = \text{sym}(\nabla\mathbf{u})$,

$$\mathcal{I}[\mathbf{u}] = \int_{\Omega} W(\boldsymbol{\varepsilon}) dV - \ell(\mathbf{u}), \quad (1.2)$$

where

$$W(\boldsymbol{\varepsilon}) = \frac{1}{2} \boldsymbol{\varepsilon} : \mathbb{C} : \boldsymbol{\varepsilon} = \frac{1}{2} \varepsilon_{i,j} \mathbb{C}_{i,j,k,l} \varepsilon_{k,l} \quad (1.3)$$

Given a strongly elliptic stiffness tensor, and with appropriate boundary conditions, the energy functional is convex – and there exists a unique minimum and solution field to the convex optimization problem (Koiter, 1965). An analogous hyperelastic model, however, does not share the same characteristics. Using the Green-Lagrange strain tensor

$$\mathbf{E}(\nabla\varphi) = \frac{1}{2} (\nabla\varphi^T \nabla\varphi - \mathbf{I}), \quad (1.4)$$

consider the energy landscape described by

$$W(\nabla\varphi) = \frac{1}{2} \mathbf{E} : \mathbb{C} : \mathbf{E} = \frac{1}{8} (\nabla\varphi^T \nabla\varphi - \mathbf{I}) : \mathbb{C} : (\nabla\varphi^T \nabla\varphi - \mathbf{I}). \quad (1.5)$$

This yields the classic St. Venant-Kirchhoff hyperelastic model, which unfortunately lacks (quasi)convexity (Le Dret and Raoult, 1995) – this is clearly illustrated using a one-dimensional projection.

The stiffness tensor of an isotropic St. Venant-Kirchhoff solid depends only on the two Lamé parameters:

$$\mathbb{C}_{IJKL} = \lambda \delta_{IJ}\delta_{KL} + \mu (\delta_{IK}\delta_{JL} + \delta_{IL}\delta_{JK}), \quad \lambda, \mu > 0. \quad (1.6)$$

Through application of a deformation gradient of uniaxial compression and shear,

$$\nabla\varphi = \begin{pmatrix} 1 - \gamma & -2\gamma & 0 \\ 0 & 1 & 0 \\ 0 & 0 & 1 \end{pmatrix}, \quad \gamma < 1, \quad (1.7)$$

the non-convex energy in Eq. (1.5) can be projected along the loading parameter γ ,

$$W(\nabla\varphi) = \frac{1}{8}\gamma^2 \left(2 \left(25\gamma^2 - 20\gamma + 12 \right) \mu + (2 - 5\gamma)^2 \lambda \right). \quad (1.8)$$

This is shown in Figure 1.4, revealing a loss of convexity as the shear modulus μ is decreased. The second derivative of this projected potential changes sign within the loading regime and indicates instability. The problem becomes ill-posed in the sense of Hadamard (1923) and the solution loses uniqueness. Eventually, as shear parameter μ approaches the zero-limit, a symmetric, bi-stable double-well potential energy landscape is attained. Symmetric bi-stable energies of this form, condensed to functions of specific loading parameters, will be encountered frequently in this thesis. As will be analyzed later in Chapter 3, unphysical patterns form when material models of this type are used. While this is simply a sub-optimal choice for material modeling, the same behavior manifests in physical systems exhibiting non-convexity and pattern formation. Several of these are shown in Figure 1.5. As mathematical preliminaries, definitions of the various notions of convexity and existence of minimizers are required for further analysis.

The generalized form of the variational boundary value problem for finite-strain elasto-plasticity deals with both internal variables and dissipation, as will be elaborated in Chapter 4, but for illustrative purposes, the finite-strain example in Eq. (1.1) is deemed sufficient. The principle of minimum potential energy dictates that the deformation gradient field $\mathbf{F} = \nabla\varphi$ (in the absence of external potentials) can be found through the minimum principle given a volume Ω ,

$$\varphi = \arg \inf \{ \mathcal{I}[\varphi] \mid \varphi = \varphi^0 \text{ on } \partial\Omega \}. \quad (1.9)$$

Often, this leads to a minimization problem which can be handled numerically. However, for the existence of a minimizer to the functional \mathcal{I} , it has to satisfy the three important conditions of boundedness, coercivity, and weakly lower semi-continuity, which are defined as follows:

(a) boundedness:

$$\exists \alpha, \beta \in \mathbb{R} : | \mathcal{I}[\mathbf{F}] | \leq \alpha (1 + \| \mathbf{F} \|^{\beta}), \quad \forall \mathbf{F}, \quad \alpha > 0, \quad \beta \geq 1 \quad (1.10)$$

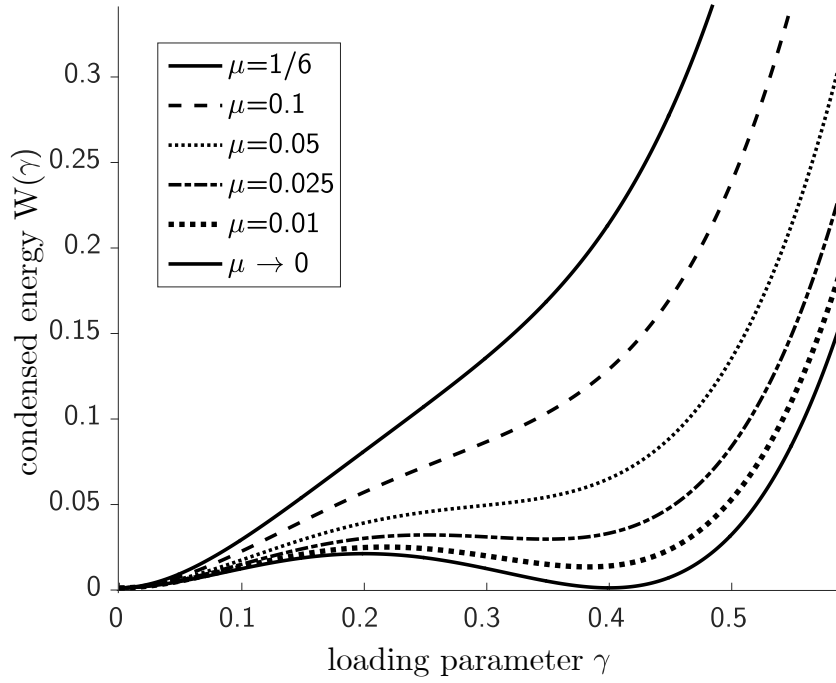


Figure 1.4: Loss of convexity of the condensed energy $W(\gamma)$ with decreasing μ , for $\lambda = 1$.

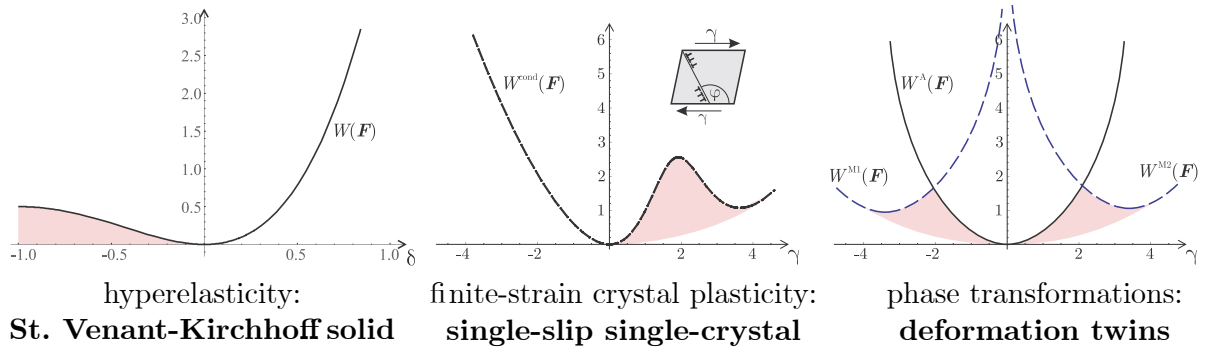


Figure 1.5: Examples of loss of convexity in systems exhibiting pattern formation.

(b) coercivity:

$$\exists \alpha, \beta, \gamma \in \mathbb{R} : |I[\mathbf{F}]| \geq (\gamma + \alpha \|\mathbf{F}\|^\beta), \forall \mathbf{F}, \alpha > 0, \beta \geq 1 \quad (1.11)$$

(c) weakly lower semi-continuity for weakly convergent sequences $\varphi \rightharpoonup \varphi_n$:

$$\liminf_{n \rightarrow \infty} I[\nabla \varphi_n] \geq I[\nabla \varphi]. \quad (1.12)$$

As shown by Ball (1977), the conditions can be recast into constraints on the energy density $W(\mathbf{F})$ of boundedness, coercivity and quasiconvexity. Before specifically examining the quasiconvexity condition, a discussion of the different notions of convexity, all of which converge for a one-dimensional functional, is imperative. The following defines these different notions for a function $W(\mathbf{F})$ (Morrey, 1952; Rockafellar, 1970; Ball, 1977; Šverák, 1992):

(a) convexity:

$$\forall \lambda \in [0, 1] : W(\lambda \mathbf{F}^1 + (1 - \lambda) \mathbf{F}^2) \leq \lambda W(\mathbf{F}^1) + (1 - \lambda) W(\mathbf{F}^2), \quad \forall \mathbf{F}^1, \mathbf{F}^2 \in \text{GL}^+(\text{d}) \quad (1.13)$$

(b) polyconvexity (*in simplified matrix notation*):

$$W(\mathbf{F}) = W(\mathbf{F}, \det \mathbf{F}, \text{cof } \mathbf{F}) \quad (1.14)$$

(c) quasiconvexity:

$$W(\mathbf{F}) \leq \frac{1}{\omega} \int_{\omega} W(\mathbf{F} + \nabla \phi) \, dV, \quad \phi = 0 \text{ on } \partial\omega, \quad \forall \omega \in \mathbb{R}^n \quad (1.15)$$

(d) rank-one convexity:

$$\forall \lambda \in [0, 1] : W(\lambda \mathbf{F}^1 + (1 - \lambda) \mathbf{F}^2) \leq \lambda W(\mathbf{F}^1) + (1 - \lambda) W(\mathbf{F}^2), \quad (1.16)$$

with the additional constraint that

$$\text{rank}(\mathbf{F}^1 - \mathbf{F}^2) \leq 1, \quad \mathbf{F}^1, \mathbf{F}^2 \in \text{GL}(\text{d}). \quad (1.17)$$

The following implication is crucial for both analysis and numerical computation:

$$W_{\text{convex}} \Rightarrow W_{\text{polyconvex}} \Rightarrow W_{\text{quasiconvex}} \Rightarrow W_{\text{rank-one convex}}, \quad (1.18)$$

but the inverse is not true. Energy hulls or envelopes can be defined for any arbitrary non-convex function, each of which satisfies the corresponding degree of convexity – namely the convex envelope (CW), polyconvex envelope (PW), quasiconvex envelope (QW), and rank-one convex envelope (RW):

$$CW(\mathbf{F}) = \inf \left\{ \sum_{i=1}^n \lambda_i W(\mathbf{F}_i) \mid \lambda_i, \mathbf{F}_i; \sum_{i=1}^n \lambda_i = 1, \lambda_i \in [0, 1], \sum_{i=1}^n \lambda_i \mathbf{F}_i = \mathbf{F} \right\} \quad (1.19)$$

$$PW(\mathbf{F}) = \inf \left\{ \sum_{i=1}^n \lambda_i W(\mathbf{F}_i) \mid \lambda_i, \mathbf{F}_i; \sum_{i=1}^n \lambda_i = 1, \lambda_i \in [0, 1], \sum_{i=1}^n \lambda_i \mathbf{F}_i = \mathbf{F}, \right. \\ \left. \sum_{i=1}^n \lambda_i \det(\mathbf{F}_i) = \det(\mathbf{F}), \sum_{i=1}^n \lambda_i \text{cof}(\mathbf{F}_i) = \text{cof}(\mathbf{F}) \right\} \quad (1.20)$$

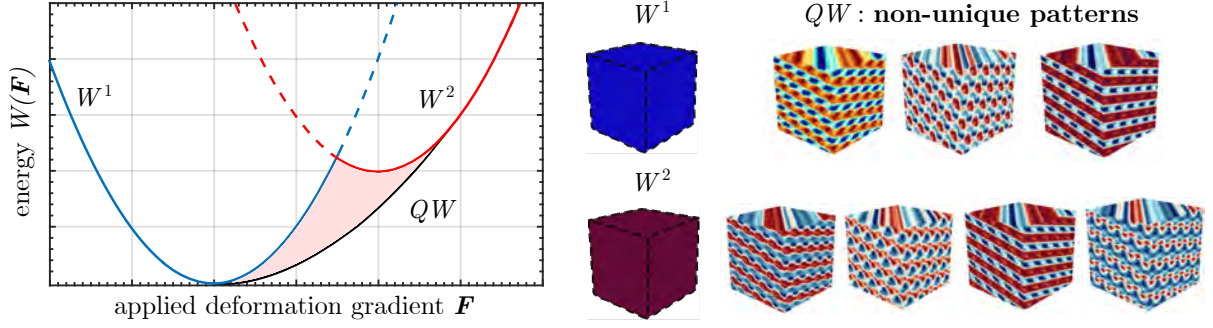


Figure 1.6: $QW(\mathbf{F})$ for phase transitions with $W(\mathbf{F}) = \min(W^1(\mathbf{F}), W^2(\mathbf{F}))$. Spontaneous breakdown of the homogeneous blue and red phases at a deformation gradient state corresponding to the quasiconvex envelope results in (non-unique) pattern formation.

$$QW(\mathbf{F}) = \inf \left\{ \frac{1}{|\omega|} \int_{\omega} W(\mathbf{F} + \nabla \phi) \, dV \mid \phi : \phi = 0 \text{ on } \partial\omega \right\}. \quad (1.21)$$

Of particular interest here is the quasiconvex envelope, which, in the most general case, requires a non-local computation within a representative volume of all possible perturbation fields (representing non-unique patterns). A visual representation of the patterns corresponding to the quasiconvex envelope is shown in Fig. 1.6 for a phase transformation example.

In the absence of *regularization*, the energy infimization problem is formulated as an infinite-dimensional non-convex optimization problem and has traditionally been regarded as intractable except for a few specific examples. Classical approaches tend to find the significantly more tractable rank-one convex hull instead. In special cases, it is possible to prove that the polyconvex hull (lower bound) coincides with the rank-one convex hull (upper bound) – with both converging to the quasiconvex hull (Ball, 1976; Conti et al., 2009, 2015).

The rank-one convex hull (RW) is defined in a recursive manner, providing a method of constructing approximations. A first-order construction with two phases yields an approximation of the rank-one convex envelope (Ortiz and Repetto, 1999; Hackl et al., 2014; Dmitrieva et al., 2015):

$$R_1 W(\mathbf{F}) = \inf \left\{ \lambda_1 W(\mathbf{F}_1) + \lambda_2 W(\mathbf{F}_2) \mid \lambda_i, \mathbf{F}_i : \sum_{i=1}^n \lambda_i = 1, \lambda_i \in [0, 1], \right. \\ \left. \sum_{i=1}^n \lambda_i \mathbf{F}_i = \mathbf{F}, \text{rank}(\mathbf{F}_1 - \mathbf{F}_2) \leq 1 \right\}, \quad \mathbf{F}_1, \mathbf{F}_2 \in GL_+(d). \quad (1.22)$$

This corresponds to a laminate-type microstructural pattern associated with the relaxed energy state. Recursive application of this procedure physically represents higher-order laminates (i.e.,

sequential lamination) (Ortiz and Repetto, 1999; Aubry et al., 2003). For example, a construction of order k is defined by

$$R_{k+1} W(\mathbf{F}) = \inf \left\{ \lambda_1 R_k W(\mathbf{F}_1) + \lambda_2 R_k W(\mathbf{F}_2) \mid \lambda_i, \mathbf{F}_i : \sum_{i=1}^n \lambda_i = 1, \lambda_i \in [0, 1], \right. \\ \left. \sum_{i=1}^n \lambda_i \mathbf{F}_i = \mathbf{F}, \text{rank}(\mathbf{F}_1 - \mathbf{F}_2) \leq 1 \right\}. \quad (1.23)$$

The $k \rightarrow \infty$ limit of sequential lamination provides the rank-one convex hull:

$$R W(\mathbf{F}) = \lim_{k \rightarrow \infty} R_k W(\mathbf{F}). \quad (1.24)$$

Laminate constructions are important tools for approximating relaxed energies in a variety of material systems including single-slip single-crystal plasticity (Ortiz and Repetto, 1999; Conti et al., 2015). However, precise geometric arrangement cannot be interpreted from the results, particularly for higher-order laminates. Realistic pattern formation in physical systems with multi-stable energy potentials, such as phase transformations (Chu and James, 1995; Bhattacharya, 2003), exhibits complexity and autonomous prediction of these patterns requires a different numerical approach.

Laminate constructions face another limitation when dealing with micro-scale heterogeneities, such as polycrystals, or multi-component volumes, where each grain or material has different energetic potentials. Compatibility, enforced at internal grain or phase boundaries, is non-trivial to incorporate into this approach. In such cases, patterns across internal interfaces, such as laminates extending across grain boundaries are strongly affected by the crystallography and grain boundary mismatch (Vidyasagar et al., 2018). Additionally, the minimizing sequence of a non-convex functional collapses into finer and finer oscillations (Kinderlehrer and Pedregal, 1991), highlighting the need for regularization and introduction of a length-scale.

In nature, patterns form at specific length scales because interfaces are associated with *interfacial energy*. Sharp gradients result in a significant increase in the energy of the system; therefore, at equilibrium, interfaces exhibit smoothness and a finite width. This determines the overall length scale of pattern formation (Giorgi, 2009).

Gurtin (1987) and subsequently Modica (1987) introduced the term interfacial energy as a gradient contribution in the energy functional to be minimized – based on the role of physical interface energies in nature. This results in an additional contribution to the infimization problem in Eq. (1.9), for Dirichlet boundary conditions,

$$\varphi = \arg \inf \left\{ \int_{\Omega} W(\nabla \varphi) + W^h(\nabla^{m+1} \varphi) \, dV - \ell(\varphi) \mid \varphi = \varphi^0 \text{ on } \partial\Omega \right\}, \quad (1.25)$$

for an order of regularity m .

While the unregularized minimization solution could lead to sharp interfaces and strong jumps in the local properties (e.g., deformation gradient or plastic slips), regularization smears out sharp contrast over a small but finite interface. Importantly, regularization does not make the minimization convex – instead, it ensures that the solution is smooth to the order of regularity (Clarke and Vinter, 1985). Regularization, through penalization of higher gradients, also increases the strength of local minima, which correspond to patterns and may affect the ability to find global minima.

Therefore, regularized, full-field numerical treatment of representative volume elements (RVEs, discussed in detail in Sec. 2.1) becomes inevitable in predicting autonomous microstructural pattern formation in complex systems while capturing interfaces. Previous work on numerical quasi-convexification has relied on the finite element method (Bartels et al., 2004; Bartels and Prohl, 2004; Carstensen and Plecháč, 1997; Bartels et al., 2006). However, direct numerical methods introduce an *implicit regularization* which results in mesh- and interpolation-dependent solutions. Particularly, the low-order local FE interpolation results in coarse microstructural patterns (Carstensen, 2005). Extensions to high resolution and polynomial-order, for simultaneously capturing complex patterns and achieving close quasiconvex hull approximations, are prohibitively expensive. This has restricted previous efforts to two-dimensional toy models such as the single-crystal single-slip problem (Klusemann and Kochmann, 2014).

The aim of this dissertation is to predict realistic and autonomous patterns while simultaneously comparing the associated relaxed energies to the quasiconvex envelopes for benchmark problems to ensure viability. The numerical method of choice is a Fourier spectral formulation (Moulinec and Suquet, 1998, 2003; Lebensohn et al., 2012) with implicit regularization, as detailed by Vidyasagar et al. (2017, 2018). Calculations are performed on representative volume elements following the principles of periodic homogenization (Miehe et al., 2002), which naturally admit the spectral interpolation. It is hence important to understand that, when computing numerical approximations, the Dirichlet boundary conditions in the classical definition of the quasiconvex hull, Eq. (1.21), may be replaced by the periodic representation,

$$QW(\mathbf{F}) = \inf \left\{ \frac{1}{|\omega|} \int_{\omega} W(\mathbf{F} + \nabla \phi) \, dV \mid \phi \text{ periodic} \right\}, \quad (1.26)$$

when the functional is non-negative, continuous and the energy density has bounded growth which is at most quadratic (Ball and Murat, 1984; Allaire and Francfort, 1998). Consequently, the perturbation fields representing patterns will be periodic rather than vanishing at the RVE boundaries $\partial\omega$.

Recently developed finite-difference-based spectral corrections inspired by Willot et al. (2014), Berbenni et al. (2014) and Lebensohn and Needleman (2016) and explained by Vidyasagar et al.

(2017, 2018) introduce an implicit regularization to the non-convex minimization problem. This is shown to vanish in the limit of mesh refinement, ensuring a consistent numerical scheme. This class of methods allow for reasonable approximations of the quasiconvex hull and reproduce autonomous patterns from homogeneous or chaotic RVE initial conditions, as shown through numerical examples in Chapter 3.

The mathematical preliminaries thus far have avoided discussions of inelasticity and internal variables but the energy-infimization strategies broadly extend to these cases. Detailed derivations will be provided in Chapters 3, 4, 5, and 6. However, understanding microstructural pattern formation through pure energy infimization strategies ignores two critical (and related) aspects of dissipation and kinetics.

1.3 Dissipation and Kinetic Models

Dissipation prevents microstructures from rapidly fluctuating in time, and is therefore crucial for modeling the time evolution of microstructures. The various prevalent kinetic models found in material modeling are briefly reviewed in this section. Previous numerical approaches to modeling dissipative systems, in particular metal visco-plasticity, include variationally consistent time-incremental formulations (Ortiz and Repetto, 1999; Miehe et al., 2002; Kochmann, 2009). Complications arise when multiple deformation-accommodating mechanisms, such as twinning and dislocation-induced plasticity, interact in complex polycrystals (Vidyasagar et al., 2018). In such situations, multiple sources of non-convexity result in highly complex microstructural features defying analytical treatment. These fine microstructural features influence macroscopic mechanical response – such as in the case of magnesium with hexagonal close-packed crystallography (see Figure 1.7). Magnesium is an ideal candidate for investigation because of experimental and atomistic evidence of strongly anisotropic inelasticity (Pollock, 2010; Dixit et al., 2015; Sun et al., 2018).

In the class of thermodynamically admissible evolution laws (satisfying the *Clausius–Duhem* inequality), gradient-flow kinetics are of particular interest because of their inherent simplicity, simulating processes which are driven by the first variation of the energy functional. There has been a plethora of efforts to study phase separations and transitions using gradient-flow kinetics and second-order regularization (see Chen (2002) and references therein). These *phase-field models* share a non-convex multi-well energetic potential, often termed the *Ginzburg-Landau*-type free energy. For kinetic models, regularization, as aforementioned, increases the strength of local minima and tends to overpredict hysteresis – therefore an appropriate length scale has to be chosen for fine scale patterns with thin interfaces to accurately reproduce the underlying physics. Phase separations require conservative evolution laws, and hence use the *Cahn-Hilliard*

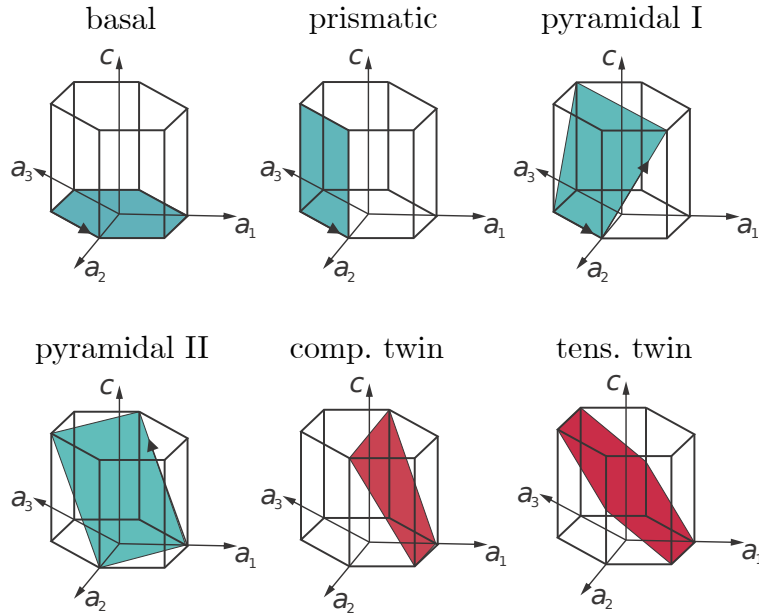


Figure 1.7: An overview of the variety of dislocation slip and twinning modes in magnesium.

(Cahn and Hilliard, 1958) approach (or equivalently H^{-1} -gradient flow), while phase transitions are non-conservative with an *Allen-Cahn* (Allen and Cahn, 1979) approach (or L^2 -gradient flow).

The Cahn-Hilliard model has classically been used to study the phenomenon of spinodal decomposition. Phase separation through spinodal decomposition occurs during dealloying (Erlebacher et al., 2001; Lu et al., 2007), thin film growth (Bergamaschini et al., 2016) and intercellular lipid-fluid demixing (Stanich et al., 2013). While previous works have focused on isotropic demixing (Chen, 2002; Fultz, 2014), understanding the influence of anisotropic free energy functionals on the kinetics of microstructural pattern formation necessitates further investigation. In addition to the fundamental insight gained from simulations, computational architectures obtained by tuning anisotropic spinodal decomposition have a variety of practical applications including the design of metamaterials.

In contrast to the role of dissipation in preventing microstructural fluctuations, kinetics drive spontaneous jumps across different (stable) equilibrium configurations in ferroelectric materials (von Schwerin and Szepessy, 2010). Allen-Cahn equations have gained traction for modeling phase transitions and ferroelectrics are of particular appeal because free energies can be adopted from *ab initio* quantum mechanical approximations through Density Functional Theory (DFT) (Völker et al., 2011; Vidyasagar et al., 2017). Additionally, there is a wealth of experimental data for the propagation of domain walls as transitions waves (or topological solitons) in ferroelectric crystals

starting with the seminal work of [Merz \(1956\)](#). Theoretical and numerical understanding regarding the relationship between the kinetic model and domain wall behavior is critical for engineering novel electromechanical devices using ferroelectrics.

1.4 Outline

Following this introduction, [Chapter 2](#) begins with a brief discussion of homogenization, and derivations of FFT-based spectral methods. Recently introduced spectral corrections based on finite-difference schemes are then detailed, and their influence on mitigating oscillatory artifacts is demonstrated.

[Chapter 3](#) details how the numerical methods are used to solve quasistatic energy-minimization problems and predict autonomous pattern formation from homogeneous initial conditions. Starting with the hyperelastic St. Venant-Kirchhoff solid as a benchmark example, with available analytic quasiconvex envelopes, a generalized constitutive model is developed for phase transitions with arbitrary transformation strains for studying pattern formation. A third example of mathematical relevance to lamination theory, the single-slip single-crystal model, concludes this chapter.

[Chapter 4](#) extends the single-slip model to full crystal plasticity in hexagonal close-packed magnesium, introducing dissipation and plastic flow. Numerical results showing additional complexity due to multiple deformation modes and slip-twinning interactions are illustrated. Periodic homogenization of polycrystals and the influence of microstructure are discussed with examples.

[Chapter 5](#) introduces gradient flow kinetics (Cahn-Hilliard), which are then used to model scalar anisotropic spinodal decomposition. Novel numerical results in understanding elastic surfaces and microstructural morphologies during the relaxation processes are discussed. This chapter concludes with applications including the design of metamaterials.

[Chapter 6](#) discusses the kinetics (Allen-Cahn) of phase transitions in ferroelectrics. Particular focus is on numerical and physical implications of scale-bridging using DFT-informed model constants for the non-convex energy landscape. Experimental validation is also performed for predictions of domain pattern formation, strain and polarization hystereses, and the motion of domain walls.

[Chapter 7](#) concludes this thesis with a summary of the original results and contributions. Suggestions for improved numerical strategies and physical models are provided together with future research directions and applications of the presented work.

Chapter 2

DEVELOPMENT OF SPECTRAL HOMOGENIZATION SCHEMES

Research presented in this chapter has been adapted from the following publications:

Vidyasagar, A., Tan, W. L., Kochmann, D. M. 2017. Predicting the effective response of bulk polycrystalline ferroelectric ceramics via improved spectral phase field methods. *Journal of the Mechanics and Physics of Solids* 106, 113-151.

URL: <https://doi.org/10.1016/j.jmps.2017.05.017>

Vidyasagar, A., Tutcuoglu, A., Kochmann, D. M. 2018. Deformation patterning in finite-strain crystal plasticity by spectral homogenization with application to magnesium. *Computer Methods in Applied Mechanics and Engineering*, 335, pp.584-609.

URL: <https://doi.org/10.1016/j.cma.2018.03.003>

2.1 Introduction to Computational Homogenization

Homogenization procedures elucidate the dependence of the macroscale response of a system on the microscale features (Suquet, 1987; Miehe and Koch, 2002; Stolz, 2010). In the case of systems exhibiting pattern formation due to non-(quasi)convexity of the energy landscape, patterns tend to form on the microscale in the short-wavelength limit, and the relaxed energy landscape manifests at the macroscale. It is important to note that the terms *micro* and *macro* do not pertain to specific length measures – but the two different scales in a system where *scale-separation* occurs.

In the process of homogenization of a two-scale problem, a key assumption involves statistical homogeneity at the macro-scale in spite of lower-scale patterns and inhomogeneous microstructures. Consequently, volume averages (with respect to the undeformed configurations) at the lower scale,

$$\langle \cdot \rangle_{\Omega} = \frac{1}{V} \int_{\Omega} (\cdot) \, dV, \quad (2.1)$$

of a statistically representative volume element (RVE) Ω , with $V = |\Omega|$, are used to obtain the homogenized macroscale response. The averaging theorems for finite-deformation kinematics (Miehe, 2003) state that, given *continuous* displacement ($\boldsymbol{\varphi}$) and traction (\boldsymbol{T}) fields, in the absence of body forces, the average deformation gradient \boldsymbol{F} and first Piola-Kirchhoff stress tensor \boldsymbol{P} become

$$\langle \boldsymbol{F} \rangle = \frac{1}{V} \int_{\partial\Omega} \boldsymbol{\varphi} \otimes \boldsymbol{N} \, dS \quad \text{and} \quad \langle \boldsymbol{P} \rangle = \frac{1}{V} \int_{\partial\Omega} \boldsymbol{T} \otimes \boldsymbol{X} \, dS. \quad (2.2)$$

Identification of statistical RVEs for homogenization requires either very high-resolution simulations (large RVEs) within volumes Ω of length L , where the characteristic length scale is denoted as l , using the limit

$$\lim_{L/l \rightarrow \infty} \langle \cdot \rangle_{\Omega(L)} = \langle \cdot \rangle_{\infty}^S \quad (2.3)$$

or by ensemble averaging over many realizations of different RVEs with different microstructures and using the central limit theorem,

$$\lim_{N \rightarrow \infty} \frac{1}{N} \sum_{i=1}^N \langle \cdot \rangle = \langle \cdot \rangle_{\infty}^E. \quad (2.4)$$

Fast spectral methods, discussed in the following Section 2.2, are well suited for both high-resolution computations, and producing many realizations of RVEs, but are limited to periodic boundary conditions. For a cubic RVE, in a finite-deformation framework, these periodic boundary conditions are given as

$$\boldsymbol{\varphi}^+ - \boldsymbol{\varphi}^- = \langle \mathbf{F} \rangle (\mathbf{X}^+ - \mathbf{X}^-) \quad \text{and} \quad \mathbf{T}^+ = -\mathbf{T}^- \quad (2.5)$$

for opposite surfaces and regions on the (+) and (-) (i.e. faces, edges and corners). Periodic homogenization yields a mechanical response that lies between homogenization by affine displacements (upper bound) and through uniform tractions (lower bound).

The equivalence of the effective homogenized variation of energy density W on the macroscale,

$$\delta W^* = \mathbf{P}^* : \delta \mathbf{F}^*, \quad (2.6)$$

and the volume average on the microscale,

$$\frac{1}{V} \int \delta W dV = \frac{1}{V} \int \frac{\partial W}{\partial \mathbf{F}} : \delta \mathbf{F} dV = \frac{1}{V} \int \mathbf{P}(\mathbf{X}) : \delta \mathbf{F} dV = \langle \mathbf{P}(\mathbf{X}) : \delta \mathbf{F}(\mathbf{X}) \rangle, \quad (2.7)$$

is an important postulate in homogenization theory, resulting in the Hill-Mandel condition (Mandel, 1966; Hill, 1972; Mandel, 1983) for effective stresses and deformation gradients,

$$\mathbf{P}^* : \delta \mathbf{F}^* = \langle \mathbf{P}(\mathbf{X}) : \delta \mathbf{F}(\mathbf{X}) \rangle. \quad (2.8)$$

This condition is satisfied by applying periodic boundary conditions:

$$\begin{aligned} \langle \mathbf{P} : \mathbf{F} \rangle &= \frac{1}{V} \int_{\partial \Omega} \mathbf{T} : \boldsymbol{\varphi} dS \\ &= \frac{1}{V} \int_{\partial \Omega^+} \mathbf{T}^+ : \boldsymbol{\varphi}^+ dS + \frac{1}{V} \int_{\partial \Omega^-} \mathbf{T}^- : \boldsymbol{\varphi}^- dS \\ &= \frac{1}{V} \int_{\partial \Omega} \mathbf{T} : \langle \mathbf{F} \rangle \mathbf{X} dS \\ &= \langle \mathbf{F} \rangle : \left(\frac{1}{V} \int_{\partial \Omega} \mathbf{T} \otimes \mathbf{X} dS \right) \\ &= \langle \mathbf{F} \rangle : \langle \mathbf{P} \rangle. \end{aligned} \quad (2.9)$$

Enforcing averages for periodic homogenization is especially suited for Fourier spectral techniques because the averages correspond to amplitude at the origin in Fourier space. In the chosen periodic homogenization scheme for the following chapters, average deformation gradients and primary external fields are imposed, and when using iterative methods in Fourier space only the higher wavenumbers ($K \neq 0$) require computation.

2.2 Fast Fourier Spectral Methods

Fast Fourier transform (FFT) algorithms began informally with the work of Carl Friedrich Gauss (Gauss, 1866), popularized with the widely used *Cooley-Tukey* method by Cooley and Tukey (1965) and expanded by Rader (1968), Bluestein (1970), Winograd (1978) and numerous others. Conveniently, these algorithms have been implemented as part of the highly optimized FFTW software package (Frigo and Johnson, 1998), which has revolutionized scientific computing in recent decades. Particularly, this has resulted in a resurgence of interest in FFT-based *spectral methods*. Spectral methods typically perform a diagonalization of the differential operator, resulting in quasi-linear scaling, matrix-free numerical algorithms. While Fourier spectral methods have been in use since Fourier (1822), various iterative methods of solving non-linear partial differential equations have attracted attention in recent decades. Such spectral methods naturally suit periodic boundary conditions due to global interpolation using (periodic) trigonometric shape functions. The problem of numerically evaluating quasiconvex envelopes through periodic homogenization, with regular cubic representative volumes, is hence ideal for this approach.

In the context of mechanics, Moulinec and Suquet (1998, 2003) developed an FFT-based iterative spectral method for periodic homogenization of composites. The original technique is a Richardson iteration scheme which avoids the expensive convolution operation, due to non-linear nature of the Lippmann-Schwinger equation in homogenization theory (Pruchnicki, 1998; Brisard and Legoll, 2014; Brisard, 2017). The key advantage of this iterative approach is the quasi-linear scaling of computational cost with grid size, due to the matrix-free nature of the solution technique (Vidyasagar et al., 2017). Simultaneously, for problems with smooth solutions, the error of spectral methods converges exponentially with grid size, making this class of solution techniques very attractive for regularized non-convex minimization problems.

There has been significant progress in using the original Moulinec-Suquet scheme for a variety of problems in mechanics including finite-strain crystal visco-plasticity (Lebensohn et al., 2012; Eisenlohr et al., 2013; Lebensohn and Needleman, 2016; Vidyasagar et al., 2018) and multi-physical systems including electro-mechanical coupling (Brenner, 2009; Vidyasagar et al., 2017). Additionally, various works have aimed at accelerating and improving the convergence behavior. A comprehensive review of Newton-Raphson and Krylov subspace methods has been presented by

Kabel et al. (2014). The work of Mishra et al. (2015) details low-memory iterative techniques for solving the Lippmann-Schwinger homogenization problem. Shanthraj et al. (2015) list a comparison of the general computational costs of non-linear extensions of the Moulinec-Suquet scheme up to generalized minimal residual method (GMRES) accelerated methods. Finally, Kochmann et al. (2016, 2017) have implemented hierarchical multi-scale FE-FFT coupled frameworks for dealing with elasto-plasticity in polycrystals.

Spectral methods have inherent drawbacks preventing their widespread use, particularly in mechanics. In the presence of interfaces or boundaries in heterogeneous domains, high contrasts in properties result in strong discontinuities. These pose numerical challenges (Michel et al., 2001; Moulinec and Silva, 2014) for the original Moulinec-Suquet method. The convergence properties of the original method depended on the spectral radius of the *Green's* operator in the Lippmann-Schwinger equation, which is a function of the initial guess for the homogenized/reference stiffness tensor. Since it is not trivial to bound this set of tensors using their spectral radius, the original method has no guarantee of convergence. When using an average elasticity tensor as the initial guess, higher contrasts have been observed to render the original method impractical because of the large number of iterations required for convergence (Willet et al., 2014).

The second major issue is fundamental to interpolations which use smooth functions to approximate discontinuities. Here ringing artifacts related to *Gibbs instabilities* (Gibbs, 1898, 1899; Hewitt and Hewitt, 1979) corrupt the approximation and render numerical methods unstable. Recently, filtering techniques based on composing finite-difference templates onto spectral schemes have gained interest for mitigating oscillatory phenomena. These involve using modified Green's operators derived from wave vectors which are analytically computed *a priori* using finite-difference approximations. To first-order, these approximations recover the Lanczos σ -correction (Lanczos, 1956; Hamming, 1986) for Fourier series. Starting with the work of Mueller (1998), first-order finite-difference approximations have been adopted by (Berbenni et al., 2014; Brisard and Dormieux, 2010; Lebensohn and Needleman, 2016) in homogenization using iterative spectral methods to avoid these ringing artifacts. Similarly, Willet et al. (2014) extended these to rotated schemes which markedly improved quality of approximations.

As will be detailed in Sec. 2.5 arbitrary higher-order schemes can be derived using analytical transforms of various difference stencils and these are both consistent and *h*-convergent with refinement (Vidyasagar et al., 2017). In the work of Vidyasagar et al. (2017), it was shown that these methods were applicable to pattern formation in the context of non-convexity in ferroelectrics – this will be discussed in further detail in Chapter 6. In addition to reducing the ringing artifacts, the augmented schemes add artificial regularization to the energy minimization problem as detailed in Vidyasagar et al. (2018); these will be described in Sec. 2.6.

2.3 Iterative Spectral Methods

In this section, the basic iterative scheme established in the original work by [Moulinec and Suquet \(1998\)](#), and improvements thereof, are applied to a finite-deformation elasticity problem. This scheme solves the non-linear Lippmann-Schwinger equation, and with modifications can be applied to linearized kinematics, multi-field coupling and visco-plasticity. A simplified derivation begins with linear momentum balance, in the absence of body forces and inertial effects, using Einstein's summation convention,

$$P_{iJ,J}(\mathbf{X}) = 0, \quad (2.10)$$

where \mathbf{P} denotes the first Piola-Kirchhoff stress tensor. Periodic boundary conditions are applied such that the average deformation gradient \mathbf{F}^0 satisfies

$$\boldsymbol{\varphi}^+ - \boldsymbol{\varphi}^- = \langle \mathbf{F} \rangle (\mathbf{X}^+ - \mathbf{X}^-), \quad \langle \mathbf{F} \rangle = \frac{1}{|\Omega|} \int_{\Omega} \mathbf{F}(\mathbf{X}) \, dV, \quad (2.11)$$

Subsequently, a linearization is performed using a reference elasticity tensor \mathbb{C}_{iJkL}^0 and a correction denoted as $\boldsymbol{\tau}$,

$$\tau_{iJ} = P_{iJ} - \mathbb{C}_{iJkL}^0 F_{kL}, \quad (2.12)$$

also known as the perturbation stress tensor. A common (yet admittedly sub-optimal) choice for the reference tensor is the volume average

$$\mathbb{C}_{iJkL}^0 = \frac{1}{V} \int_V \mathbb{C}_{iJkL}(\mathbf{X}) \, dV, \quad \mathbb{C}_{iJkL}(\mathbf{X}) = \frac{\partial^2 W}{\partial F_{iJ} \partial F_{kL}}. \quad (2.13)$$

By substitution of Eq. (2.10) into Eq. (2.12), with $\mathbf{F} = \nabla \boldsymbol{\varphi}$,

$$\tau_{iJ,J} + \mathbb{C}_{iJkL}^0 \varphi_{k,LJ} = 0. \quad (2.14)$$

The discrete (inverse) Fourier transform applied to the quasistatic deformation mapping $\boldsymbol{\varphi}(\mathbf{X})$ gives

$$\boldsymbol{\varphi}(\mathbf{X}) = \sum_{\mathbf{K} \in \mathcal{T}} \hat{\boldsymbol{\varphi}}(\mathbf{K}) \exp(-ih\mathbf{K} \cdot \mathbf{X}), \quad \text{and} \quad i = \sqrt{-1}, \quad (2.15)$$

where $\mathcal{T} = \{\mathbf{K}_1, \dots, \mathbf{K}_n\}$ denotes the reciprocal lattice in \mathbf{K} -space (also known as Fourier space) which is chosen to ensure periodicity. In standard FFT-implementations, $h = \frac{2\pi}{n}$ and $\mathbf{K} = [0 : n/2; -n/2 + 1 : -1]$. By defining a wave vector $\boldsymbol{\omega} = -ih\mathbf{K}$, the Fourier transform applied to Eq. (2.14) yields

$$\hat{\tau}_{iJ}\omega_J + \mathbb{C}_{iJkL}^0 \hat{\varphi}_k \omega_L \omega_J = 0. \quad (2.16)$$

Rearranging and introducing the reference acoustic tensor \mathbb{A}^0 results in

$$\hat{\varphi}_k = -(\mathbb{A}_{ki}^0)^{-1} \hat{\tau}_{iJ}\omega_J, \quad \text{where} \quad \mathbb{A}_{ik}^0 = \mathbb{C}_{iJkL}^0 \omega_L \omega_J. \quad (2.17)$$

Repeating the differentiation operation once more, and introducing the Green's operator $\hat{\Gamma}^0$,

$$\begin{aligned}\hat{F}_{kN} &= -(\mathbb{A}_{ki}^0)^{-1} \hat{\tau}_{iJ} \omega_J \omega_N \\ &= -(\mathbb{A}_{ki}^0)^{-1} (\hat{P}_{iJ} - \mathbb{C}_{iJqR}^0 \hat{F}_{qR}) \omega_J \omega_N \quad \text{where} \quad \hat{\Gamma}_{kNiJ}^0 = (\mathbb{A}_{ki}^0)^{-1} \omega_J \omega_N. \\ &= \hat{\Gamma}_{kNiJ}^0 \mathbb{C}_{iJqR}^0 \hat{F}_{qR} - \hat{\Gamma}_{kNiJ}^0 \hat{P}_{iJ},\end{aligned}\quad (2.18)$$

Transforming back to real space,

$$F_{kL}(X) = \mathcal{F}^{-1}\{\hat{F}_{kL}(\mathbf{K})\} \quad \text{and} \quad \hat{F}_{kL}^{n+1}(\mathbf{K}) = \begin{cases} \mathbb{A}_{ik}^{-1}(\mathbf{K}) \hat{\tau}_{iJ}(\mathbf{K}) K_J K_L & \text{for } \mathbf{K} \neq \mathbf{0} \\ \langle F_{kL} \rangle & \text{for } \mathbf{K} = \mathbf{0}. \end{cases} \quad (2.19)$$

Data: Current average deformation gradient, initial guess, stress field, material model container, spatial information

Initialization of spatial distribution, declaration of data types, initial guess \mathbf{F}, \mathbb{C}^0 ;

while $\| \mathbf{F}^{i+1}(X) - \mathbf{F}^i(X) \|_{L_2} > tol$ **do**

$\tau(X) = \text{ComputeStress}(\mathbf{F}^i(X)) - \mathbb{C}^0 : \mathbf{F}^i(X)$;

$\hat{\tau}(\mathbf{K}) = \text{FFT}(\tau(X))$;

if $\mathbf{K} == \mathbf{0}$ **then**

$\hat{\mathbf{F}}^{i+1} = \langle \mathbf{F} \rangle$;

else

 Cycle through \mathbf{K} -space:

$\hat{F}_{kN}^{i+1}(\mathbf{K}) = -(\mathbb{A}_{ki}^0(\mathbf{K}))^{-1} \hat{\tau}_{iJ}(\mathbf{K}) \omega_J \omega_N = -\hat{\Gamma}_{kNiJ}^0(\mathbf{K}) \hat{\tau}_{iJ}(\mathbf{K})$;

end

$\mathbf{F}^{i+1}(X) = \text{iFFT}(\hat{\mathbf{F}}^{i+1}(\mathbf{K}))$ and increment i ;

end

Algorithm 1: Moulinec-Suquet Implementation

The algorithm described thus far is shown as pseudo-code in Alg. 2.3, and can be considered as a non-linear Richardson iteration scheme performed to solve the Lippmann-Schwinger equation. The convergence and stability of this method can be tuned to a limited extent by selective weighting along the march direction using a damping factor α (Kabel et al., 2014),

$$\hat{\mathbf{F}}^{i+1} = (1 - \alpha) \hat{\mathbf{F}}^i + \alpha \hat{\mathbf{F}}^{i+1}. \quad (2.20)$$

For a convex optimization problem, when the spectral radius of the Green's operator is within range for convergence, the method can be accelerated by marching further along the descent direction. Similarly, if the choice of reference stiffness results in ill-conditioning, the method can be damped through appropriately choosing the parameter α . This is shown in Alg. 2.3.

Data: Current average deformation gradient, initial guess, stress field, material model container, spatial information

Initialization of spatial distribution, declaration of data types, initial guess \mathbf{F}, \mathbb{C}^0 ;

while $\| \mathbf{F}^{i+1}(\mathbf{X}) - \mathbf{F}^i(\mathbf{X}) \|_{L_2} > tol$ **do**

$\boldsymbol{\tau}(\mathbf{X}) = \text{ComputeStress}(\mathbb{F}^i(\mathbf{X})) - \mathbb{C}^0 : \mathbf{F}^i(\mathbf{X});$

$\hat{\boldsymbol{\tau}}(\mathbf{K}) = \text{FFT}(\boldsymbol{\tau}(\mathbf{X}));$

if $\mathbf{K} == \mathbf{0}$ **then**

$\hat{\mathbf{F}}^{i+1} = \langle \mathbf{F} \rangle;$

else

Cycle through \mathbf{K} -space:

$\hat{\mathbf{F}}_{kN}^{i+1}(\mathbf{K}) = -(\mathbb{A}_{ki}^0(\mathbf{K}))^{-1} \hat{\boldsymbol{\tau}}_{iJ}(\mathbf{K}) \omega_J \omega_N = -\hat{\Gamma}_{kNiJ}^0(\mathbf{K}) \hat{\boldsymbol{\tau}}_{iJ}(\mathbf{K});$

end

$\mathbf{F}^{i+1}(\mathbf{X}) = (1 - \alpha) \mathbf{F}^i(\mathbf{X}) + (\alpha) \text{iFFT}(\hat{\mathbf{F}}^{i+1}(\mathbf{K}))$ and increment i ;

end

Algorithm 2: Damped Moulinec-Suquet Implementation

The non linear Lippmann-Schwinger equation can be recast as a root-finding problem, which allows for the use of quasi-Newton schemes,

$$\left(\delta_{kq} \delta_{NR} - \hat{\Gamma}_{kNiJ}^0(\mathbf{k}) \mathbb{C}_{iJqR}^0 \right) \hat{\mathbf{F}}_{qR}(\mathbf{k}) + \hat{\Gamma}_{kNiJ}^0(\mathbf{k}) \hat{\mathbf{P}}_{iJ}(\mathbf{k}) = 0. \quad (2.21)$$

The derivative can be evaluated knowing the material model, and assuming that the reference stiffness stays constant during the Newton-Raphson iteration (dropping indices for conciseness),

$$\Delta \mathbf{F}^{i+1} = \left(\mathbb{I} + \Gamma^0 : \left(\frac{\partial \mathbf{P}}{\partial \mathbf{F}} - \mathbb{C}^0 \right) \right)^{-1} : \left(\langle \mathbf{F} \rangle - \langle \mathbf{F}^i \rangle - \Gamma^0 : \mathbf{P} \right). \quad (2.22)$$

It is possible to use a fixed point iteration once again to obtain the increment at every iteration – with the scheme representing a linearized iterative version of the original algorithm, which is

depicted in Alg. 2.3,

$$\widehat{\Delta \mathbf{F}_{n+1}^{i+1}} = -\hat{\Gamma}^0 : FFT \left[\left(\left(\frac{\partial \mathbf{P}}{\partial \mathbf{F}} - \mathbb{C}^0 \right) : \Delta \mathbf{F}_n^{i+1} + \mathbf{P} \right) \right].$$

Data: Current average deformation gradient, initial guess, stress field, material model container, spatial information

Initialization of spatial distribution, declaration of data types, initial guess \mathbf{F}, \mathbb{C}^0 ;

Perform one iteration of Moulinec-Suquet iterations to start;

```

while  $\| \Delta \mathbf{F}^i(\mathbf{X}) \|_{L_2} > tol$  do
  while  $\| \Delta \mathbf{F}_{n+1}^i(\mathbf{X}) - \Delta \mathbf{F}_n^i(\mathbf{X}) \|_{L_2} > tol$  do
     $\beta(\mathbf{X}) = \text{ComputeTangentMatrix}(\mathbf{F}^i(\mathbf{X})) - \mathbb{C}^0 : \Delta \mathbf{F}_n^i(\mathbf{X}) +$ 
       $\text{ComputeStress}(\mathbf{F}^i(\mathbf{X}));$ 
     $\hat{\beta}(\mathbf{K}) = \text{FFT}(\beta(\mathbf{X}));$ 
    if  $\mathbf{K} == \mathbf{0}$  then
       $\Delta \hat{\mathbf{F}}_{n+1}^i = \langle \mathbf{F}^{\text{loadstep}} \rangle - \langle \mathbf{F}^i \rangle;$ 
    else
      Cycle through  $\mathbf{K}$ -space:
       $\Delta \hat{\mathbf{F}}_{kN}^{i,n+1}(\mathbf{K}) = -(\mathbb{A}_{ki}^0(\mathbf{K}))^{-1} \hat{\beta}_{iJ}(\mathbf{K}) \omega_J \omega_N = -\hat{\Gamma}_{kNiJ}^0(\mathbf{K}) \hat{\beta}_{iJ}(\mathbf{K});$ 
    end
     $\Delta \mathbf{F}_{n+1}^i = \text{iFFT}(\Delta \hat{\mathbf{F}}_{n+1}^i(\mathbf{K}));$ 
  end
   $\mathbf{F}^{i+1}(\mathbf{X}) = \mathbf{F}^i(\mathbf{X}) + \Delta t \text{iFFT}(\Delta \hat{\mathbf{F}}^{i+1}(\mathbf{K}))$  and increment  $i$ ;
end

```

Algorithm 3: Newton-Raphson Implementation

2.4 Ringing Artifacts

The aforementioned ringing artifacts present in spectral interpolations can be illustrated using basic examples. Starting with a rectangular step function, the evaluation of the (n to n) discrete Fourier transform (DFT) at nodes and the continuous expression of the mathematical definition of the DFT by a truncated Fourier series yields the graph shown in Fig. 2.1 (a) for a 1D interpolation. The Gibbs phenomenon manifests in the continuous expression because of the non-uniform con-

vergence of the truncated Fourier approximation when performing the (n to n) transform (Gibbs, 1898, 1899; Hewitt and Hewitt, 1979).

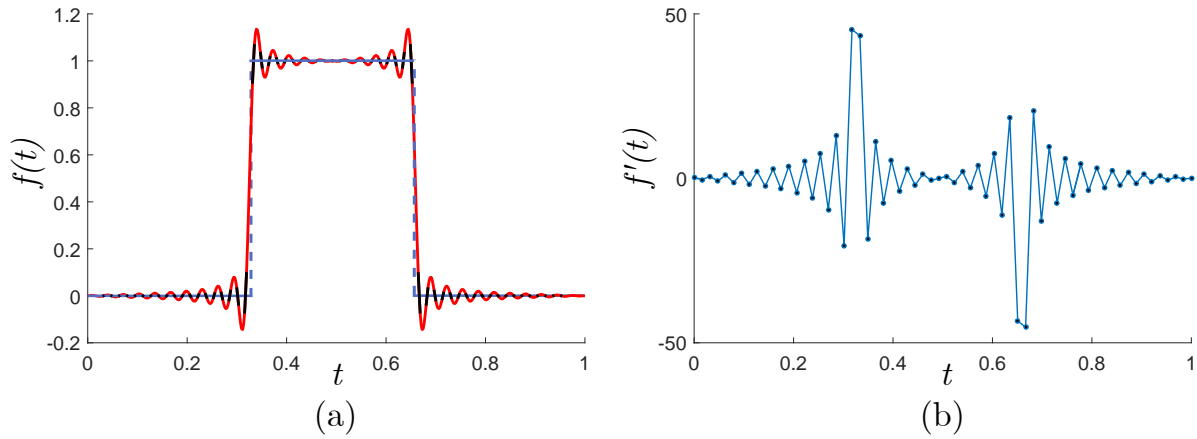


Figure 2.1: An FFT-based interpolation of a rectangular function $f(x) = \text{rect}(\frac{1}{3}, \frac{2}{3})$ (a) results in oscillatory approximations with the Gibbs phenomenon. Here, the slopes are shown in black at the grid points, and this directly results in the oscillations of the derivative $f'(x)$, shown in (b), which is computed using the wave vector multiplied by the Fourier transform of $f(x)$.

Also included in this graph is the slope at grid points (see the black lines), which become spurious oscillations when computing the derivative by taking the product of the DFT by its frequency, as shown in Fig. 2.1 (b). FFT-differentiation (or product of frequency and DFT) utilizes slopes at the grid points (of the interpolated function) in order to compute the derivative, explaining the presence of oscillations. Note that the grid point values themselves may be free of artifacts, but linear momentum balance requires calculating the divergence of the stress (i.e., derivatives of strains), so the black slopes in Fig. 2.1 (a) enter the calculation and affect results. This is not present when using a smooth periodic function whereby exponential convergence is reached with increasing grid points, and hence minimal Gibbs phenomena, and consequently mitigated oscillations upon differentiation.

From an analytical point of view, the Gibbs phenomenon is explained by the non-uniform convergence of a truncated Fourier series

$$\hat{f}_N = \sum_{k \in \mathcal{T}} \hat{f}(k) \exp(-ihk \cdot \mathbf{x}), \quad (2.23)$$

of a function $f(x)$, where \mathcal{T} denotes the *finite* set of points in spectral space used for the numerical approximation while \mathcal{T}_∞ is the countably infinite set of the corresponding exact Fourier representation, and $\mathcal{T}^* = \mathcal{T}_\infty \setminus \mathcal{T}$. Fourier coefficients have pointwise convergence; however, the error of a truncated Fourier series, due to the high-frequency terms, depends on the smoothness of the

function. The error bound can be derived by analytical Fourier expansion through

$$\begin{aligned}
|f_N - \hat{f}| &= \left| \sum_{k \in \mathcal{T}^*} \hat{f}(\mathbf{k}) \exp(-i h \mathbf{k} \cdot \mathbf{x}) \right| \\
&= \left| \sum_{k \in \mathcal{T}^*} \hat{a}(\mathbf{k}) \sin(h \mathbf{k} \cdot \mathbf{x}) + \hat{b}(\mathbf{k}) \cos(h \mathbf{k} \cdot \mathbf{x}) \right| \\
&\leq \sum_{k \in \mathcal{T}^*} |\hat{a}(\mathbf{k}) + \hat{b}(\mathbf{k})| \\
&\leq \sum_{k \in \mathcal{T}^*} |\hat{a}(\mathbf{k})| + |\hat{b}(\mathbf{k})|.
\end{aligned} \tag{2.24}$$

Applying Poincaré's inequality to the transform and using Parseval's identity,

$$\begin{aligned}
\sum_{k \in \mathcal{T}^*} |\hat{a}(\mathbf{k})| + |\hat{b}(\mathbf{k})| &\leq \sum_{k \in \mathcal{T}^*} \frac{1}{|\mathbf{k}|} (|\hat{a}'(\mathbf{k})| + |\hat{b}'(\mathbf{k})|) \\
&\leq \sqrt{2} \left[\sum_{k \in \mathcal{T}^*} |\hat{a}'(\mathbf{k})|^2 + |\hat{b}'(\mathbf{k})|^2 \right]^{1/2} \\
&\leq \sqrt{\frac{2}{\pi N}} \|f'\|_{L_2}^{1/2}.
\end{aligned} \tag{2.25}$$

The error bound reads

$$\sup_{x \in \Omega} |f_N - f| \leq \sqrt{\frac{2}{\pi N}} \|f'\|_{L_2}^{1/2}. \tag{2.26}$$

Therefore, the error depends on the smoothness of the function, and the decay rate of the Fourier coefficients results in non-uniform convergence. The work of [Gelb and Gottlieb \(2007\)](#) and the references therein include further discussion on the origin of oscillatory artifacts in spectral methods.

2.5 Finite-Difference Corrections for Spectral Differentiation

In order to overcome these oscillatory artifacts, finite-difference stencils are used to derive differential operators in Fourier space. This bounds the operator near discontinuities and weights the higher frequencies depending on mesh resolution. The drawback of this technique is that the exponential convergence character of the spectral method with h -refinement reduces to the order of the finite-difference stencil. Consequently, this motivates the use of higher-order and compact schemes.

Applying an inverse Fourier transform (2.15) to the derivative of a function $f \in \mathbb{R}^d$ yields

$$\mathcal{F}^{-1} \left(\frac{\partial f}{\partial x_i} \right) = -i h k_i \mathcal{F}^{-1}(f). \tag{2.27}$$

However, if a central-difference approximation is first applied to the derivative, such that for grid spacing $|\Delta x_i| \ll 1$ in the coordinate direction x_i with unit vector \mathbf{e}_i (no summations over i)

$$\frac{\partial f}{\partial x_i}(\mathbf{x}) = \frac{f(\mathbf{x} + \Delta x_i \mathbf{e}_i) - f(\mathbf{x} - \Delta x_i \mathbf{e}_i)}{2\Delta x_i} + O(\Delta x_i^2). \quad (2.28)$$

Neglecting higher-order terms in the equation, the first order term can be transformed analytically into Fourier space, leaving

$$\begin{aligned} \frac{\partial f}{\partial x_i}(\mathbf{x}) &\approx \sum_{\mathbf{k} \in \mathcal{T}} \hat{f}(\mathbf{k}) \frac{\exp[-i\mathbf{h}\mathbf{k} \cdot (\mathbf{x} + \Delta x_i \mathbf{e}_i)] - \exp[-i\mathbf{h}\mathbf{k} \cdot (\mathbf{x} - \Delta x_i \mathbf{e}_i)]}{2\Delta x_i} \\ &= - \sum_{\mathbf{k} \in \mathcal{T}} \hat{f}(\mathbf{k}) \exp(-i\mathbf{h}\mathbf{k} \cdot \mathbf{x}) \frac{i \sin(\mathbf{h}\mathbf{k}_i \Delta x_i)}{\Delta x_i}, \end{aligned} \quad (2.29)$$

where summation is not performed over i . In the presence of a uniform grid (i.e., with equal spacing), $\Delta x_i = \Delta x$. In such a case it is easy to see that difference scheme approximates the exact derivative when

$$\mathcal{F}^{-1} \left(\frac{\partial f}{\partial x_i} \right) = -i\mathbf{h}\mathbf{k}_i \mathcal{F}^{-1}(f) \quad \text{is replaced by} \quad \mathcal{F}^{-1} \left(\frac{\partial f}{\partial x_i} \right) \approx -\frac{i \sin(\mathbf{h}\mathbf{k}_i \Delta x)}{\Delta x} \mathcal{F}^{-1}(f). \quad (2.30)$$

The fractional term in this equation closely relates to a sinc filter in signal processing or the Lanczos σ -factor (Lanczos, 1956; Hamming, 1986) in Fourier series as a means of avoiding ringing. Additionally, in the limit $\Delta x \rightarrow 0$,

$$\lim_{\Delta x \rightarrow 0} \frac{i \sin(\mathbf{h}\mathbf{k}_i \Delta x)}{\Delta x} = \mathbf{h}\mathbf{k}_i. \quad (2.31)$$

This can be extended to arbitrary finite-difference stencils in higher dimensions. As examples, consider the simple central-difference schemes from fourth to twelfth-order. The fourth-order-accurate central difference approximation becomes

$$\frac{\partial f}{\partial x_i}(\mathbf{x}) = \frac{-f(\mathbf{x} + 2\Delta x \mathbf{e}_i) + 8f(\mathbf{x} + \Delta x \mathbf{e}_i) - 8f(\mathbf{x} - \Delta x \mathbf{e}_i) + f(\mathbf{x} - 2\Delta x \mathbf{e}_i)}{12\Delta x} + O(\Delta x^4). \quad (2.32)$$

Similar to the previous scheme,

$$\mathcal{F} \left(\frac{\partial f}{\partial x_i} \right) \approx -i \left[\frac{8 \sin(\mathbf{h}\mathbf{k}_i \Delta x)}{6\Delta x} - \frac{\sin(2\mathbf{h}\mathbf{k}_i \Delta x)}{6\Delta x} \right] \mathcal{F}(f). \quad (2.33)$$

The exact solution is once again obtained in the limit, except convergence is achieved at $O(\Delta x^4)$

$$\lim_{\Delta x \rightarrow 0} \left[\frac{8 \sin(\mathbf{h}\mathbf{k}_i \Delta x)}{6\Delta x} - \frac{\sin(2\mathbf{h}\mathbf{k}_i \Delta x)}{6\Delta x} \right] = \mathbf{h}\mathbf{k}_i. \quad (2.34)$$

For sixth-order,

$$\begin{aligned} \frac{\partial f}{\partial x_i}(\mathbf{x}) &= \frac{f(\mathbf{x} + 3\Delta x \mathbf{e}_i) - 9f(\mathbf{x} + 2\Delta x \mathbf{e}_i) + 45f(\mathbf{x} + \Delta x \mathbf{e}_i) - 45f(\mathbf{x} - \Delta x \mathbf{e}_i)}{60\Delta x} \\ &\quad + \frac{9f(\mathbf{x} - 2\Delta x \mathbf{e}_i) - f(\mathbf{x} - 3\Delta x \mathbf{e}_i)}{60\Delta x} + O(\Delta x^6). \end{aligned} \quad (2.35)$$

The transform relation becomes

$$\mathcal{F}\left(\frac{\partial f}{\partial x_i}\right) \approx -i \left[\frac{9 \sin(hk_i \Delta x)}{6\Delta x} - 3 \frac{\sin(2hk_i \Delta x)}{10\Delta x} + \frac{\sin(3hk_i \Delta x)}{30\Delta x} \right] \mathcal{F}(f). \quad (2.36)$$

The limit as $\Delta x \rightarrow 0$ again shows that

$$\lim_{\Delta x \rightarrow 0} \left[\frac{9 \sin(hk_i \Delta x)}{6\Delta x} - 3 \frac{\sin(2hk_i \Delta x)}{10\Delta x} + \frac{\sin(3hk_i \Delta x)}{30\Delta x} \right] = hk_i. \quad (2.37)$$

Analogously, the eighth-order accurate approximation leads to (Vidyasagar et al., 2017)

$$\mathcal{F}\left(\frac{\partial f}{\partial x_i}\right) \approx -i \left[\frac{8 \sin(hk_i \Delta x)}{5\Delta x} - 2 \frac{\sin(2hk_i \Delta x)}{5\Delta x} + 8 \frac{\sin(3hk_i \Delta x)}{105\Delta x} - \frac{\sin(4hk_i \Delta x)}{140\Delta x} \right] \mathcal{F}(f). \quad (2.38)$$

As before, convergence with decreasing grid spacing, comes from

$$\lim_{\Delta x \rightarrow 0} \left[\frac{8 \sin(hk_i \Delta x)}{5\Delta x} - 2 \frac{\sin(2hk_i \Delta x)}{5\Delta x} + 8 \frac{\sin(3hk_i \Delta x)}{105\Delta x} - \frac{\sin(4hk_i \Delta x)}{140\Delta x} \right] = hk_i. \quad (2.39)$$

Finally, a central-difference scheme of 12th order with constant spacing Δx is

$$\begin{aligned} \frac{df}{dx}(x) \approx \frac{1}{27720\Delta x} & \left[5f(x - 6\Delta x) - 72f(x - 5\Delta x) + 495f(x - 4\Delta x) - 2200f(x - 3\Delta x) \right. \\ & + 7425f(x - 2\Delta x) - 23760f(x - \Delta x) + 23760f(x + \Delta x) - 7425f(x + 2\Delta x) \\ & \left. + 2200f(x + 3\Delta x) - 495f(x + 4\Delta x) + 72f(x + 5\Delta x) - 5f(x + 6\Delta x) \right]. \end{aligned} \quad (2.40)$$

Application of the discrete Fourier transform and simplification yields the approximation

$$\begin{aligned} \mathcal{F}\left\{\frac{df}{dx}(x)\right\} & \approx \left(-\frac{12i \sin(\Delta x h k)}{7\Delta x} + \frac{15i \sin(2\Delta x h k)}{28\Delta x} - \frac{10i \sin(3\Delta x h k)}{63\Delta x} \right. \\ & \left. + \frac{i \sin(4\Delta x h k)}{28\Delta x} - \frac{2i \sin(5\Delta x h k)}{385\Delta x} + \frac{i \sin(6\Delta x h k)}{2772\Delta x} \right) \mathcal{F}\{f(x)\} \\ & = \tilde{\omega} \mathcal{F}\{f(x)\}. \end{aligned} \quad (2.41)$$

The above approximation maintains also consistency with the exact Fourier transform in the limit of vanishing grid spacing, as can be verified through a Taylor expansion:

$$\lim_{\Delta x \rightarrow 0} \tilde{\omega} = \lim_{\Delta x \rightarrow 0} \omega \cdot \left(1 - \frac{\Delta x^{12}(hk)^{12}}{12012} + \frac{\Delta x^{14}(hk)^{14}}{27720} + O(\Delta x^{16}) \right) = \omega. \quad (2.42)$$

It is possible to tune the balance between convergence order and spurious artifacts by choosing different finite-difference stencils. The same procedure can be applied to finite-difference approximations of arbitrary order (Vidyasagar et al., 2018), to result in controllable accuracy and

efficiency. Similar works by Willot (2015) and Schneider et al. (2017) have used weighted difference schemes to compute the higher-dimensional derivatives, involving compact stencils using nodes on the off-diagonals. This results in more local approximations, with possibly improved numerical stability.

The effectiveness of these approximations in mitigating oscillatory artifacts can be visualized through numerical examples. Beginning with the double-step function,

$$f(x) = \delta(x - \frac{1}{4} + 2^{-10}) + \delta(x - \frac{3}{4} - 2^{-10}), \quad \text{with period } x \in [0, 1), \quad (2.43)$$

the derivatives obtained from the classical Fourier spectral method, the modified Fourier transform (first-order and fourth-order correction), and the exact analytical solution are compared in Fig. 2.2. Similarly, for the case of a smooth but discontinuous half-sine function, defined by

$$f(x) = \pi \cos(\pi x), \quad \text{with period } x \in [0, 1), \quad (2.44)$$

the derivative is plotted in Fig. 2.3. It is clear that there is still limited oscillatory phenomena in the higher-order corrections which can be directly attributed to the less severe weighting of higher frequencies compared to the first-order scheme. However, there is marked reduction of oscillations when both finite-difference schemes are used. The main motivation behind higher order schemes becomes clear when considering smoother functions. The first-order correction results in critical damping of the oscillations at reduced accuracy in smooth regions, while higher-order corrections give sub-critical damping but better overall accuracy away from discontinuities.

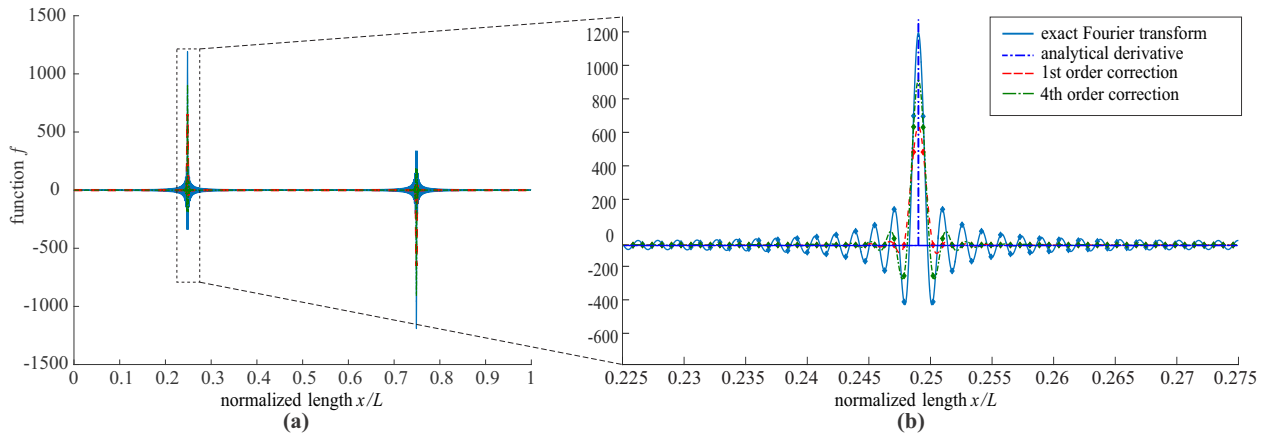


Figure 2.2: Spectral derivative of the double step function using first- and fourth-order finite-difference correction, compared with classical FFT, and analytical solution (Vidyasagar et al., 2017).

In order to quantify the error of approximation, the mesh convergence order of Euclidean error-norm

$$E = \|u_h - u\|_{L_2} \quad (2.45)$$

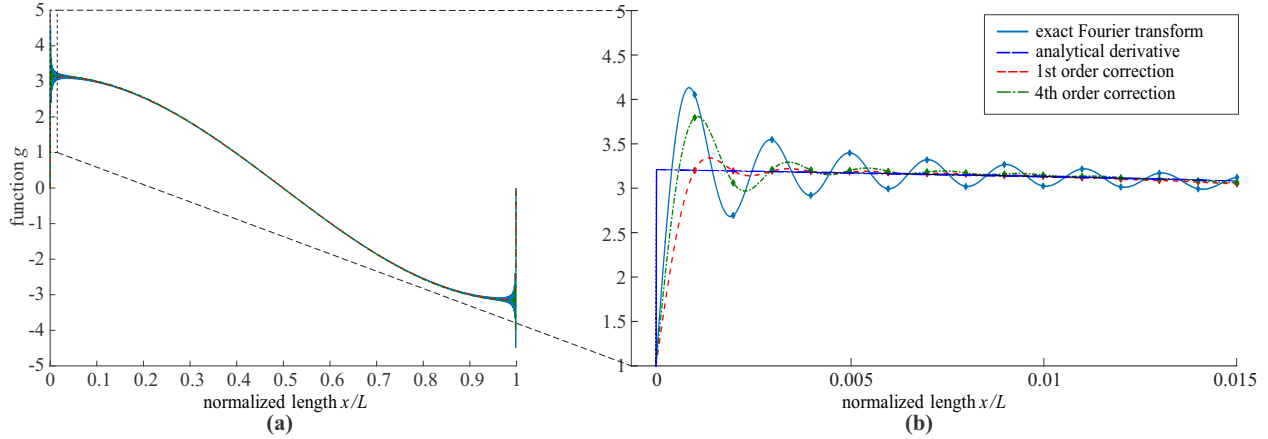


Figure 2.3: Spectral derivative of the half-sine function using first- and fourth-order finite-difference correction, compared with classical FFT, and analytical solution (Vidyasagar et al., 2017).

serves as a convenient measure. The smooth function,

$$f(x) = \sum_{n=1}^{n=9} \sin(2n\pi x), \quad (2.46)$$

is used to present the effectiveness of the various corrections, and the results are shown in Fig. 2.4. Unsurprisingly, since the function exhibits smooth properties, spectral accuracy reduces to the finite-difference order. The \log_2 -convergence order exponentially reaches the order of the finite-difference approximation. As expected, the spectral convergence reaches machine precision with an equal number of grid-points as sinusoidal terms in $f(x)$. Therefore, the correction order has to be carefully chosen in order to minimize the competing error mechanisms arising from both the ringing artifacts and finite-difference approximations.

The next benchmark test of interest is the influence of finite-difference corrections for an elastic homogenization problem. Here, a representative volume element in 2D, with two constituents, is subjected to a biaxial tensile test. The linear elastic composite RVE consists of a matrix (normalized Lamé moduli $\lambda_{\text{mat}} = 0.6$, $\mu_{\text{mat}} = 0.6$, outer side length L) with a circular inclusion (radius $0.25L$; normalized Lamé moduli $\lambda = 1$, $\mu = 1$). A grid of size 256×256 is used and Fig. 2.5 shows the resulting stress distribution. In this case the first-order correction 2.5 (c) over-smooths the solution as seen through the green coloration at the interface, while the fourth-order correction 2.5 (b) still produces mild oscillations as compared to the heavy oscillations in the uncorrected scheme 2.5 (a).

Interestingly, several previous approaches have aimed to mitigate this oscillatory behavior by terminating the iterative solver prematurely. In such cases, the accuracy of the numerical method is compromised, particularly in time evolution problems. For explicit time-stepping routines, the propagation of error through time would not converge with refinement. Additionally, depending

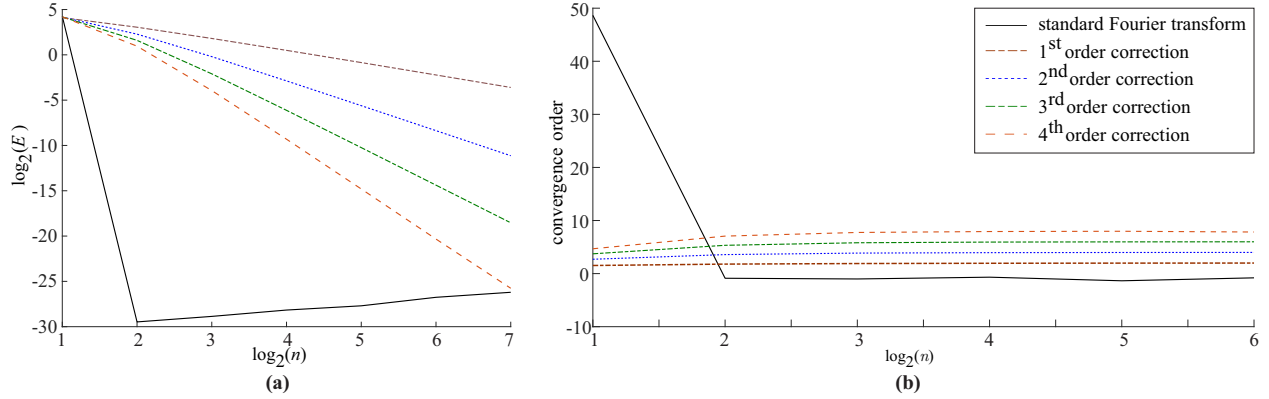


Figure 2.4: (a) Finite-difference approximation indicates loss of accuracy when the mesh convergence is computed. The plot shows error-norm against number of grid-points n . (Vidyasagar et al., 2017) (b) The convergence orders plotted against the number of grid-points (Vidyasagar et al., 2017).

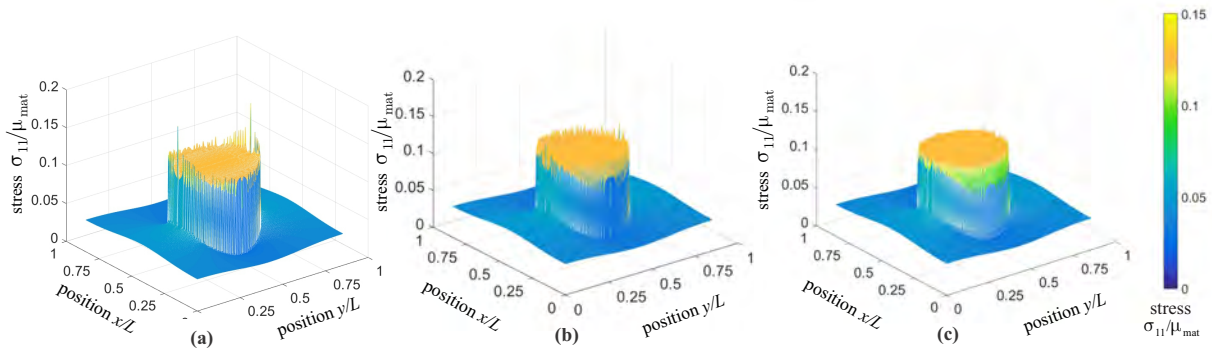


Figure 2.5: Stress distribution $\frac{\sigma_{11}}{\mu_{\text{mat}}}$ (a) the standard iterative spectral method (b) fourth-order finite-difference corrections and (c) first-order corrections (Vidyasagar et al., 2017).

on the descent direction, this could lead to divergent results due to numerical instabilities. Finally, such techniques would not converge with h -refinement unlike the method presented thus far.

2.6 Special Considerations for Non-Convex Problems

Unfortunately, the spectral formulation presented thus far is based on the strong form of the governing differential equations. Unlike in convex problems, in non-convex minimization, there are meta-stable high-energy states that satisfy linear momentum balance.

As a means to circumvent this, the addition of an insignificant amount of stochastic white noise perturbs the system away from the meta-stable equilibrium state. For non-convex energies, the local loss of strong ellipticity introduces further problems. When the acoustic tensor \mathbb{A}_{ik} ,

computed using the reference tangent stiffness tensor,

$$\mathbb{C}_{iJkL}^0 = \frac{1}{V} \int_V \mathbb{C}_{iJkL}(\mathbf{X}) \, dV, \quad \mathbb{C}_{iJkL}(\mathbf{X}) = \frac{\partial^2 W(\mathbf{F})}{\partial F_{iJ} \partial F_{kL}}. \quad (2.47)$$

becomes close to loss of positive definiteness, the matrix inversion becomes ill-conditioned. In order to prevent this, the local tangent stiffness tensor used to compute the reference stiffness is derived from a convex approximation of the non-convex energy. While this affects the descent direction, it does not change the nature of the root-finding iterative approach and the final solution.

Finally, these finite-difference approximations introduce *numerical regularization* to the non-convex optimization problem (Vidyasagar et al., 2018). Specifically, any finite-difference stencil leads to an approximation of the deformation gradient. For a stencil that is m th-order accurate in each spatial dimension, the approximation becomes

$$F_{iJ}^h = \varphi_{i,J}^h = \varphi_{i,J} + \frac{(\Delta X)^m}{(m+1)!} \frac{\partial^{(m+1)} \varphi_i}{\partial X_J^{m+1}} + O\left((\Delta X)^{m+2}\right). \quad (2.48)$$

Assuming an energy density $W(\nabla \boldsymbol{\varphi})$, the contribution of additional energy can be quantified. Performing a Taylor expansion of $W(\nabla \boldsymbol{\varphi})$,

$$W(\nabla \boldsymbol{\varphi}^h) \approx W(\nabla \boldsymbol{\varphi}) + \frac{(\Delta X)^m}{(m+1)!} \frac{\partial W}{\partial \varphi_{i,J}}(\nabla \boldsymbol{\varphi}) \frac{\partial^{(m+1)} \varphi_i}{\partial X_J^{m+1}} = W(\nabla \boldsymbol{\varphi}) + W^h(\nabla^{m+1} \boldsymbol{\varphi}), \quad (2.49)$$

the additional contribution can be quantified. It is clear that the additional non-local contribution $W^h(\nabla^{m+1} \boldsymbol{\varphi}) \sim (\Delta X)^m$, introduced by the finite-difference scheme, asymptotically converges to 0 with decreasing grid spacing ΔX . This implies consistency with grid or h -refinement. Additionally, the length scale which is introduced as a consequence is relative to the absolute size of RVE. For example, for a cubic RVE of length L and n grid points, the grid spacing $\Delta X = L/(n^{1/3} - 1)$. Therefore, ΔX is relative to the RVE size, hence microstructural patterns will be independent of the absolute size of RVE, and converge with grid resolution. It will be shown that it is possible to expand the given form in some cases, such as finite-strain single-slip single-crystal plasticity in Sec. 3.4.

These higher-order gradients in the energy density penalize strong discontinuities and therefore result in a finite width of interfaces. This has qualitatively the same effect of smearing out interfaces. For example, in phase-transforming solids interfaces exist between the different variants, in ferroelectrics between different domains, or in finite-strain crystal plasticity between regions of different (but approximately constant) plastic slip (Ortiz and Repetto, 1999). The grid-based smearing of interfaces would be anisotropic, as evidenced by the form of Eq. (2.49), but the influence this has on pattern formation is considerably reduced with grid refinement depending

on the order of stencil used, and only interface thickness is penalized and not pattern orientation. However, grid-orientation has an influence on laminte orientation and hence the minima found by the spectral homogenization scheme. These patterns with interfaces have been observed also experimentally ([Dmitrieva et al., 2009](#)).

NUMERICAL SOLUTIONS TO NON-CONVEX PROBLEMS

Research presented in this chapter has been adapted from the following publication:

Vidyasagar, A., Tutcuoglu, A., Kochmann, D. M. 2018. Deformation patterning in finite-strain crystal plasticity by spectral homogenization with application to magnesium. *Computer Methods in Applied Mechanics and Engineering*, 335, pp.584-609.

URL: <https://doi.org/10.1016/j.cma.2018.03.003>

3.1 Introduction

The numerical homogenization techniques developed in Chapter 2 are used to solve specific problems involving non-quasiconvex energy landscapes in this chapter. The discussion begins with the St. Venant-Kirchoff model (Sec. 3.2), which is still widely used in commercial and academic codes, where unphysical patterns are shown to form even for admissible choices of elastic constants. Following this, a generalized model for phase transformation is derived (Sec. 3.3) and demonstrates intricate pattern formation when mathematical toy examples of transformation strains are used. Finally, numerical homogenization is performed to find relaxed energies and predict pattern formation in the single-slip single crystal model in Sec. 3.4. In all three cases, pure energy minimization is performed (ignoring dissipative effects), for symmetric and asymmetric bi-stable energies (upon projection along a specific loading parameter), together with an evaluation of associated patterns.

3.2 The St. Venant-Kirchoff Model

An excellent first benchmark test for finding energy-minimizing microstructures without the complications of viscoplasticity or coupled fields is the elastic energy density named after St. Venant and Kirchhoff, defined as

$$W(\mathbf{F}) = \frac{1}{2}(\mathbf{F}^T \mathbf{F} - \mathbf{I}) \cdot \mathbb{C}(\mathbf{F}^T \mathbf{F} - \mathbf{I}). \quad (3.1)$$

As introduced in Chapter 1, consider a solid with isotropic elastic modulus tensor $\mathbb{C}_{IJKL} = \lambda \delta_{IJ} \delta_{KL} + \mu(\delta_{IK} \delta_{JL} + \delta_{IL} \delta_{JK})$ and moduli $\lambda, \mu > 0$. This solid is subjected to a uniaxial tension-

compression with simple shear test described by the applied deformation gradient

$$\mathbf{F}_{\text{ex}} = \begin{pmatrix} 1 - \gamma & -2\gamma & 0 \\ 0 & 1 & 0 \\ 0 & 0 & 1 \end{pmatrix}, \quad \gamma < 1. \quad (3.2)$$

Insertion into (3.1) yields

$$W(\mathbf{F}_{\text{ex}}) = \frac{1}{2}\gamma^2 \left(2 \left(25\gamma^2 - 20\gamma + 12 \right) \mu + (2 - 5\gamma)^2 \lambda \right), \quad (3.3)$$

which has two minima and one local maximum, respectively, at

$$\gamma_1 = 0, \quad \gamma_2 = \frac{\sqrt{\lambda^2 - 28\lambda\mu - 60\mu^2} + 3\lambda + 6\mu}{10(\lambda + 2\mu)} \quad (3.4)$$

and

$$\gamma_3 = \frac{-\sqrt{\lambda^2 - 28\lambda\mu - 60\mu^2} + 3\lambda + 6\mu}{10(\lambda + 2\mu)} \quad (3.5)$$

given that

$$\left(\frac{\lambda}{\mu} \right)^2 - 28 \left(\frac{\lambda}{\mu} \right) - 60 > 0 \quad \Rightarrow \quad 0 < \frac{\mu}{\lambda} < \frac{1}{30} \quad (3.6)$$

and is strictly convex if and only if

$$\frac{\partial^2 W}{\partial \gamma^2} > 0 \quad \Rightarrow \quad \frac{\mu}{\lambda} > \frac{1}{6}. \quad (3.7)$$

This is illustrated in Fig. 3.1, where decreasing the ratio of $\frac{\mu}{\lambda}$ increases the non-convexity of the condensed energy landscape. Therefore, a compression-shear test with $\gamma > 0$ is expected to form microstructural patterns as energy minimizers. As shown by [Le Dret and Raoult \(1995\)](#), the quasiconvex envelope of a St. Venant-Kirchhoff solid with isotropic moduli E and ν is given by

$$\begin{aligned} QW(\mathbf{F}) &= \frac{E}{2} [v_3^2 - 1]_+^2 + \frac{E}{2(1 - \nu^2)} [v_2^2 + \nu v_3^2 - (1 + \nu)]_+^2 \\ &+ \frac{E}{2(1 - \nu^2)(1 - 2\nu)} [(1 - \nu)v_1^2 + \nu(v_2^2 + v_3^2) - (1 + \nu)]_+^2, \end{aligned} \quad (3.8)$$

where (v_1, v_2, v_3) are the singular values of \mathbf{F} and

$$E = \frac{\mu(3\lambda + 2\mu)}{\lambda + \mu}, \quad \nu = \frac{\lambda}{2(\lambda + \mu)}. \quad (3.9)$$

For the chosen example of (3.2), v_i are the singular values of \mathbf{F}_{ex} , and in the limit $\mu \rightarrow 0$ the analytical quasiconvex hull evaluates as

$$QW(\mathbf{F}_{\text{ex}}) = \begin{cases} 0 & \text{if } \gamma \in [\gamma_1, \gamma_2], \\ W(\mathbf{F}_{\text{ex}}) & \text{else.} \end{cases} \quad (3.10)$$

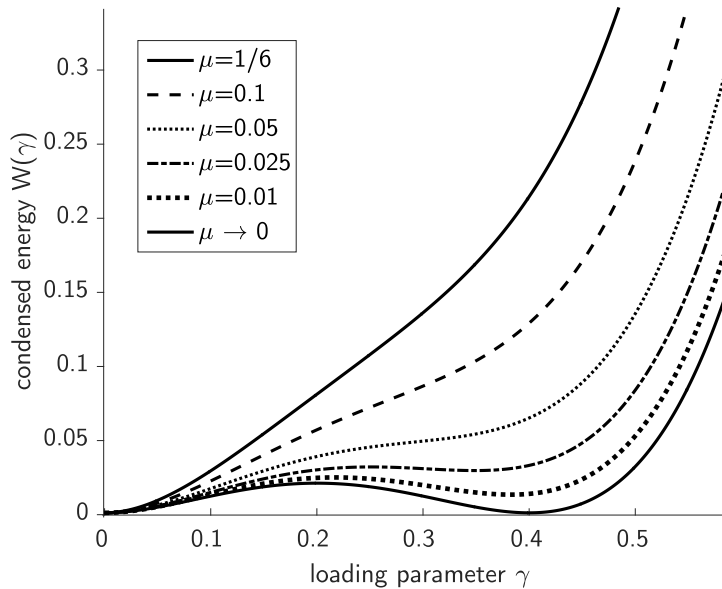


Figure 3.1: Loss of convexity of the condensed energy $W(\gamma)$ as the shear modulus μ decreases, for $\lambda = 1$.

This is a particularly appealing test case, as recursive lamination can produce the rank-one-convex hull by numerically evaluating (1.24) for $\gamma < 0$. Results show that $RW_1(\mathbf{F}_{\text{ex}}) \approx QW(\mathbf{F}_{\text{ex}})$ for $\gamma < 0$, i.e., a first-order laminate construction is sufficiently close to the quasiconvex hull.

In order to compute the patterns which form during loading, the spectral technique, outlined in Section. 2 is used to perform numerical quasiconvexification for this benchmark test for which both the analytical and rank one lamination results are known. In this regard, a representative volume element (RVE) is subjected to periodic boundary conditions and the macroscopic (volume average) deformation gradient given in Eq. (3.2). The spectral solution scheme then solves for the evolution of the internal deformation gradient field $\mathbf{F}(\mathbf{X})$, together with the associated volume average energy of the RVE.

For this computation, the parameters of $\lambda = 1$ and $\mu = 1.0 \cdot 10^{-5}$ are used. In order to ensure that the acoustic tensor \mathbb{A}^0 is invertible, $\mu = \frac{1}{6}$ is used to compute the reference stiffness tensor \mathbb{C}^0 . One cycle of loading and unloading is performed, using the fourth-order central difference approximation technique, to obtain the numerically computed average energy. Fig. 3.2 summarizes the results, whereby the formation of a checkerboarding and laminate patterns are observed. As seen in the energy plot, after an initial homogeneous phase whereby the spectral solution follows the non-convex energy, the RVE breaks down into domains, allowing the numerically computed average energy to march towards the quasiconvex envelope. The computed quasiconvex hull is very close to the analytical solution.

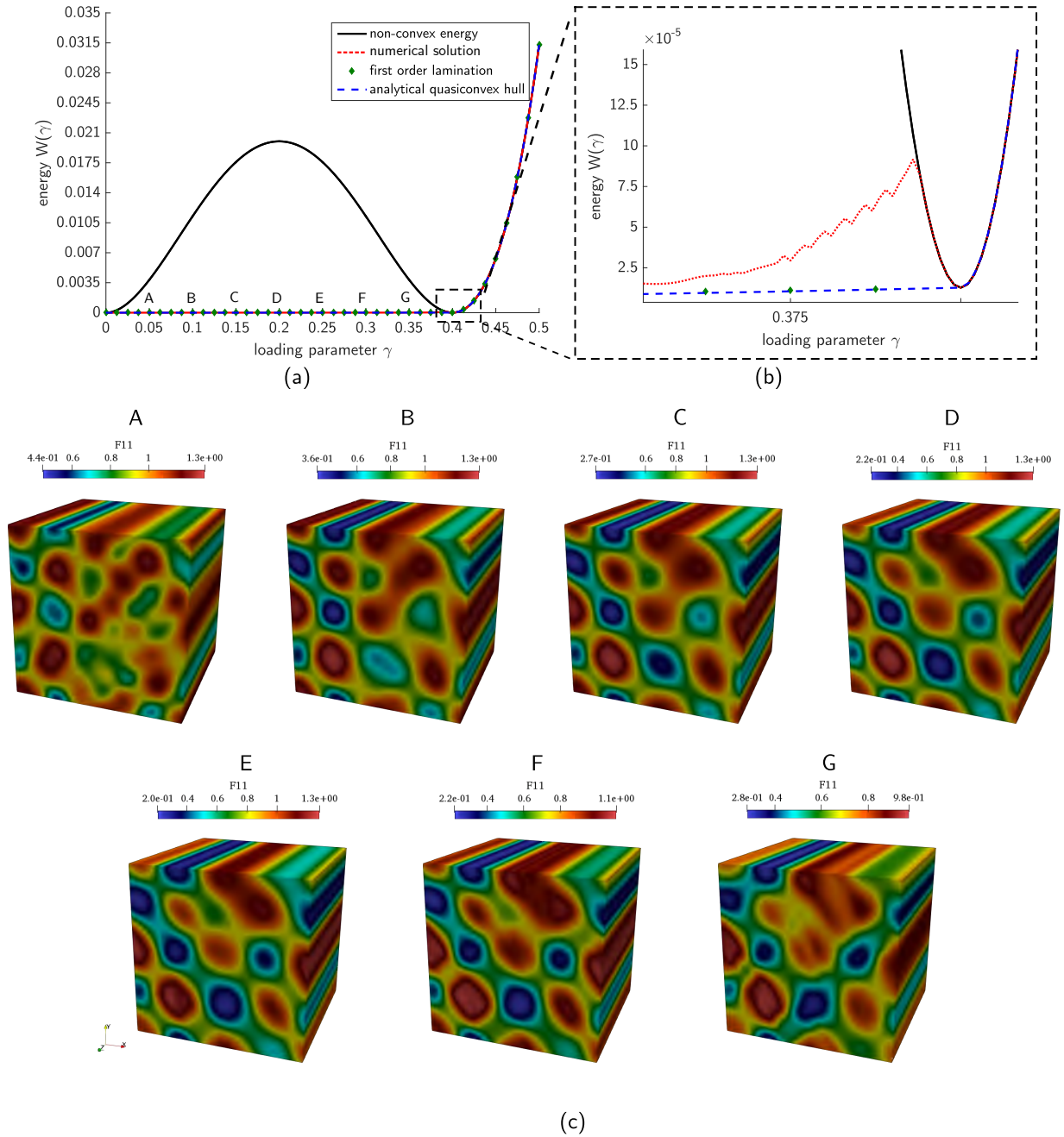


Figure 3.2: The calculated numerical hull shown in (a) shown near the origin in (b). Corresponding microstructural patterns are shown in sequence in (c) during the loading process through the deformation gradient component F_{11} .

It is possible to approximate the quasiconvex hull of non-symmetric potentials with different magnitudes of non-convexity by varying the shear modulus μ . The results of the computed energy landscape are shown in Fig.3.3. It is interesting to note that both the lamination approach and the

numerical approach deviate from the analytical quasiconvex hull as the degree of non-convexity is decreased. This is due to increased energy of finite-width interfaces that exist when numerical (or otherwise) regularization is added to the non-convex optimization as aforementioned.

The autonomous patterns obtained using this approach, shown in Fig. 3.4, indicate a higher level of complexity than with simple lamination theory. In the limit of first-order difference schemes, ellipsoidal patterns are found. In all cases, the patterns found are different for each component of deformation gradient, indicating that the system does not break down into simple heterogeneous domains.

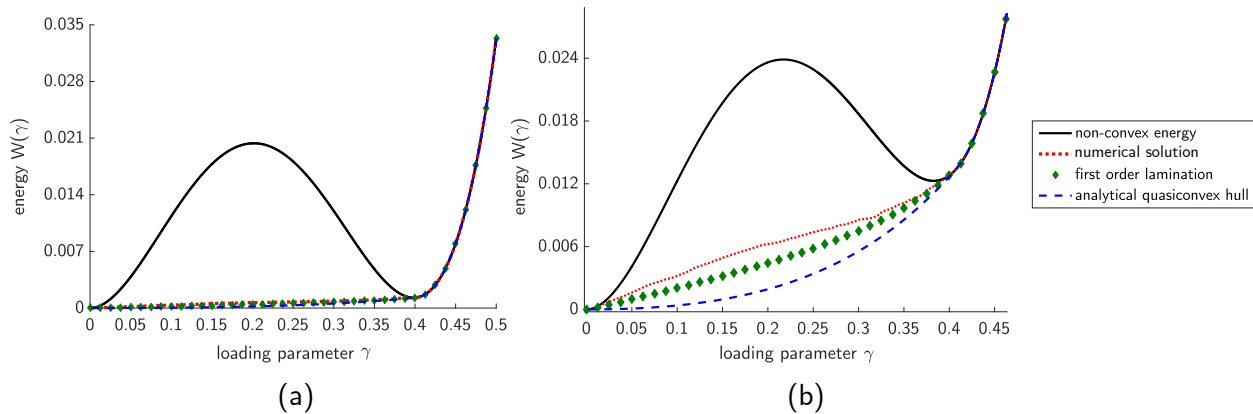


Figure 3.3: The numerically calculated hulls at $\gamma = -0.25$ shown for different degrees of non-convexity with given parameters $\lambda = 1$ from (a) $\mu = 0.001$ and (b) $\mu = 0.01$.

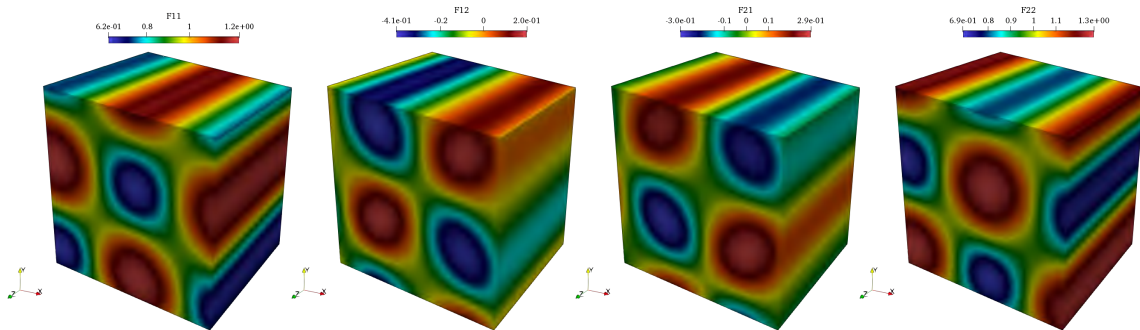


Figure 3.4: The largest patterns formed using first-order central difference approximation demonstrate complexity of pattern formation, with each component of deformation showing different patterns that are compatible.

3.3 Generalized Finite-Strain Phase Transition Model

Multi-well energetic landscapes are often associated with phase transformations, and originate from a competition between multiple stable crystallographic *phases*. Depending on the specific

nature of transformation these could represent different physically distinct forms (e.g., high- vs. low-temperature phases in martensitic transformations) or of *variants* of the same form (such as all symmetries of a tetragonal low-temperature phase). For the purposes of this work, this definition is kept general in applicability to (but not limited by) either of those scenarios. In the context of mechanics, n phases are described by transformation strains \mathbf{U}_α ($\alpha = 1, \dots, n$), such that the total deformation gradient at \mathbf{X} is

$$\mathbf{F}(\mathbf{X}) = \nabla\varphi(\mathbf{X}) = \mathbf{F}_e(\mathbf{X}) \mathbf{U}_\alpha(\mathbf{X}), \quad \mathbf{F}_e \in GL_+(d) \quad (3.11)$$

if the material point is in phase α . Here, \mathbf{F}_e represents the elastic deformation gradient assuming multiplicative decomposition. The definition here is kept general and the classic assumption of $\mathbf{F}_e \in SO(d)$ is not made, as is often the case in the mathematics literature. Here, both rotations and elastic deformation are considered. The elastic strain energy density is denoted by W_e and the chemical energy density of phase α is denoted by Ψ_α . The energy density of each phase is denoted by W_α and consequently the effective Helmholtz free energy density W at a material point (Ball and James, 1987; Govindjee et al., 2003) becomes

$$W_\alpha(\mathbf{F}) = W_e(\mathbf{F}\mathbf{U}_\alpha^{-1}) + \Psi_\alpha \quad \Rightarrow \quad W(\mathbf{F}) = \min_{\alpha=1,\dots,n} \left\{ W_\alpha(\mathbf{F}) \right\}. \quad (3.12)$$

Since $W(\mathbf{F})$ is not quasiconvex, insertion into (1.1) yields a functional that lacks weakly lower semi-continuity and thus forms microstructural patterns. While this framework is mathematically elegant, it is numerically problematic due to discontinuities in the energy upon phase transformations and associated non-uniqueness and jumps in the stresses $\mathbf{P} = \partial W / \partial \mathbf{F}$. Therefore, the following physically motivated approximate theory of phase transformations is presented, building upon the linearized-kinematics model for ferroelectrics introduced by Tan and Kochmann (2017).

The framework presented thus far is ‘relaxed’ by allowing multiple phases to co-exist at any given material point. The volume fractions of these phases are denoted by $\boldsymbol{\lambda} = \{\lambda_1, \dots, \lambda_n\}$. The Voigt’s (upper) bound for Helmholtz free energy is then obtained from a Taylor model (where compatibility is not enforced between phases), as

$$W(\mathbf{F}, \boldsymbol{\lambda}) = \sum_{\alpha=1}^n \lambda_\alpha W_\alpha(\mathbf{F}) = \sum_{\alpha=1}^n \lambda_\alpha [W_e(\mathbf{F}\mathbf{U}_\alpha^{-1}) + \Psi_\alpha]. \quad (3.13)$$

Ignoring dissipative effects, the energy-minimizing volume fractions are obtained for a given \mathbf{F} as

$$\boldsymbol{\lambda} = \arg \min \left\{ W(\mathbf{F}, \boldsymbol{\lambda}) \mid 0 \leq \lambda_\alpha \forall \alpha = 1, \dots, n, \sum_{\alpha=1}^n \lambda_\alpha = 1 \right\}. \quad (3.14)$$

In order to observe and simulate phase patterning similar to the original model, (3.12), the phase mixtures require penalization, here performed using a concept of configurational entropy (with a

constant $k_T > 0$),

$$S(\boldsymbol{\lambda}) = k_T \lambda_\alpha \log \lambda_\alpha, \quad (3.15)$$

such that the above energy density becomes the free energy density $A(\mathbf{F}, \boldsymbol{\lambda})$

$$A(\mathbf{F}, \boldsymbol{\lambda}) = W(\mathbf{F}, \boldsymbol{\lambda}) - S(\boldsymbol{\lambda}) = \sum_{\alpha=1}^n \lambda_\alpha [W_\alpha(\mathbf{F}) + k_T \log \lambda_\alpha]. \quad (3.16)$$

Without dissipation, the volume fractions can be obtained by minimization of (3.16) for a given \mathbf{F} ,

$$\lambda_\alpha^* = \arg \min_{0 \leq \lambda_\alpha, \sum_{\alpha=1}^n \lambda_\alpha = 1} A(\mathbf{F}, \boldsymbol{\lambda}) = \frac{\exp\left(-\frac{W_\alpha(\mathbf{F})}{k_T}\right)}{\sum_{\beta=1}^n \exp\left(-\frac{W_\beta(\mathbf{F})}{k_T}\right)}. \quad (3.17)$$

Insertion into the free energy yields the *condensed* energy $A^*(\mathbf{F})$,

$$A^*(\mathbf{F}) = A(\mathbf{F}, \boldsymbol{\lambda}^*) = -k_T \log \left[\sum_{\alpha=1}^n \exp\left(-\frac{W_\alpha(\mathbf{F})}{k_T}\right) \right]. \quad (3.18)$$

Similar to physical (statistical mechanical) configurational entropy, k_T here becomes a numerical tuning parameter that determines the penalization of phase mixtures. As k_T is increased, in the limit $k_T \rightarrow \infty$, $\lambda_\alpha \rightarrow 1/n$ for $\alpha = 1, \dots, n$. By contrast, as k_T is decreased in the limit $k_T \rightarrow 0$,

$$\lambda_\alpha^* = \frac{\exp\left(-\frac{W_\alpha(\mathbf{F})}{k_T}\right)}{\sum_{\beta=1}^n \exp\left(-\frac{W_\beta(\mathbf{F})}{k_T}\right)} = \frac{1}{1 + \sum_{\beta \neq \alpha} \exp\left(-\frac{W_\beta(\mathbf{F}) - W_\alpha(\mathbf{F})}{k_T}\right)}, \quad (3.19)$$

such that

$$\lim_{k_T \rightarrow 0} \lambda_\alpha^* = \begin{cases} 1 & \text{if } W_\alpha(\mathbf{F}) < W_\beta(\mathbf{F}) \forall \beta \neq \alpha, \\ 0 & \text{if } \exists \beta \text{ s.t. } W_\beta(\mathbf{F}) < W_\alpha(\mathbf{F}), \\ 1/m & \text{if there are } m \text{ phases with equal } W_\alpha(\mathbf{F}) < W_\beta(\mathbf{F}) \text{ for all other phases } \beta. \end{cases} \quad (3.20)$$

In other words, in the limit $k_T \rightarrow 0$ the solution becomes ‘sharp’, reproducing the effect of Eq. (3.12) and the free energy approaches

$$\lim_{k_T \rightarrow 0} F^*(\mathbf{F}) = \min_{\alpha=1, \dots, n} \{W_\alpha(\mathbf{F})\}. \quad (3.21)$$

As long as $k_T > 0$, the energy (3.12) is only approximated and allows some lower-scale microstructural pattern formation. However, for $k_T \neq 0$ this approximate formulation is advantageous because it uniquely defines continuously differentiable stresses and tangent stiffness tensors. For example, the first Piola-Kirchhoff stress tensor becomes

$$\mathbf{P} = \frac{dF^*}{d\mathbf{F}} = \sum_{\alpha=1}^n \lambda_{\alpha}^* \frac{\partial W_{\alpha}}{\partial \mathbf{F}}(\mathbf{F}) = \sum_{\alpha=1}^n \lambda_{\alpha}^* \mathbf{P}(\mathbf{F} \mathbf{U}_{\alpha}^{-1}) \mathbf{U}_{\alpha}^{-T}, \quad (3.22)$$

where the fact that λ^* is a minimizer of F^* is exploited such that $\partial F^* / \partial \lambda_{\alpha}(\lambda^*) = 0$. Likewise, the components of the incremental elasticity tensor (using the summation convention and writing $U_{\alpha, IJ}$ for the IJ -component of tensor \mathbf{U}_{α}) can be derived. This is unfortunately more involved as the aforementioned partial derivative does not vanish:

$$\begin{aligned} \mathbb{C}_{iJkL} &= \frac{dP_{iJ}}{dF_{kL}} = \frac{\partial P_{iJ}}{\partial F_{kL}} + \sum_{\alpha} \frac{\partial P_{iJ}}{\partial \lambda_{\alpha}} \frac{\partial \lambda_{\alpha}}{\partial F_{kL}} \\ &= \sum_{\alpha} \lambda_{\alpha} \mathbb{C}_{iMkN}(\mathbf{F} \mathbf{U}_{\alpha}^{-1}) U_{JM}^{-1} U_{LN}^{-1} + \sum_{\alpha} P_{iM}(\mathbf{F} \mathbf{U}_{\alpha}^{-1}) U_{\alpha, JM}^{-1} \frac{\partial \lambda_{\alpha}}{\partial F_{kL}}, \end{aligned} \quad (3.23)$$

with

$$\begin{aligned} \frac{\partial \lambda_{\alpha}}{\partial F_{kL}} &= \frac{\partial}{\partial F_{kL}} \frac{\exp(-W_{\alpha}/k_T)}{\sum_{\beta} \exp(-W_{\beta}/k_T)} \\ &= -\frac{\exp(-W_{\alpha}/k_T)}{\sum_{\beta} \exp(-W_{\beta}/k_T)} \frac{1}{k_T} \frac{\partial W_{\alpha}}{\partial F_{kL}} \\ &\quad - \frac{\exp(-W_{\alpha}/k_T)}{[\sum_{\beta} \exp(-W_{\beta}/k_T)]^2} \sum_{\gamma} \left(-\frac{1}{k_T}\right) \exp(-W_{\beta}/k_T) \frac{\partial W_{\beta}}{\partial F_{kL}}. \end{aligned} \quad (3.24)$$

This can be further simplified into

$$\begin{aligned} \frac{\partial \lambda_{\alpha}}{\partial F_{kL}} &= -\lambda_{\alpha} \frac{1}{k_T} \frac{\partial W_{\alpha}}{\partial F_{kL}} + \frac{1}{k_T} \sum_{\gamma} \frac{\exp(-W_{\gamma}/k_T) \exp(-W_{\alpha}/k_T)}{[\sum_{\beta} \exp(-W_{\beta}/k_T)]^2} \frac{\partial W_{\gamma}}{\partial F_{kL}} \\ &= -\lambda_{\alpha} \frac{1}{k_T} \frac{\partial W_{\alpha}}{\partial F_{kL}} + \frac{1}{k_T} \sum_{\gamma} \lambda_{\alpha} \lambda_{\gamma} \frac{\partial W_{\gamma}}{\partial F_{kL}} \\ &= \frac{\lambda_{\alpha}}{k_T} \left(\sum_{\gamma} \lambda_{\gamma} \frac{\partial W_{\gamma}}{\partial F_{kL}} - \frac{\partial W_{\alpha}}{\partial F_{kL}} \right) = \frac{\lambda_{\alpha}}{k_T} \sum_{\gamma \neq \alpha} \lambda_{\gamma} \frac{\partial W_{\gamma}}{\partial F_{kL}} \\ &= \frac{\lambda_{\alpha}}{k_T} \sum_{\gamma \neq \alpha} \lambda_{\gamma} P_{kN}(\mathbf{F} \mathbf{U}_{\gamma}^{-1}) U_{\gamma, LN}^{-1}. \end{aligned} \quad (3.25)$$

Overall, the elasticity tensor takes the form

$$\begin{aligned} \mathbb{C}_{iJkL} &= \sum_{\alpha} \lambda_{\alpha} \mathbb{C}_{iMkN}(\mathbf{F} \mathbf{U}_{\alpha}^{-1}) U_{JM}^{-1} U_{LN}^{-1} \\ &\quad + \frac{1}{k_T} \sum_{\alpha} \sum_{\gamma \neq \alpha} \lambda_{\alpha} \lambda_{\gamma} P_{iM}(\mathbf{F} \mathbf{U}_{\alpha}^{-1}) U_{\alpha, JM}^{-1} P_{kN}(\mathbf{F} \mathbf{U}_{\gamma}^{-1}) U_{\gamma, LN}^{-1}. \end{aligned} \quad (3.26)$$

Note that

$$\lim_{k_T \rightarrow 0} \frac{\lambda_\alpha \lambda_\gamma}{k_T} = \begin{cases} 0, & \text{if } W_\alpha \neq W_\gamma, \\ \infty, & \text{else.} \end{cases} \quad (3.27)$$

Therefore, as long as there are no two (or more) energetically-equivalent variants, the limit $k_T \rightarrow 0$ is well behaved and produces the expected result, viz. that the stress and incremental stiffness tensors are those of the dominant, lowest-energy variant.

As explained thus far, the energy density $F^*(\nabla\varphi)$ is used in the following as a numerically convenient approximation of the energy density in (3.12). k_T is chosen small but non-zero so as to provide smooth stress and tangent matrices while approximating (3.12) sufficiently. Fig. 3.5 illustrates the influence of the choice of k_T for a two-well potential energy as a starting example, defined by

$$\mathbf{U}_1 = \mathbf{I}, \quad \mathbf{U}_2 = \begin{pmatrix} 5/4 & 0 & 0 \\ 0 & 4/5 & 0 \\ 0 & 0 & 1 \end{pmatrix}, \quad \Psi_1 = 0, \quad \Psi_2 = 0.02, \quad (3.28)$$

with a compressible Neo-Hookean energy density

$$W_e(\mathbf{F}) = \frac{\mu}{2} \left(\frac{\text{tr}(\mathbf{F}^T \mathbf{F})}{J^{2/3}} - 3 \right) + \frac{\kappa}{2} (J - 1)^2, \quad J = \det \mathbf{F}, \quad (3.29)$$

with shear and bulk moduli μ and κ , respectively. The same elastic energy density is also used in the subsequent finite-strain examples. The loading is parameterized by

$$\mathbf{F} = \begin{pmatrix} 1 + \varepsilon & 0 & 0 \\ 0 & \frac{1}{1+\varepsilon} & 0 \\ 0 & 0 & 1 \end{pmatrix}. \quad (3.30)$$

Fig. 3.5 shows the two energy wells W_1 and W_2 as functions of the loading parameter ε as well as the approximated effective energy F^* for various values of k_T , with $k_T \rightarrow 0$ showing convergence to (3.12).

While the energy-minimizing examples in this chapter do not deal with dissipation, the above framework can be extended to materials systems in which volume fraction changes dissipate energy. In such cases, λ is no longer obtained by energy minimization but through the introduction of a (dual) dissipation potential $\psi^*(\dot{\lambda})$. Therefore, the variational principle can be treated by approaches including the implicit methods of variational constitutive updates (Ortiz and Stainier, 1999). A detailed discussion (within the analogous setting of linearized kinematics) is included in Tan and Kochmann (2017).

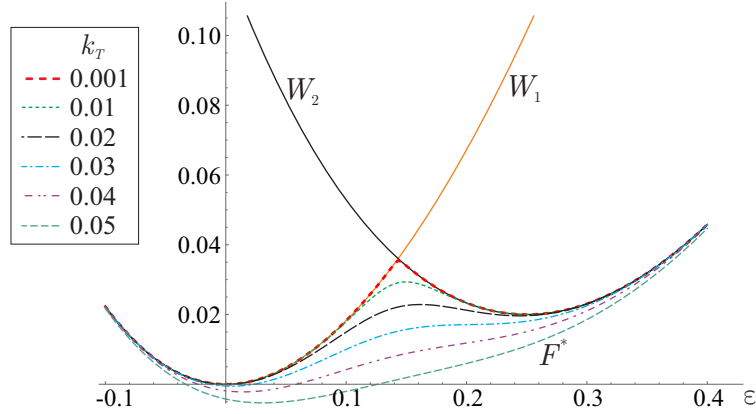


Figure 3.5: Plot of F^* from (3.18) for the biaxial loading defined by (3.30) with $\mu = 1$ and $\kappa = 3$ for various values of k_T from 0.001 to 0.05.

Double-Well Energy

As a first example, a double-well energy density is considered; this is defined by the transformation strains and chemical energies, respectively,

$$\mathbf{U}_1 = \begin{pmatrix} 1 & 0 & 0 \\ 0 & 1 & 0 \\ 0 & 0 & 1 \end{pmatrix}, \quad \mathbf{U}_2 = \begin{pmatrix} 1.2 & 0 & 0 \\ 0 & 1/1.2 & 0 \\ 0 & 0 & 1 \end{pmatrix}, \quad \Psi_1 = 0, \quad \Psi_2 = 4.5 \cdot 10^{-5}. \quad (3.31)$$

For the free energy, a Neo-Hookean energy density (3.29) with $\mu = 1$, $\kappa = 3$ is used and an RVE (of grid resolution 128^3) is subject to the applied average deformation gradient (3.30) for $\varepsilon > 0$.

For these and subsequent simulations using the phase-transformation model, the 8th-order central difference stencil will be used to perform regularization as numerical experiments show its optimality. In order to draw a comparison, a first-order lamination model is also presented in the results. The results indicate that the RVE initially deforms homogeneously up to strains $\varepsilon = 0.03$, whereupon needle-like second phase domains begin to nucleate. The growth of these interfaces induces the RVE to transition into a homogeneous second phase by $\varepsilon = 0.18$.

The computed numerical quasiconvex hull lies above the first-order lamination result, and this is postulated to be due to the contributions of interfacial energy between the two phases because of the existence of a strain gradient and stress concentration at the tips of the needle-shaped domains. The plot of deformation gradient component F_{12} , shown in Fig. 3.6, indicates complex hierarchical microstructural patterns in terms of strain and phase distribution that cannot easily be captured by simple first- or second-order lamination theory.

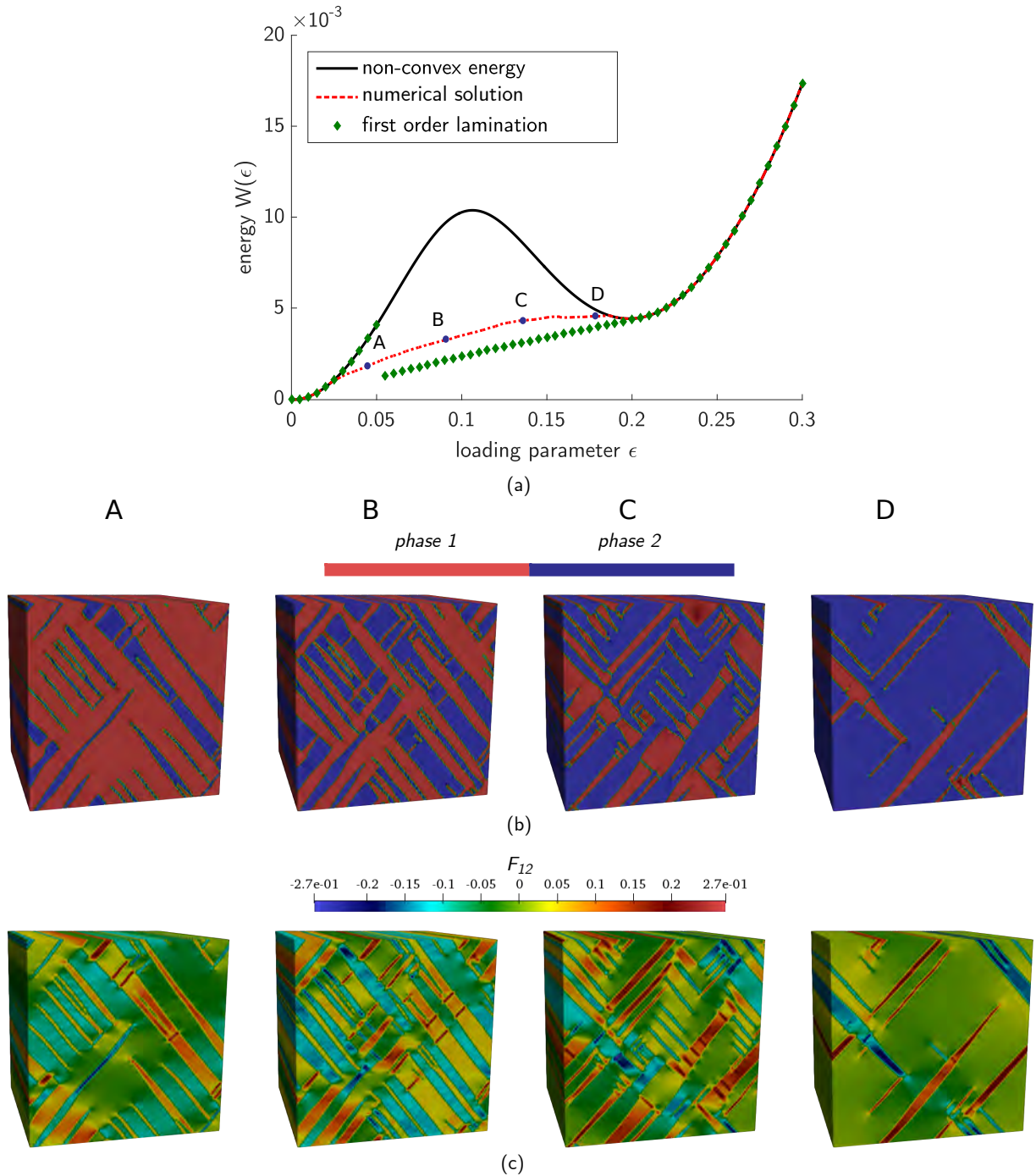


Figure 3.6: The calculated numerical hull is shown in (a). The corresponding microstructural patterns are shown in the volume fractions (b) & deformation gradient component F_{12} (c) during the loading process.

Three-Well Energies

In order to understand the influence of having multiple subsequent wells in the energetic landscape, a third well is added to the previous example in order to explore two scenarios. First,

consider the transformation strains and chemical energies given by

$$\begin{aligned} \mathbf{U}_1 &= \begin{pmatrix} 1 & 0 & 0 \\ 0 & 1 & 0 \\ 0 & 0 & 1 \end{pmatrix}, & \mathbf{U}_2 &= \begin{pmatrix} 1.2 & 0 & 0 \\ 0 & \frac{1}{1.2} & 0 \\ 0 & 0 & 1 \end{pmatrix}, & \mathbf{U}_3 &= \begin{pmatrix} 1.4 & 0 & 0 \\ 0 & \frac{1}{1.4} & 0 \\ 0 & 0 & 1 \end{pmatrix}, \\ \Psi_1 &= 0, & \Psi_2 &= 3.5 \cdot 10^{-5}, & \Psi_3 &= 8 \cdot 10^{-5}. \end{aligned} \quad (3.32)$$

In this case, the simulation results, depicted in Fig. 3.7, indicate that the RVE undergoes sequential phase transformations. Starting from a homogeneous RVE with the phase one (corresponding to \mathbf{U}_1 or identity), identical to the two-well example, needle-like domains emerge to induce a transformation to a homogeneous RVE of phase two (corresponding to \mathbf{U}_2).

In this regime direct nucleation of phase corresponding to \mathbf{U}_3 does not occur. Once the RVE transforms to a homogeneous second phase, it undergoes a second simple transformation from phase two to phase three, and within this regime domains of phase one do not emerge.

In contrast, when the third-well is lowered significantly, the phase transformation exhibits all three phases during the loading process. This is clear from the microstructure plots in Fig. 3.8. The material constants, transformation strains and loading path is identical to the three-well example above but chemical potentials used for this example are shown in Eq. (3.33).

$$\Psi_1 = 0, \quad \Psi_2 = 4.5 \cdot 10^{-5}, \quad \Psi_3 = 0. \quad (3.33)$$

An immediate consequence of this choice is that the RVE does not undergo the same manner of phase transformation as the two-well example, but immediately nucleates domains of the third phase from the first phase. From the plot of energy, included in Fig. 3.8, the numerically computed result does not touch, and goes below, the second well, which is also indicated by the RVE not exhibiting a homogeneous second phase microstructure during the loading path.

3.4 Single-Slip in Single- and Bi-Crystals

Hyperelasticity with the St. Venant-Kirchhoff model was an example of how an inappropriate choice of material model leads to unphysical patterns, and the phase transformation model showed the applicability of this approach to real physical phase transforming systems. To complement these, the single-slip model, which has attracted the attention of mathematicians (Carstensen et al., 2002; Conti and Theil, 2005; Conti and Ortiz, 2005; Albin et al., 2009; Anguige and Dondl, 2014; Kochmann and Hackl, 2011) in recent decades, is studied as a canonical benchmark problem. The finite-strain crystal plasticity model employed later in Chapter 4 also displays non-convexity along

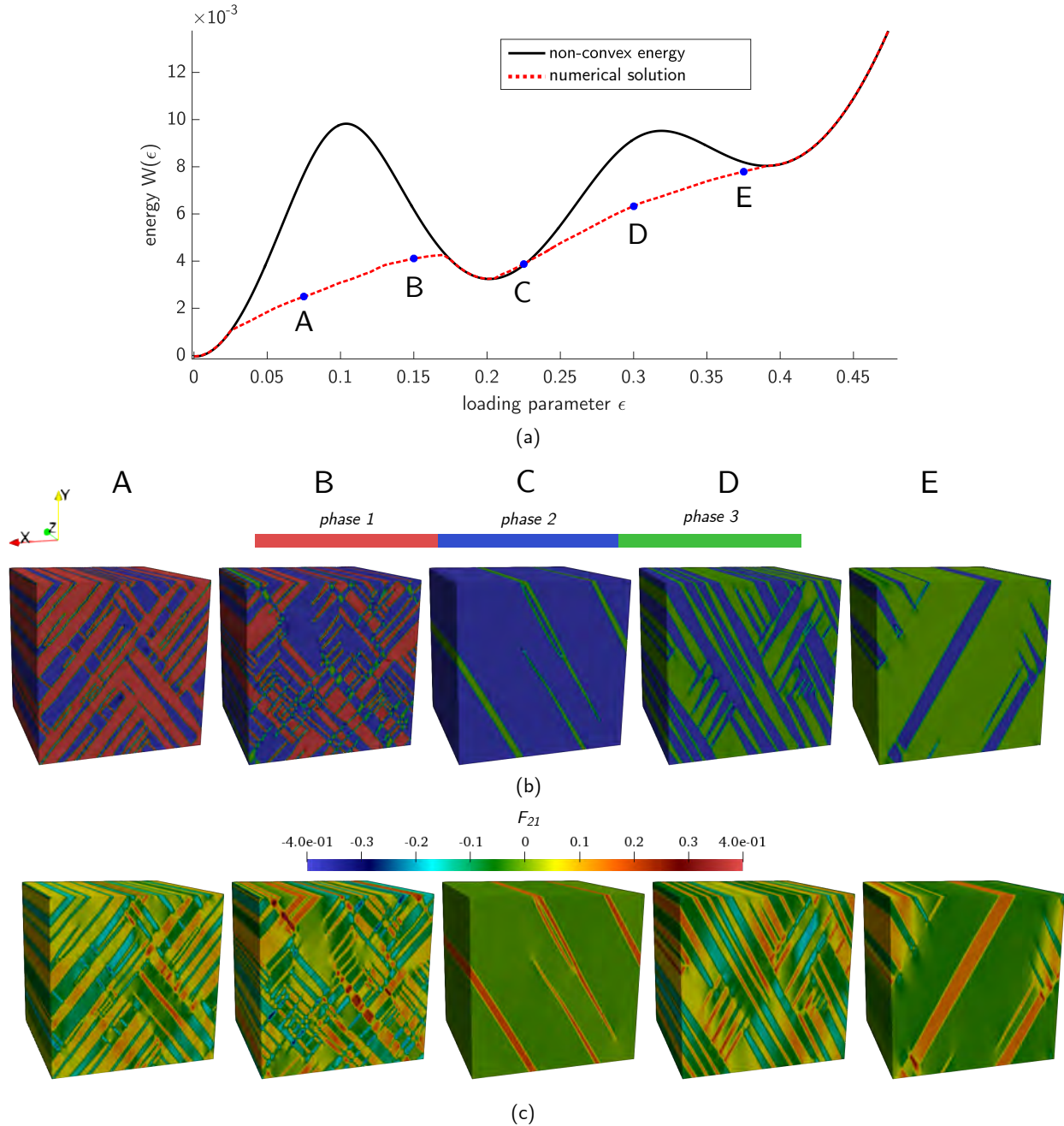


Figure 3.7: The calculated numerical hull is shown in (a) for the three-well case. The corresponding microstructural patterns are shown in the volume fractions (b) & deformation gradient component F_{21} (c) during the loading process.

certain loading paths, and hence it is imperative to study the numerical viability and patterning in a simplified single-slip system using the spectral scheme.

In the case of just a single active slip system, internal variables reduce to γ (*slip activity*) and ϵ (*accumulated slip* accounting for history). The accumulated slip activity is computed using the

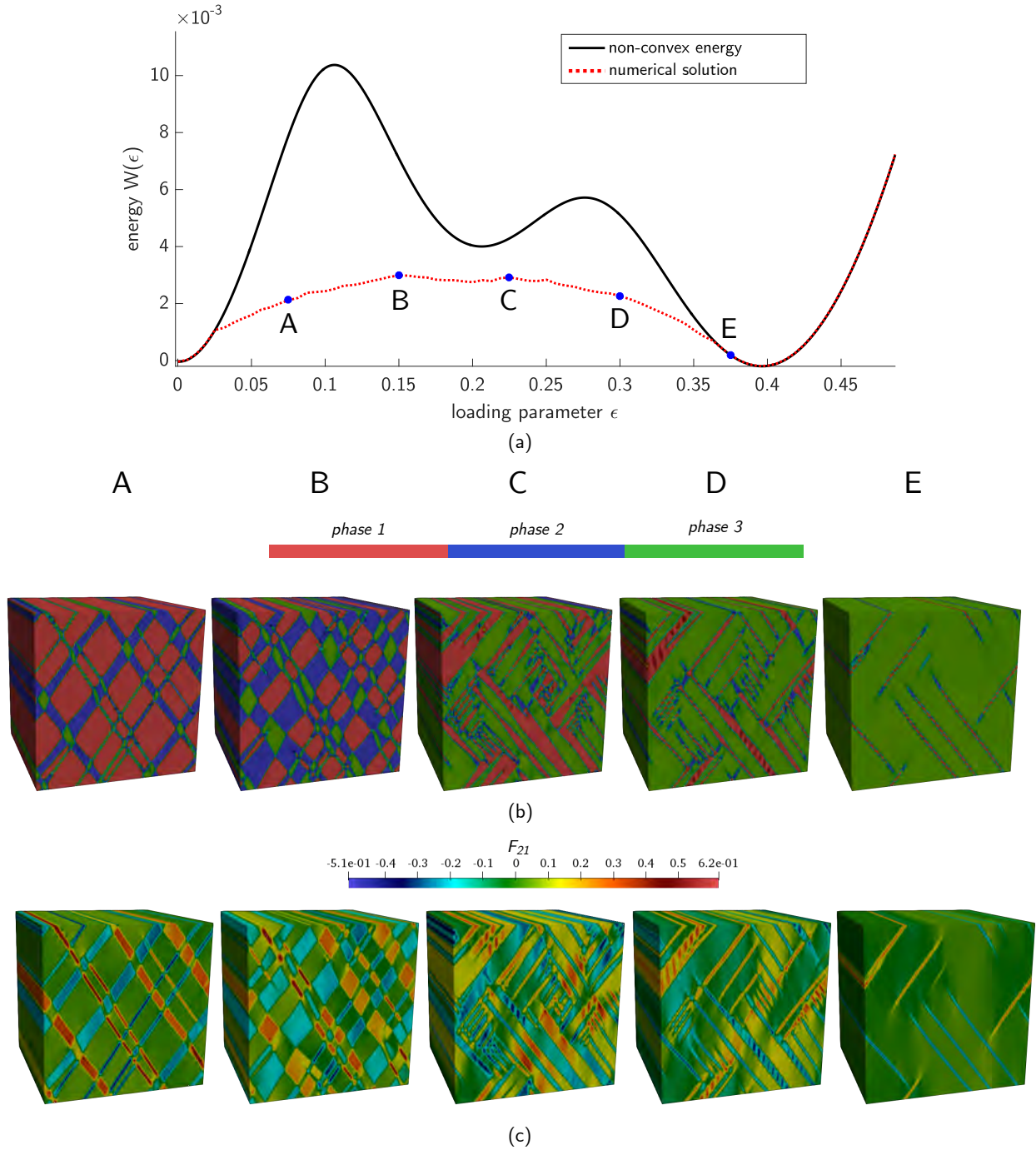


Figure 3.8: The calculated numerical hull is shown in (a) for the three-well case where the extremal wells lie below the middle-well. The corresponding microstructural patterns are shown in the volume fractions (b) & deformation gradient component F_{21} (c) during the loading process.

sum of absolute value of the incremental slip. Consequently, the inelastic deformation gradient F_p becomes

$$F_p = I + \gamma s \otimes m, \quad (3.34)$$

where \mathbf{s}, \mathbf{m} denote slip plane and normal vectors. The total deformation gradient is then assumed to undergo the multiplicative decomposition

$$\mathbf{F} = \mathbf{F}_e \mathbf{F}_p \quad \Rightarrow \quad \mathbf{F}_e = \mathbf{F} \mathbf{F}_p^{-1} \quad (3.35)$$

Substituting this into the energy density given by the sum of a compressible Neo-Hookean and quadratic plastic hardening energy,

$$A(\mathbf{F}, \epsilon) = \frac{\mu}{2} \left(\tilde{I}_{e,1} - 3 \right) + \frac{\kappa}{2} (J - 1)^2 + \frac{H}{2} \epsilon^2, \quad (3.36)$$

where μ represents the shear modulus, κ represents the bulk modulus and H represents a hardening parameter, and compressibility condition results in the modified invariant

$$\begin{aligned} \tilde{I}_{e,1} &= \frac{1}{J_e^{2/3}} \left(\text{tr}(\mathbf{F}_e^T \mathbf{F}_e) \right) \\ &= \frac{1}{J^{2/3}} \left(\text{tr} \mathbf{C} - 2\gamma \mathbf{m} \cdot \mathbf{C} \mathbf{s} + \gamma^2 \mathbf{s} \cdot \mathbf{C} \mathbf{s} \right). \end{aligned} \quad (3.37)$$

When a simple-shear test is performed, the deformation gradient is described by a macroscopic applied shear λ such that

$$\mathbf{F} = \mathbf{I} + \lambda \mathbf{b} \otimes \mathbf{c}, \quad \mathbf{b} \cdot \mathbf{c} = 0, \quad |\mathbf{b}| = |\mathbf{c}| = 1. \quad (3.38)$$

The slip angle φ describes the slip plane and slip normal (in-plane), while applied shear angle θ determines the angle at which shear is applied. Consequently, the definition of vectors $\mathbf{s}, \mathbf{m}, \mathbf{b}$, and \mathbf{c} are

$$\mathbf{s} = \begin{pmatrix} \cos \varphi \\ \sin \varphi \\ 0 \end{pmatrix}, \quad \mathbf{m} = \begin{pmatrix} -\sin \varphi \\ \cos \varphi \\ 0 \end{pmatrix}, \quad \mathbf{b} = \begin{pmatrix} \cos \theta \\ \sin \theta \\ 0 \end{pmatrix}, \quad \mathbf{c} = \begin{pmatrix} -\sin \theta \\ \cos \theta \\ 0 \end{pmatrix}. \quad (3.39)$$

Upon expansion, the free energy density, $A(\gamma, \epsilon, \lambda)$ becomes

$$\begin{aligned} A(\gamma, \epsilon, \lambda) &= \frac{1}{4} \left[\mu \left(\gamma^2 (\lambda^2 + 2) + 2\lambda^2 \right) + \gamma \lambda \mu [2(\lambda - \gamma) \sin(2(\theta - \varphi)) \right. \\ &\quad \left. - (\gamma \lambda + 4) \cos(2(\theta - \varphi))] + 2H\epsilon^2 \right]. \end{aligned} \quad (3.40)$$

Assuming monotonous loading, $\epsilon = |\gamma|$ along each increment. For any choice of slip and shear angles satisfying $\varphi = \theta$,

$$A(\gamma, \lambda) = \frac{1}{2} \left[\mu (\gamma - \lambda)^2 + H\gamma^2 \right]. \quad (3.41)$$

Minimizing with respect to the internal variable $\gamma = \gamma(\lambda)$, the *condensed energy* $A^*(\lambda)$ becomes

$$A^*(\lambda) = A(\lambda, \gamma(\lambda)) = \frac{H\lambda^2 \mu}{2(H + \mu)} \quad \forall \quad H \neq -\mu. \quad (3.42)$$

For any physically reasonable range of shear modulus μ and hardening parameter H , the condensed energy density is quadratic and therefore convex. As seen thus far, if an RVE with slip angle φ is subject to shear such that $\varphi = \theta$, it will deform homogeneously throughout the applied loading.

However, this is not true when considering the space of all possible orientations (φ, θ) such that $\varphi \neq \theta$. For instance, taking the case of slip and shear angles $\varphi = -\pi/3$ and $\theta = \pi/12$ and, and only considering monotonous loading as before, the energy reduces to

$$A(\gamma, \lambda) = \frac{1}{8} \left[2\gamma\lambda \left(\lambda + 2\sqrt{3} \right) \mu + \gamma^2 \left(4H + \left[\lambda \left((\sqrt{3} + 2) \lambda - 2 \right) + 4 \right] \mu \right) + 4\lambda^2 \mu \right]. \quad (3.43)$$

The condensed energy density now becomes

$$A^*(\lambda) = \frac{16H\lambda^2\mu + 7\lambda^4\mu^2 + 4\sqrt{3}\lambda^4\mu^2 - 4\sqrt{3}\lambda^3\mu^2 - 8\lambda^3\mu^2 + 4\lambda^2\mu^2}{8 \left(4H + 2\lambda^2\mu + \sqrt{3}\lambda^2\mu - 2\lambda\mu + 4\mu \right)} \quad (3.44)$$

which holds for all

$$\lambda > 0 \quad \wedge \quad H > \frac{1}{4} \left[- \left(3\sqrt{3} + 6 \right) \lambda^2 + 6\lambda - 12 \right]. \quad (3.45)$$

It can be shown that the condensed energy (3.44) is non-convex in λ for a particular range of values in (H, λ) -space. For example, Fig. 3.9 plots the condensed energy (3.44) as a function of the loading parameter λ for various different hardening parameters H at fixed $\mu = 3$.

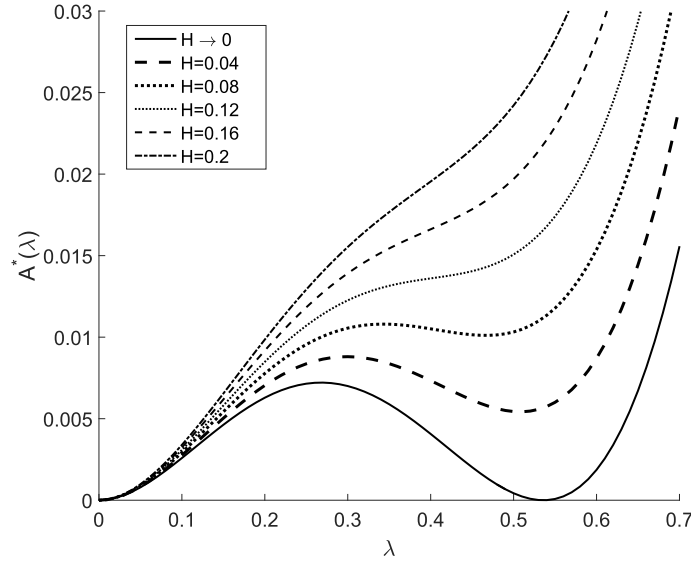


Figure 3.9: Loss of convexity of the condensed energy $A^*(\lambda)$ as the hardening parameter H decreases (Vidyasagar et al., 2018).

In the theme of previous models, as the hardening parameter H decreases, the energy landscape becomes increasingly non-convex, which in turn implies that the energy can be lowered by breaking up the homogeneous deformation into heterogeneous domains (Klusemann and Kochmann, 2014).

Previous analytical studies have used laminate constructions to approximate the rank-one-convex (and thus the quasiconvex) hull (Ortiz and Repetto, 1999; Miehe et al., 2004; Kochmann and Hackl, 2011). Here, energy-minimizing patterns are calculated by applying the spectral technique to a single-crystal RVE. For fair comparisons between analytical solutions and numerical results, energy-minimizing microstructures are sought irrespective of loading history (i.e., dissipation-free kinetic model) with the same parameters as the analytical model ($H = 2.0 \cdot 10^{-4}$, $\mu = 3$, $\kappa = 3$, $\varphi = -\pi/3$, and $\theta = \pi/12$; note that the magnitude of the moduli does not affect the microstructure, so they are given in arbitrary units). While subsequent polycrystal Mg simulations in Chapter 4 will account for all dissipative effects of (visco)plasticity (and realistic material parameters); in the theme of this chapter, a dissipation-free example is used to illustrate a clean benchmark for energy-minimizing microstructural pattern formation.

The relationship between the finite-difference schemes and microstructural length scales and interface energies has not been quantified thus far, but single-crystal single-slip finite plasticity gives the opportunity to do so. Considering the standard spectral method without finite-difference smoothing, a plot of the relevant energies and slip activity in the reference configuration is shown in Fig. 3.10.

While the analytical solution of the quasiconvex hull corresponds to a laminate having zero strain energy between the two energy wells (Kochmann and Hackl, 2011), the numerical approximation is non-zero and experiences a series of jumps along the loading path, corresponding to sudden changes in microstructure. The initial state equilibrates into checkerboard-like patterns, followed by the gradual formation of transient laminate patterns that evolve with increasing load. Macro-laminates emerge at larger loads, displaying characteristics of first-, second- and higher-order laminates. However, due to the lack of a length scale, the observation of clean laminate patterns is rare and the numerical approximation of the quasiconvex hull produces complex, generally non-laminate patterns.

Like analytical lamination schemes (Ortiz and Repetto, 1999; Miehe et al., 2004; Kochmann and Hackl, 2011), the model whose results are shown in Fig. 3.10 neglects interface energies and therefore does not have an intrinsic length scale (as explained in Chapter 1 this results in infinitely fine infimizing sequences). In our numerical setting, interfaces between laminate domains contribute energy only when the finite-difference smoothing described in Section 2.5 is applied. Therefore, the simulation of Fig. 3.10 is repeated with the modified Fourier transform of Section 2.5, which introduces an artificial, regularizing contribution to the stored energy (see Eq. (2.49)). The analogous results are presented in Fig. 3.11. Both first- and second-order laminate patterns are observed, and the patterns are considerably cleaner than those without finite-difference regularization. The finite-difference regularization results in thicker interfaces with a characteristic

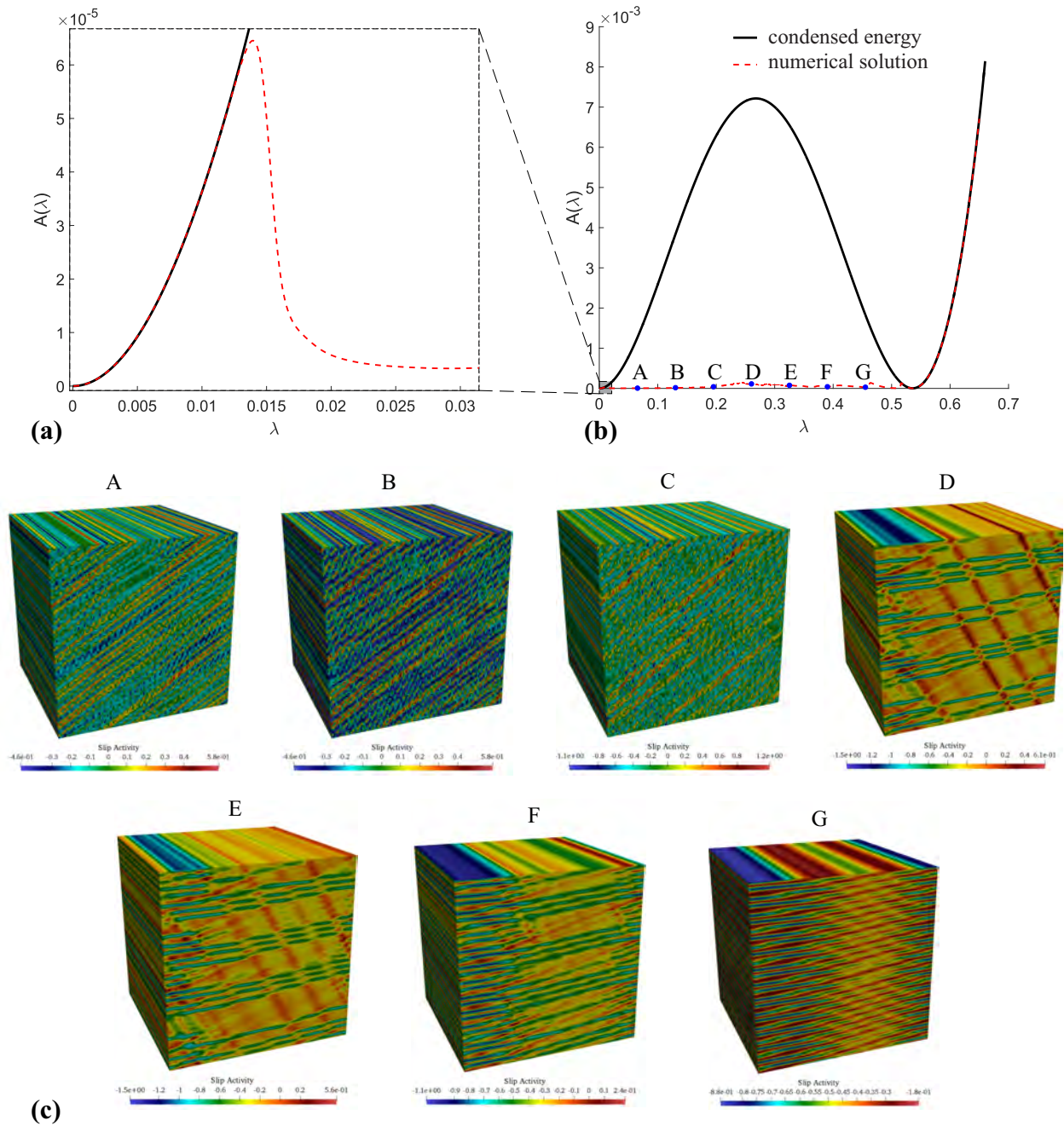


Figure 3.10: Approximation of the quasiconvex envelope obtained by spectral homogenization without finite-difference approximation: the average energy of the RVE is compared to the non-convex condensed energy with (a) showing a magnification of (b); (c) shows the microstructural slip activity within the RVE at stages A through G along the loading path as indicated in (b) (Vidyasagar et al., 2018).

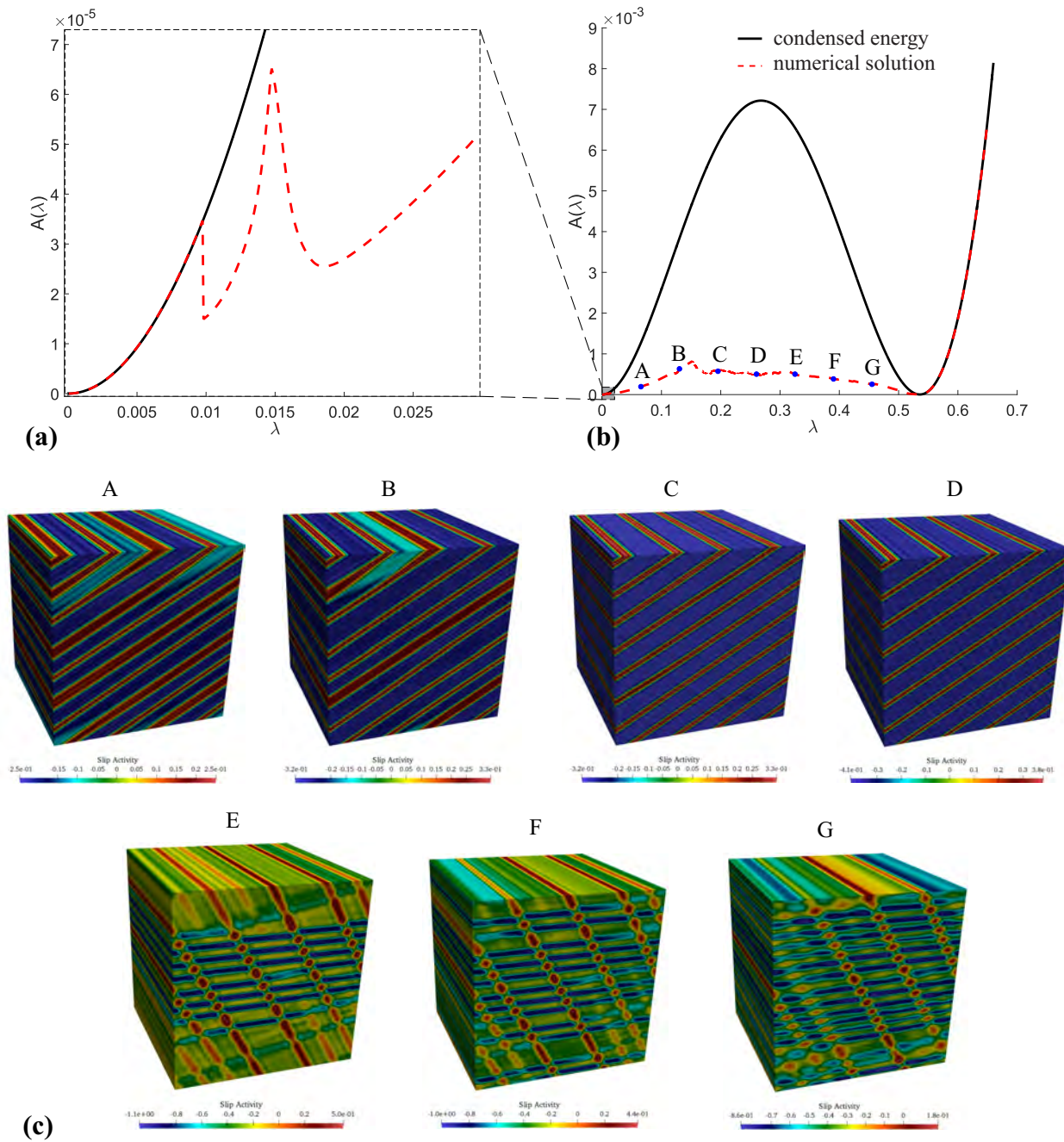


Figure 3.11: Approximation of the quasiconvex envelope obtained by spectral homogenization with the twelfth-order finite-difference approximation: the average energy of the RVE is compared to the non-convex condensed energy with (a) showing a magnification of (b); (c) shows the microstructural slip activity within the RVE at stages A through G along the loading path as indicated in (b) (Vidyaasagar et al., 2018).

relative length scale; these regions, in turn, produce a diffuse interface-type contribution to the energy. Consequently, the path followed by the approximated quasiconvex hull is farther from the theoretical (zero-energy) envelope.

Quantification of Numerical Regularization

The special case of a single-slip model with Neo-Hookean elastic energy makes it possible to quantify the exact form of numerical regularization. The following approximation holds for a second-order central difference scheme:

$$F_{m,N}^h(\mathbf{X}_0) = \varphi_{m,N}^h(\mathbf{X}_0) = \varphi_{m,N}(\mathbf{X}_0) + \frac{(\Delta X)^2}{6} \frac{\partial^3 \varphi_m}{\partial X_N^3}(\mathbf{X}_0) + O(\Delta X^4). \quad (3.46)$$

Substituting the approximation of the total deformation gradient given by (3.46) leads to

$$\begin{aligned} W_e(\mathbf{F}_e) &= \frac{\mu}{2} \left(\text{tr} \bar{\mathbf{C}}_e - 3 \right) + \frac{\kappa}{2} (J - 1)^2 \\ &\approx \frac{\mu}{2} \left[\text{tr} \left(\frac{(\mathbf{F}^h \mathbf{F}_{\text{in}}^{-1})^T (\mathbf{F}^h \mathbf{F}_{\text{in}}^{-1})}{(\det \mathbf{F}^h)^{2/3}} \right) - 3 \right] + \frac{\kappa}{2} (\det \mathbf{F}^h - 1)^2 \\ &= \frac{\mu}{2} \left[(\det \mathbf{F}^h)^{-2/3} \text{tr} \left((\mathbf{F}^h \mathbf{F}_{\text{in}}^{-1})^T (\mathbf{F}^h \mathbf{F}_{\text{in}}^{-1}) \right) - 3 \right] + \frac{\kappa}{2} (\det \mathbf{F}^h - 1)^2. \end{aligned} \quad (3.47)$$

If the determinant and the first invariant of the elastic deformation gradient are expanded via a matrix Taylor series, one arrives at

$$F_{m,N}^h(\mathbf{X}_0) = F_{m,N}(\mathbf{X}_0) + \frac{(\Delta X)^n}{(n+1)!} \frac{\partial^{n+1} \varphi_m}{\partial X_N^{n+1}}(\mathbf{X}_0) + O(\Delta X^{n+2}). \quad (3.48)$$

Upon defining the error coefficient and using the chain rule of differentiation,

$$h^{(n)} = \frac{(\Delta X)^n}{(n+1)!}, \quad \text{and} \quad G_{iJ}^{(n)} = \sum_v \frac{\partial^{n+1} \varphi_i}{\partial X_v^{n+1}}(\mathbf{X}_0) \left(\mathbf{F}_{\text{in}}^{-1}(\mathbf{X}_0) \right)_{vJ}, \quad (3.49)$$

one obtains that

$$\det \mathbf{F}^h = \det \mathbf{F}_e^h = \det \mathbf{F} \left(1 + h^{(n)} \text{tr}(\mathbf{F}^{-1} \mathbf{G}^{(n)}) \right) + O(\Delta X^{n+2}) \quad (3.50)$$

and

$$\text{tr} \left((\mathbf{F}^h \mathbf{F}_{\text{in}}^{-1})^T (\mathbf{F}^h \mathbf{F}_{\text{in}}^{-1}) \right) = \text{tr} \left((\mathbf{F} \mathbf{F}_{\text{in}}^{-1})^T (\mathbf{F} \mathbf{F}_{\text{in}}^{-1}) \right) + 2h^{(n)} \text{tr}(\mathbf{F}^T \mathbf{G}^{(n)}) + O(\Delta X^{n+2}). \quad (3.51)$$

By substituting into the Neo-Hookean energy density and performing a matrix series expansion, the lowest-order error is obtained as

$$\tilde{W}_e = W_e + W^h + O(\Delta X^{n+2}) \quad (3.52)$$

$$W^h = \frac{(\Delta X)^n}{2(n+1)!} \left(2\kappa(J-1)J \text{tr} \left(\mathbf{F}_e^{-1} \mathbf{G}^{(n)} \right) - \frac{\mu}{J^{2/3}} \left[\text{tr} \mathbf{C}_e \text{tr} \left(\mathbf{F}_e^{-1} \mathbf{G}^{(n)} \right) - 3 \text{tr} \left((\mathbf{G}^{(n)})^T \mathbf{F}_e \right) \right] \right). \quad (3.53)$$

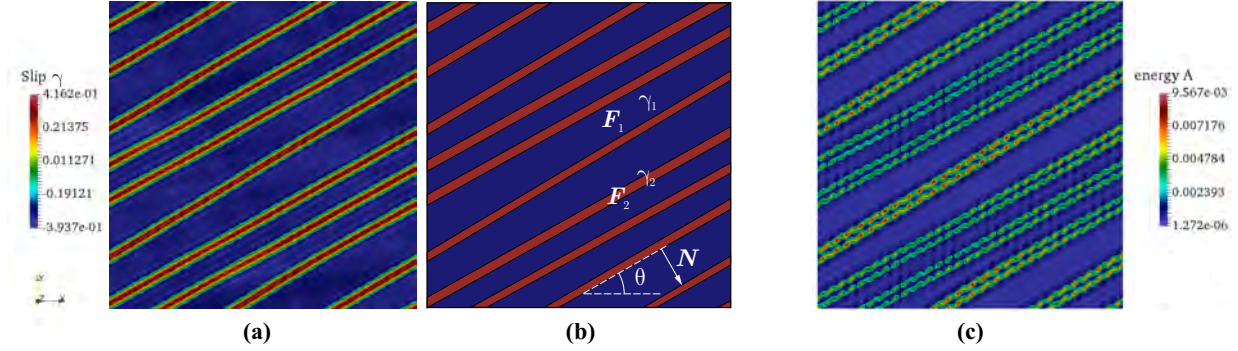


Figure 3.12: Laminate patterns for the simple shear test case at $\lambda = 0.208$ obtained from (a) numerical simulations using the above spectral homogenization framework and (b) the equivalent sharp-interface description. (c) shows the local energy density distribution of the numerical solution in (a), which shows concentrated energy within interfaces (Vidyasagar et al., 2018).

Interface Energy and Equivalent Laminate Microstructure

Unlike in the case of hyperelasticity or phase transformations where computationally predicted patterns did not generally conform to laminate definitions, in single slip the patterns (in the regularized case) visually correspond to laminates.

As such, it is reasonable to find out if the rank-one convex hull (Ortiz and Repetto, 1999; Aubry et al., 2003; Miehe et al., 2004; Kochmann and Hackl, 2011) obtained analytically matches the numerical result. These models assume sharp interfaces (as opposed to the diffuse interfaces from numerics) and construct laminates by enforcing kinematic compatibility. For convenience, the first-order laminate approximation of the rank-one convex hull (repeated from Eq. (1.22)) of $A(\mathbf{F})$ is given by

$$R_1 A(\mathbf{F}) = \inf \left\{ \nu_1 A(\mathbf{F}_1, \gamma_1) + \nu_2 A(\mathbf{F}_2, \gamma_2) \mid \nu_i, \mathbf{F}_i : 0 \leq \nu_i \leq 1, \sum_i \nu_i = 1, \sum_i \nu_i \mathbf{F}_i = \mathbf{F}, \text{rank}(\mathbf{F}_1 - \mathbf{F}_2) \leq 1 \right\}, \quad \mathbf{F}_1, \mathbf{F}_2 \in \text{GL}^+(d), \quad (3.54)$$

where ν_i denotes the volume fraction of laminate phases $i = 1, 2$. In order to satisfy the Hadamard compatibility constraint, it is required that $\mathbf{F}_2 - \mathbf{F}_1 = \mathbf{a} \otimes \mathbf{N}$, where \mathbf{N} is normal to the laminate interfaces and \mathbf{a} being the projected amplitude of jump in deformation gradient across the interface. As discussed above, in the non-convex region of the above example in the absence of hardening one obtains that $R_1 A(\mathbf{F}) = 0$.

As an example, results obtained from the numerically regularized diffuse-interface calculation and an equivalent sharp-interface laminate for the same simple shear test of Fig. 3.11 at an applied shear of $\lambda = 0.208$ are compared in Fig. 3.12 (a) and (b). From the simulated RVE solution, the

average quantities for each of the two laminate phases are determined, evaluating to

$$\begin{aligned} \mathbf{F}_{e,1} &\approx \begin{pmatrix} 0.956 & -0.291 & 0 \\ 0.291 & 0.956 & 0 \\ 0 & 0 & 1 \end{pmatrix}, & \mathbf{F}_{e,2} &\approx \begin{pmatrix} 0.933 & 0.358 & 0 \\ -0.358 & 0.933 & 0 \\ 0 & 0 & 1 \end{pmatrix}, & \gamma_1 &\approx 0.312, & \gamma_2 &\approx -0.357, \\ \mathbf{a} &\approx \begin{pmatrix} 0.581 \\ 0.308 \\ 0 \end{pmatrix}, & \mathbf{N} &\approx \begin{pmatrix} 0.480 \\ -0.877 \\ 0 \end{pmatrix}, & \theta &\approx 28.7^\circ, & \text{and} & \nu_1 &\approx 0.0993, \end{aligned} \quad (3.55)$$

where θ denotes the laminate orientation with $\mathbf{N} = (\sin \theta, -\cos \theta, 0)^\top$; see Fig. 3.12(b). The corresponding sharp-interface energy is

$$A_{\text{laminate}} = \nu_1 A_1 + (1 - \nu_1) A_2 = 1.61 \cdot 10^{-5}, \quad (3.56)$$

which is not (but very close to) zero (as in the ideal case of a sharp-interface laminate) but significantly less than the condensed energy for homogeneous deformation at the same applied shear ($\lambda = 0.208$), which is $A^* = 6.49 \cdot 10^{-3}$ with

$$\gamma = -\frac{3(\lambda^2 + 2\sqrt{3}\lambda)}{4H + 3\sqrt{3}\lambda^2 + 6\lambda^2 - 6\lambda + 12} = -0.204 \quad \text{and} \quad \mathbf{F}_e = \begin{pmatrix} 1.00 & 0.225 & 0 \\ -0.176 & 0.958 & 0 \\ 0 & 0 & 1 \end{pmatrix}. \quad (3.57)$$

Note that the above value of A_{laminate} is also considerably lower than the energy reported at point C in Fig. 3.11(b). This is because, due to the spectral regularization, the diffuse interfaces contribute additional energy, which raises the energy of the system as seen in the numerical simulation with $A_{\text{RVE}} = 5.66 \cdot 10^{-4}$ (point C in Fig. 3.11). Therefore, interface energy is significant and clearly the reason for the higher energy path followed by the numerical solution with spectral regularization. This is confirmed by a plot of the local energy density in Fig. 3.12(c), showing an increased energy localized within diffuse interfaces.

Extension to Bi-Crystals

The above laminate microstructures are expected to emerge in infinite, periodic crystals, neglecting the abundance of defects at the mesoscale of metals. As a first step towards a polycrystal, consider a bi-crystal made of two perfectly-bonded grains separated by a sharp interface, each grain undergoing single-slip on their respective slip system. The effect on the energy of changing the misorientation while keeping the other parameters fixed is shown in Fig. 3.13 (using $H = 2.0 \cdot 10^{-4}$, $\mu = 3$, and $\theta = \pi/12$). Assigning two different slip system orientations to the two grains of the

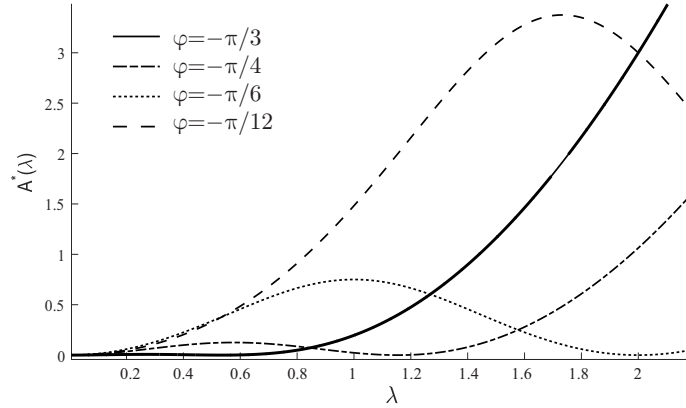


Figure 3.13: Influence of the slip system orientation φ on the non-convex, condensed energy landscape of a single-crystal, with all shown energies exhibiting non-convexity at different range of values for the shear parameter λ (Vidyasagar et al., 2018).

bicrystal and applying a macroscopic simple shear deformation (using the same finite-difference correction outlined in Section 2.5, which provides a relative length scale as discussed above), the results are shown in Fig. 3.14.

While each crystal would produce periodic laminate patterns as shown in the previous section, the bi-crystal shows more interesting features. If loaded separately, each grain would reduce its energy by forming independent laminates whose orientations depend on the slip system orientation. When fused together in a bi-crystal, compatibility across the interface imposes constraints that affect the emerging microstructural patterns, as shown in Fig. 3.14. As the misorientation between the two grains increases (here, varying φ_2 from $-\pi/4$ to $-\pi/12$ while keeping φ_1 constant), first-order laminates are suppressed in the central grain, with some indication of higher order microstructure. As can be expected, low misorientation results in laminate patterns spreading across grain boundaries and into adjacent grains. However, increasing the misorientation leads to the suppression of such patterns. The conclusion is that the presence of compatibility constraints significantly restricts the formation of energy-minimizing patterns within grains and results in a more complex picture, dependent on the misorientation and shape of grain boundaries. The expectation is that this effect is dramatically more pronounced in polycrystals with abundant grain boundaries (GBs), such as those discussed in the next chapter. Therefore, polycrystals are anticipated to form more general patterns (not necessarily clean laminates) but such patterns may emerge due to the non-(quasi)convexity of the energy.

3.5 Conclusion

In this chapter, energy minimizing strategies discussed in Chapter 1 using the numerical methods of Chapter 2 have been applied to three problems: hyperelasticity with the St. Venant-

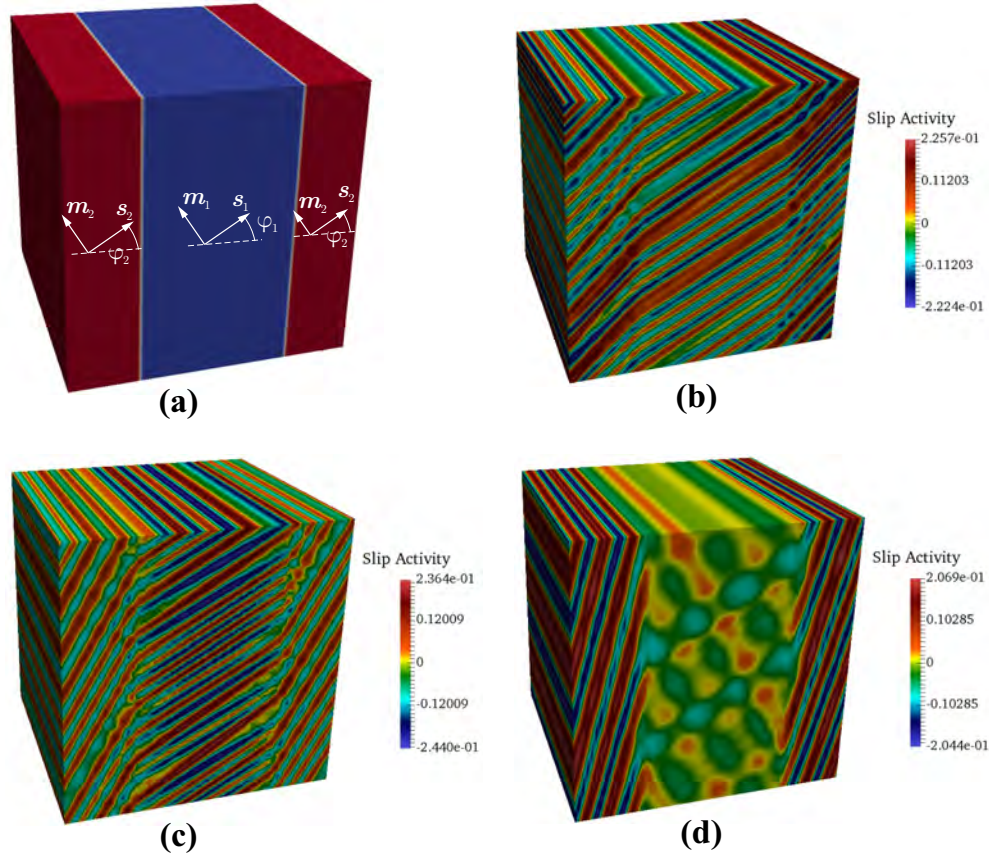


Figure 3.14: Laminate pattern formation in bicrystals at an applied shear strain of $\lambda = 0.03$: (a) the geometric arrangement of the two grains within the bicrystal RVE along with the definition of angles φ_1 and φ_2 in the blue and red grains, respectively. Results are shown for (b) $\varphi_1 = -\pi/3$ and $\varphi_2 = -\pi/4$, (c) $\varphi_1 = -\pi/3$ and $\varphi_2 = -\pi/6$, and (d) $\varphi_1 = -\pi/3$ and $\varphi_2 = -\pi/12$ (Vidyasagar et al., 2018).

Kirchhoff solid, a generalized phase transformation model, and finally single-(and bi-)crystal plasticity.

From Sec. 3.2 it is clear that the St. Venant-Kirchhoff model, while still popular in commercial finite element codes, predicts unphysical ‘patterns’ for a wide range of elastic constants. Additionally, these patterns cannot easily be geometrically encompassed by lamination theory, showing interesting ellipsoidal geometries that differ in each component. It is also of note that the finite-difference corrections do not influence the numerical solver’s ability to find the quasiconvex hull, but change the size (and relative grid-based length scale) of patterns. Finally, contrary to initial expectations, the numerical solver is able to better predict the quasiconvex hull of a double-well potential as opposed to one where the second well is lifted. The reason for this is postulated to be due to increased contribution from interfaces and indirectly from numerical regularization.

From the generalized phase transformation model in Section 3.3, it is clear that the method can be used to model systems with arbitrary transformation strains without simplifying mathematical assumptions such as elastic rigidity. An additional parameter is introduced, as a representation of configurational entropy, which tunes the interface thickness. The interplay between this factor and numerical regularization is shown to result in very complex pattern formation, including some second order laminate-like structures. As a novelty, the model is extended to the three-well problem, and it has been proven (and shown in Fig. 3.8) that the numerical method is able to find patterns corresponding to an energetic path which autonomously avoids local minima if extremal wells are suitably lower.

As a mathematically relevant final example, the single-slip crystal plasticity model has been shown numerically to produce very similar (qualitatively and quantitatively) patterns to analytical and experimental results. Additionally, the influence of numerical regularization have been analytically quantified. Extensions have also been shown for bi-crystals.

These have not dealt with dissipation or time evolution except for a nominal contribution arising from numerics of explicit updates. The following chapters will aim to address dissipation and kinetics, starting with an extension of the bi-crystal study in Section 3.4 to polycrystalline magnesium in Chapter 4.

DEFORMATION PATTERNS AND CRYSTAL VISCO-PLASTICITY IN MAGNESIUM POLYCRYSTALS

Research presented in this chapter has been adapted from the following publication:

Vidyasagar, A., Tutcuoglu, A., Kochmann, D. M. 2018. Deformation patterning in finite-strain crystal plasticity by spectral homogenization with application to magnesium. *Computer Methods in Applied Mechanics and Engineering*, 335, pp.584-609.

URL: <https://doi.org/10.1016/j.cma.2018.03.003>

4.1 Introduction

Magnesium (Mg) and magnesium alloys of various compositions have drawn interest for structural applications, primarily due to their high specific strength and low density (Pollock, 2010; Dixit et al., 2015). However, predicting the macroscopic mechanical response of bulk polycrystalline magnesium presents an open challenge. The hexagonal closed-packed (hcp) crystal structure of Mg results in anisotropic inelastic deformation mechanisms (Graff et al., 2007; Stanford et al., 2011), remarkably low ductility and an asymmetric tension-compression behavior (Máthis et al., 2011; Park et al., 2014; Zachariah et al., 2013; Kurukuri et al., 2014). Dislocation slip and deformation twinning occur as competing mechanisms, and their mechanistic influences drive complex microstructure evolution paths observed in magnesium polycrystals (Agnew and Duygulu, 2005; Chang et al., 2017). It is hence important to understand and enable the prediction of mesoscale microstructure evolution by high-fidelity methods, to gain insight into the link between processing conditions, resulting microstructure and, ultimately, effective material properties. Simulations, in principle, must span a wide range of length and time scales to accurately capture interactions between twinning and dislocation slip, both of which are affected by the polycrystalline texture and grain size distribution. To this end, a combination of numerically efficient solvers and reliable constitutive models is required.

Previous work in modeling Mg has involved atomistic investigations (Tomé et al., 2011; Wang et al., 2012), phase field models (Steinbach et al., 1996; Levitas et al., 2009; Clayton and Knap, 2011), relaxation-based techniques (Simo, 1988), and various phenomenological continuum theories (Oppedal et al., 2013; Becker and Lloyd, 2016; Kalidindi, 2001; Izadbakhsh et al., 2011; Cheng and Ghosh, 2017; Zhang and Joshi, 2012). Chang and Kochmann (2015) recently devel-

oped a continuum constitutive model for Mg which combines conventional hcp crystal plasticity, accounting for the full set of hcp slip systems, with an effective description of the twin systems based on effective volume fractions; i.e., instead of resolving individual twin lamellae as in phase field approaches (Clayton and Knap, 2011), the mesoscopic description only considers the effective volume fractions of twinned and untwinned phases at a given point on the continuum scale. The reorientation of slip systems arising from deformation twinning is considered in a similar manner to previous work by Homayonifar and Mosler (2011, 2012) and Zhang and Joshi (2012). Chang et al. (2017) compared the performance of the model with reduced-order kinematic models and showed that lattice reorientation is critical for capturing experimentally observed behavior at large strains. However, the numerical inefficiencies of implementing the detailed constitutive model as compared to the reduced-order model within a conventional finite element (FE) framework discourages its use in modeling the micro-to-macro transition. Therefore, this work reports methods and results of periodic homogenization using spectral techniques of Chapter 2 along with a modified version of the constitutive model of Chang and Kochmann (2015) at the mesoscale of polycrystalline, pure Mg. Such periodic homogenization enables the prediction of microstructural evolution paths arising from various loading conditions and the extraction of the effective macroscopic stress-strain performance for comparisons to experimental observations. A key question in this context is the level of microstructural details required in order to reliably predict the effective macroscopic performance through a compromise of accuracy vs. efficiency.

Finite-deformation crystal plasticity models (especially those accounting for latent hardening and slip-twinning interactions) introduce particular numerical challenges. Certain loading paths result in a loss of quasiconvexity in regions of the energetic landscape, as seen in the previous Section 3.4. As is the theme of this thesis, energy relaxation in those regions is accomplished by breaking up the homogeneous deformation state into complex microstructural patterns (Ball, 1977) which result in energy-infinimizing sequences (Carstensen et al., 2002; Conti and Theil, 2005; Conti et al., 2009; Hackl and Kochmann, 2008; Kochmann and Hackl, 2011). Since those patterns are generally non-unique and the energy landscape offers numerous local minima, the prediction of minimizing microstructures (and the resulting stress-strain response as the volume average) is demanding.

Here, a beneficial combination is applied of several of the above approaches to study the microstructure formation and evolution in finite-strain crystal plasticity applied to polycrystalline Mg. The remainder of the chapter is hence structured as follows. In Section 4.2, the constitutive model is briefly summarized for finite-strain plasticity in pure Mg. Next, in Section 4.4 the extension of the Fourier spectral setup of Chapter 2 and Section 3.4 is extended to multiple-slip for use in high-resolution crystal plasticity simulations. Section 4.5 summarizes results of microstructure

evolution and effective properties of polycrystalline Mg with varying grain size and texture, before concluding the present study in Section 4.6.

4.2 Constitutive Model: Finite-Strain Crystal Plasticity in Magnesium

The constitutive model is reviewed here to the extent necessary for subsequent discussions; more details can be found in [Chang and Kochmann \(2015\)](#) and [Vidyasagar et al. \(2018\)](#). The deformation at a point $\mathbf{x} \in \Omega$ of a body Ω at time $t \geq 0$ is described by the deformation mapping

$$\varphi(\mathbf{X}, t) : \Omega \times t \rightarrow \mathbb{R}^n. \quad (4.1)$$

Under the assumption of isochoric plasticity, the deformation gradient

$$\mathbf{F}(\mathbf{X}, t) = \text{Grad}(\varphi(\mathbf{X}, t)) \quad (4.2)$$

is multiplicatively decomposed into its elastic and inelastic parts, i.e.,

$$\mathbf{F} = \mathbf{F}_e \mathbf{F}_{in}. \quad (4.3)$$

The hcp crystallography of Mg includes n_s slip systems, described by slip directions \mathbf{s}_α and normal vectors \mathbf{m}_α . Similarly, the n_t twin systems are described by twin normals \mathbf{n}_β and twinning shears \mathbf{a}_β . Dislocation slip is described by slips γ_α and twinning through effective twin volume fractions λ_β subject to the constraints

$$0 \leq \lambda_\beta \leq 1, \quad 0 \leq \sum_{\beta=1}^{n_t} \lambda_\beta \leq 1. \quad (4.4)$$

The plastic velocity gradient tensor incorporates an additive decomposition into slip and twinning contributions, assuming these mechanisms occur simultaneously (with dots denoting material time derivatives):

$$\mathbf{l} = \dot{\mathbf{F}}\mathbf{F}^{-1} = \mathbf{l}_e + \mathbf{l}_{in} = \dot{\mathbf{F}}_e\mathbf{F}_e^{-1} + \mathbf{F}_e\tilde{\mathbf{l}}_{in}\mathbf{F}_e^{-1}, \quad \tilde{\mathbf{l}}_{in} = \dot{\mathbf{F}}_{in}\mathbf{F}_{in}^{-1} = \tilde{\mathbf{l}}_p + \tilde{\mathbf{l}}_{tw}. \quad (4.5)$$

Following earlier works of [Kalidindi \(2001\)](#) and [Zhang and Joshi \(2012\)](#), the modified kinetic flow rule accounts for slip on both parent and twin systems. The crystallographic reorientation due to twinning is described by reflection tensors $\mathbf{Q}_\beta = \mathbf{I} - 2\mathbf{n}_\beta \otimes \mathbf{n}_\beta$ such that

$$\tilde{\mathbf{l}}_{tw} = \sum_{\beta} \dot{\lambda}_\beta \mathbf{a}_\beta \otimes \mathbf{n}_\beta, \quad \tilde{\mathbf{l}}_p = \left[1 - \sum_{\beta} \lambda_\beta \right] \sum_{\alpha} \dot{\gamma}_\alpha \mathbf{s}_\alpha \otimes \mathbf{m}_\alpha + \sum_{\beta} \lambda_\beta \sum_{\alpha} \dot{\gamma}_\alpha \mathbf{Q}_\beta \mathbf{s}_\alpha \otimes \mathbf{Q}_\beta \mathbf{m}_\alpha. \quad (4.6)$$

The hardening behavior is captured by introducing the accumulated plastic slips ϵ_α , evolving according to $\dot{\epsilon}_\alpha = |\dot{\gamma}_\alpha|$. The thermodynamic description is based on the Helmholtz free energy density

$$A(\mathbf{F}_e, \boldsymbol{\epsilon}, \boldsymbol{\lambda}) = W_e(\mathbf{F}_e) + W_p(\boldsymbol{\epsilon}) + W_{tw}(\boldsymbol{\lambda}), \quad (4.7)$$

containing, respectively, elastic, slip and twin contributions and depending on the internal variables $\lambda = \{\lambda_1, \dots, \lambda_{n_t}\}$, $\gamma = \{\gamma_1, \dots, \gamma_{n_s}\}$ and $\epsilon = \{\epsilon_1, \dots, \epsilon_{n_s}\}$. For simplicity, the elastic energy density is assumed approximately isotropic and taken as that of a compressible Neo-Hookean solid (μ and κ are, respectively, the shear and bulk moduli)¹:

$$W_e(\mathbf{F}_e) = \frac{\mu}{2} \left(\text{tr } \bar{\mathbf{C}}_e - 3 \right) + \frac{\kappa}{2} (J - 1)^2, \quad \bar{\mathbf{C}}_e = \bar{\mathbf{F}}_e^T \bar{\mathbf{F}}_e, \quad \bar{\mathbf{F}}_e = \frac{\mathbf{F}_e}{J^{1/3}}, \quad J = \det \mathbf{F}. \quad (4.8)$$

The stored plastic energy density accounts for latent and self-hardening for each slip system, formulated as

$$W_p(\epsilon) = \frac{1}{2} \epsilon \cdot H \epsilon + \begin{cases} \frac{h_0}{2} \epsilon_\alpha^2 & \text{for basal systems,} \\ \sigma_\infty \left[\epsilon_\alpha + \frac{\sigma_\infty}{h} \exp\left(-\frac{h_0 \epsilon_\alpha}{\sigma_\infty}\right) \right] & \text{for prismatic and pyramidal systems,} \end{cases} \quad (4.9)$$

where the parameters are specific to each slip system and given in 4.3. Similarly, the stored twin energy is assumed of the form

$$W_{tw}(\lambda) = \frac{1}{2} \lambda \cdot \mathcal{K} \lambda + \frac{h_\beta}{2} \lambda_\beta^2. \quad (4.10)$$

As discussed in [Chang and Kochmann \(2015\)](#), simultaneous multiple twin systems at a single point are avoided by high latent twin hardening (i.e., high values of the off-diagonal components of the twin hardening matrix \mathcal{K}).

The rate-dependent evolution laws for slip and twinning are defined by dual dissipation potentials $\Psi_p^*(\dot{\gamma})$ and $\Psi_{tw}^*(\dot{\lambda})$, respectively, akin to previous approaches in crystal plasticity; see, e.g., [Ortiz and Stainier \(1999\)](#)

$$\Psi_p^*(\dot{\gamma}) = \sum_\alpha \frac{\tau_0 \dot{\gamma}_0}{m+1} \left(\frac{\dot{\gamma}_\alpha}{\dot{\gamma}_0} \right)^{m+1}, \quad \Psi_{tw}^*(\dot{\lambda}) = \sum_\beta \frac{\eta_\beta}{2} \dot{\lambda}_\beta^2 \quad (4.11)$$

with reference slip rate $\dot{\gamma}_0$, hardening exponent m , back-stress τ_0 , and twin resistance (inverse mobility) η for each system. Note that in contrast to the rate-independent formulation of [Chang and Kochmann \(2015\)](#), here the rate-dependent formulation for twinning is adopted from ([Chang et al., 2017](#)) with the above quadratic dissipation potential to facilitate a simple explicit update scheme for slip and twinning (to be discussed in Section 4.4).

The principle of minimum dissipation potential ([Ortiz and Repetto, 1999](#); [Carstensen et al., 2002](#); [Conti and Ortiz, 2008](#); [Hackl and Fischer, 2008](#)) is invoked to derive the evolution laws for the internal variables γ and λ , viz.

$$0 \in \frac{\partial}{\partial \dot{\gamma}} \left(\dot{A} + \Psi_p^* \right), \quad 0 \in \frac{\partial}{\partial \dot{\lambda}} \left(\dot{A} + \Psi_{tw}^* \right). \quad (4.12)$$

¹The elastic anisotropy is relatively mild and was shown to have little effect on the effective material response ([Chang and Kochmann, 2015](#)).

For the rate-dependent model considered here, the differential inclusions can be replaced by equalities. Minimizing the total stress power using (4.12) results in the kinetic update rules

$$\begin{aligned} \dot{\gamma}_\alpha &= \left(\frac{|\tau_\alpha^p| - \tau_\alpha^h}{\tau_0} \right)^{\frac{1}{m}} & \text{with} & \quad \tau_\alpha^h = \sum_{\zeta} h_{\alpha\zeta} \epsilon_\zeta + \sigma_\infty \left[1 + \exp \left(-\frac{h_0 \epsilon_\alpha}{\sigma_\infty} \right) \right], \\ \dot{\lambda}_\beta &= \frac{\tau_\beta^{\text{tw}} - \tau_\beta^h}{\eta_\beta} & \text{with} & \quad \tau_\beta^h = \sum_{\zeta} k_{\beta\zeta} \lambda_\zeta + h_0 \lambda_\beta, \end{aligned} \quad (4.13)$$

where τ_α and τ_β are the resolved shear stresses on the respective slip and twin systems.

4.3 Material Constants for the Mg Constitutive Model

The material constants used for the simulations are summarized in Table 4.1. The slip and twin systems in Mg are visualized in Fig 4.1.

material and numerical parameters used in simulations of pure Mg							
description	parameter	value	units	description	parameter	value	units
elastic constants	κ	36.7	GPa	hardening & dissipation (pyramidal $\langle c + a \rangle$)	h_α	30	GPa
	μ	34.0	GPa		σ_∞	150	MPa
hardening & dissipation (basal)	h_α	7.1	GPa		h_{ij}	25	MPa
	σ_∞	0.7	MPa		τ_0	17.5	MPa
	h_{ij}	0.0	MPa		m	0.05	-
	τ_0	17.5	MPa		$\dot{\gamma}_0$	1.0	s^{-1}
	m	0.05	-		extension twins	h_0	1.7
$\dot{\gamma}_0$	1.0	s^{-1}	k_{ij}	40		GPa	
hardening & dissipation (prismatic)	h_α	9	GPa	simulation parameters	Δt	0.01	s
	σ_∞	85	MPa		$n_{\text{domain}, \mathcal{T}}$	128 ³	-
	h_{ij}	20	MPa				
	τ_0	17.5	MPa				
	m	0.05	-				
	$\dot{\gamma}_0$	1.0	s^{-1}				

Table 4.1: Material parameters are adopted from [Chang and Kochmann \(2015\)](#) who obtained their constants by fitting to experimental results of [Kelley and Hosford \(1968\)](#) for individually activated slip and twin systems, together with simulation parameters.

4.4 Numerical Solution Strategy – Explicit Updates

The above equations, using the spectral methods discussed in Chapter 2, are solved in an incremental, staggered fashion for the unknown fields $\mathbf{F}(\mathbf{X})$, $\lambda(\mathbf{X})$, and $\gamma(\mathbf{X})$ at the RVE grid points, using an explicit scheme. First, at each load step $n + 1$, with a known $(\mathbf{F}^0)^{n+1}$ the elastic

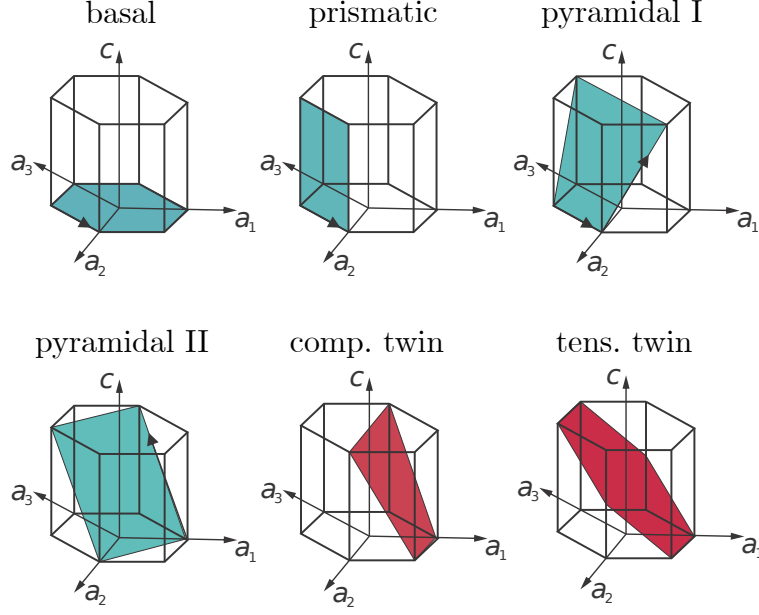


Figure 4.1: An overview of the variety of dislocation slip and twinning modes in magnesium (Vidyasagar et al., 2018).

problem is solved assuming constant internal variables,

$$F_{kL}^{n+1}(\mathbf{X}) = \mathcal{F}^{-1}\{\hat{F}_{kL}^{n+1}(\mathbf{K})\} \quad \text{and} \quad \hat{F}_{kL}^{n+1}(\mathbf{K}) = \begin{cases} \mathbb{A}_{ik}^{-1}(\mathbf{K}) \hat{\tau}_{ij}^{n+1}(\mathbf{K}) K_J K_L & \text{for } \mathbf{K} \neq \mathbf{0} \\ (F_{kL}^0)^{n+1} & \text{for } \mathbf{K} = \mathbf{0}. \end{cases} \quad (4.14)$$

The nonlinear equations are solved using a fixed-point iteration scheme. Due to the non-linearity of the elastic problem, the deformation-dependent acoustic tensor \mathbb{A} is re-evaluated periodically during the iterations. Next, the internal variables are updated in real space at each material point, with the update for slip activity given by

$$\gamma_\alpha^{n+1} = \gamma_\alpha^n + \Delta\gamma_\alpha^n = \gamma_\alpha^n + \dot{\gamma}_\alpha^0 \Delta t \left(\frac{|\tau_\alpha^p| - \tau_\alpha^{\text{cr}}}{\tau_\alpha^0} \right)^{\frac{1}{m}} \quad (4.15)$$

with

$$\tau_\alpha^p = \left(\mathbf{F}_e^T \frac{\partial W_e}{\partial \mathbf{F}} \mathbf{F}_{\text{in}}^T \right) \cdot \left(\left(1 - \sum_\beta \lambda_\beta^n \right) \mathbf{s}_\alpha \otimes \mathbf{m}_\alpha + \sum_\beta \lambda_\beta^n \mathbf{Q}_\beta \mathbf{s}_\alpha \otimes \mathbf{Q}_\beta \mathbf{m}_\alpha \right) \quad (4.16)$$

and

$$\tau_\alpha^{\text{cr}} = \frac{\partial W_p(\boldsymbol{\gamma})}{\partial \gamma_\alpha}, \quad (4.17)$$

both to be evaluated at the previous load step n . The update for the twin volume fractions follows analogously as

$$\lambda_\beta^{n+1} = \lambda_\beta^n + \Delta\lambda_\beta^n = \lambda_\beta^n + \lambda_\beta^0 \Delta t \left(\frac{\tau_\beta^{\text{tw}} - \tau_\beta^{\text{cr}}}{\tau_\beta^0} \right) \quad (4.18)$$

with

$$\tau_\beta^{\text{tw}} = \bar{\gamma}_\beta^{\text{tw}} \left(\mathbf{F}_e^T \frac{\partial W_e}{\partial \mathbf{F}} \mathbf{F}_{\text{in}}^T \right) \cdot (\mathbf{a}_\beta \otimes \mathbf{n}_\beta) \quad \text{and} \quad \tau_\beta^{\text{cr}} = \frac{\partial W_{\text{tw}}(\lambda)}{\partial \lambda_\beta}, \quad (4.19)$$

again to be evaluated at step n . Finally, the inelastic deformation gradient is evaluated by a linearized forward-Euler step, using the slip and twin updates. In order to suppress numerical errors and to ensure that the inelastic deformation gradient is volume-preserving, only the deviatoric part of the update s used, resulting in

$$\begin{aligned} \mathbf{F}_{\text{in}}^{n+1} &= \text{dev} \left(\mathbf{F}_{\text{in}}^n + \Delta t \tilde{\mathbf{l}}_{\text{in}} \mathbf{F}_{\text{in}}^n \right) \\ &= \text{dev} \left[\mathbf{I} + \sum_{\alpha=1}^{n_s} \Delta\gamma_\alpha^n (1 - \sum_{\beta} \lambda_\beta^n) \mathbf{s}_\alpha \otimes \mathbf{m}_\alpha \right. \\ &\quad \left. + \sum_{\beta} \lambda_\beta^n \mathbf{Q}_\beta \mathbf{s}_\alpha \otimes \mathbf{Q}_\beta \mathbf{m}_\alpha + \sum_{\beta=1}^{n_t} \Delta\lambda_\beta^n \bar{\gamma}_\beta^{\text{tw}} (\mathbf{a}_\beta \otimes \mathbf{n}_\beta) \right] \mathbf{F}_{\text{in}}^n. \end{aligned} \quad (4.20)$$

4.5 Plasticity in Polycrystalline Magnesium

The same techniques used for single- and bi-crystals in Section 3.4 and then used to model polycrystals of pure Mg described by the constitutive model of Section 4.2. The material and numerical parameters used in this section are listed in 4.3. Polycrystalline representative volume elements (RVEs), whose effective response is obtained from homogenization with periodic boundary conditions, using the spectral scheme of Chapter 2. Periodic polycrystals with a specified number of grains are generated using the open-source package *Neper* as described by [Quey et al. \(2011\)](#). Grain orientations are assigned with random permutations such that the overall texture matches the shown (inverse) pole figures. The spectral scheme admits sufficient grid resolution to capture large numbers of grains, which is why this setup is used to investigate the relation between microstructural details and the effective response. In Section 4.5, RVEs are subjected to simple shear loading, and effective stress-strain responses together with spatial distributions of inelastic activity are shown. Additionally, the influence of increasing grain misorientation (i.e., increasing the spread of the texture pole) on the effective macro- and meso-scale behavior is analyzed. Subsequently, in Section 4.5 polycrystals undergo combined compressive/shear loading to mimic the effects of cold rolling. Here, the focus is on the influence of the number of grains per RVE (for approximately constant texture) on the effective macroscale stress-strain response.

Simple Shear and the Influence of Misorientation

Polycrystalline RVEs containing 100 grains are subjected to simple shear loading with an average deformation gradient

$$\mathbf{F}^0 = \begin{pmatrix} 1 & \lambda & 0 \\ 0 & 1 & 0 \\ 0 & 0 & 1 \end{pmatrix}, \quad (4.21)$$

where λ is raised from 0 to 10% at a rate of $\dot{\lambda} = 0.02 \text{ s}^{-1}$. The chosen texture, representative of extruded Mg (Chang et al., 2017), is shown in the pole figure in Fig. 4.2(b). The resulting effective stress-strain relation is illustrated in Fig. 4.2(a) and exhibits a plateau near $P_{12} = 0.1 \text{ GPa}$ at $\lambda \approx 0.05$, caused by stress relaxation due to slip and twinning mechanisms across grains. The emergence of heterogeneous stresses and inelastic activity within grains and stress concentrations at grain boundaries, even at low misorientation, is observed. In particular, twinning is initiated primarily at triple junctions as seen in the total twin activity shown in Fig. 4.2(c), which also visualizes how the texture distribution results in only a subset of all grains exhibiting deformation twinning by extension twins. The total volume fraction of the $\langle \bar{1}012 \rangle$ extension twins increases to a maximum of 0.183 and the activity on $\langle 11\bar{2}0 \rangle$ prismatic slip systems to 0.0974 during the deformation at $\lambda = 0.09$.

To gain quantitative insight into how increasing the grain misorientation affects the effective material response, the RVE is endowed with increasingly greater degrees of misorientation and subjected to the same shear loading parametrized by (4.21). In Fig. 4.3(a) the resulting effective stress-strain responses for different textures indicate an increasingly softer response with increasing misorientations, even at low strains of around $\lambda = 0.01$, which is indicative of the anisotropy of slip-twin interactions. The spreading of the texture pole leads to the activation of more slip and twin systems across a wider range of grains, leading to a softer response but also stronger stress gradients and concentrations particularly near grain boundaries, see Fig. 4.3(c). The stress-strain curves indicate that decreasing the misorientation leads to a slightly lower yield stress but a significantly higher hardening: at higher strains of, e.g., $\lambda = 0.01$, there is a deviation in the shear stress of $\Delta P_{12} \approx 36\%$ between the extremal cases of misorientation cases (A) and (E) in Fig. 4.3. The increased number of inelastic-strain-accommodating slip planes and twin systems in highly misoriented polycrystals such as case (E) induces stress relaxation, which in turn results in the observed changes in hardening. For instance, at $\lambda = 0.01$, for case (A) the peak total twin activity is 0.105, whereas for case (E) it is 0.252. Similarly, the maximal basal slip activity for case (A) is 0.0177, while that of case (E) is 0.0797. Notice how several of the grains display pattern-like stress and slip/twin distributions; the effect is much less pronounced than in the single-crystal case discussed before due to the abundance of available twin/slip mechanisms. However, there

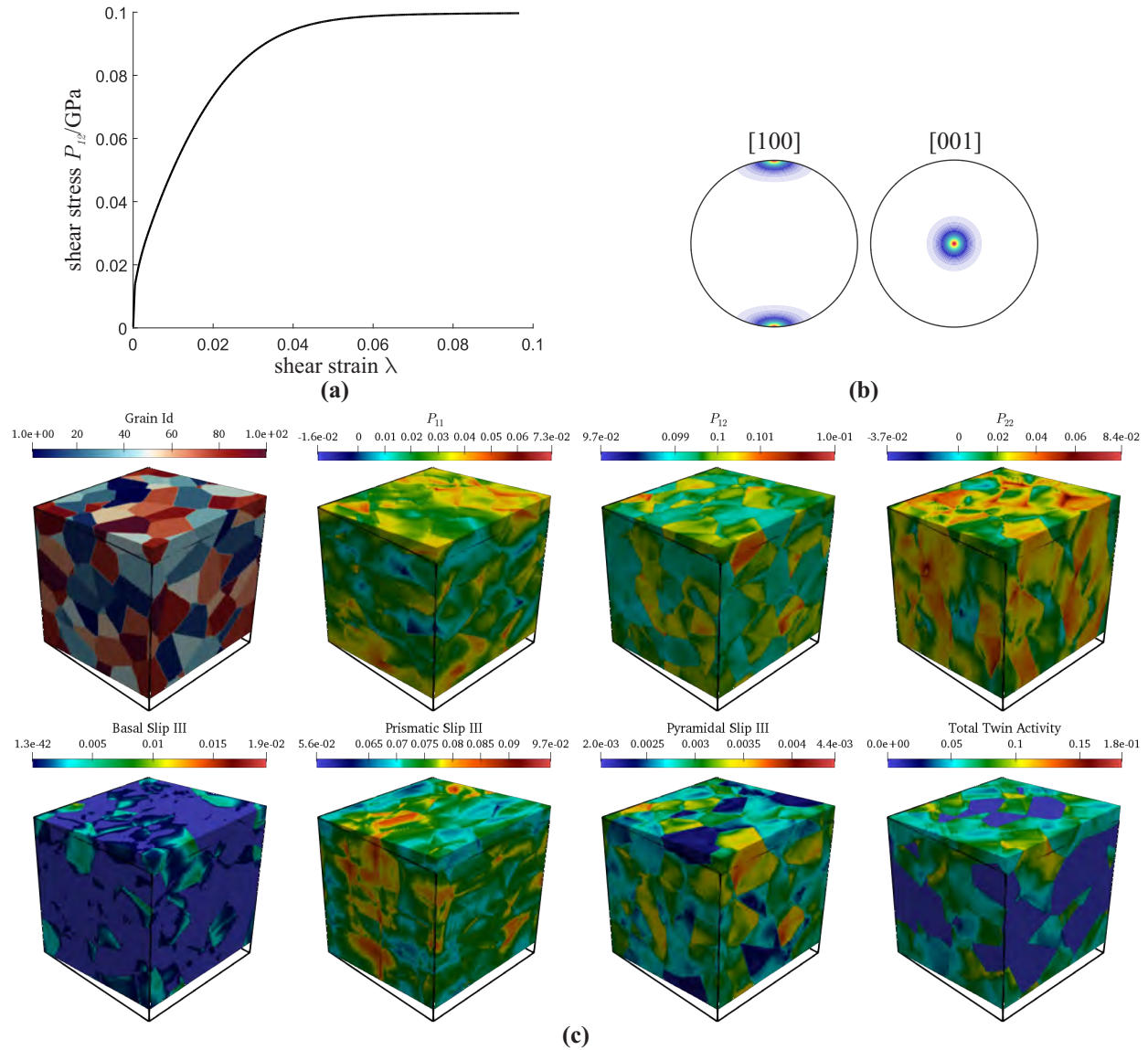


Figure 4.2: (a) Effective stress-strain response of a simple shear test of an RVE containing 100 grains whose orientations are shown in the pole figure (b). (c) State of the RVE at an applied average shear strain of $F_{12}^0 = \lambda = 0.09$. RVEs are shown in the deformed configuration, whereas the bounding box indicates the undeformed shape. Plots illustrate the grain shapes and components of the first Piola-Kirchhoff stress tensor \mathbf{P} as well as the distribution of prismatic slip and of the total volume fraction of all extension-twinned regions. The shown stress distributions are in units of GPa (Vidyasagar et al., 2018).

are still individual grains demonstrating energy-minimizing microstructural pattern formation, as highlighted in Fig 4.4.

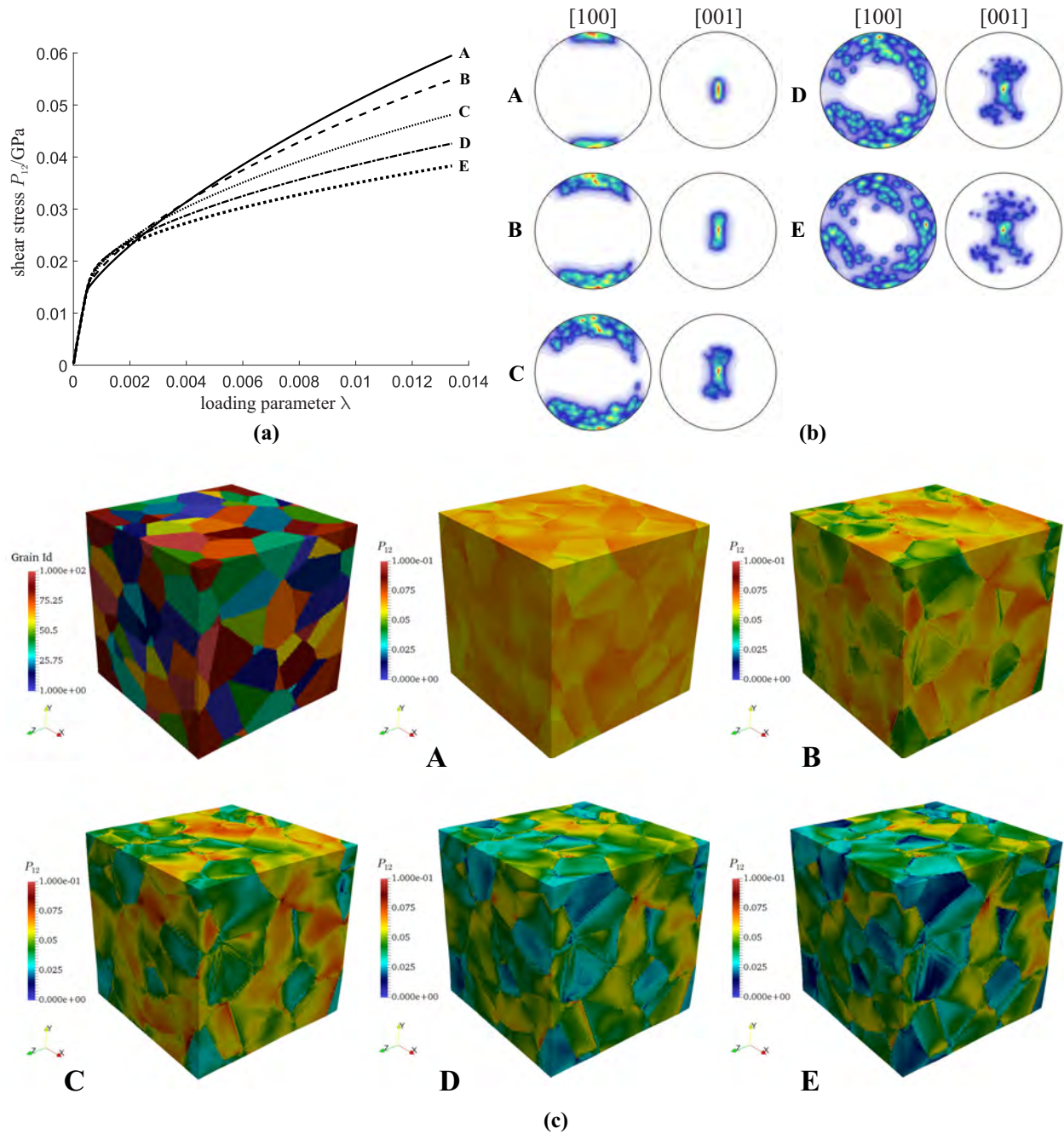


Figure 4.3: Using the same grain geometry as in Fig. 4.2(a), an investigation is performed on how the effective stress-strain response in (a) changes with increasing grain misorientation, as shown by the pole figures in (b). Increasing the spread of the texture allows more easy-slip and -twin systems to become active across a larger number of grains, resulting in significant softening even at low strains. (c) The resulting shear stress distribution illustrates stronger stress differences and concentrations with increasing misorientation. The shown stress distributions are in units of GPa (Vidyasagar et al., 2018).

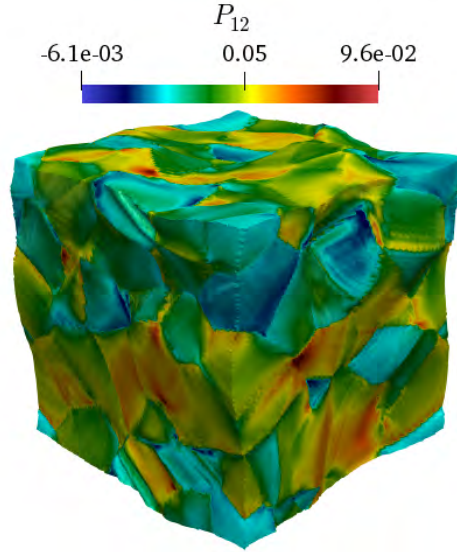


Figure 4.4: Polycrystalline case (E) of the simple shear experiment (see the pole figure in Fig. 4.3): shown is the shear stress distribution (in GPa) with all displacements magnified by a factor of 10 for better visibility. Several of the grains display laminate-like patterns, as may be expected due to the non-quasiconvexity in finite-strain crystal plasticity, as discussed above (Vidyasagar et al., 2018).

Cold Rolling and the Influence of the Number of Grains

Having a computational model and toolset at hand to simulate the RVE response with high resolution, the question arises as to what level of microstructural detail is required to predict the effective, macroscopic stress-strain response. As an example test case, the cold rolling process is chosen which is classically modeled as a combination of shear and compression; see, e.g., (Lee and Duggan, 1991; Ahzi et al., 1993). For ease of implementation, a deformation history described by the effective isochoric deformation gradient

$$\mathbf{F}^0 = \begin{pmatrix} 1 + \frac{\lambda}{3} & 0 & \lambda \\ 0 & 1 & 0 \\ 0 & 0 & \frac{3}{3+\lambda} \end{pmatrix} \quad (4.22)$$

with loading parameter $\lambda \geq 0$ is chosen. The effective responses of four different RVEs are simulated, containing 20, 50, 100, and 1000 grains. All grain orientations were generated randomly from the same pole figure, viz. case C from Fig. 4.3(b). Since this does not produce a unique assignment of orientations to grains, the statistics are considered and an ensemble of ten RVE realizations are simulated for each number of grains (i.e., the ten realizations for a given grain geometry differ by the permutation of grain orientations while keeping the same set of orientations from the pole figure). This yields an envelope of stress-strain responses summarized in Fig. 4.5, showing the mean and standard deviation for each of the four different RVEs studied. As expected,

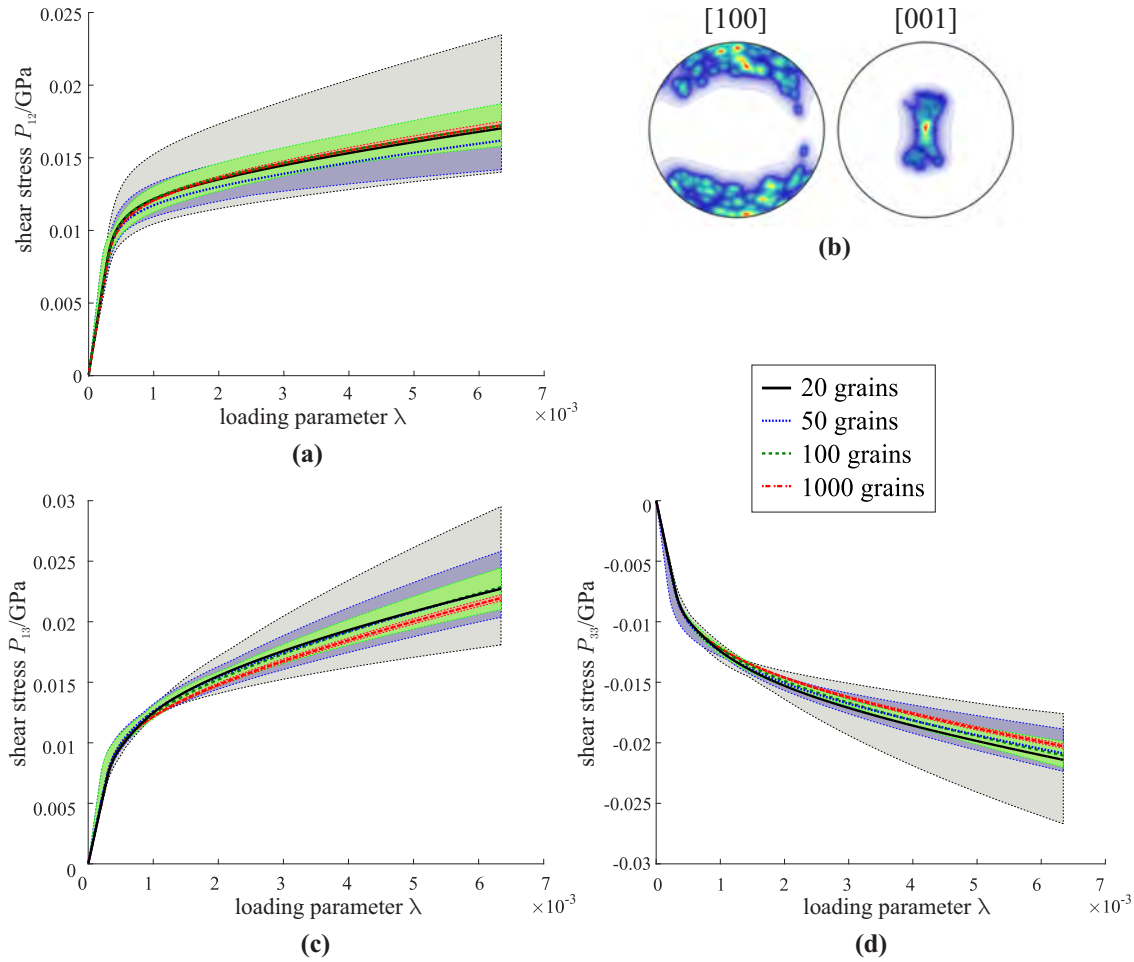


Figure 4.5: Influence of permuting the grain orientations within an RVE with fixed grain geometry: stress-strain behavior shown in terms of mean and standard deviation of ten RVE realizations with different permutations of grain-orientation assignments for RVEs containing 20, 50, 100, and 1000 grains. Grain orientations are taken from the pole shown in (b); the given components of the first Piola-Kirchhoff stress tensor include (a) tensile, (c) shear, and (d) compressive stresses. Mean stresses are shown as thick lines and standard deviations as shaded color regions (Vidyasagar et al., 2018).

the envelope of possible stress-strain responses (shown as the shaded region) is large when using only 20 grains, but converges towards a narrow stress-strain envelope as the number of grains within the RVE increases. Interestingly, but not entirely unexpectedly, there is also (non-monotonic) convergence of the mean stress-strain response shown by the solid lines in Fig. 4.5, where the curves vary only little between 20 and 1000 grains. In other words, while the envelope of possible stress-strain responses is large for an RVE with a relatively small number of grains (e.g., 20), the mean response over many possible geometric permutations and sampling sequences reproduces approximately the same effective material response as an RVE with many more grains (e.g., 1000).

Fig. 4.6 demonstrates representative stress states within the four different polycrystals at $\lambda = 0.01$, visualizing the effect of homogenizing the effective material response across increasing numbers of grains.

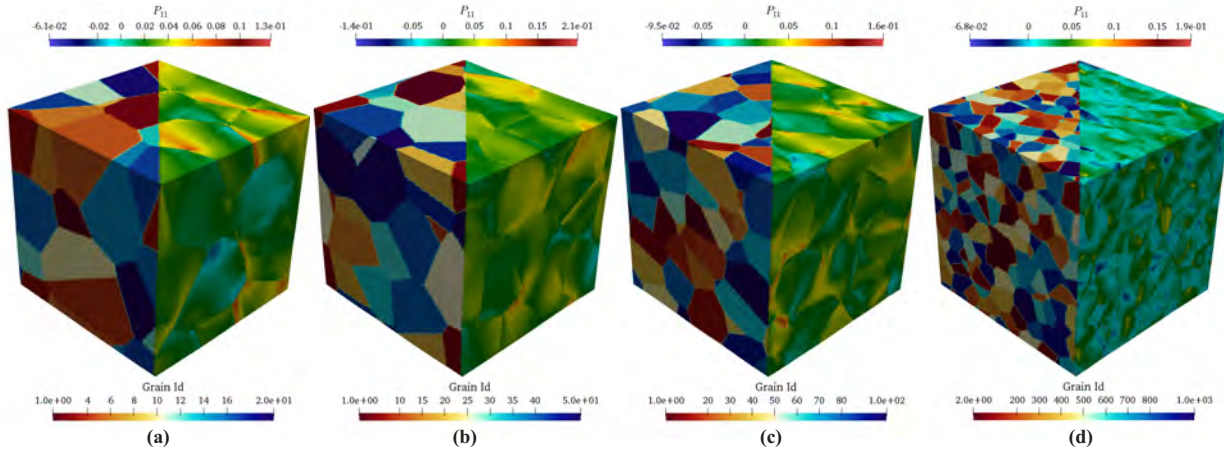


Figure 4.6: Polycrystalline RVEs with (a) 20, (b) 50, (c) 100, and (d) 1000 grains. The left half of each graphic illustrates the grain size and arrangement, whereas the right half shows the tensile/compressive stress distribution at a representative load of $\lambda = 0.01$ (Vidyasagar et al., 2018).

Overall, these results demonstrate that, although the high-resolution spectral scheme admits high-fidelity simulations of mesoscale slip and twin mechanisms, the effective stress-strain response as obtained from homogenization does not require highest levels of mesoscale resolution but may be approximated sufficiently well with small numbers of grains inside an RVE. Obtaining the mean response over a large number of RVE realizations, together with periodic boundary conditions, converges to an effective constitutive behavior. Of course, the converged response and the convergence behavior depend on the chosen material model and the geometric complexity, but the above examples with the chosen finite-strain crystal plasticity model, including slip and twinning as well as diffuse interfaces due to non-convex pattern formation in geometrically complex polycrystals, confirm this observation.

Finally, it is important to understand the influence of the order of the finite-difference approximation on the obtained polycrystalline results. To this end, Fig. 4.7 summarizes the stress-strain response for a simple-shear test of an RVE containing 100 grains. As expected, deviations are moderate and the effective response converges quickly towards the solution obtained from the uncorrected, standard Fourier spectral method when increasing the order of the finite-difference stencil. Fig. 4.8 illustrates the corresponding local fields (shown are two representative stress components as well as the total basal slip activity and the total twin activity). Again as expected, the standard scheme reveals oscillations in the local fields (corrupting convergence with

h -refinement), which are removed by the finite-difference-approximated schemes, where increasing the finite-difference order again leads to convergence towards the standard scheme.

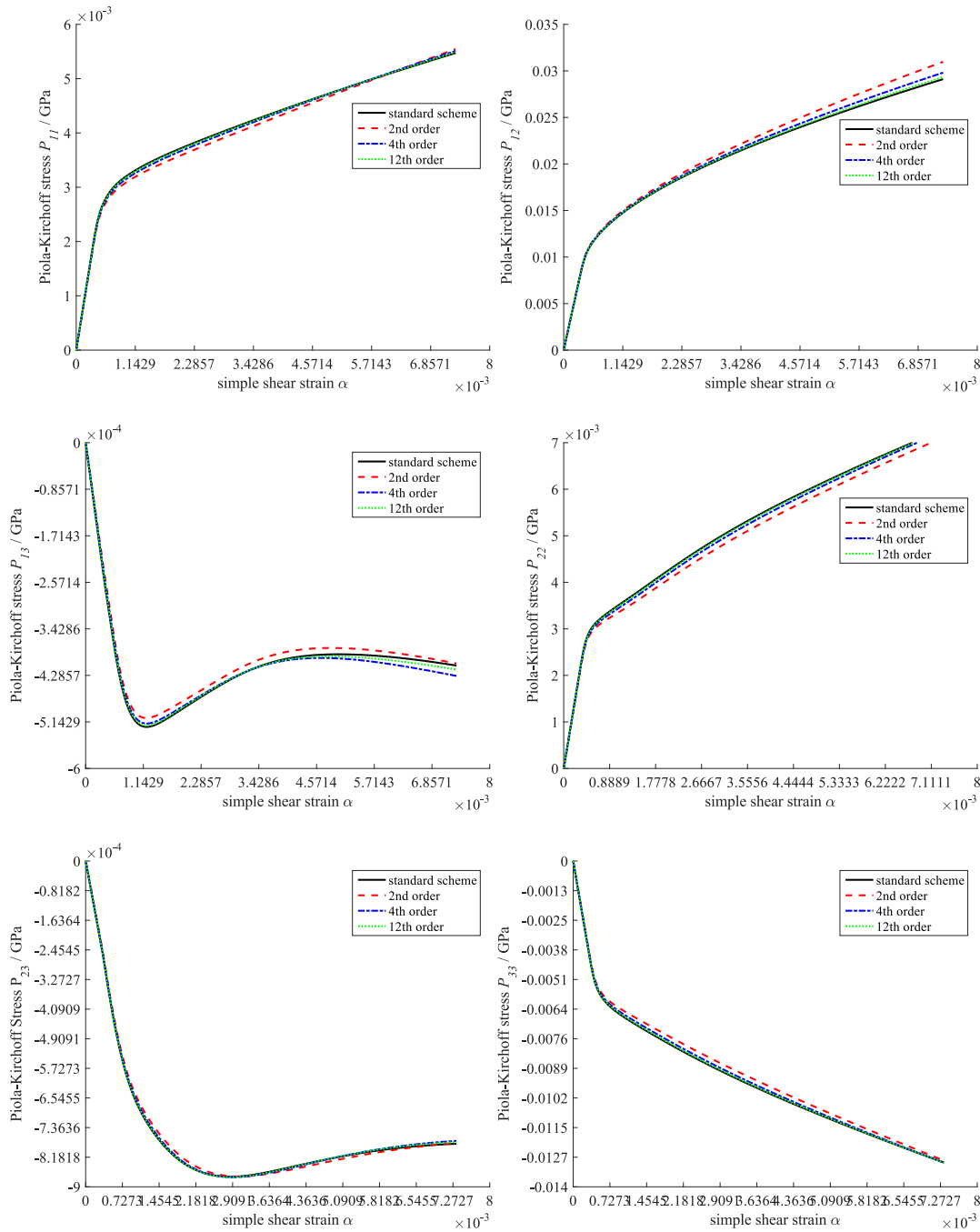


Figure 4.7: Illustration of the stress–strain response for simple shear loading ($F_{12}^0 = \alpha$) showing convergence with increasing order of the finite-difference approximation to the standard Fourier spectral scheme (Vidyasagar et al., 2018).

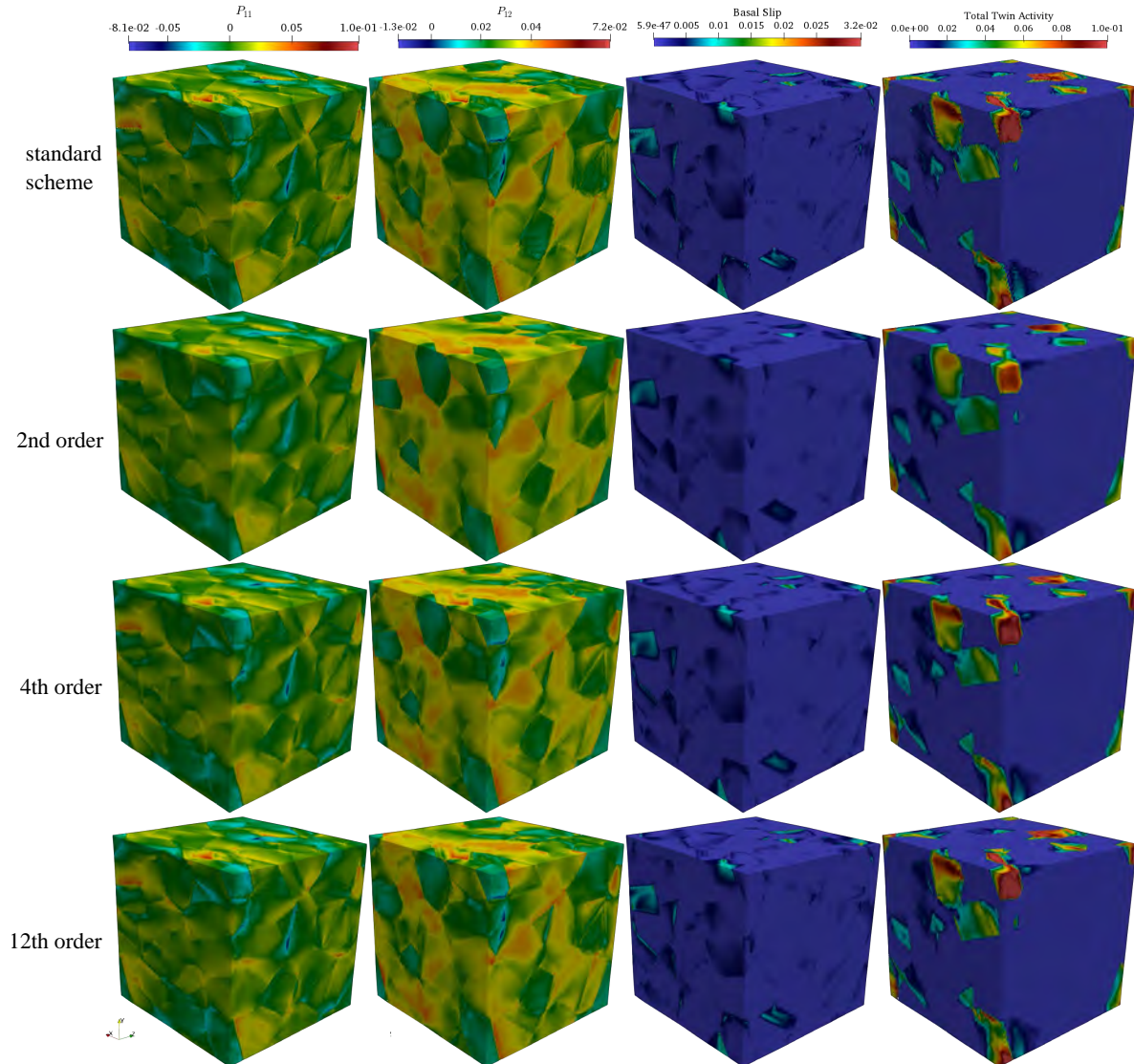


Figure 4.8: Illustration of the local stress fields and inelastic activity within the same RVE, obtained with different orders of the finite-difference approximation, shown at the maximum shear strain shown in Fig. 4.7 (Vidyasagar et al., 2018).

4.6 Conclusions

In this chapter, a finite-difference-corrected spectral homogenization scheme along with an extended crystal plasticity model is used to describe the effective, macroscale response of polycrystalline pure Mg. There is a strong influence of the initial texture on the effective stress-strain response, and the convergence of the effective material behavior with an increasing number of grains within the RVE (enabled by the high-resolution spectral formulation employed here) has been demonstrated. Although high resolution is achieved by the presented scheme, lower fidelity may be sufficient to capture the effective response through averaging over different RVE realizations.

PATTERNS AND ELASTIC SURFACE EVOLUTION DURING ANISOTROPIC SPINODAL DECOMPOSITION

Research presented in this chapter has been adapted from the following publication:

Vidyasagar, A., Krödel, S., Kochmann, D. M. 2018. Microstructural patterns with tunable mechanical anisotropy obtained by simulating anisotropic spinodal decomposition. Proceedings of the Royal Society A: Mathematical, Physical and Engineering Sciences 474, 20180535.

Dissipative effects have been discussed in Chapter 4, but full crystal plasticity serves as a very complicated model when striving to understand the kinetics of generalized pattern formation processes. Taking a very different perspective on naturally occurring microstructural pattern formation, the kinetics of the spinodal decomposition, driven by mass-conservative gradient flow theories, is presented in this chapter. Additionally, the manipulation of the interface energy induced by physical regularization is also studied in detail in what follows.

5.1 Introduction

Phase separation is a ubiquitous phenomenon in both natural and artificial systems. One of the prevalent underlying physical processes is *spinodal decomposition*, a mean-conservative process that separates a mixture into its two constituent phases. The driving force behind spinodal decomposition is the minimization of the overall interface energy between the phases (Cahn and Hilliard, 1958). Prior studies on spinodal decomposition have primarily focused on physical phase-separation processes such as the degradation of mechanical properties during corrosion of metals (Sun et al., 2015) or dealloying to produce nanoporous foams (Biener et al., 2005; Volkert et al., 2006; Erlebacher et al., 2001; Lu et al., 2007; Lang et al., 2011; Li et al., 2013; Geslin et al., 2015).

This contribution provides an alternative perspective by utilizing spinodal decomposition with anisotropic interface energies to tailor the effective elasticity of the resulting microstructured medium. That is, the computational simulation of spinodal decomposition is exploited to produce media with target elastic properties. By choosing one of the two phases in the spinodal decomposition process as void, porous microstructures are obtained with controllable relative density, which are simple to fabricate by modern means of additive manufacturing (Schaedler and Carter, 2016). For the special case of isotropic surface energy, functional decomposition yields isotropic domain interfaces which are similar to surface-minimal gyroids (Nishikawa et al., 1998) due to

their almost constant curvature. However, if the surface energy is anisotropic (Eggleston et al., 2001; Torabi et al., 2009; Salvalaglio et al., 2015), energetically favorable directions exist, resulting in strong faceting of the interfaces and, consequently, microstructural patterns along the preferred orientations. This mechanism is commonly observed in the growth of thin films (Bergamaschini et al., 2016) and quantum dots (Salvalaglio et al., 2015). In the following, numerical predictions show the formation of bi-continuous phase networks through anisotropic spinodal decomposition, and analysis is performed on the resulting structures in terms of their morphology and topology (Ziehmer et al., 2016; Park et al., 2017; Kwon et al., 2010; Geslin et al., 2015).

By exploiting the faceting phenomenon and the associated directional evolution of microstructural patterns, the effective anisotropic mechanical response of the resulting medium can be manipulated. For example, the formation of elongated structures increases stress-bearing capacity along particular directions or planes, leading to an anisotropic elastic surface akin to the anisotropic elasticity and strength of atomic lattices arising from the underlying crystallographic packing (Chung and Buessem, 1967). While the latter is restricted by crystallography and typically results in, e.g., elastic cubic symmetry (like in face-centered cubic or body-centered cubic metals) or transverse isotropy (like in hexagonal close-packed metals), utilizing anisotropic spinodal decomposition allows to generate elastically anisotropic microstructures with, in principle, arbitrary and controllable symmetries (or lack thereof) by choosing specific surface energies when simulating spinodal decomposition. Energetically favorable directions for microstructural growth can be realized by the construction of appropriate penalizations in the surface free energy functional. As will be shown, a non-trivial relationship exists between the chosen favorable surface directions and the resulting elastic surfaces arises due to the presence of flat-faceted interfaces.

When it comes to micro- and nano-architected (meta-)materials with tunable properties, most recent advances have focused on truss- or plate-based architectures on macro- and microscopic scales (Deshpande et al., 2001; Schaedler and Carter, 2016; Bauer et al., 2017; Berger et al., 2017), and their mechanical properties are commonly evaluated under uniaxial loading, see for instance Zheng et al. (2014). Simulating spinodal decomposition to generate microstructures expands the mechanical property space by considering the entire elastic surface as well as by sampling across a much wider space of microstructural architectures not limited to traditional truss architectures. The chosen simulation methodology on a periodic representative volume element (RVE) also trivially ensures domain connectivity and compatibility across RVEs, which is a strong topological constraint when it comes to periodic unit cells. By using the presented computational tools, (meta-)materials with target properties can be designed, which offers a pathway towards scalability in manufacturing nano-architected materials. For instance, naturally occurring anisotropic spinodal decomposition such as during the dealloying of gold-silver solutions (Erlebacher et al., 2001; Lu et al., 2007; Lang

et al., 2011; Li et al., 2013; Geslin et al., 2015), demixing of polymer blends (Bruder and Brenn, 1992; Higgins and Jones, 2000), or coarsening of intercellular lipid fluid mixtures (Stanich et al., 2013) can potentially be utilized for this purpose. At larger scales, as-designed architectures can be realized by 3D printing. When compared to topology optimization, the present approach aims to tailor the entire three-dimensional (3D) elastic surface by suitably selecting the anisotropic surface free energy as opposed to optimizing for specific load cases.

Spinodal decomposition is modeled computationally using the Cahn-Hilliard-type phase-field equations (Elliott, 1989; Bates and Fife, 1990; Zhu et al., 1999; Badalassi et al., 2003). Incorporating anisotropic surface energy within a Cahn-Hilliard framework is challenging (Torabi et al., 2009) due to the ill-posed nature of the equations at large anisotropies, which in turn stem from non-convex surface energy and negative diffusive processes (Torabi et al., 2009; Salvalaglio et al., 2015). In this work, a classic phase field model previously used to predict faceting in individual domains (Torabi et al., 2009; Salvalaglio et al., 2015) is employed. The solution is found on an RVE with random initial conditions by using a robust spectral formulation. The spectral regularization techniques introduced in Chapter 2 are used to avoid oscillatory artifacts at phase interfaces and to prevent short-wavelength instabilities, which avoids the need for further regularization of the non-convex problem. The resulting numerical scheme describes the evolution of the two continuous phases (viz., material and void) under periodic boundary conditions. After phase separation the homogenized elastic stiffness tensor of the RVE is computed using finite elements under periodic boundary conditions so as to identify the elastic properties of a homogeneous comparison medium.

The remainder of this chapter is structured as follows. Section 5.2 details the constitutive phase field model and the kinetics solved subsequently by using the numerical spectral techniques presented in Chapter 2 (expanded in Section 5.3). Section 5.5 describes the pattern formation during phase separation as well as the influence of the target relative density and strength of surface anisotropy on the resulting porous structures. The kinetics of decomposition are further analyzed together with the detailed morphology of simulated microstructures and its correlation with surface anisotropy. Parametric studies of relative density and strength of anisotropy demonstrate the effective mechanical property space of the resulting microstructures. Finally, Section 5.6 concludes the investigation in this chapter.

5.2 Constitutive Model and Kinetics

Consider an RVE $\Omega \subset \mathbb{R}^d$ in d -dimensional space, which is endowed with a scalar field

$$\varphi(\mathbf{X}, t) : \Omega \times \mathbb{R} \rightarrow \mathbb{R}, \quad (5.1)$$

where $\mathbf{X} \in \Omega$ denotes position and $t \geq 0$ time. $\varphi(\mathbf{X}, t) = 1$ implies that point \mathbf{X} at time t is filled with solid material, whereas $\varphi(\mathbf{X}, t) = 0$ implies a void. The kinetic evolution of $\varphi(\mathbf{X}, t)$

across Ω is governed by the Cahn-Hilliard phase field model (Torabi et al., 2009; Salvalaglio et al., 2015) which describes mean-conservative phase separation. Specifically, the phase field variable φ is locally driven to one of the two stable phases (solid or void) through the introduction of a Ginzburg-Landau double-well potential $B(\varphi)$, defined as (Torabi et al., 2009)

$$B(\varphi) = \frac{1}{4}\varphi^2(1 - \varphi)^2. \quad (5.2)$$

The surfaces within the RVE (i.e., the interfaces between solid and void) are tracked by the inward normal

$$\mathbf{n}(\mathbf{X}, t) = \frac{\nabla\varphi(\mathbf{X}, t)}{|\nabla\varphi(\mathbf{X}, t)|}, \quad (5.3)$$

which is defined for all $\mathbf{X} \in \Omega$ and $t \geq 0$ unless $|\nabla\varphi(\mathbf{X}, t)| = 0$. In order to account for anisotropic surface energy, a set of unit vectors, $\mathbf{M} = \{\mathbf{m}_1, \mathbf{m}_2, \dots, \mathbf{m}_\alpha\}$, are introduced, which represent the normals to the desired interface facet planes with examples shown in Fig. 5.1. Note that for versatility of the method, each \mathbf{m}_i is endowed with a unique direction, i.e., the $\pm \mathbf{m}$ directions can be chosen independently to tune internal facet orientations. Based on the set \mathbf{M} , the interface energy density per unit volume, $\gamma(\mathbf{n})$, is assumed of the form (Salvalaglio et al., 2015)

$$\gamma(\mathbf{n}) = \gamma_0 \left[1 - \sum_{i=1}^{\alpha} a_i (\mathbf{n} \cdot \mathbf{m}_i)^{w_i} H(\mathbf{n} \cdot \mathbf{m}_i) \right], \quad (5.4)$$

where H denotes the Heaviside step function. Coefficients $a_i \geq 0$ represent the degree of surface anisotropy, and $a_i = 0$ results in isotropic surface energy. For simplicity, the exponents $w_i = 4$ (kept constant), and reference value $\gamma_0 = 1$, are chosen the remainder of this chapter.

Assuming diffuse interfaces, the total free energy functional, including bulk and surface energy, is written as

$$E[\varphi] = \int_{\Omega} \frac{\gamma(\mathbf{n})}{\epsilon} \left[B(\varphi(\mathbf{X}, t)) + \frac{\epsilon^2}{2} |\nabla\varphi(\mathbf{X}, t)|^2 \right] dV, \quad (5.5)$$

where $\epsilon > 0$ characterises an intrinsic length scale. Note that, following Torabi et al. (2009), both the Ginzburg-Landau energy and the gradient term are scaled by the anisotropic interface energy density $\gamma(\mathbf{n})$ to ensure that the interface thickness is isotropic (while having no impact within homogeneous phases).

Using the approach previously presented in Torabi et al. (2009); Salvalaglio et al. (2015), the local chemical potential $\mu(\mathbf{X}, t)$ is approximated by

$$\mu(\mathbf{X}, t) = \frac{\gamma(\mathbf{n})}{\epsilon} \frac{\partial B(\varphi)}{\partial \varphi} - \epsilon \nabla \cdot [\gamma(\mathbf{n}) \nabla \varphi + |\nabla \varphi| (\mathbf{I} - \mathbf{n} \otimes \mathbf{n}) \nabla_n \gamma(\mathbf{n})], \quad (5.6)$$

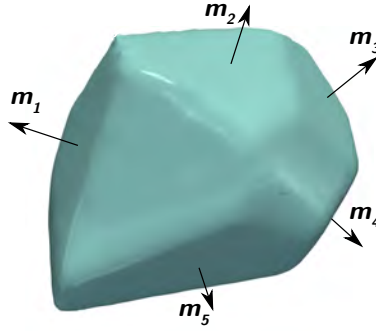


Figure 5.1: Depiction of a possible choice of the \mathbf{m}_α unit vectors to obtain facets on the associated normal planes.

where the dependence of φ and \mathbf{n} on (\mathbf{X}, t) is dropped for convenience, and $\nabla_{\mathbf{n}}(\cdot)$ represents the gradient with respect to the surface normal. Note that Equation (5.6) is an approximation of the exact variational derivative, which exploits the limit [Torabi et al. \(2009\)](#); [Salvalaglio et al. \(2015\)](#)

$$\lim_{\epsilon \rightarrow 0} \left[\frac{1}{\epsilon} B(\varphi) - \frac{\epsilon}{2} |\nabla \varphi|^2 \right] = 0. \quad (5.7)$$

The evolution of the phase field $\varphi(\mathbf{X}, t)$ follows as [Wise et al. \(2007\)](#); [Torabi et al. \(2009\)](#); [Salvalaglio et al. \(2015\)](#)

$$\eta \frac{\partial \varphi}{\partial t}(\mathbf{X}, t) = \nabla \cdot \left[\sqrt{B(\varphi(\mathbf{X}, t))} \nabla \mu(\mathbf{X}, t) \right] \quad (5.8)$$

with an inverse mobility $\eta > 0$. This evolution law deviates from the classical Cahn-Hilliard form, in which $\sqrt{B(\varphi(\mathbf{X}, t))}$ would be replaced by a constant. The present choice of the kinetic law leads to an increased relative mobility of the phase field parameter $\varphi(\mathbf{X}, t)$ at and near interface regions as opposed to in homogeneous bulk regions (where $\varphi \approx 0$ or 1). This results in increased relative interface motion (as compared to bulk rearrangement within homogeneous phases) but an overall deceleration of the energy relaxation process.

The kinetic evolution equation (5.8) is solved on an RVE $\Omega = [0, L]^d$ with periodic boundary conditions on the boundary $\partial\Omega$, i.e.,

$$\varphi(\mathbf{X}^+, t) = \varphi(\mathbf{X}^-, t) \quad \text{and} \quad \langle \varphi(t) \rangle = \frac{1}{|\Omega|} \int_{\Omega} \varphi(\mathbf{X}, t) dV, \quad (5.9)$$

where \mathbf{X}^\pm denote periodically matching points on opposite faces of $\partial\Omega$, and $\langle \varphi(t) \rangle$ is the RVE-average of φ at time $t \geq 0$. For mass conservation in the RVE $\langle \varphi(t) \rangle = \langle \varphi \rangle = \text{const}$.

5.3 Numerical Solution Strategy

The RVE is discretized into a regular grid of n points, $\chi = \{\mathbf{X}_1, \mathbf{X}_2, \dots, \mathbf{X}_n\}$, whose reciprocal points in Fourier space, $\mathcal{T} = \{\mathbf{K}_1, \mathbf{K}_2, \dots, \mathbf{K}_n\}$, lie on a Bravais lattice; here an equal number of points are chosen in \mathbf{K} -space for convenience when using Fast Fourier Transforms (FFTs).

The application of a discrete (inverse) Fourier transform to the phase field yields

$$\varphi(\mathbf{X}) = \mathcal{F}^{-1}(\hat{\varphi}) = \sum_{\mathbf{K} \in \mathcal{T}} \hat{\varphi}(\mathbf{K}) \exp(-ih\mathbf{K} \cdot \mathbf{X}), \quad h = \frac{2\pi}{n}, \quad i = \sqrt{-1}. \quad (5.10)$$

For added stability of the Fourier spectral scheme in the presence of strong gradients such as across phase boundaries, a fourth-order finite-difference approximation from 2.5 on the RVE grid. The time evolution of the phase field is simulated by applying the aforementioned modified inverse Fourier transform at every time step t to compute the components of the gradient as

$$\varphi_i(\mathbf{X}, t) = \mathcal{F}^{-1}(\hat{\varphi}(\mathbf{K}, t)\tilde{\omega}_i) \quad (5.11)$$

for the calculation of the inward normal $\mathbf{n}(\mathbf{X}_i, t)$ and the interface energy $\gamma(\mathbf{n}(\mathbf{X}_i, t))$ at every grid point $\mathbf{X}_i \in \mathcal{X}$ in real space. Having individually computed each term in real space, the approximate chemical potential is evaluated in Fourier space as (with summation over index i) as

$$\hat{\mu}(\mathbf{K}, t) = \mathcal{F} \left(\frac{\gamma(\mathbf{n})}{\epsilon} \frac{\partial B(\varphi)}{\partial \varphi} \right) - \epsilon \left[\mathcal{F}(\gamma(\mathbf{n})\nabla\varphi) + \mathcal{F}(|\nabla\varphi|(\mathbf{I} - \mathbf{n} \otimes \mathbf{n})\nabla_n\gamma(\mathbf{n})) \right]_i \tilde{\omega}_i(\mathbf{K}). \quad (5.12)$$

The gradient of the chemical potential is next evaluated in real space, viz.

$$\mu_i(\mathbf{X}, t) = \mathcal{F}^{-1}(\hat{\mu}(\mathbf{K}, t)\tilde{\omega}_i(\mathbf{K})). \quad (5.13)$$

Finally, the time evolution in real space is evaluated using an explicit, forward-Euler finite-difference scheme in time for all $\mathbf{X}_j \in \mathcal{X}$ (again, with summation over index i):

$$\varphi(\mathbf{X}_j, t + \Delta t) = \varphi(\mathbf{X}_j, t) + \frac{\Delta t}{\eta} \mathcal{F}^{-1} \left(\left[\mathcal{F}(\sqrt{B(\varphi(\mathbf{X}, t))} \nabla\mu(\mathbf{X}, t)) \right]_i \tilde{\omega}_i \right). \quad (5.14)$$

The explicit updates are computationally fast but require the choice of a sufficiently small time step Δt for stability. Subsequent simulations are performed on a cubic RVE of side length $L = 6.4$ (in arbitrary units due to scale invariance) discretized by a regular grid consisting of $128 \times 128 \times 128$ points. The interface width is set to $\epsilon = 0.03$. To ensure smooth initial conditions, the system is seeded randomly by perturbing the average relative density $\langle \varphi \rangle$ using a set of p Gaussian functions in 3D-space such that

$$\varphi(\mathbf{X}, 0) = \langle \varphi \rangle \pm \sum_{l=1}^p \exp \left(\frac{(\mathbf{X} - \boldsymbol{\mu}_l) \cdot (\mathbf{X} - \boldsymbol{\mu}_l)}{\sqrt{2p} s^2} \right). \quad (5.15)$$

The mean positions $\boldsymbol{\mu}_l(\mathbf{X})$ are chosen randomly for each of the $p = 2500$ functions with a standard deviation of $s = 0.2$. The sign of the Gaussian perturbation is chosen at random. Specific choices of $\gamma(\mathbf{n})$ and resulting microstructures are summarized in Section 5.5.

5.4 Elastic Surface Calculation

During the iterative energy relaxation process, the system quickly converges towards the stable equilibrium phases. The evolution process is stopped once an approximately stable end distribution $\varphi(\mathbf{X}, t_{\text{end}})$ has emerged. For each thus-obtained architecture, the effective elastic properties of the RVE are obtained by computational homogenization (Kouznetsova et al., 2001; Miehe and Koch, 2002). The field $\varphi(\mathbf{X}, t)$ is interpreted as a distribution of solid and void inside the RVE, and the governing equations of linear elastic equilibrium in linearized kinematics to extract the effective elastic moduli.

The primary mechanical unknown here is the displacement field $\mathbf{u}(\mathbf{X}, t) : \Omega \times t \rightarrow \mathbb{R}^d$, which satisfies the periodic boundary conditions (Kouznetsova et al., 2001; Miehe and Koch, 2002)

$$\mathbf{u}(\mathbf{X}^+) - \mathbf{u}(\mathbf{X}^-) = \langle \boldsymbol{\varepsilon} \rangle (\mathbf{X}^+ - \mathbf{X}^-) \quad \forall \mathbf{X}^\pm \in \partial\Omega, \quad (5.16)$$

where $\langle \boldsymbol{\varepsilon} \rangle$ is the average of the infinitesimal strain tensor $\boldsymbol{\varepsilon} = \text{sym}(\nabla \mathbf{u})$. The base material is assumed to be homogeneous, and linear elastic with a spatially constant fourth-order elasticity tensor \mathbb{C}^M , such that (using Einstein's summation convention) the infinitesimal stress tensor components σ_{ij} are given by

$$\sigma_{ij}(\mathbf{X}) = \mathbb{C}_{ijkl}^M \varepsilon_{kl}(\mathbf{X}). \quad (5.17)$$

In all subsequent case studies, we assume an isotropic base material for the solid phase with a Poisson's ratio of $\nu^M = 0.33$ (Young's modulus is irrelevant as all results will be normalized with respect to the base material's Young's modulus E^M).

The commercial code COMSOL[®] is used to solve the balance equations of linear momentum, $\text{div } \boldsymbol{\sigma}(\mathbf{X}, t) = 0$, inside Ω with periodic boundary conditions (5.16) and in the absence of body forces or inertial effects. To this end, the cubic RVE is discretized into $100 \times 100 \times 100$ hexahedral elements with quadratic interpolation. The distribution $\varphi(\mathbf{X}, t_{\text{end}})$ is interpolated over the domain of the RVE and results in a location-dependent Young's modulus of the base material, assigning to each point $\mathbf{X} \in \Omega$ a modulus $E(\mathbf{X}) = \varphi(\mathbf{X}, t_{\text{end}})E^M$. To avoid numerical instability, a lower-bound $\varphi \geq 10^{-6}$ is enforced (this was verified to have a vanishing effect on the obtained homogenized moduli). The equations of linear elasticity are solved over the entire RVE. Once the equilibrium solution has been found, the average stress tensor $\langle \boldsymbol{\sigma} \rangle$ is derived by volume averaging. The effective fourth-order modulus tensor \mathbb{C}_{eff} is defined via the relation

$$\langle \boldsymbol{\sigma} \rangle = \mathbb{C}_{\text{eff}} \langle \boldsymbol{\varepsilon} \rangle \quad (5.18)$$

and can be computed in one of two ways: either directly from the stiffness matrices of the RVE Miehe and Koch (2002) or by applying a sequence of $d(d+1)/2$ average (random but linearly independent)

strain tensors $\langle \boldsymbol{\varepsilon} \rangle$, computing the corresponding average stress tensor $\langle \boldsymbol{\sigma} \rangle$ and solving (5.18) for the effective stiffness tensor \mathbb{C}_{eff} and the associated effective compliance tensor $\mathbb{S}_{\text{eff}} = \mathbb{C}_{\text{eff}}^{-1}$.

For visualization purposes, it is convenient to compute stiffness surfaces illustrating Young's modulus $E(\mathbf{d})$ in any direction $\mathbf{d} \in S(d)$ on the unit ball. Using Einstein's summation convention, the directional modulus is obtained as [Böhlke and Brüggemann \(2001\)](#)

$$E^{-1}(\mathbf{d}) = \mathbb{S}_{ijkl} d_i d_j d_k d_l. \quad (5.19)$$

Analogously, the effective Poisson's ratio $\nu(\mathbf{d}, \mathbf{n})$, which characterises the inverse, negative ratio between the strain in the direction of applied stretch \mathbf{d} and in the perpendicular direction \mathbf{n} becomes [Böhlke and Brüggemann \(2001\)](#):

$$\nu(\mathbf{d}, \mathbf{n}) = -E(\mathbf{d}) \mathbb{S}_{ijkl} d_i d_j n_k n_l. \quad (5.20)$$

The above procedure can be applied both to the resulting final microstructures as well as to the evolving phase distribution inside the RVE. Hence the homogenized elastic properties of the periodic medium during and after the process of spinodal decomposition can be obtained.

5.5 Pattern Formation Process

Anisotropic Spinodal Decomposition

Spinodal decomposition is simulated in two-phase RVEs by solving the Cahn-Hilliard phase field model for a fixed volume fraction of the solid phase in a time-incremental fashion as outlined in Section 5.2. Fig. 5.2 illustrates a representative overview of resulting microstructures obtained from different choices of the surface energy $\gamma(\mathbf{n})$ in (5.4) (for all examples in Fig. 5.2, $\gamma_0 = 1$, $w_i = 4$ and $a_i = 0.3$ for all $i = 1, \dots, \alpha$).

Without any preferred orientations (i.e., $\gamma(\mathbf{n}) = \gamma_0 = \text{const.}$) the resulting microstructure is isotropic, as shown in Fig. 5.2(a). By contrast, assigning preferred directions along the coordinate axes $\{\mathbf{e}_1, \mathbf{e}_2, \mathbf{e}_3\}$ (i.e., $\mathbf{m}_1 = \mathbf{e}_1$, $\mathbf{m}_2 = -\mathbf{e}_1$, $\mathbf{m}_3 = \mathbf{e}_2$, etc.) results in more ordered microstructures, in which surfaces align with the coordinate axes, as shown in Fig. 5.2(b). Even more pronounced directional phase growth is observed when choosing fewer preferred orientations such as for the columnar structures in in Fig. 5.2(c) with elongated ligaments in the \mathbf{e}_3 -direction, which are obtained from $\mathbf{m}_1 = \mathbf{e}_1$, $\mathbf{m}_2 = -\mathbf{e}_1$, $\mathbf{m}_3 = \mathbf{e}_2$, $\mathbf{m}_4 = -\mathbf{e}_2$. Similarly, the lamellar microstructure in Fig. 5.2(d) grows in the \mathbf{e}_1 - \mathbf{e}_2 -plane as the result of $\mathbf{m}_1 = \mathbf{e}_3$, $\mathbf{m}_2 = -\mathbf{e}_3$. In all four cases, the chosen anisotropic surface energy leads to strong faceting along the preferred directions. It is interesting to note that for the shown choice of $\langle \varphi \rangle = 0.5$ and random initialization, all resulting geometries are (probabilistically) bi-continuous, i.e., both phases are fully interconnected, which ensures stress-bearing capacity.

The resulting microstructures with an anisotropic surface strength of $a_i = a = 0.3$ (see Eq. (5.4)) show sharp corners, as the result of unattainable surface orientations. Interestingly, although the energy surface is non-convex for $a > 1/15$ (Torabi et al., 2009), the evolution process is stable with a monotonously decreasing energy. Therefore, the chosen spectral scheme is able to describe the microstructure evolution without higher-order Willmore regularization as, e.g., in Torabi et al. (2009) and Salvalaglio et al. (2015). The reason for this is two-fold.

The phase field is initiated using a smooth perturbation of small magnitude around the mean. This ensures that new domains can form with sharp corners without having to remove certain present orientations, since the process is driven not only by the anisotropic energy contribution (which would be encountered during morphing of previously equilibrated phases Torabi et al. (2009)) but also by the phase separation. Admittedly, the smoothness condition cannot be guaranteed throughout the simulation because of physical short- and long-wavelength instabilities, caused by the presence of non-convex interface energies $\gamma(\mathbf{n})$, which cause faceting phenomena. Here, the stabilized spectral scheme avoids surface wrinkling artifacts (short-wavelength oscillations) by a weighted smoothing of high frequencies in Fourier space and numerical regularization as shown in Sec. 2.5. Note that this method is not a complete replacement of the Willmore-type regularization in Torabi et al. (2009); Salvalaglio et al. (2015), as the latter may still be important to avoid large-wavelength faceting at corners. However, due to the (relative) short-wavelength nature of domains formed in simulations, this method is sufficient for stability.

Influence of Porosity and Degree of Anisotropy

Next, the investigation moves to the influence of varying relative densities $\langle \varphi \rangle$ and degrees of anisotropy a_i for the example of cubic symmetry as shown in Fig. 5.2(b). For high relative densities of, e.g., $\langle \varphi \rangle = 0.7$, the resulting structure resembles a solid RVE with cubic holes, see Fig. 5.3(b). By contrast, decreasing the relative density below 0.3 leads to the formation of disconnected domains and thus to the loss of the bi-continuity of the equilibrated microstructure, as shown in Fig. 5.3(a). Therefore, only relative densities of $\langle \varphi \rangle > 0.3$ are considered in the remainder of this chapter to ensure stable systems with strongly-elliptic elastic moduli (implying non-zero Young's moduli in all directions).

Additionally, the choice of the anisotropy strength a strongly influences the resulting periodic structures. For low anisotropy (e.g., $a = 0.15$) the impact on the microstructure is minimal, as shown in Fig. 5.3(c), with structures that are close to the isotropic case. With increasing anisotropy, interface corners inside the RVE become sharper (compare Fig. 5.3(c) for $a = 0.15$ to Fig. 5.3(d) for $a = 0.4$). These parameters hence admit tuning of the microstructural features.

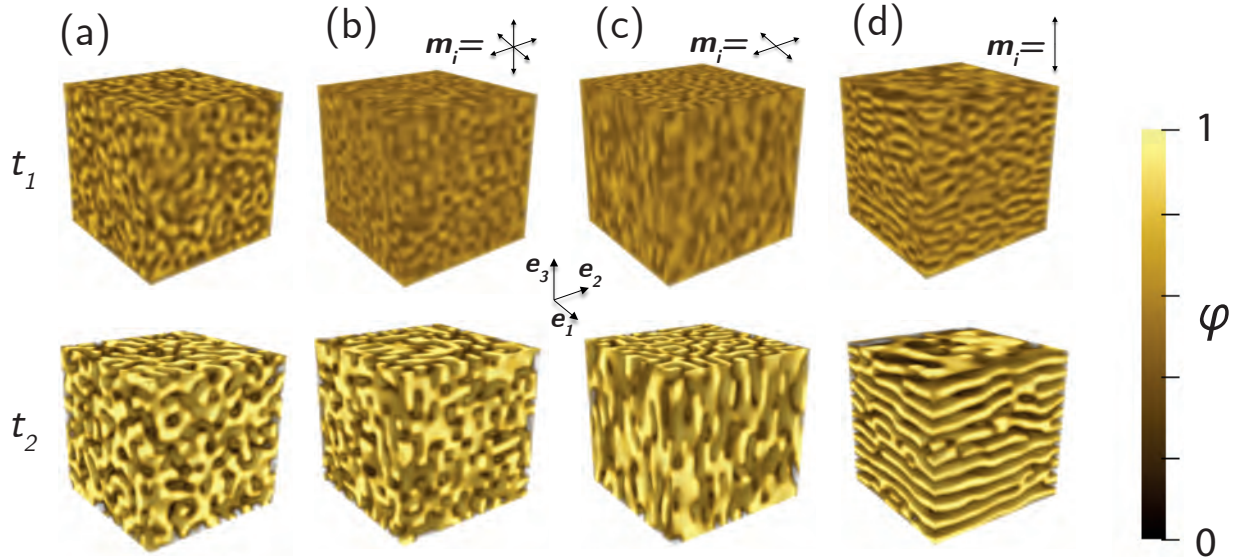


Figure 5.2: Periodic structures obtained from the anisotropic spinodal decomposition process for (a) an isotropic medium (no preferred orientations), (b) cubic symmetry with six energetically favorable directions along the coordinate axes, (c) a columnar structure with four energetically favorable in-plane directions, and (d) a lamellar structure with a single energetically favorable orientation. Results are shown at two different times t_1 and t_2 , where t_2 indicates the final, equilibrated state, whereas t_1 is the state of fastest energy decrease, which occurs at approximately half of the energy relaxation time. For all anisotropic structures $a_i = 0.3$ with an average relative density of $\langle \varphi \rangle = 0.5$.

Kinetics of Spinodal Decomposition

The model parameters influence not only the resulting microstructures but also the kinetics of phase separation. While this model does not aim to describe the kinetics in a specific material system, it is essential to inspect the kinetic evolution for the identification of approximately equilibrated patterns as well as to understand the influence of model parameters on the simulation efficiency. The gradual relaxation of the energy functional (5.5) is quantified by the total mobility measure (cf. Eq. (5.8))

$$\Lambda(t) = \int_{\Omega} \left| \eta \frac{\partial \varphi}{\partial t}(\mathbf{X}, t) \right| dV = \int_{\Omega} \left| \nabla \cdot \left[\sqrt{B(\varphi(\mathbf{X}, t))} \nabla(\mu(\mathbf{X}, t)) \right] \right| dV. \quad (5.21)$$

Results in Fig. 5.4 contrast the total energy and the total mobility of the RVE for different values of $\langle \varphi \rangle$ and different anisotropies a_i . As expected, the highest mobilities are at those times where changes in the energy are maximal (see Figs. 5.4(a,c) and (b,d)). In the isotropic case, decreasing the relative density decelerates the decomposition process (see Figs. 5.4(a) and (c)) as a consequence of the diffusion process that condenses the material towards the stable phases. The decrease in the reaction speed is non-linear, resulting in a 55% speed increase when the

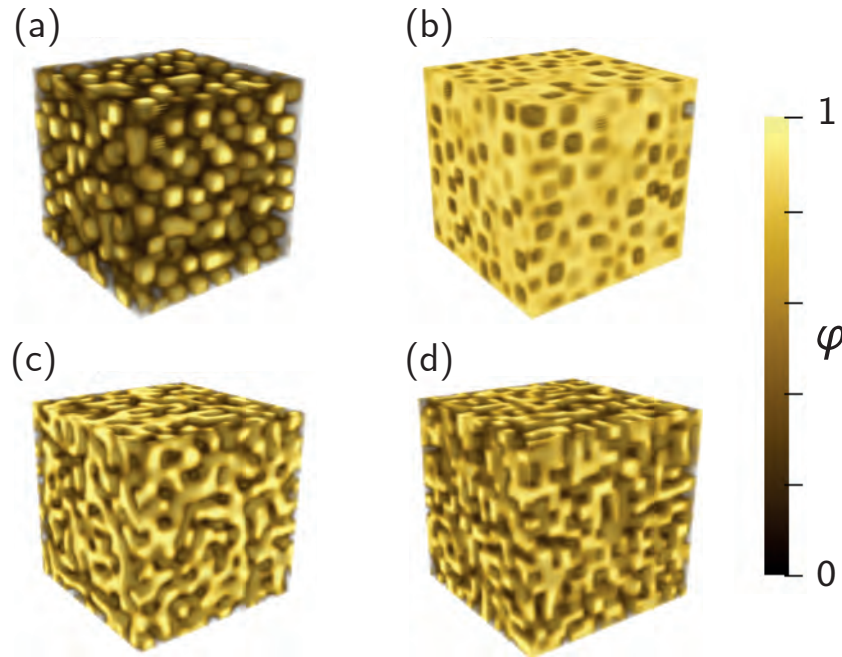


Figure 5.3: Periodic structures with cubic symmetry (case (b) in Fig. 5.2) shown for varying degrees of anisotropy a and relative density $\langle\varphi\rangle$: (a) $\langle\varphi\rangle = 0.2$, $a = 0.3$, (b) $\langle\varphi\rangle = 0.7$, $a = 0.3$, (c) $\langle\varphi\rangle = 0.5$, $a = 0.15$, (d) $\langle\varphi\rangle = 0.5$, $a = 0.4$.

relative density is increased from $\langle\varphi\rangle = 0.3$ to 0.5. Fig. 5.4(e) also captures the different stages of microstructure evolution during an example decomposition process. The small initial perturbations (of e.g. $\langle\varphi\rangle \pm 0.05$ in Fig. 5.4(e)) evolve into equilibrated domains.

Besides the relative density, the choice of the degree of anisotropy a also influences the kinetics of the process. Stronger anisotropy results in constraints on the decomposition and therefore slows down the process significantly, as seen in Fig. 5.4(b). For instance, at $\langle\varphi\rangle = 0.5$ a strong anisotropy of $a = 0.4$ increases the relaxation time by approximately 120% (compare the solid blue lines in Figs. 5.4(a) and (b)). In general, the mobility during anisotropic decomposition is at least an order of magnitude higher than the mobility that is associated with isotropic surface energies (compare Figs. 5.4(c) and (d)).

Interface Morphology

As a quantitative measure of the morphology of microstructures resulting from anisotropic spinodal decomposition, the interfacial shape distribution (ISD) is derived using contours of constant $\varphi = 0.5$ within the RVE. The ISD is used to investigate self-similarity of bi-continuous structures and is related to the genus or the topology of microstructures (Kwon et al., 2010; Park et al., 2017; Ziehmer et al., 2016). Representative interface contours are visualized in Fig. 5.5(a)-

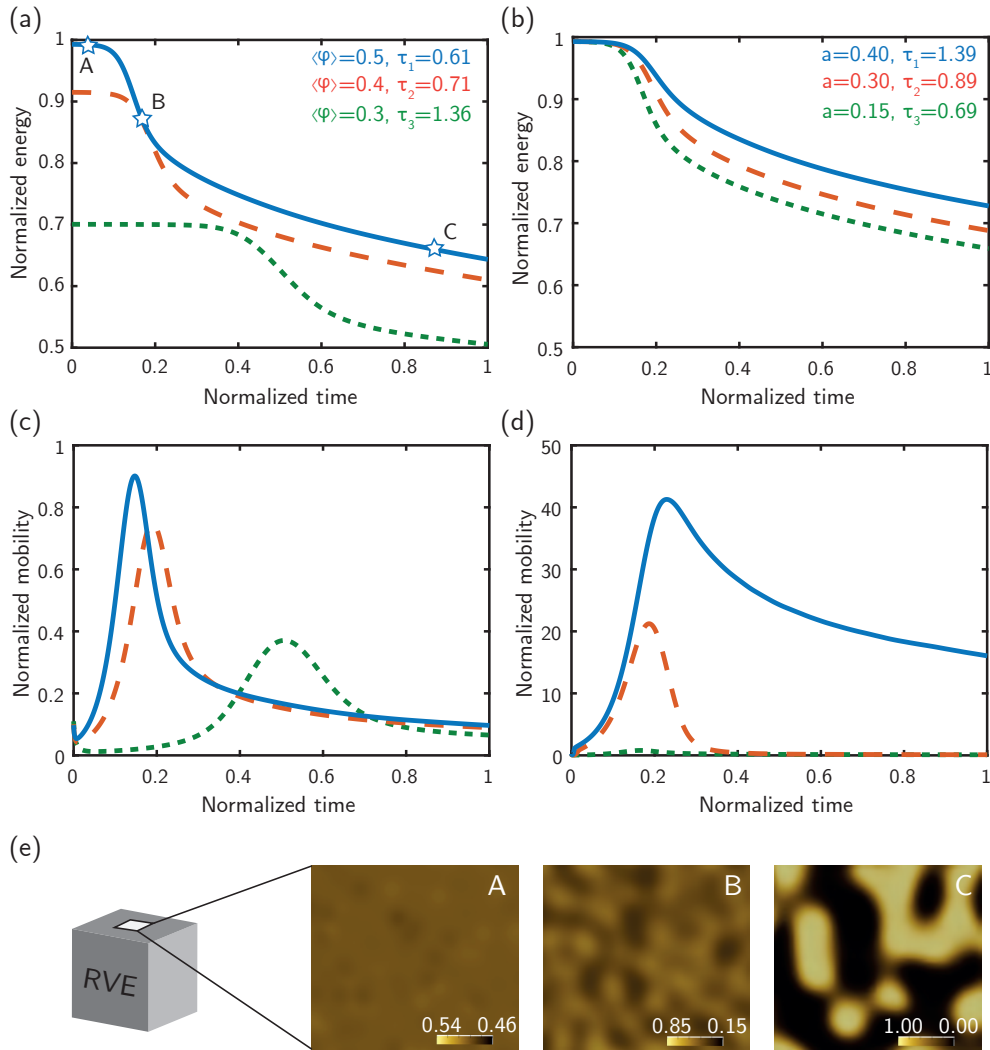


Figure 5.4: Kinetics of the spinodal decomposition process measured by the evolution of the total energy E and of the total mobility Λ . Isotropic surface energy leads to the interfacial energy (a) and mobility (c), whereas cubic symmetry with $a = 0.15$ generates the interfacial energy (b) and mobility (d). In all plots the shown curves are for $\langle\varphi\rangle = 0.3$ (green, dotted), $\langle\varphi\rangle = 0.4$ (red, dashed), and $\langle\varphi\rangle = 0.5$ (blue, solid). The interfacial energies, mobility and time scales have been normalized by their respective maximum. For (c) and (d) the maximum of the isotropic mobility function is used. An exemplary microstructure evolution is shown in (e) for the three times labeled A through C in (a).

(d). Each discrete segment of the interface with an area A_i has an associated normal vector \mathbf{n} which is related to the mean and Gaussian curvatures, H and K , respectively defined as

$$H = \frac{1}{2}\nabla \cdot \mathbf{n}, \quad K = \frac{1}{2} [(\nabla \cdot \mathbf{n})^2 - \|\nabla \mathbf{n}\|^2], \quad (5.22)$$

where $\|\nabla \mathbf{n}\|$ denotes the Hilbert-Schmid norm of the gradient tensor. To derive the ISD the principal curvatures κ_1 and κ_2 are calculated as functions of the mean and Gaussian curvatures:

$$\kappa_1 = H - \sqrt{H^2 - K}, \quad \kappa_2 = H + \sqrt{H^2 - K}. \quad (5.23)$$

The probability of finding a patch with a set of principal curvatures κ_1, κ_2 is described by

$$P_{\text{ISD}}(\kappa_1, \kappa_2) = \frac{A_{\text{ISD}}(\kappa_1, \kappa_2)}{A_{\text{tot}}}, \quad (5.24)$$

where $A_{\text{ISD}}(\kappa_1, \kappa_2) = \sum_i A_i(\kappa_1, \kappa_2)$ is the total area of all area segments with principal curvatures κ_1, κ_2 , and A_{tot} is the total area of all interfaces within the RVE.

For bi-continuous structures the principal curvatures are spread within the upper left quadrant ($\kappa_1 < 0$ and $\kappa_2 > 0$). As shown in Fig. 5.5(a), in the isotropic case the principal curvatures are dispersed largely along the line of zero-mean curvature ($\kappa_1 = -\kappa_2$). In the case of anisotropy the overall average curvatures are remarkably diminished and converge towards planar interfaces ($\kappa_1 = \kappa_2 = 0$), see Fig. 5.5(b)-(d). In particular, for the anisotropic cases there is a reduced probability of interfaces having a saddle-like morphology. This results in an increased likelihood of non-zero mean curvature, while the contrary is true for the Gaussian curvature.

Manipulating the Elastic Property Space

For the calculation of the effective elastic properties, the generated microstructures are subjected to periodic homogenization. Although structures are inherently random, the redistribution of mass within the RVE during spinodal decomposition results in mechanically stiff and compliant directions. It is therefore expected that the different microstructures – from isotropic to columnar to lamellar – respond differently to applied loads. This is demonstrated by subjecting example RVEs to uniaxial extension. The resulting spatial distribution of the von Mises stress $\sigma_m = \sqrt{[(\sigma_1 - \sigma_2)^2 + (\sigma_1 - \sigma_3)^2 + (\sigma_2 - \sigma_3)^2]}/2$ with principal stresses $\sigma_1, \sigma_2, \sigma_3$ is illustrated in Fig. 5.6, where cases (a)-(c) are loaded in the \mathbf{e}_3 -direction and (d)-(f) in the \mathbf{e}_1 -direction.

Unlike typical truss- or plate-based architectures, the generated microstructures avoid acute corners and edges, as shown by the morphological analysis above, so that the emergence of strong stress concentrations is prevented. As expected, the isotropic microstructure shows no significant difference in stress magnitude for the two load cases. On the contrary, the columnar structure in Fig. 5.6(b),(e) shows noticeably higher stresses when loaded in the \mathbf{e}_3 -direction, since the columns align with the direction of loading. The opposite is observed for the lamellar structure, where material is elongated in the \mathbf{e}_1 - \mathbf{e}_2 -plane. The resulting behavior is close to that of the classical Reuss and Voigt bounds, with largest stresses occurring when the load is aligned with the lamellae orientation (Fig. 5.6(c),(f)).

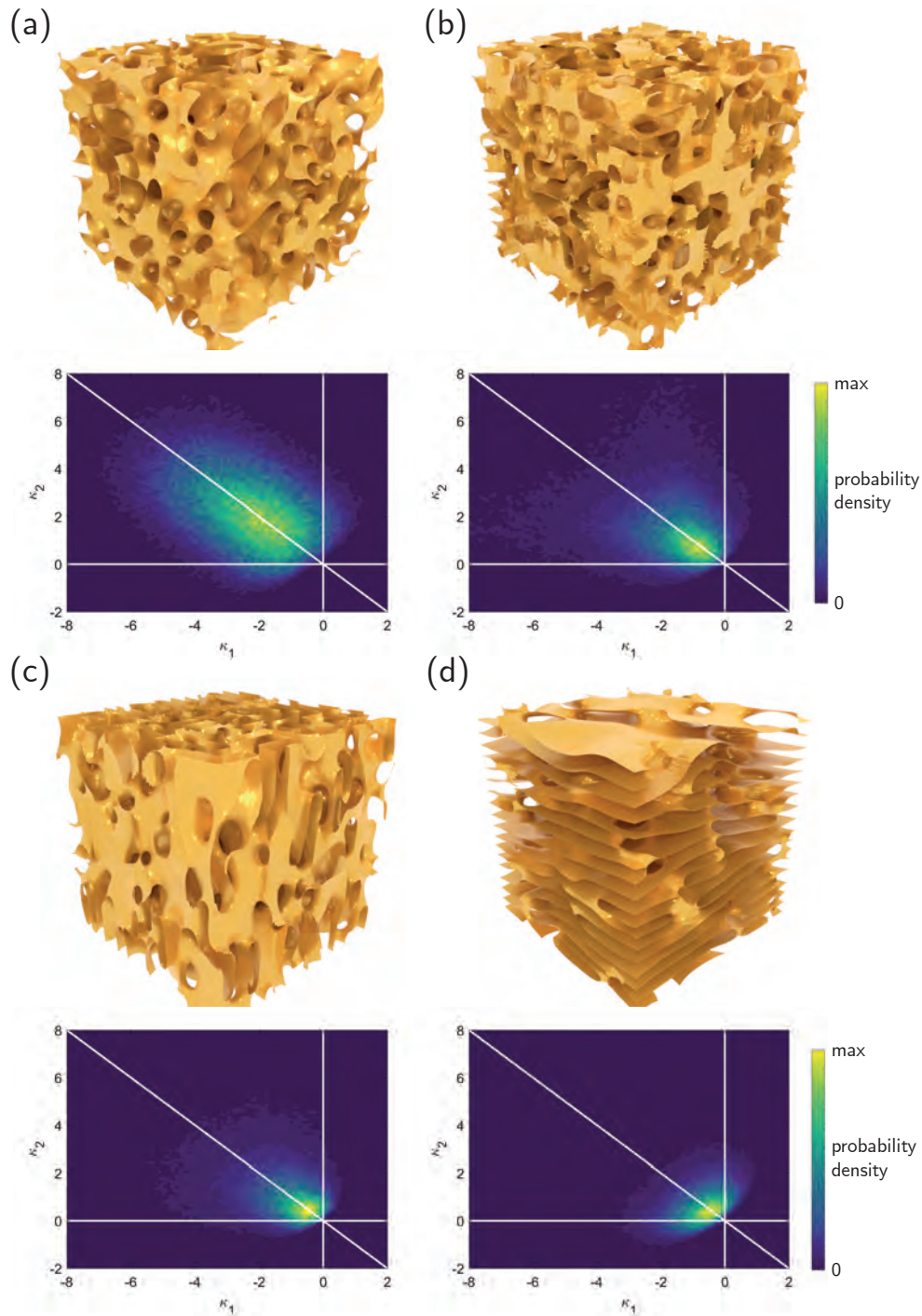


Figure 5.5: Contour plots of the solid-void interfaces (visualized at constant $\varphi = 0.5$) and the interfacial shape distribution as a function of the principal curvatures (κ_1, κ_2) of (a) isotropic, (b) cubic, (c) columnar, and (d) lamellar microstructures.

These observations are quantified by calculating the associated elastic surfaces, which illustrate Young's modulus in all directions in 3D (and reduce to a sphere in case of isotropy). For cubic,

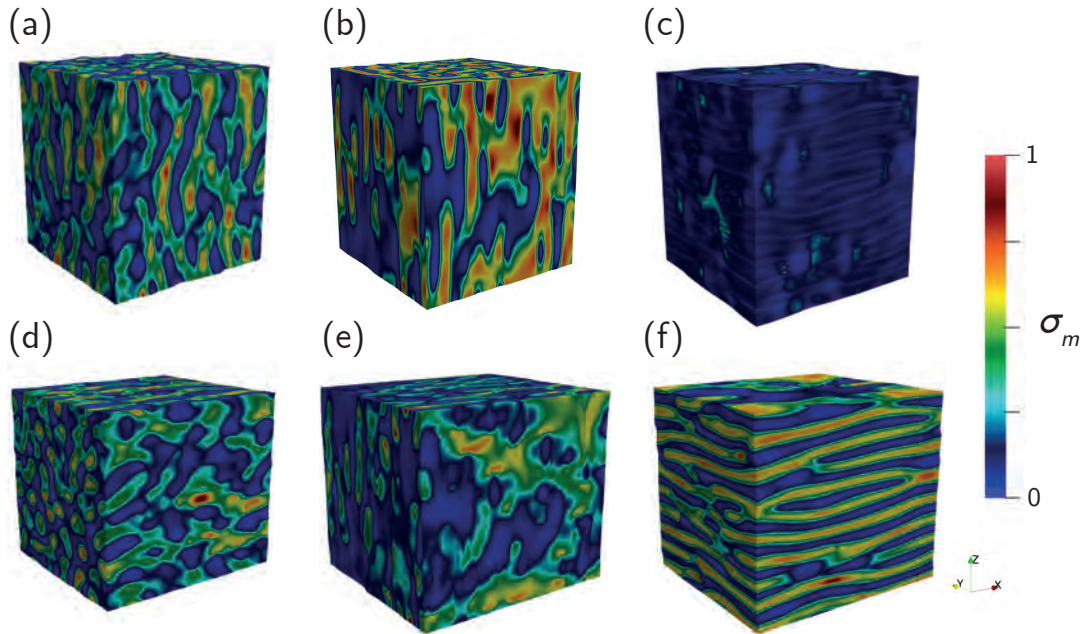


Figure 5.6: Distribution of the von Mises stress σ_m for an applied average strain ε_0 in the \mathbf{e}_3 -direction (i.e., $\langle \varepsilon_{33} \rangle = \varepsilon_0$ and $\langle \varepsilon_{ij} \rangle = 0$ else) for (a) isotropic, (b) columnar and (c) lamellar microstructures. Analogously, the von Mises stress distribution is shown for an applied average strain in the \mathbf{e}_1 -direction (i.e., $\langle \varepsilon_{11} \rangle = \varepsilon_0$ and $\langle \varepsilon_{ij} \rangle = 0$ else) for (d) isotropic, (e) columnar and (f) lamellar microstructures. Stresses are normalised by the peak stress among (a)-(f).

columnar and lamellar structures, Fig. 5.7 contrasts the obtained elastic surfaces and the directional surface energy density $\gamma(\mathbf{n})$, showing a clear and logical correlation: largest stiffness generally appears in those directions perpendicular to the lowest surface energies (because structures are prone to emerge in those directions). Therefore, the lamellar structure of Fig. 5.7(c),(f) shows pronounced transverse isotropy, whereas the columnar case in Fig. 5.7(b),(e) displays two-fold symmetry in the \mathbf{e}_1 - \mathbf{e}_2 -plane and significantly higher stiffness out-of-plane. Finally, the cubic microstructure in Fig. 5.7(a),(d) is closer to isotropy while showing the expected cubic symmetry of the elastic stiffness due to alignment of material with the three coordinate axes.

In addition, the directional Poisson's ratio is computed for the analyzed structures in the \mathbf{e}_1 - \mathbf{e}_2 -plane and the \mathbf{e}_1 - \mathbf{e}_3 -plane, see Fig. 5.8 (due to inherent symmetries one might expect statistically similar properties in the \mathbf{e}_2 - \mathbf{e}_3 -plane). The directions are chosen such that \mathbf{n} is perpendicular to the stretch direction \mathbf{d} and lies in the plane of interest. In the \mathbf{e}_1 - \mathbf{e}_2 -plane all given structures show a large degree of isotropy with Poisson's ratios slightly below the value of the base material ($\nu_b = 0.3$). In contrast, for the perpendicular planes the columnar and lamellar structures show a highly direction-dependent Poisson's ratio, varying between 0.15 – 0.45. This strong variation has potential for generating auxetic materials with directional dilatational properties.

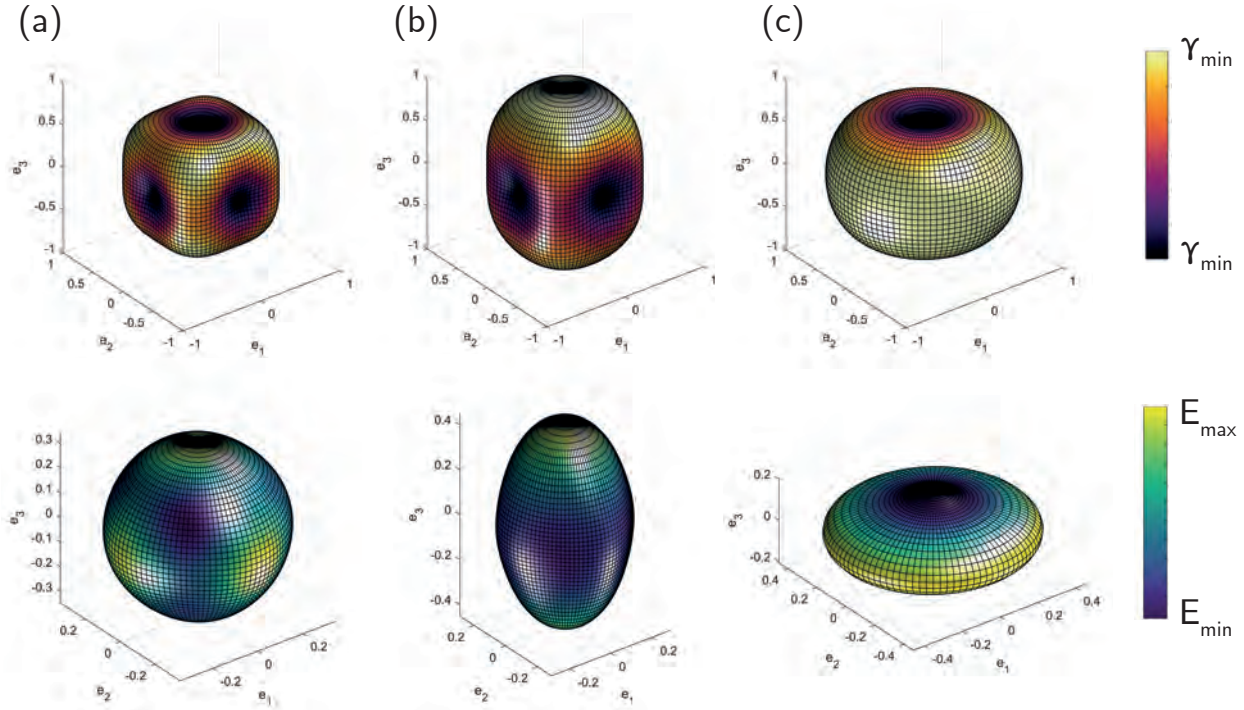


Figure 5.7: Surface plots of the directional surface energy density $\gamma(\mathbf{n})$ from Eq. (5.4) and the corresponding homogenised directional normalized Young's modulus $E(\mathbf{d})$ from Eq. (5.19) for (a,d) cubic (b,e) columnar and (c,f) lamellar microstructures, as seen in Fig. 5.2.

By systematically calculating the elastic properties for varying relative densities $\langle\varphi\rangle$ and degrees of anisotropy a , the reachable elastic property space of microstructures created by anisotropic spinodal decomposition can be mapped as seen in Fig. 5.9. The large size of the chosen RVE makes the computed elastic properties consistent across different geometric realizations (for twelve different microstructure realizations generated with the same parameters but different initial perturbations a standard deviation of less than 2.5% exists for all components of the effective stiffness tensor). Therefore, only the properties obtained from one realization are shown for every choice of $\langle\varphi\rangle$ and a without loss of generality.

To highlight the directional property space, the average as well as the minimum and maximum directional values of the elastic Young's modulus across all possible directions are plotted as functions of the average relative density $\langle\varphi\rangle$, resulting in Fig. 5.9. For isotropic structures, the relative Young's modulus varies as shown in Fig. 5.9(a); the directional variation (indicated by the grey region highlighting minimum/maximum values of $E(\mathbf{d})$) is negligible and stems from randomness in the decomposition process and the finite size of the RVE. The cubic structure (Fig. 5.9(b)) reveals a similar scaling as the isotropic case and shows only a small spread, implying low levels of directionality. At large anisotropy, corresponding to higher a -values, the relative

Young's modulus is increased, and a stronger difference between the maximum and minimum directional E/E_S is visible (cf. cases $a = 0.15$ and $a = 0.4$ in Figs. 5.9(b)). Interestingly, the cubic anisotropy tends to increase the average stiffness as well as the difference between minimum and maximum directional stiffness values.

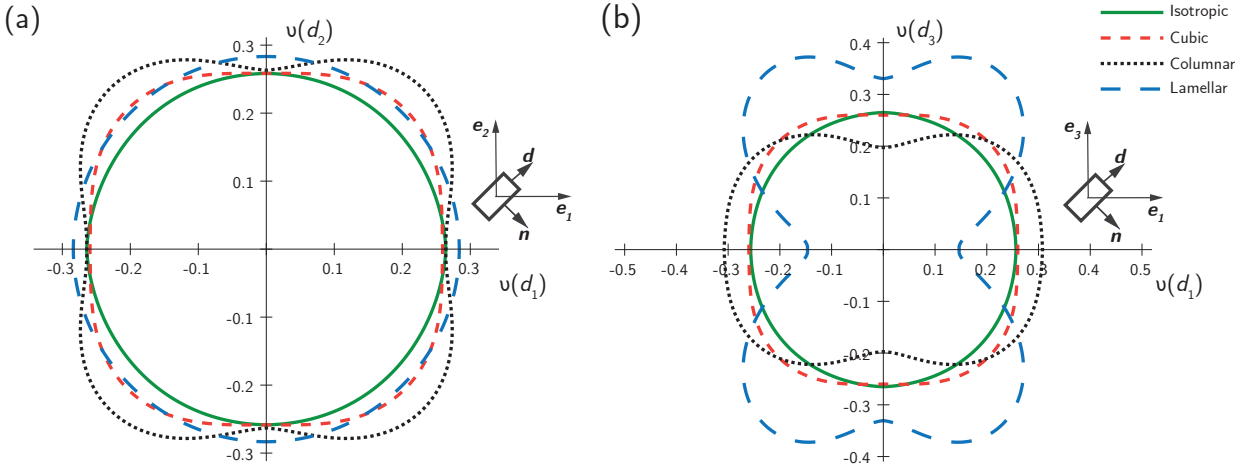


Figure 5.8: Directional Poisson's ratio for isotropic (green, solid), cubic (red, small dashed), columnar (black, dotted), and lamellar structures (blue, dashed). (a) shows Poisson's ratio in the e_1 - e_2 -plane, and (b) shows Poisson's ratio in the e_1 - e_3 -plane. The direction n in the definition of Poisson's ratio, cf. Eq. (5.20), lies in the plane and is always perpendicular to the stretch direction d (see the inset schematic).

The columnar and the lamellar microstructures show a more pronounced variation of their global stiffness properties with anisotropy and relative density, see Fig. 5.9(c),(d). In particular, the ratio between the maximum and the minimum directional Young's modulus is large, approximately 1.45 for the columnar and 2.20 for the lamellar structure at the $\langle \varphi \rangle$ of widest variation. The maximum anisotropy is reached at intermediate densities around $\langle \varphi \rangle \approx 0.5$. Indeed, when approaching high relative densities, the impact of microstructural details is expected to vanish (the analogous holds true for low relative densities). There is also a strong relative density-dependence of the elastic moduli of the columnar and lamellar structures.

For completeness, Fig. 5.9 includes the Voigt upper bound on the effective stiffness of general, anisotropic two-phase media (Hill, 1952; Paul, 1960) (the Reuss lower bound vanishes identically due to the void phase), which naturally forms an upper attainability limit for the average Young's modulus. As can be expected, the maximum directional Young's modulus for both the columnar and lamellar structures approaches the Voigt bound for high anisotropy ($a = 0.4$), because the microstructure in the directions of the lamellae (e_1 - e_2 plane) and in the e_3 -direction of the columns resembles the Voigt iso-strain construction.

Microstructures with Reduced Symmetry and Orthogonality

The outlined computational procedure is sufficiently general to function not only with orthogonal symmetries (characterized by a set of orthogonal vectors, \mathbf{M}); non-orthogonal, asymmetric microstructures can be produced in an analogous fashion with less intuitive effective elastic properties. Two examples of such systems are shown in Fig. 5.10. First, two proximate, non-orthogonal directions were chosen in Fig. 5.10(a) (effectively splitting the single direction from the case of lamellar microstructures into two nearby orientations). The resulting overall symmetry of the elastic surface is reduced, as shown in Fig. 5.10(c). Moreover, the corresponding Poisson's ratios are no longer identical in the e_1 - e_3 - and e_2 - e_3 -planes but show a stronger degree of anisotropy in the plane with the larger variation of Young's modulus (Fig. 5.10(g)). Second, a trigonal system with the six different m_i directions is investigated and shown in Fig. 5.10(b),(d). The resulting elastic surface displays stiff directions of trigonal symmetry, as opposed to the classical, orthogonal symmetries of the systems studied above (see Fig. 5.7), highlighting the flexibility of the presented approach in tailoring the directional stiffness. While such elastic anisotropies are usually not found in natural materials or crystalline systems, they can readily be produced, for example, by additively manufacturing the shown periodic porous media.

5.6 Conclusion

In this chapter, a numerical technique has been presented to simulate the process of anisotropic spinodal decomposition in the presence of anisotropic surface energies. The resulting microstructures and their effective elastic properties have been analyzed in detail. It has been shown that by introducing energetically favorable orientations during phase separation, the resulting geometric distribution of solid and void in a representative volume element can be tuned. This includes simple bi-continuous microstructures such as lamellar, columnar, and cubic as well as more complex microstructures with reduced symmetries (the numerical tools shown here are sufficiently general for their application to arbitrary anisotropies).

Using periodic homogenization, the effective elastic properties of the resulting porous media have been computed, including their directional elastic surfaces and Poisson's ratios, thus establishing a link between surface anisotropy, resulting microstructure and effective mechanical properties. Finally, these methods can be used to generate porous (meta-)materials with tunable mechanical properties, opening a new perspective for architected materials with controllable effective performance. Work in progress includes attempts to fabricate these at both the macroscale (see Figs. 5.11 and 5.13) and the the nanoscale (see Fig. 5.12).

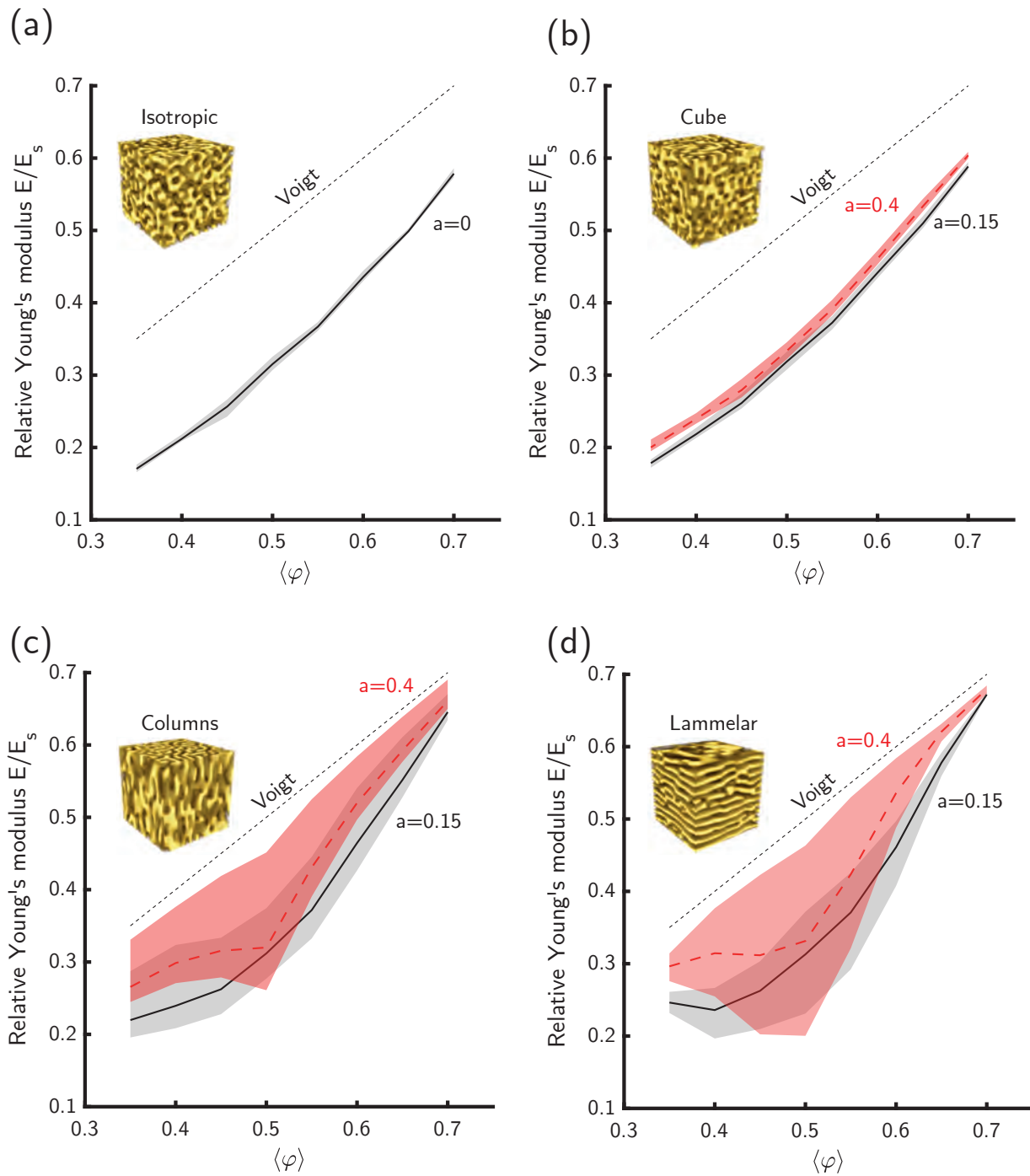


Figure 5.9: Relative Young's modulus of four different microstructures vs. relative densities $\langle \varphi \rangle$, where solid lines indicate the mean modulus and shaded envelopes show the maximum/minimum directional variations of Young's modulus across all 3D directions. Shown are results for (a) isotropic microstructures, (b) cubic microstructures, (c) columnar microstructures, and (d) lamellar microstructures. In (b)-(d) solid black lines represent a low degree of anisotropy ($a = 0.15$) and red dashed lines high degree of anisotropy ($a = 0.4$). Also included is the Voigt upper bound.

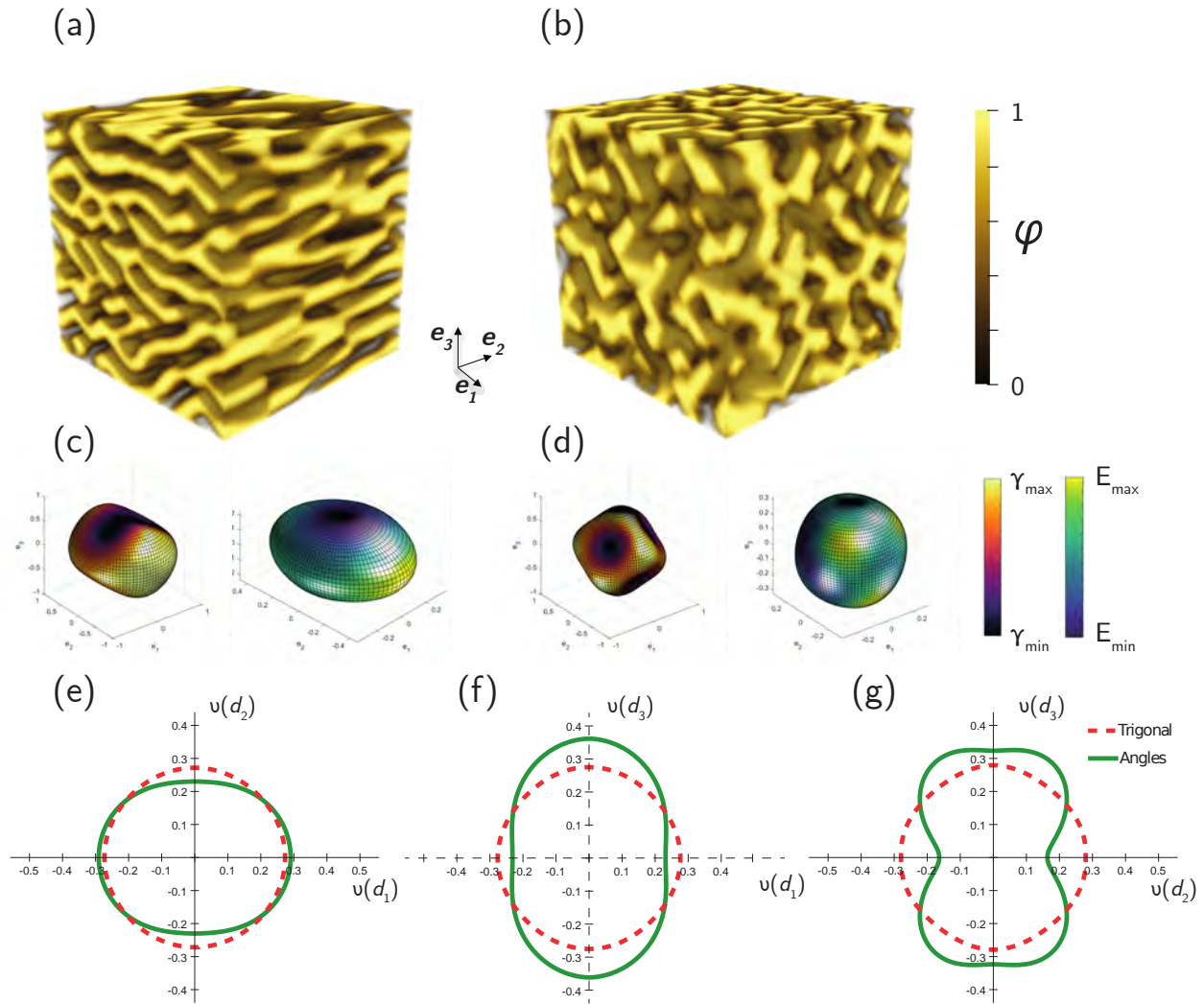


Figure 5.10: Microstructures obtained from non-orthogonal \mathbf{m}_i -vectors: (a) sharp angles with the four directions $[\pm \frac{1}{\sqrt{5}}, 0, \pm \frac{2}{\sqrt{5}}]$, (b) trigonal system with six preferential directions $[0, \frac{1}{\sqrt{3}}, \frac{2}{\sqrt{3}}]$, $[\pm \frac{1}{2}, -\frac{1}{2\sqrt{3}}, \sqrt{\frac{2}{3}}]$, $[\frac{1}{\sqrt{3}}, 0, -\frac{\sqrt{2}}{\sqrt{3}}]$, $[-\frac{1}{2\sqrt{3}}, \pm \frac{1}{2}, \sqrt{\frac{2}{3}}]$. (c) and (d) show the corresponding normalized $\gamma(\mathbf{n})$ surfaces and the normalized directional Young's moduli. (e), (f) and (g) show Poisson's ratio for the two microstructures in all three orthogonal planes.

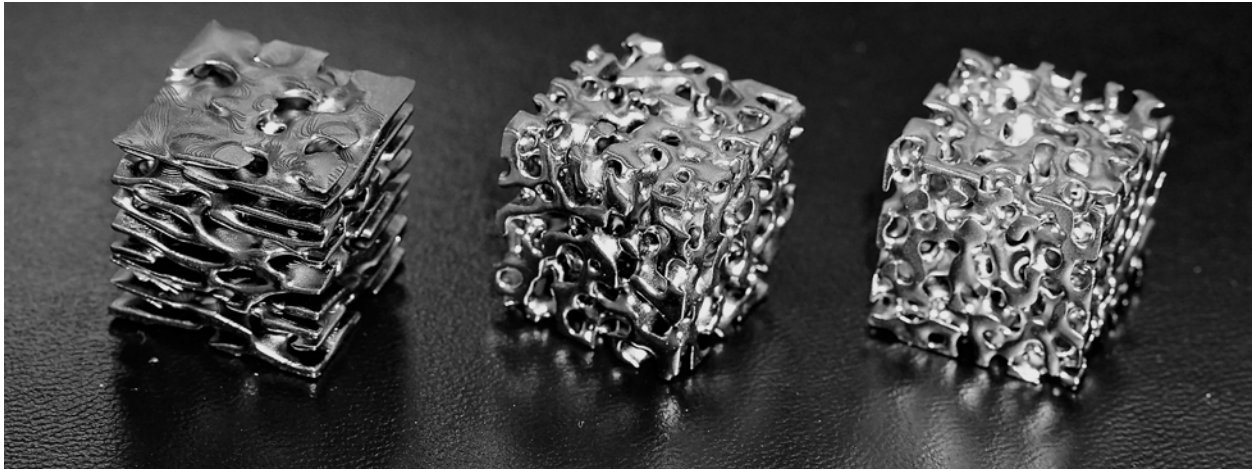


Figure 5.11: Spinodal microstructures printed at the macroscale with 5mm thickness and RVE width 120 mm. Original work.

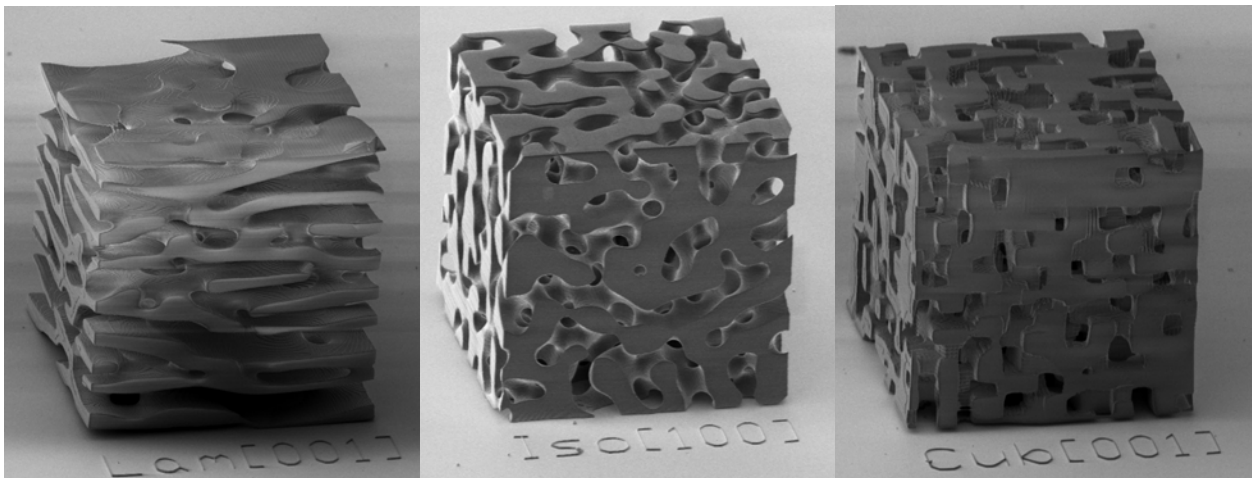


Figure 5.12: Spinodal microstructures printed at the nanoscale with 10nm thickness and RVE width 120 μm . Original joint work, courtesy of Carlos Portela, Greer Group, Caltech.



Figure 5.13: Spinodal microstructures from Fig. 5.11 after heat treatment, colored by oxide layers.

KINETICS OF DOMAIN PATTERNS IN FERROELECTRICS

Research presented in this chapter has been adapted from the following publication:

Vidyasagar, A., Tan, W. L., Kochmann, D. M. 2017. Predicting the effective response of bulk polycrystalline ferroelectric ceramics via improved spectral phase field methods. *Journal of the Mechanics and Physics of Solids* 106, 113-151.

URL: <https://doi.org/10.1016/j.jmps.2017.05.017>

Chapter 5 focused on scalar conservative gradient flow driven regularized potentials, which led to the conservative, scalar Cahn-Hilliard equations for phase separation. Phase transitions, however, are not conservative and often involve vector quantities in multiple dimensions. Ferroelectrics are a case in point, with a wealth of experimental data, analytical results, and numerical interest. Here, non-conservative gradient flow leads to Allen-Cahn kinetics for the evolution of the polarization vector within an electromechanically coupled ferroelectric sample. The exposition that follows extends the current narrative to understand kinetics in this highly complex system, and an example for bridging scales all the way from density functional theory (DFT, approximate quantum mechanical calculations) to predicting and matching experiments.

6.1 Introduction

Ferroelectric ceramics exhibit electro-mechanical coupling below their Curie temperature, which makes this class of materials prime candidates, e.g., for actuators and sensors. Conventional use of ferroelectric ceramics lies in the piezoelectric regime with approximately linear coupling between electrical and mechanical fields (Taylor, 1985; Yang, 2006). Under sufficiently large applied electric fields or mechanical loads, the atomic-level dipole structure can be permanently altered (Chaplya and Carman, 2001; Bhattacharya and Ravichandran, 2003), accommodated by ferroelectric switching and the associated irreversible changes in the electro-mechanical fields. Although the quasistatic material behavior and energy-derived properties (such as stiffness, piezoelectric or dielectric constants) are well understood, current understanding of the kinetics and hysteresis associated with the rate-dependent ferroelectric switching process is still incomplete (Merz, 1956; Arlt and Dederichs, 1980; Zhou et al., 2001; Wojnar et al., 2014; le Graverend et al., 2015), especially in complex polycrystalline materials with abundant defects and grain boundaries (GBs) acting as both nucleation sites for switching and obstacles for domain wall motion (Lambeck and

Jonker, 1986; Rodriguez et al., 2008; Marincel et al., 2015). This lack of understanding stems primarily from the large range of length and time scales involved (from atomic-scale interactions to macroscopic samples, from fast switching events to the experimentally-observed hysteresis). This makes the underlying phenomena difficult to model computationally and hard to access experimentally. Much prior work has focused on thin films (see, e.g., Chen (2008) and references therein), where both experimental TEM imaging of ferroelastic switching and atomistic simulations have helped understand the relation between domain wall motion and the collective switching behavior under electrical and mechanical loads (Gao et al., 2013, 2014). Domain wall kinetics have also been investigated experimentally, e.g., by Merz (1956); Miller and Savage (1958); Savage and Miller (1960); Arlt and Dederichs (1980); Chaplya and Carman (2002a). At larger scales, Wojnar et al. (2014) recently performed experiments using Broadband Electromechanical Spectroscopy to quantify the dissipation in bulk polycrystalline samples during domain switching. Our focus here is on the mesoscale of polycrystalline ferroelectric ceramics, above atomistic resolution but below macroscopic sample extensions so as to enable the extraction of homogenized material behavior.

At the continuum scale, ferroelectric models typically make use of one of three approaches: (i) *phenomenological models* use an effective material description and do not resolve the microstructure (see e.g. Bassiouny et al. (1988); Cocks and McMeeking (1999); Landis (2002); Arockiarajan et al. (2006); Miehe and Rosato (2011); Idiart (2014)); (ii) *sharp-interface models* account for domain mixtures in an efficient manner (e.g., Huber et al. (1999); Huber and Fleck (2004); Xiao and Bhattacharya (2008)); and (iii) *phase field models* fully resolve the domain structure in a diffuse-interface fashion at the mesoscale – this is the approach of choice here. Previously, Zhang and Bhattacharya (2005a,b) used a phase field approach to model ferroelectric domains; they calibrated the phenomenological constants associated with the Landau-Devonshire equations, and solved the associated boundary value problems. Similarly, Su and Landis (2007a) thermodynamically developed a more complex phase field model and demonstrated domain switching. These two approaches will form the basis for the barium titanate (BaTiO_3) examples studied in this chapter. More recently, Völker et al. (2011) obtained phase field constants through adjusted first principles DFT computations, which will be adopted here for the modeling of lead zirconate titanate (PZT).

Using Landau-Devonshire theory, Chen (2008) provided a comprehensive review on modeling phase transitions and domain structures in ferroelectric thin films. Dayal and Bhattacharya (2007) developed a non-local model of ferroelectric domain patterns in complex geometries and used the boundary element method to resolve the electrostatic fields. Li et al. (2002) studied the effects of different types of boundary conditions on the switching behavior in thin film ferroelectric ceramics and analyzed the stability of domain structures. Chu et al. (2014) used a phase field approach of Landau-type to study switching behavior upon electrical loading, and the demonstrated

a relationship between the kinetics of 90°-domain wall motion, mesoscopic frequency dielectric response, and elastic energy. [Schrade et al. \(2007\)](#) provide an alternative phase field model whose order parameter is taken as the spontaneous polarization as opposed to the total material polarization. More recently, the same authors presented an invariant formulation of their phase field model for transversely-isotropic material behavior ([Schrade et al., 2014](#)).

The phase field formulation in all those studies is ideally suited to be treated by spectral methods analogous to the formulation in Chapter 2. [Choudhury et al. \(2005\)](#) have previously studied polarization switching and domain evolution in ferroelectric polycrystals using a linear semi-implicit Fourier spectral method for isotropic linear elastic solids, but the study was limited to 2D simulations for computational complexity and had a simplified energetic potential without electro-mechanical coupling. They also analyzed the effect of grain orientations and boundaries on the switching behavior of simplified bicrystals ([Choudhury et al., 2007](#)). [Kalinin et al. \(2007\)](#) performed experiments to investigate intrinsic single-domain switching in ferroelectrics, and showed good agreement of their findings with the phase field model with semi-implicit linear Fourier spectral method developed by [Chen and Shen \(1998\)](#).

Here, the numerical models developed in Chapter 2 are applied to phase field models of polycrystalline ferroelectrics, and comparisons are made with between the predicted effective material performance of PZT and new experimental data. To this end, Section 6.2 summarizes the constitutive model (which unites several previous approaches) whose governing equations are solved at the RVE-level, as described in Section 6.4 along with convergence benchmark tests. Section 6.5 presents simulation results of ferroelectric switching in BaTiO₃ and PZT, and Section 6.6 concludes the analysis.

6.2 Ferroelectric Constitutive Model

Consider a body $\Omega \subset \mathbb{R}^d$ in d -dimensional space, whose deformation at position $\mathbf{x} \in \Omega$ and time $t \geq 0$ is described by the displacement field $\mathbf{u} : \Omega \times t \rightarrow \mathbb{R}^d$. In contrast with preceding models in previous chapters, the small strains typical for ferroelectric ceramics admit linearized kinematics with the infinitesimal strain tensor

$$\boldsymbol{\varepsilon} = \text{sym}(\nabla \mathbf{u}). \quad (6.1)$$

Conservation of linear momentum in the absence of body forces requires

$$\text{div } \boldsymbol{\sigma} = \rho \ddot{\mathbf{u}} \quad (6.2)$$

with infinitesimal stress tensor $\boldsymbol{\sigma}$ and mass density ρ , and dots denoting time derivatives. Essential boundary conditions $\mathbf{u} = \mathbf{u}_0$ are imposed on $\partial\Omega_u \subset \partial\Omega$, whereas natural boundary conditions $\boldsymbol{\sigma} \mathbf{n} = \mathbf{t}_0$ with outward unit normal \mathbf{n} and traction vector \mathbf{t}_0 are applied on $\partial\Omega_t \subset \partial\Omega$.

The electric description is based on the voltage potential $\phi : \mathbb{R}^d \times t \rightarrow \mathbb{R}$; the resulting electric vector field

$$\mathbf{e} = -\nabla\phi \quad (6.3)$$

produces electric displacements \mathbf{d} . Gauss' law requires

$$\operatorname{div} \mathbf{d} = q \quad (6.4)$$

with volume charge density q . No free charges q are assumed to exist within Ω . Essential boundary conditions are $\phi = \phi_0$ on $\partial\Omega_\phi \subset \partial\Omega$, and natural boundary conditions apply surface charges \hat{q} on $\partial\Omega_d \subset \partial\Omega$ such that $\mathbf{d} \cdot \mathbf{n} = \hat{q}$. In addition to the elastic fields \mathbf{u} and ϕ , the state of the ferroelectric ceramic is described by the polarization field $\mathbf{p} : \Omega \times \mathbb{R} \rightarrow \mathbb{R}^d$. While the former two are governed by the balance of linear momentum and Gauss' law, the latter field is dissipative and requires a kinetic law to define the time-continuous evolution. The resulting system of equations must be closed by appropriate constitutive laws.

To this end, the Helmholtz free energy density Ψ becomes (using index notation)

$$\sigma_{ij} = \frac{\partial\Psi}{\partial\varepsilon_{ij}} \quad e_i = \frac{\partial\Psi}{\partial d_i}. \quad (6.5)$$

Following [Zhang and Bhattacharya \(2005a\)](#) and [Su and Landis \(2007a\)](#), an additive structure is assumed for the internal energy density, viz.

$$\Psi(\boldsymbol{\varepsilon}, \mathbf{d}, \mathbf{p}, \nabla\mathbf{p}) = \Psi_{\text{mech}}(\boldsymbol{\varepsilon}) + \Psi_{\text{el}}(\mathbf{d}, \mathbf{p}) + \Psi_{\text{coupl}}(\boldsymbol{\varepsilon}, \mathbf{p}) + \Psi_{\text{pol}}(\mathbf{p}) + \Psi_{\text{inter}}(\nabla\mathbf{p}) \quad (6.6)$$

with the following individual components. The mechanical strain energy density with fourth-order elastic modulus tensor \mathbb{C} and the electric energy density with isotropic permittivity κ_0 are, respectively,

$$\Psi_{\text{mech}}(\boldsymbol{\varepsilon}) = \frac{1}{2} \varepsilon_{ij} \mathbb{C}_{ijkl} \varepsilon_{kl}, \quad (6.7)$$

$$\Psi_{\text{el}}(\mathbf{d}, \mathbf{p}) = \frac{1}{2\kappa_0} (d_i - p_i)(d_i - p_i). \quad (6.8)$$

Here and in the following, Einstein's summation convention is used unless explicitly stated otherwise. The electro-mechanical coupling energy density is assumed as

$$\Psi_{\text{coupl}}(\boldsymbol{\varepsilon}, \mathbf{p}) = \varepsilon_{ij} \mathbb{B}_{ijkl} p_k p_l + \varepsilon_{ij} \mathbb{F}_{ijklmn} \varepsilon_{kl} p_m p_n + \varepsilon_{ij} \mathbb{G}_{ijklmn} p_k p_l p_m p_n, \quad (6.9)$$

where only the first term with fourth-order tensor \mathbb{B} was used by [Zhang and Bhattacharya \(2005a\)](#), whereas the other two terms with sixth-order tensors \mathbb{F} and \mathbb{G} were introduced by [Su and Landis \(2007a\)](#) to allow for reproducing all elastic, electric, and piezoelectric material parameters.

Ferroelectric ceramics of the perovskite family below the Curie temperature possess six tetragonal variants whose ground state polarization vectors correspond to the local minima of a multistable energy landscape. The generic multi-stable Landau-Devonshire energy needed to enforce the symmetric equilibrium states of tetragonal perovskites has the form

$$\begin{aligned} \Psi_{\text{pol}}(\mathbf{p}) = & \frac{1}{2}\tilde{p}_i\mathbb{A}_{ij}^1\tilde{p}_j + \frac{1}{4}\tilde{p}_i\tilde{p}_j\mathbb{A}_{ijkl}^2\tilde{p}_k\tilde{p}_l + \frac{1}{6}\tilde{p}_i\tilde{p}_j\tilde{p}_k\mathbb{A}_{ijklmn}^3\tilde{p}_l\tilde{p}_m\tilde{p}_n \\ & + \frac{1}{8}\tilde{p}_i\tilde{p}_j\tilde{p}_k\tilde{p}_l\mathbb{A}_{ijklmnop}^4\tilde{p}_m\tilde{p}_n\tilde{p}_o\tilde{p}_p. \end{aligned} \quad (6.10)$$

Two particular examples of BaTiO₃ and PZT are investigated in this chapter. For BaTiO₃ the phenomenological model of [Su and Landis \(2007a\)](#) is adopted with the specific form (in 3D)

$$\begin{aligned} \Psi_{\text{pol,BTO}}(\mathbf{p}) = & \frac{a_1}{2}(p_1^2 + p_2^2 + p_3^2) + \frac{a_2}{4}(p_1^4 + p_2^4 + p_3^4) + \frac{a_3}{2}(p_1^2p_2^2 + p_2^2p_3^2 + p_1^2p_3^2) \\ & + \frac{a_4}{6}(p_1^6 + p_2^6 + p_3^6) + \frac{a_5}{4}(p_1^4p_2^4 + p_2^4p_3^4 + p_1^4p_3^4) \\ & + a_6 [p_1^4(p_2^2 + p_3^2) + p_2^4(p_1^2 + p_3^2) + p_3^4(p_1^2 + p_2^2)], \end{aligned} \quad (6.11)$$

where a_i are material constants. For tetragonal PZT, the first principles-informed potential of [Völker et al. \(2011\)](#) is used with non-convex energy density

$$\begin{aligned} \Psi_{\text{pol,PZT}}(\mathbf{p}) = & \frac{a_1}{2}(p_1^2 + p_2^2 + p_3^2) + \frac{a_2}{4}(p_1^4 + p_2^4 + p_3^4) + \frac{a_3}{2}(p_1^2p_2^2 + p_2^2p_3^2 + p_1^2p_3^2) \\ & + \frac{a_4}{6}(p_1^6 + p_2^6 + p_3^6) + \frac{a_5}{4}p_1^2p_2^2p_3^2 \\ & + a_6 [p_1^4(p_2^2 + p_3^2) + p_2^4(p_1^2 + p_3^2) + p_3^4(p_1^2 + p_2^2)]. \end{aligned} \quad (6.12)$$

Figure 6.1 illustrates the nature of these energy landscape in 2D, with four wells, at temperatures below the Curie point.

Finally, the energy stored in ferroelectric domain walls is captured by the regularizing interface energy density

$$\Psi_{\text{inter}}(\nabla\mathbf{p}) = \frac{1}{2}p_{i,j}\mathbb{K}_{ijkl}p_{k,l}, \quad (6.13)$$

where an isotropic interface energy is assumed for simplicity such that

$$\mathbb{K}_{ijkl} = a\delta_{ij}\delta_{kl}, \quad (6.14)$$

using Kronecker's delta, and

$$\Psi_{\text{inter}}(\nabla\mathbf{p}) = \frac{a}{2}|\nabla\mathbf{p}|^2. \quad (6.15)$$

In a polycrystal, the local crystallographic orientation is described by a rotation tensor $\mathbf{R} \in \text{SO}(d)$ whose components are $R_{ij} = \mathbf{a}_i \cdot \mathbf{e}_j$, where $\{\mathbf{e}_1, \dots, \mathbf{e}_d\}$ is the coordinate basis in \mathbb{R}^d and

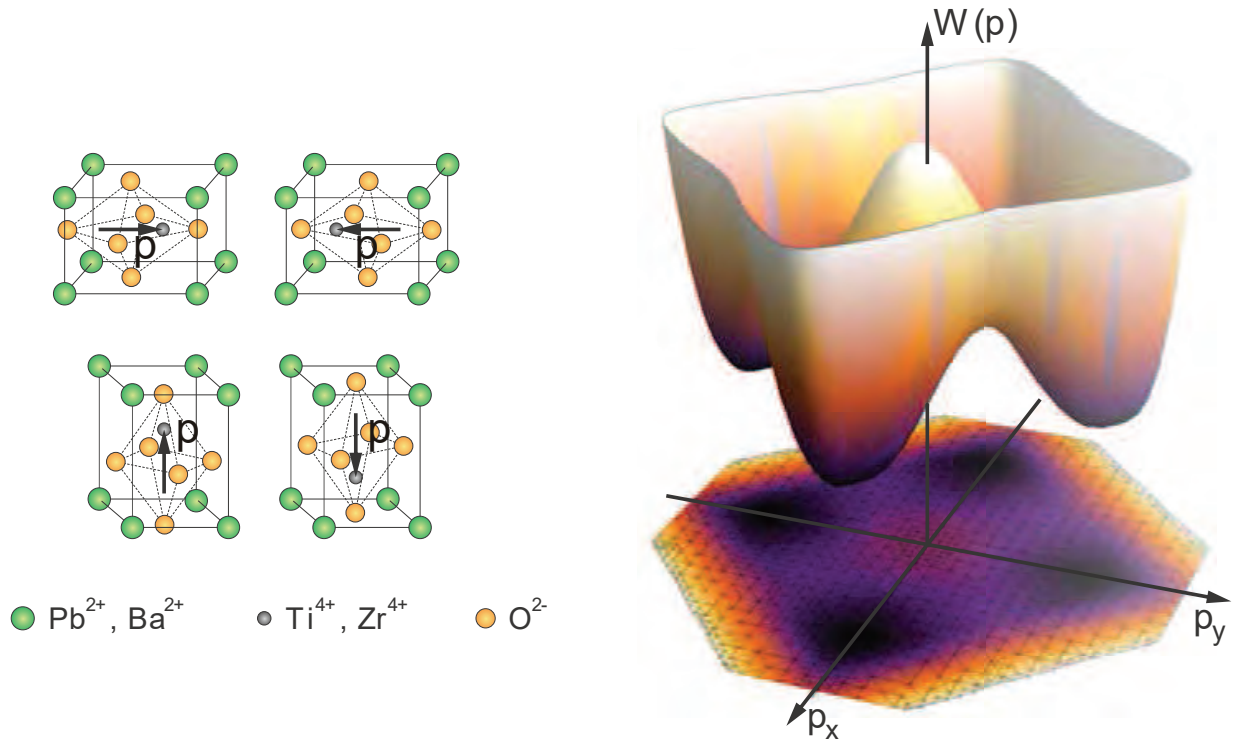


Figure 6.1: Visualization of the non-convex energy potential (in 2D) for both ferroelectrics.

$\{\mathbf{a}_1, \dots, \mathbf{a}_d\}$ are unitary vectors that define the local Bravais lattice. Thus, all of the above energy densities are transformed according to the respective coordinate rotation in each grain. Note that in this section, isothermal room-temperature conditions are assumed so that all material constants can be assumed constant.

For convenience, the electric enthalpy density W , which is obtained via a Legendre transform, is assumed to be

$$W = \sup_{\mathbf{d}} \{\Psi - \mathbf{e} \cdot \mathbf{d}\} \quad \text{so that} \quad \sigma_{ij} = \frac{\partial W}{\partial \varepsilon_{ij}}, \quad d_i = -\frac{\partial W}{\partial e_i}, \quad (6.16)$$

which results in

$$W(\boldsymbol{\varepsilon}, \mathbf{e}, \mathbf{p}, \nabla \mathbf{p}) = \Psi_{\text{mech}}(\boldsymbol{\varepsilon}) + \Psi_{\text{coupl}}(\boldsymbol{\varepsilon}, \mathbf{p}) + \Psi_{\text{pol}}(\mathbf{p}) - \frac{\kappa_0}{2} \mathbf{e} \cdot \mathbf{e} - \mathbf{e} \cdot \mathbf{p} + \Psi_{\text{inter}}(\nabla \mathbf{p}). \quad (6.17)$$

The constitutive relations now follow from the traditional Coleman-Noll approach. Specifically, the components of the infinitesimal stress tensor are

$$\sigma_{ij} = \frac{\partial W}{\partial \varepsilon_{ij}} = (\mathbb{C}_{ijkl} + 2\mathbb{F}_{ijklmn} p_m p_n) \varepsilon_{kl} + \mathbb{B}_{ijkl} p_k p_l + \mathbb{G}_{ijklmn} p_k p_l p_m p_n = \tilde{\mathbb{C}}_{ijkl} (\varepsilon_{kl} - \varepsilon_{kl}^r), \quad (6.18)$$

where the effective elasticity tensor $\tilde{\mathbb{C}} = \mathbb{C}_{ijkl} + 2\mathbb{F}_{ijklmn}p_m p_n$ and the remnant strain tensor $\varepsilon_{ij}^r = -\tilde{\mathbb{C}}_{ijkl}^{-1}(\mathbb{B}_{klmn}p_m p_n + \mathbb{G}_{ijklmn}p_k p_l p_m p_n)$. The electric displacement vector follows as

$$d_i = -\frac{\partial W}{\partial e_i} = p_i + \kappa_0 e_i. \quad (6.19)$$

Under quasistatic conditions and in the absence of free charges, the elastic (mechanical and electric) fields are now governed by linear momentum balance, $\sigma_{ij,j} = 0$, and Gauss' law, $d_{i,i} = 0$.

The polarization \mathbf{p} evolves in a dissipative fashion, which is assumed to be governed by the Allen-Cahn equation of linear L^2 gradient flow (Zhang and Bhattacharya, 2005a; Su and Landis, 2007a),

$$\eta \dot{\mathbf{p}} = \mathbf{y} \quad (6.20)$$

with a drag coefficient $\eta > 0$ and the thermodynamic-conjugate driving force

$$y_i = -\frac{\delta W}{\delta p_i} = -\frac{\partial W}{\partial p_i} + \left(\frac{\partial W}{\partial p_{i,j}} \right)_j = e_i - \frac{\partial \Psi_{\text{coupl}}}{\partial p_i} - \frac{\partial \Psi_{\text{pol}}}{\partial p_i} + \mathbb{K}_{ijkl} p_{k,lj}. \quad (6.21)$$

It has been shown in the ferroelectrics literature (see, e.g., the experimental-theoretical findings of Wojnar et al. (2014)), that linear gradient flow, although simple, does not capture well the intricate switching kinetics, which may motivates refinements of the kinetic rule.

This can also be cast into a variational structure by introducing the dual kinetic potential

$$\phi^*(\dot{\mathbf{p}}) = \frac{\eta}{2} |\dot{\mathbf{p}}|^2, \quad (6.22)$$

so that (6.20) is equivalent to

$$\frac{\delta W}{\delta \mathbf{p}} + \frac{\partial \phi^*}{\partial \dot{\mathbf{p}}} = \mathbf{0} \quad \text{or} \quad \dot{\mathbf{p}} = \arg \min [\dot{W} + \phi^*]. \quad (6.23)$$

In summary, the unknown fields $\mathbf{u}(\mathbf{x}, t)$, $\phi(\mathbf{x}, t)$ and $\mathbf{p}(\mathbf{x}, t)$ are determined from the coupled system of equations consisting of linear momentum balance, Gauss' law, and the kinetic evolution law:

$$\left[(\mathbb{C}_{ijkl} + 2\mathbb{F}_{ijklmn}p_m p_n) u_{k,l} + \mathbb{B}_{ijkl} p_k p_l + \mathbb{G}_{ijklmn} p_k p_l p_m p_n \right]_j = 0, \quad (6.24a)$$

$$p_{i,i} - \kappa_0 \phi_{,ii} = 0, \quad (6.24b)$$

$$e_i - \frac{\partial \Psi_{\text{coupl}}}{\partial p_i} - \frac{\partial \Psi_{\text{pol}}}{\partial p_i} + \mathbb{K}_{ijkl} p_{k,lj} = \eta \dot{p}_i. \quad (6.24c)$$

The specific material parameters chosen here for BaTiO₃ and PZT are summarized in 6.3. Following Zhang and Bhattacharya (2005a), $\mathbb{F}_{ijklmn} = 0$ and $\mathbb{G}_{ijklmn} = 0$ for both PZT and

BaTiO₃, which satisfies average stress-free conditions exactly. This may incur inaccuracies in the linear piezoelectric properties which are, however, of minor importance in the investigation of full nonlinear ferroelectric hysteresis. It is important to note that the mean stress-free condition does not necessitate these specific constitutive parameters (further discussed in Section 6.4), but otherwise would require an iterative numerical scheme to impose mean stresses. Alternatively, the dual stress reformulation of [Bhattacharya and Suquet \(2005\)](#) could be used but complicates the explicit implementation of the coupled electromechanical problem.

To the same end, isotropic elasticity is assumed with Lamé moduli λ and μ so that $\mathbb{C}_{ijkl} = \lambda\delta_{ij}\delta_{kl} + \mu(\delta_{ik}\delta_{jl} + \delta_{il}\delta_{jk})$. The moduli were obtained from an isotropic adjustment of the cubic elastic moduli of [Zhang and Bhattacharya \(2005a\)](#) and [Völker et al. \(2011\)](#) for, respectively, BaTiO₃ and PZT (specifically, Voigt stiffness moduli C_{11} and C_{12} and

$$C_{44} = (C_{11} - C_{12})/2. \quad (6.25)$$

Tetragonal variants are not isotropic, but the level of anisotropy is moderate and the mean stress-free condition is expected to let the elastic anisotropy have an insignificant effect on the switching behavior in the following examples. The electro-mechanical coupling tensor \mathbb{B}_{ijkl} is expressed in terms of coefficients b_1 through b_3 through

$$\mathbb{B}_{ijkl} = \frac{1}{2} \begin{cases} b_1 & \text{if } i = j = k = l, \\ b_2 & \text{if } i = j \neq k = l \\ b_3 & \text{if } i = k \neq j = l \\ 0 & \text{else} \end{cases} \quad (6.26)$$

For convenience, a normalization constant e_0 is introduced for the electric field (specified in 6.3).

6.3 Material Constants for BaTiO₃ and PZT

The material constants used for the simulations of BaTiO₃ and PZT are summarized in Tables 6.1 and 6.2, respectively.

6.4 Boundary Value Problem at the RVE Level

Effective Material Response

The effective material behavior of an RVE is simulated at the mesoscale of a polycrystalline ferroelectric ceramic. As in conventional micro-to-macro transition theories ([Miehe et al., 2002](#); [Schröder, 2009](#)), the effective fields are obtained from volume averaging over the periodic RVE. In order to compare the simulated response with experimental data, an average (total) electric field is imposed where

$$\bar{\mathbf{e}} = \langle \mathbf{e} \rangle \quad \text{where} \quad \langle \cdot \rangle = \frac{1}{|\Omega|} \int_{\Omega} (\cdot) dV \quad (6.27)$$

material and numerical parameters used in simulations of BaTiO ₃					
parameter	value	units	parameter	value	units
a_0	10^{-10}	Vm ³ /C	μ	37	GPa
a_1	$-1.0355 \cdot 10^8$	Vm/C	λ	111	GPa
a_2	$-1.96947 \cdot 10^9$	Vm ⁵ /C ³	p_s	0.26	C/m ²
a_3	$3.93894 \cdot 10^9$	Vm ⁵ /C ³	$\bar{\kappa}$	$1.771 \cdot 10^{-8}$	F/m
a_4	$8.4489 \cdot 10^{10}$	Vm ⁹ /C ⁵	ϕ_0	0.3162277	V
a_5	$2.39433 \cdot 10^{14}$	Vm ¹³ /C ⁷	e_0	$3.84615 \cdot 10^6$	V/m
a_6	$2.38795 \cdot 10^9$	Vm ⁹ /C ⁵	η	$2.95858 \cdot 10^8$	kg m ³ / C ² s
b_1	$-2.11272 \cdot 10^{10}$	Vm/C	L_x	$8.222 \cdot 10^{-8}$	m
b_2	$2.73669 \cdot 10^9$	Vm/C	L_y	$8.222 \cdot 10^{-8}$	m
b_3	$-1.1932 \cdot 10^{10}$	Vm/C	L_z	$8.222 \cdot 10^{-8}$	m

Table 6.1: Material parameters for BaTiO₃, adopted from [Zhang and Bhattacharya \(2005a\)](#), as well as simulation parameters used in numerical examples.

material and numerical parameters used in simulations of tetragonal PZT					
parameter	value	units	parameter	value	units
a_0	$9.0 \cdot 10^{-11}$	Vm ³ /C	μ	123	GPa
a_1	$-1.6998 \cdot 10^9$	Vm/C	λ	115	GPa
a_2	$7.8 \cdot 10^8$	Vm ⁵ /C ³	p_s	0.58	C/m ²
a_3	$-1.95 \cdot 10^9$	Vm ⁵ /C ³	$\bar{\kappa}$	$8.8556 \cdot 10^{-9}$	F/m
a_4	$1.2702 \cdot 10^{10}$	Vm ⁹ /C ⁵	ϕ_0	0.178511	V
a_5	$1.9292 \cdot 10^{10}$	Vm ¹³ /C ⁷	e_0	$1.72414 \cdot 10^5$	V/m
a_6	$1.687 \cdot 10^{10}$	Vm ⁹ /C ⁵	η	$1.0 \cdot 10^{11}$	kg m ³ / C ² s
b_1	$-2.3386 \cdot 10^{10}$	Vm/C	L_x	$5.0 \cdot 10^{-8}$	m
b_2	$-3.1528 \cdot 10^9$	Vm/C	L_y	$5.0 \cdot 10^{-8}$	m
b_3	$-1.892 \cdot 10^{10}$	Vm/C	L_z	$5.0 \cdot 10^{-8}$	m

Table 6.2: Material parameters for PZT, adopted in modified form from [Völker et al. \(2011\)](#), as well as simulation parameters used in numerical examples.

denotes the volume average with $|\Omega|$ the volume of the RVE. Consider a parallel arrangement of surface electrodes, so that a unidirectional voltage differential is applied across the thickness h of a sample through surface electrodes, as in experiments ([Wojnar et al., 2014](#); [le Graverend et al., 2015](#)). By assuming a separation of scales between the macroscale (where the field \bar{e} is applied) and the polycrystalline grain scale, the uniform electric field

$$\bar{e} = (\phi^+ - \phi^-)/h \quad (6.28)$$

in the homogeneous macro-reference medium can indeed be identified as the RVE average $\langle e \rangle$.

Experiments measure total charges Q on the two opposite, parallel surface electrodes (with electrode surface area A , specimen volume $V = Ah$, and z being the unit vector pointing across

the specimen thickness). The measured electric displacement $d = Q/A$ is related to the volume average via

$$\begin{aligned} \frac{Q}{A}z &= \frac{Q}{V}hz = \frac{1}{V} \int_{\partial\Omega} q_s \mathbf{x} \, ds = \frac{1}{V} \int_{\Omega} \operatorname{div}(\mathbf{x} \otimes \mathbf{d}) \, dv \\ &= \frac{1}{V} \int_{\Omega} (\mathbf{x} \operatorname{div} \mathbf{d} + \mathbf{d}) \, dv = \frac{1}{V} \int_{\Omega} \mathbf{d} \, dv = \langle \mathbf{d} \rangle. \end{aligned} \quad (6.29)$$

Therefore, the RVE-averaged electric displacement is interpreted as the experimentally measurable quantity $\bar{\mathbf{d}} = \langle \mathbf{d} \rangle$. The average polarization can be related to the average electric displacements by averaging the constitutive relation, viz.

$$\langle p \rangle = \kappa_0 \langle e \rangle + \langle d \rangle, \quad (6.30)$$

which is used for a comparison between numerical simulations and experimental results in Section 6.5.

Finally, to mimic experiments using approximately free-standing samples, the examples will prescribe average stress-free conditions, i.e., enforcing $\langle \boldsymbol{\sigma} \rangle = \mathbf{0}$.

Spectral Solution Scheme

In order to numerically solve equations (6.24), the numerical strategy of Chapter 2 is used. Objectively, the linearity of Gauss' law encourages its solution in Fourier space. Applying the discrete inverse Fourier transform to electric and polarization fields transforms Gauss' law into

$$-ihk_j \hat{p}_j(\mathbf{k}) - h^2 |\mathbf{k}|^2 \kappa_0 \hat{\phi}(\mathbf{k}) = 0, \quad (6.31)$$

so that for all $\mathbf{k} \neq \mathbf{0}$, using $\mathbf{e} = -\nabla \phi$,

$$\hat{\phi}(\mathbf{k}) = -i \frac{k_j \hat{p}_j(\mathbf{k})}{h \kappa_0 |\mathbf{k}|^2} \quad \Rightarrow \quad \hat{e}_i(\mathbf{k}) = -ihk_i \hat{\phi}(\mathbf{k}) = \begin{cases} -\frac{k_j \hat{p}_j(\mathbf{k})}{\kappa_0 |\mathbf{k}|^2} k_i & \text{if } \mathbf{k} \neq \mathbf{0}, \\ \bar{e}_i & \text{if } \mathbf{k} = \mathbf{0}, \end{cases} \quad (6.32)$$

and the discrete inverse Fourier transform leads to $\phi(\mathbf{x})$ and $\mathbf{e}(\mathbf{x})$ in real space.

The second equation of (6.32) can be solved directly for the electric field \mathbf{e} without computing the electric potential ϕ , which increases computational efficiency. Since, however, the problem is formulated in terms of the electric potential, it is easy to verify that the form of (6.32)₂ ensures a curl-free electric field,

$$e_{i,l} = -ihk_l \hat{e}_i = ihk_l \frac{k_j \hat{p}_j(\mathbf{k})}{\kappa_0 |\mathbf{k}|^2} k_i \quad (6.33)$$

such that

$$(\operatorname{curl} \mathbf{e})_k = e_{i,l} \epsilon_{lik} = ih \frac{k_j \hat{p}_j(\mathbf{k})}{\kappa_0 |\mathbf{k}|^2} k_i k_l \epsilon_{lik} = 0 \quad (6.34)$$

with the Levi-Civita permutation symbol ϵ_{ijk} .

Analogously, the mechanical governing equation of linear momentum balance is transformed into Fourier space. Due to the spatial heterogeneity stemming from the non-linearity of the coupled mechanical problem in the general polycrystalline case, this requires an iterative solution strategy. Analogous to the finite-strain setting of Section 2.3, a perturbation stress tensor $\boldsymbol{\tau}(\mathbf{x})$ is introduced such that here

$$\sigma_{ij}(\mathbf{x}) = \tilde{\mathbb{C}}_{ijkl}^0 \epsilon_{kl}^e(\mathbf{x}) - \tau_{ij}(\mathbf{x}), \quad \epsilon_{kl}^e(\mathbf{x}) = \epsilon_{kl}(\mathbf{x}) - \epsilon_{kl}^r(\mathbf{x}), \quad (6.35)$$

where $\tilde{\mathbb{C}}^0$ is a reference effective elasticity tensor (e.g., the volume average $\tilde{\mathbb{C}}^0 = \langle \tilde{\mathbb{C}} \rangle$). As has been emphasized thus far, the particular choice of $\tilde{\mathbb{C}}^0$ does not affect the accuracy of the result but it does influence the convergence of the iterative solution scheme.

Transforming linear momentum balance into Fourier space gives

$$\tilde{\mathbb{C}}_{ijkl}^0 [hk_j k_l \hat{u}_k(\mathbf{k}) + ik_j \hat{\epsilon}_{kl}^r(\mathbf{k})] + ik_j \hat{\tau}_{ij}(\mathbf{k}) = 0, \quad (6.36)$$

$$\hat{u}_k(\mathbf{k}) = -\frac{i}{h} A_{ik}^{-1}(\mathbf{k}) \left[\hat{\tau}_{ij}(\mathbf{k}) + \tilde{\mathbb{C}}_{ijkl}^0 \hat{\epsilon}_{kl}^r(\mathbf{k}) \right] k_j \quad (6.37)$$

where $A_{ik}(\mathbf{k}) = \tilde{\mathbb{C}}_{ijkl}^0 k_j k_l$ are the components of the acoustic tensor (which is invertible for $\mathbf{k} \neq \mathbf{0}$ if \mathbb{C}^0 is positive-definite). Insertion of (6.37) into the strain–displacement relation, $\boldsymbol{\epsilon} = \text{sym}(\nabla \mathbf{u})$ or $\hat{\epsilon}_{ij}(\mathbf{k}) = -ih[\hat{u}_i(\mathbf{k})k_j + \hat{u}_j(\mathbf{k})k_i]/2$,

$$\hat{\epsilon}_{ij}(\mathbf{k}) = \begin{cases} -\frac{1}{2} \left[A_{ni}^{-1}(\mathbf{k}) k_m k_j + A_{nj}^{-1}(\mathbf{k}) k_m k_i \right] \left[\hat{\tau}_{nm}(\mathbf{k}) + \tilde{\mathbb{C}}_{nmkl}^0 \hat{\epsilon}_{kl}^r(\mathbf{k}) \right] & \text{if } \mathbf{k} \neq \mathbf{0}, \\ \langle \epsilon_{ij} \rangle & \text{if } \mathbf{k} = \mathbf{0}. \end{cases} \quad (6.38)$$

This equation has to be solved for $\hat{\boldsymbol{\epsilon}}$ iteratively since the perturbation stress $\hat{\boldsymbol{\tau}}$ depends on strains. Therefore, $\hat{\boldsymbol{\epsilon}}$ is computed from (6.38) and $\boldsymbol{\epsilon} = \mathcal{F}^{-1}(\hat{\boldsymbol{\epsilon}})$ is used in real space to update $\boldsymbol{\tau}(\mathbf{x})$ via (6.35). Next, the updated $\hat{\boldsymbol{\tau}} = \mathcal{F}(\boldsymbol{\tau})$ can be inserted into (6.38) for a complete iteration step. Although there is no guarantee for convergence, this fixed-point iteration scheme performs well from numerical experience. Note that $\langle \epsilon_{ij} \rangle$ is not known a-priori if average stresses are to be enforced.

For the special case of isotropy (i.e., $\mathbb{C}(\mathbf{x}) = \text{const}$) and vanishing higher-order coupling ($\mathbb{F} = \mathbf{0}$, $\mathbb{G} = \mathbf{0}$), the above problem reduces considerably and the mechanical constitutive law reduces to

$$\sigma_{ij}(\mathbf{x}) = \mathbb{C}_{ijkl} \epsilon_{kl}(\mathbf{x}) + \sigma_{ij}^r(\mathbf{x}) \quad (6.39)$$

$$\sigma_{ij}^r(\mathbf{x}) = \mathbb{B}_{ijkl}(\mathbf{x}) p_k(\mathbf{x}) p_l(\mathbf{x}). \quad (6.40)$$

Despite the spatial heterogeneity of $\boldsymbol{\sigma}^r(\mathbf{x})$, it is possible solve in Fourier space analytically for

$$\hat{u}_k = -\frac{i}{h} A_{ik}^{-1}(\mathbf{k}) \hat{\sigma}_{ij}^r(\mathbf{k}) k_j \quad (6.41)$$

and

$$\hat{\varepsilon}_{kl}(\mathbf{k}) = \begin{cases} -\frac{1}{2} [A_{ik}^{-1}(\mathbf{k})k_l + A_{il}^{-1}(\mathbf{k})k_k] \hat{\sigma}_{ij}^r(\mathbf{k})k_j, & \text{if } \mathbf{k} \neq \mathbf{0}, \\ \langle \varepsilon_{kl} \rangle & \text{if } \mathbf{k} = \mathbf{0}. \end{cases} \quad (6.42)$$

In this case, no iterative solution scheme is required.

Note that, although the above (iterative and direct) schemes determine $\boldsymbol{\varepsilon}$ without the necessity of computing \mathbf{u} explicitly, kinematic compatibility is guaranteed – analogous to the curl-free condition of the electric field. Here, compatibility requires $\text{curl}(\text{curl } \boldsymbol{\varepsilon}) = \mathbf{0}$ or $\varepsilon_{ikm}\varepsilon_{jln}\varepsilon_{klmn} = 0$. This is verified by inserting e.g. (6.38), which yields

$$\varepsilon_{ikm}\varepsilon_{jln}k_mk_n[A_{ok}^{-1}(\mathbf{k})k_l + A_{ol}^{-1}(\mathbf{k})k_k]\hat{\tau}_{op}(\mathbf{k})k_p = 0, \quad (6.43)$$

and both terms can be shown to vanish since

$$\begin{aligned} \varepsilon_{ikm}\varepsilon_{jln}k_mk_nk_lA_{ok}^{-1}(\mathbf{k})\hat{\tau}_{op}(\mathbf{k})k_p &= \varepsilon_{ikm}\varepsilon_{jnl}k_mk_lk_nA_{ok}^{-1}(\mathbf{k})\hat{\tau}_{op}(\mathbf{k})k_p \\ &= -\varepsilon_{ikm}\varepsilon_{jln}k_mk_nk_lA_{ok}^{-1}(\mathbf{k})\hat{\tau}_{op}(\mathbf{k})k_p. \end{aligned} \quad (6.44)$$

Ferroelectric Problem

The polarization field evolves in a dissipative fashion, following the kinetic law

$$\eta \dot{\mathbf{p}} = \mathbf{g}(\boldsymbol{\varepsilon}, \mathbf{e}, \mathbf{p}) + \mathbb{K}_{ijkl}p_{k,jl}, \quad (6.45)$$

where $\mathbf{g} = -\partial W/\partial \mathbf{p}$ is the thermodynamic driving force.

Employing a forward-Euler finite difference approximation in time to discretize the above kinetic law in an explicit manner,

$$\eta \frac{\mathbf{p}^{\alpha+1} - \mathbf{p}^\alpha}{\Delta t} = \mathbf{g}(\boldsymbol{\varepsilon}^{\alpha+1}, \mathbf{e}^{\alpha+1}, \mathbf{p}^\alpha) + \mathbb{K}_{ijkl}p_{k,jl}^\alpha, \quad (6.46)$$

where $\mathbf{p}^\alpha = \mathbf{p}(\mathbf{x}, t_\alpha)$ denotes the polarization field at time $t_\alpha = \alpha \Delta t$ with constant time increments $\Delta t = t_{\alpha+1} - t_\alpha$. A staggered solution scheme is used which solves the mechanical and electrical problems first, so $\boldsymbol{\varepsilon}^{\alpha+1}$ and $\mathbf{e}^{\alpha+1}$ are known when the above nonlinear equation is solved for the new polarization field $\mathbf{p}^{\alpha+1}$. This explicit solution strategy is, admittedly, numerically inefficient. In particular for linear kinetics, the linear semi-implicit scheme of [Chen and Shen \(1998\)](#) provides improved efficiency. However, the explicit scheme, despite numerical disadvantages, allows for a straight-forward implementation and for a simple extension to nonlinear kinetic laws.

Rather than applying the Fourier transform to (6.46), only the non-local driving force is computed in Fourier space, i.e.,

$$\mathbb{K}_{ijkl}p_{k,jl}^\alpha(\mathbf{x}) = \mathcal{F} \left(-h^2 \mathbb{K}_{ijkl}k_jk_l\hat{p}_k^\alpha \right). \quad (6.47)$$

The fixed-point iteration for $\mathbf{p}^{\alpha+1}$ is computed in real space. This entails the following two advantages. First, unlike for the linear Allen-Cahn equation, any nonlinear kinetic relation would result in a convolution on the left-hand side of (6.46) when applying the Fourier transform; even though $\mathbf{p}(\mathbf{x}, t_\alpha)$ is known, this adds significant complexity. Second, time stepping in Fourier space produces unpleasant numerical instabilities by allowing short-wavelength noise to amplify since updates are performed in \mathbf{k} -space. Finally, the new polarization is obtained from

$$p_i^{\alpha+1} = p_i^\alpha + \Delta t f_i^{-1} \left[g_m(\boldsymbol{\varepsilon}^{\alpha+1}, \mathbf{e}^{\alpha+1}, \mathbf{p}^\alpha) + \mathcal{F} \left(-h^2 \mathbb{K}_{mjkl} k_j k_l \hat{p}_k^\alpha \right) \right]. \quad (6.48)$$

Solution Strategy

The governing equations (6.24) are solved in a time-incremental staggered fashion to determine the unknown fields $\boldsymbol{\varepsilon}(\mathbf{x})$, $\mathbf{e}(\mathbf{x})$ and $\mathbf{p}(\mathbf{x})$ for known $\bar{\mathbf{e}}^{\alpha+1}$ at time $t_{\alpha+1}$. First, strains $\boldsymbol{\varepsilon}^{\alpha+1}$ are obtained from (6.41):

$$\{\boldsymbol{\varepsilon}^{\alpha+1}\} = \mathcal{F}^{-1} \left(\{\hat{\boldsymbol{\varepsilon}}^{\alpha+1}\} \right) \quad (6.49)$$

and

$$\hat{\varepsilon}_{kl}^{\alpha+1}(\mathbf{k}) = \begin{cases} -\frac{1}{2} [A_{ik}^{-1}(\mathbf{k})k_l + A_{il}^{-1}(\mathbf{k})k_k] \hat{\sigma}_{ij}^{r,\alpha}(\mathbf{k})k_j, & \text{if } \mathbf{k} \neq \mathbf{0}, \\ \bar{\varepsilon}_{ij}^{\alpha+1} & \text{if } \mathbf{k} = \mathbf{0}, \end{cases} \quad (6.50)$$

with all other fields held constant and $\sigma_{ij}^{r,\alpha}(\mathbf{x}) = \mathbb{B}_{ijkl}(\mathbf{x})p_k^\alpha(\mathbf{x})p_l^\alpha(\mathbf{x})$ in real space. Next, with all other fields held constant, the electric field is obtained explicitly from

$$\{\mathbf{e}^{\alpha+1}\} = \mathcal{F}^{-1} \left(\{\hat{\mathbf{e}}^{\alpha+1}\} \right) \quad \text{and} \quad \hat{e}_i^{\alpha+1}(\mathbf{k}) = \begin{cases} -\frac{k_j \hat{p}_j^\alpha(\mathbf{k})}{\kappa_0 |\mathbf{k}|^2} k_i & \text{if } \mathbf{k} \neq \mathbf{0}, \\ \bar{e}^{\alpha+1} & \text{if } \mathbf{k} = \mathbf{0}. \end{cases} \quad (6.51)$$

Finally, the polarization field is updated via

$$\{p_i^{\alpha+1}\} = \{p_i^\alpha\} + \Delta t f_i^{-1} \left[g_m(\{\boldsymbol{\varepsilon}^{\alpha+1}\}, \{\mathbf{e}^{\alpha+1}\}, \{p^\alpha\}) + \mathcal{F} \left(-h^2 \mathbb{K}_{mjkl} k_j k_l \{\hat{p}_k^\alpha\} \right) \right]. \quad (6.52)$$

Although (6.49) and (6.51) are solved exactly, the explicit nature of (6.52) as well as the staggered scheme require a sufficiently small time step Δt for numerical stability. This is also where spectral ringing artifacts become essential (to be discussed in Section 2.5) since the explicit time integration scheme leads to the propagation and escalation of small numerical errors.

To comply with experiments having stress-free boundary conditions, it is possible to determine $\bar{\boldsymbol{\varepsilon}}^{\alpha+1} = \langle \boldsymbol{\varepsilon}^{\alpha+1} \rangle$ from the condition $\langle \boldsymbol{\sigma}^{\alpha+1} \rangle = \mathbf{0}$. The average stress tensor components in the RVE are obtained from (6.18) as

$$\langle \sigma_{ij} \rangle = \langle \mathbb{C}_{ijkl} \varepsilon_{kl} \rangle + \langle \mathbb{B}_{ijkl} p_k p_l \rangle + \langle \mathbb{G}_{ijklmn} p_k p_l p_m p_n \rangle + 2 \langle \mathbb{F}_{ijklmn} \varepsilon_{kl} p_m p_n \rangle. \quad (6.53)$$

Using the above staggered solution algorithm, the polarization field is known and held fixed when computing the strain tensor. Since the polarization energies chosen here use $\mathbb{F}_{ijklmn} = 0$ (Zhang and Bhattacharya, 2005a; Völker et al., 2011), it is possible to solve (6.53) for

$$\bar{\varepsilon}_{ab}^{\alpha+1} = -\mathbb{C}_{abkl}^{-1} (\langle \mathbb{B}_{ijkl} P_k^\alpha P_l^\alpha \rangle + \langle \mathbb{G}_{ijklmn} P_k^\alpha P_l^\alpha P_m^\alpha P_n^\alpha \rangle), \quad (6.54)$$

where the assumption holds that the elastic constants are approximately isotropic (due to stress-free conditions, the influence of elasticity is relatively small in subsequent examples). Otherwise, as mentioned previously, an iterative solution scheme (or dual formulation) would be required to impose zero mean stresses.

As an alternative (expected to produce a lower bound), one could assume that the stresses vanish pointwise, i.e., $\boldsymbol{\varepsilon}(\mathbf{x}) = \boldsymbol{\varepsilon}^r(\mathbf{x})$. and thus

$$\begin{aligned} \bar{\varepsilon}_{ij} &= \frac{1}{|\Omega|} \int_{\Omega} \varepsilon_{ij}^r \, dV \\ &= -\frac{1}{|\Omega|} \int_{\Omega} (\mathbb{C}_{ijkl} + 2\mathbb{F}_{ijklmn} P_m P_n)^{-1} (\mathbb{B}_{klop} P_o P_p + \mathbb{G}_{klmnop} P_m P_n P_o P_p) \, dV, \end{aligned} \quad (6.55)$$

which can be computed in real space when the polarization field is known. However, this assumption is physically questionable as it removes all stress concentrations, e.g., near grain or domain boundaries. Finally, one could also keep the simulation volume fixed, i.e., suppress spontaneous straining, which has been applied to the simulation of ferroelectric switching (see e.g. Wang et al. (2004)), but results in a considerably stiffened material response.

6.5 Simulations of Domain Patterns Evolution and Experimental Validation

Microstructure Initialization

For subsequent simulations of ferroelectric switching, electric cycling is performed using a triangle-wave profile for the bias field at a quasistatic frequency of 0.04 Hz. Initial conditions are obtained by sample equilibration from a random polarization distribution in the absence of an applied average electric field. Complex domain patterns form which show the commonly observed 90° and 180°-domain walls as well as (anti-)vortices, see Fig. 6.2 for example results for BaTiO₃. While enforcing that average stresses vanish across the RVE, local stress concentrations appear near domain walls, especially shear stresses; the latter are thus ideal to visualize the network of domain walls (see Fig. 6.2(b)). This equilibration process is used to generate (approximately stable) initial polarization patterns. The resulting domain wall width is approximately 2.6 nm, in agreement with experimental observations (Zhang and Goddard, 2006). Note that this also dictates the required grid resolution (to ensure that the domain wall is represented by several grid points).

Analogous simulation results are shown in Fig. 6.3 for a BaTiO₃ polycrystal whose grain orientations are chosen randomly around a mean orientation aligned with the applied electric field

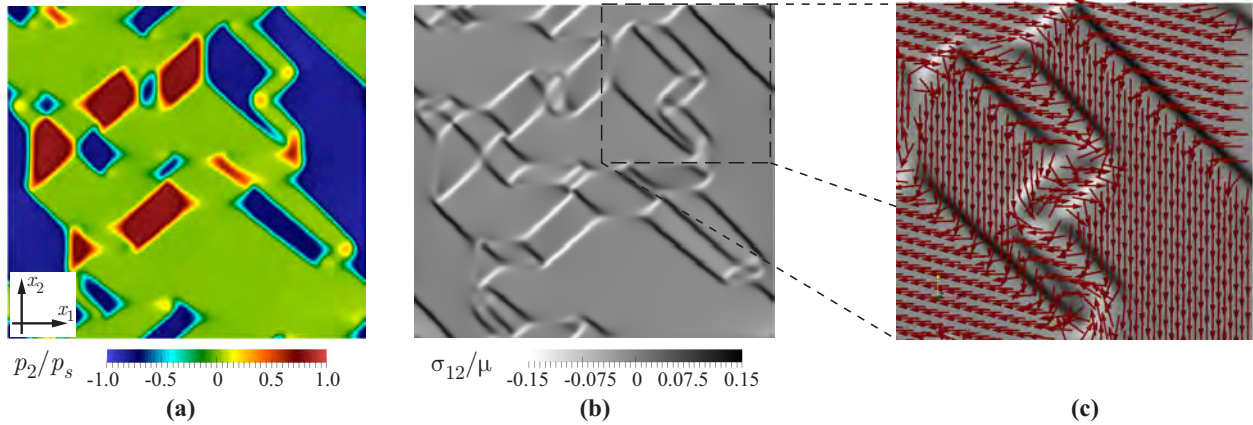


Figure 6.2: Domain formation in a 3D BaTiO₃ single-crystal with domain walls visualized by color-coding the shear stress σ_{12} (starting from initial random polarizations, the system is relaxed (Vidyasagar et al., 2017)).

$\bar{e} = e_2 e_2$ in the x_2 -direction. In the spectral formulation, a special treatment of grain boundaries is circumvented by simply assigning each grid point to a unique grain. The mismatch in elastic and electro-mechanical material parameters results in sharp contrasts across grain boundaries, which is where the Fourier correction of Section 2.5 becomes essential and convergence with h -refinement could not be guaranteed without.

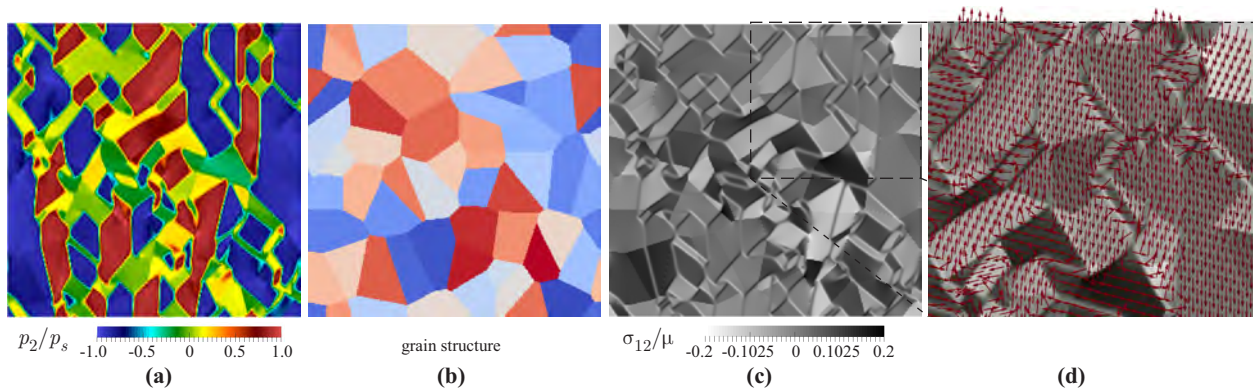


Figure 6.3: The formation of domain structures from an initially random polarization distribution in a BaTiO₃ polycrystal: (a) polarization component p_2 (normalized by the saturated polarization p_s), (b) grain distribution, (c) shear stresses, and (d) magnification of the shear stress distribution with polarizations highlighted by the vector field. (Vidyasagar et al., 2017)

Ferroelectric switching in Barium Titanate

With the above initialization protocol, ferroelectric switching is simulated in BaTiO₃ by applying a cyclic average bias field $\bar{e}(t) = e_2(t)e_2$ of triangular-wave type. It is important to note that grain orientations in real ferroelectric polycrystals often align with a pre-purposed polarization direction due to electric fields during fabrication. The effects of grain misorientation is demonstrated by computing the electric hysteresis (specifically, the average polarization in the x_2 -direction vs. applied electric field) as well as the butterfly curve (i.e., the evolution of the average RVE strain ε_{22} as a function of the applied electric field). Fig. 6.4 shows both curves for different levels of grain misorientation, where the orientations of 50 grains have been randomly selected with the specified maximum c -axis deviations from the poling direction. Simulations show that the chosen number (of 50 grains) is sufficient to ensure statistical representation, while maintaining sufficient resolution and grain area to encourage domain pattern formation. For simplicity and ease of visualization (and following prior work (Zhang and Bhattacharya, 2005a,b; Su and Landis, 2007b)) these results are for 2D crystals.

The single-crystal (aligned with the applied electric field) displays the widest hysteresis, i.e., the largest spontaneous polarization (viz., $|p_2| = p_s = 0.26 \text{ C/m}^2$) and the largest coercive field ($e_c = 0.011268e_0 = 0.433 \text{ kV/cm}$). With increasing misorientation, the average spontaneous polarization, the coercive field, and also the remnant strain decrease monotonously. The average polarization decreases since less and less grains align with the poling direction, whereas the coercive field decreases due to stronger contrasts at GBs acting as stress/electric field concentrations that promote the initiation of local switching (while also counteracting domain walls by pinning). The effect of misorientation and impedance to domain wall motion in case of highly-misoriented adjacent grains promotes lamellar domain patterns. Domain patterning is more pronounced with misorientations rising up to 90° (note that 90° implies random orientations without preference). Fig. 6.5 illustrates the polarization distribution across the RVE for different levels of misorientation; each plot shows the (normalized) polarization component p_2/p_s at a vanishing average applied field ($\bar{e}_2 = 0$) on the increasing-electric-field branch of the hysteresis. Higher misorientation results in a larger number of observable domains, owing to (i) high stress and electric field concentrations as nucleation sites and (ii) domain wall pinning at GBs. The average polarization behavior consequently changes with misorientation and, consequently, the average strains indicate a less steep profile at the point of switching, which agrees with butterfly curves seen in the literature (see, e.g., Burcsu et al. (2000)).

Ferroelectric Switching in Lead Zirconate Titanate

For polycrystalline PZT, the DFT-based potential energy of Völker et al. (2011) is adopted. The DFT-based potentials overpredict the coercive electric field (as can be expected from the

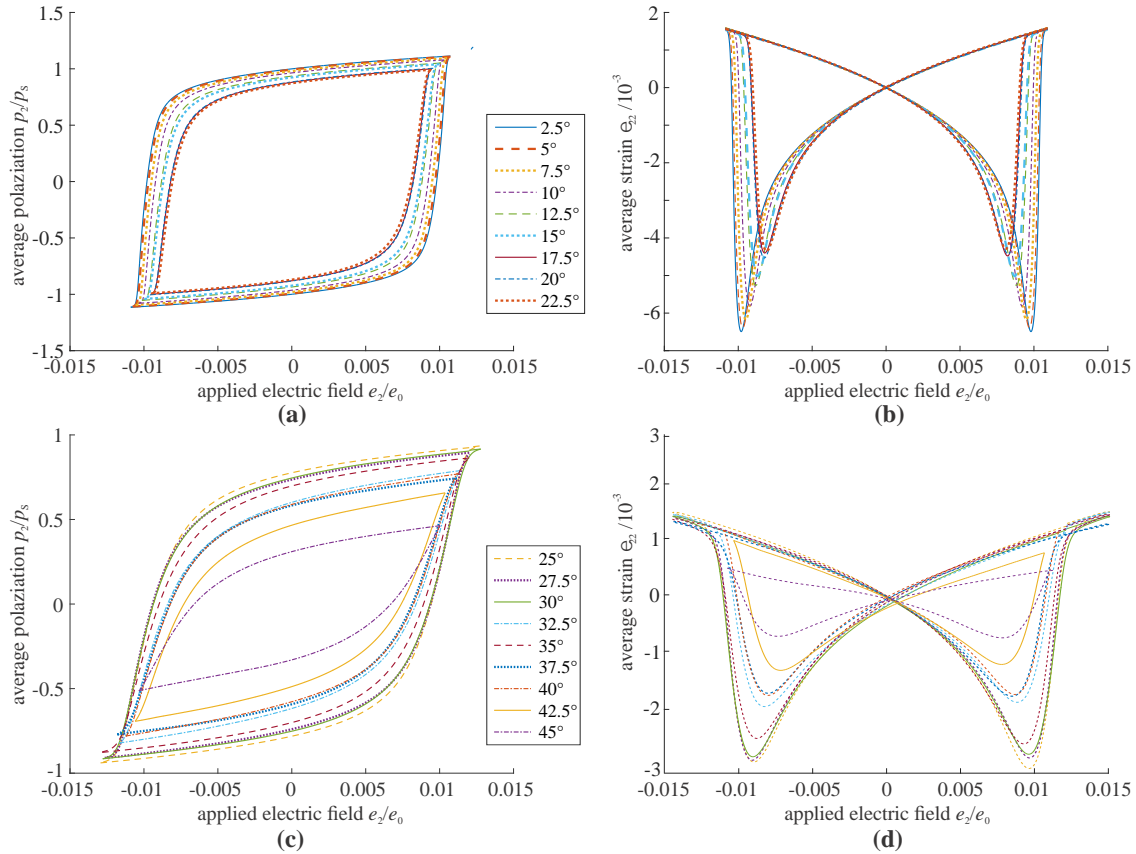


Figure 6.4: Electrical hysteresis and butterfly curve for BaTiO₃ polycrystals with increasing levels of grain misorientation for a total of 50 grains with random orientations deviating by the shown maximum degrees from the electric loading axis (50 grains were chosen ensure a sufficiently large representation while being able to capture domain patterns) (Vidyasagar et al., 2017).

absence of point defects as local nucleation sites), while the qualitative behavior is reasonable and the effective normalized hystereses show excellent agreement with our experimental data.

Fig. 6.6 illustrates the simulated microstructural evolution in a 3D PZT polycrystal during the electric hysteresis, as before starting from random initial polarizations. Note that the electric field in the hysteresis is normalized by the coercive field e_c^{DFT} obtained from the DFT potential. Also shown are the local distributions of the polarization as well as the von Mises stress (as an effective stress measure indicating stress concentrations and possible sites for damage initiation). The RVE contains 50 grains whose orientation is randomly assigned using a Gaussian profile with mean 0° and a standard deviation of 18.9° (the grain structure is schematically shown in Fig. 6.6). As seen for BaTiO₃, GBs serve as nucleation and pinning sites and influence the hysteresis behavior of the effective response.

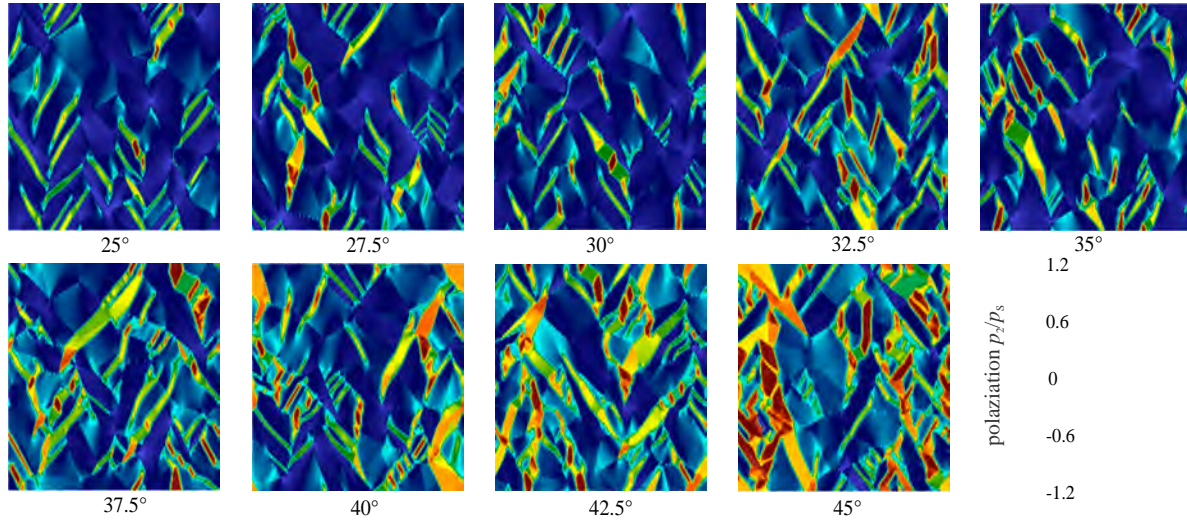


Figure 6.5: Illustration of laminate patterns arising in BaTiO_3 polycrystals of high crystal misorientation; shown is the (normalized) vertical polarization component p_2/p_s (50 grains with random orientation deviating by the shown maximum degrees from the electric loading axis) (Vidyasagar et al., 2017).

Comparison to Experiments

The 3D homogenized polarization and strain response are compared to experimental data obtained for polycrystalline lead zirconate titanate (PZT-5A from Piezo Systems Inc., USA). Polarization and strain hysteresis measurements were performed on cantilevered beam specimens using the setup of Fig. 6.7. Specimens had an average grain size of $2 \mu\text{m}$ and measured $38.1 \times 3.1 \times 1.0 \text{ mm}$, poled through-thickness, with vacuum-sputtered Ni electrodes. A triangular wave of amplitude $\pm 2.0 \text{ MVm}^{-1}$ was applied through-thickness at a frequency of 0.1 Hz using a high-voltage amplifier and waveform generator (10/10B-HS from Trek, USA; RM 3100/AFG 3022B from Tektronix, USA). Average electric displacements were measured using the circuit of Sawyer and Tower (1930) with a reference capacitor of $100 \mu\text{F}$ (le Graverend et al., 2015). In-plane strain measurements were taken using 3D digital image correlation (DIC) (using two IL4 high-speed cameras from Fastec Imaging Corporation, USA; processed using VIC-3D from Correlated Solutions, USA). All measurements were carried out at room temperature ($20 - 24^\circ\text{C}$).

Fig. 6.8 compares the simulated electric and strain hystereses to the experimentally measured data in a normalized fashion. The basis for the normalization of simulation results comes from the nature of the single-crystal electric enthalpy density, which intrinsically defines a characteristic coercive field (viz., the maximum peak of the derivative of the non-convex Landau potential) and a characteristic switching polarization (viz., the polarization which minimizes the Landau potential). Further, through the coupling coefficients the enthalpy density also defines the critical strain compo-

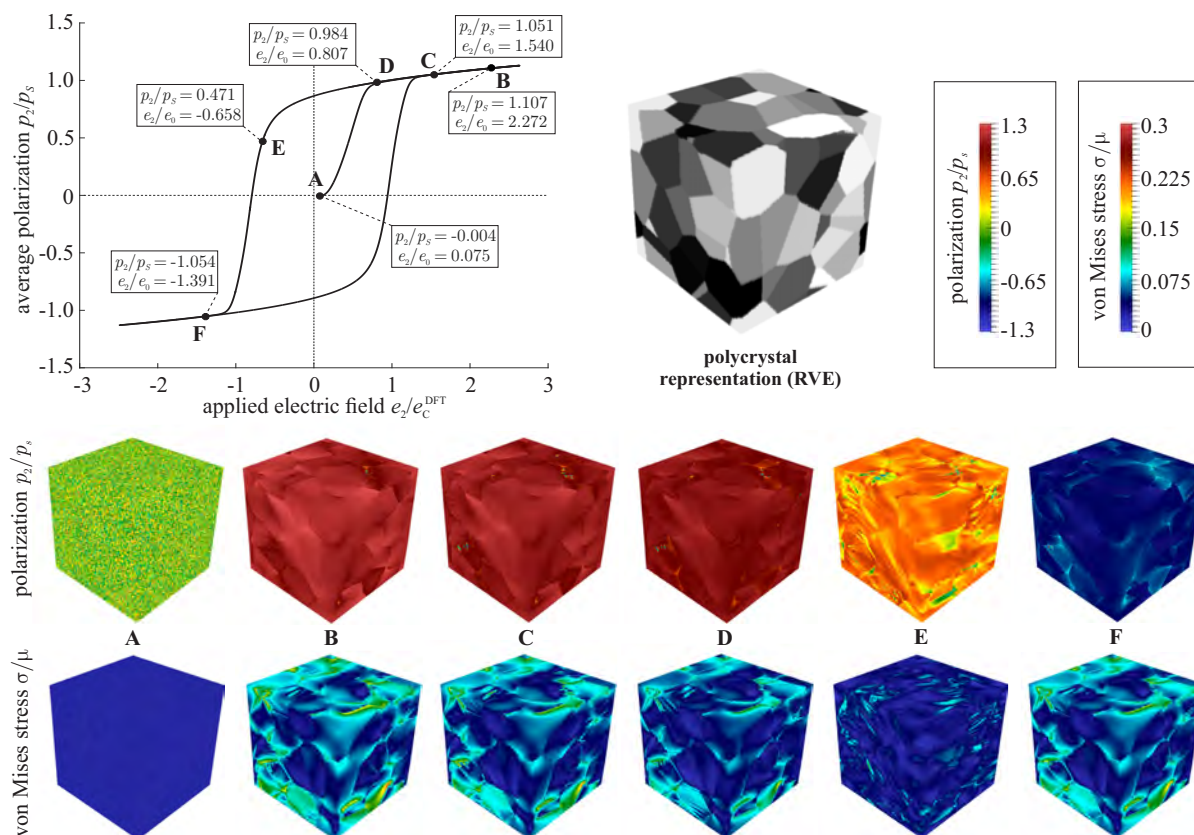


Figure 6.6: Local distribution of (normalized) polarization and von Mises stress in an RVE of polycrystalline PZT throughout the electric hysteresis (Vidyasagar et al., 2017).

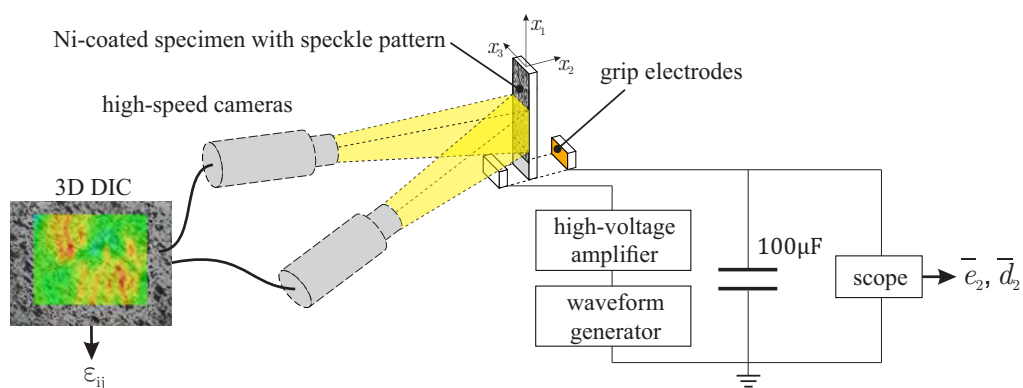


Figure 6.7: Sketch of the experimental setup used to measure the average electric displacement and the (surface) strain hystereses in polycrystalline PZT samples (Vidyasagar et al., 2017).

nents at switching. Linearly renormalizing the energetic potential using these intrinsic properties to account for a polycrystal is tantamount to energetic superposition in the absence of complex

domain patterns; this is demonstrated by Figure 6.4 where – at sufficiently low misorientation (approximately below 20°) – there is a degree of renormalized self similarity (viz., rescaling the coercive electric field and switching polarization yields qualitatively similar results). Accordingly, the simulated response is normalized with respect to $e_c^{\text{DFT}} = 5.025 \cdot 10^8$ V/m, whereas the experiments are normalized by $e_c^{\text{exp}} = 1.6 \cdot 10^6$ V/m, in order to enable a fair comparison. Similarly, the mechanical strain is normalized using critical strain $\varepsilon_{\text{crit}} = Qp_s^2$, where

$$Q^{\text{DFT}} = \frac{(b_1 - b_2)\lambda - 2b_2\mu}{12\mu(\lambda + \frac{2}{3}\mu)} \quad (6.56)$$

is obtained from the energetic coefficients (see 4.3), which results in $Q^{\text{DFT}} = -5.335 \cdot 10^{-3} \text{ C}^{-2}\text{m}^4$ and $p_s^{\text{DFT}} = 0.58 \text{ Cm}^{-2}$. Best agreement with simulations is achieved for $Q^{\text{exp}} = -7.00 \cdot 10^{-3} \text{ C}^{-2}\text{m}^4$ and $p_s^{\text{exp}} = 0.31 \text{ Cm}^{-2}$, whose results are shown in Fig. 6.8. The DFT-based potential energy, as expected, significantly overpredicts the coercive field and the coupled critical strain, so that the un-normalized data show a considerably broader hysteresis. However, the normalization leads to the periodically homogenized, randomly generated polycrystal response and experiments displaying a convincingly similar behavior; this hints at the possibility of rescaling the electric and coupling enthalpy densities to quantitatively match experiments.

There are several key assumptions that may explain the strong differences in absolute values observed in simulations and experiments – despite the observed excellent agreement of the rescaled data in Fig. 6.8. In simulations, an ideal, average-stress-free RVE is assumed. Additionally, as customary in phase field modeling, the polarization kinetics are described by an Allen-Cahn type gradient-flow law, which may not adequately describe the complex kinetics behind the switching process. In experiments, surface stresses are assumed representative of the bulk response, and boundary conditions, microstructure and texture in simulations only capture effective, average features of experimental samples. Also, computations assume tetragonal variants, whereas experimentally-tested PZT shows both tetragonal and rhombohedral phases. More importantly, the DFT-based potential was derived for zero-temperature conditions, which is expected to slow down microstructural kinetics considerably (the strong difference is still remarkable). The significant difference between e_c^{exp} and e_c^{DFT} is still remarkable, especially when considering the abundance of defects in simulations (in the form of GBs).

6.6 Conclusions

The work in this chapter has shown how the electromechanical responses of tetragonal perovskite ferroelectric ceramics, such as barium titanate and lead zirconate titanate, are governed by the micromechanics of electrical domain formation and motion in bulk polycrystals. The energetics of ferroelectric ceramics at the polycrystalline mesoscale is shown to favor domain formation

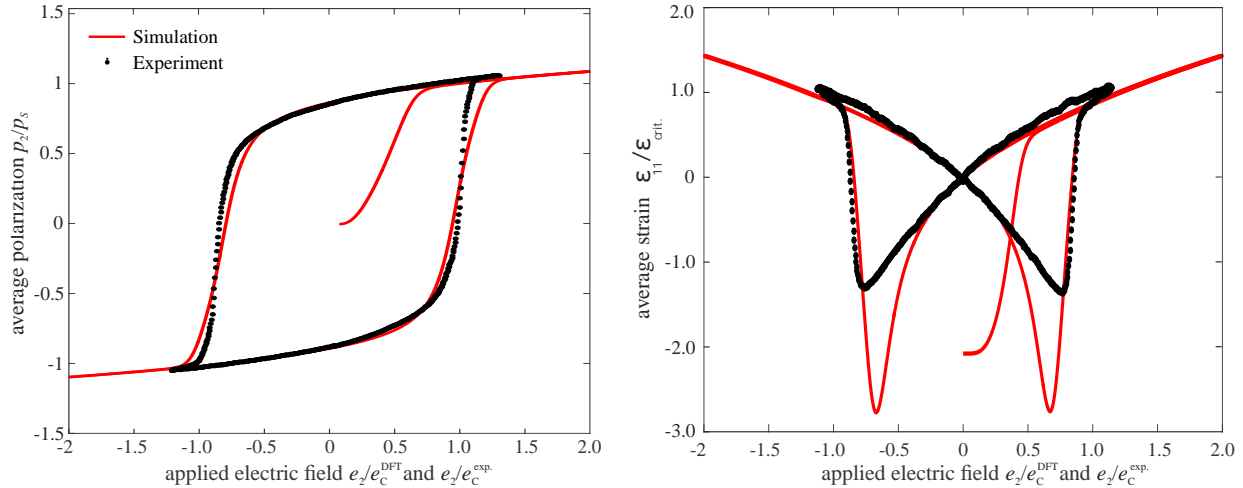


Figure 6.8: Comparison between simulated and experimental hysteretic (simulations used the same periodic polycrystal with 50 grains with Gaussian orientation distribution with mean 0° and standard deviation 20.42°). Note that for both curves simulated and experimental data were normalized with respect to their own values of e_c , p_s , and ϵ_{crit} , as explained in Section 6.5 (Vidyasagar et al., 2017).

from initial random polarization, while the application of bias electric fields leads to the typical hysteretic behavior. Grain size and texture are shown to influence domain patterns and the electrical hysteresis, and the micromechanical stress distribution during an electrical cycling process indicates strong stress concentrations at grain junctions. All examples deliberately target bulk polycrystals rather than thin films. For validation, the simulated response has been compared to in-house experimental results (viz., electrical hysteresis and butterfly curves) of PZT polycrystals. Although the DFT-based electric enthalpy – as may be expected – results in a simulated coercive field that is significantly too high, a renormalization of results (considering the nature of the electric-field-dependent non-convex enthalpy density) results in agreement of experiments and simulations. Overall, this work shows promise for bridging the scales from zero-temperature DFT calculations at the quantum scale to predicting macroscale response of ferroelectrics.

CONCLUSIONS

7.1 Summary

As explained in Chapter 1, patterns and microstructures share underlying causal principles; in particular, they manifest in systems with non-(quasi)convex energy landscapes. These systems are also associated with instabilities and the equations driving their evolution are ill-posed with non-smooth and non-unique solutions. While a large class of problems in physics share this character – arguably the primary mechanism for nature to form order out of chaotic initial conditions – these have been relatively unexplored from a numerical perspective until recent years. This work has provided insight in this regard, and a path to solving non-(quasi)convex energy minimization problems and predicting pattern formation autonomously.

The stabilized spectral homogenization methodology outlined in this thesis is robust at tackling this class of problems. In Chapter 2, three algorithms have been presented for homogenization in finite-strains, building upon existing FFT-based spectral techniques enhanced by high-order finite-difference compositions. A discussion of how implicit regularization for non-convex problems is introduced through these compositions has been included.

Benchmark problems, where numerical approximations to quasi-convex envelopes demonstrate the efficiency and accuracy of the numerical method, have been solved in Chapter 3. Demonstrating unphysical pattern formation for the commonly used St. Venant-Kirchoff energy model, difficulties faced by the solver in approximating the quasiconvex hull with increasing asymmetry in energy, primarily owing to higher interface energy, have been discussed. Subsequently, a novel finite-strain phase transformation model has been presented, producing needle-like and higher-order laminate patterns. Three-well problems have also been solved, hinting that the mechanisms of autonomous pattern formation might lead to energies below local minima in multi-stable landscapes. The subsequent example of finite-strain single-slip plasticity has predicted laminate patterns which have been compared to analytical lamination theory. Additionally, by studying bi-crystals of varying misorientation, the influence of compatibility constraints, through grain boundaries, on pattern formation has been demonstrated.

As a further extension of this discussion, in Chapter 4, multiple slip systems, twinning, and dissipative kinetics have been introduced to the model – capturing slip-twinning interactions in magnesium polycrystals. Dissipation has been shown to influence pattern formation within and across grains. Homogenization of RVEs with multiple realizations has been used to derive envelopes

of responses depending on grain size misorientation and texture. Through these simulations, it has been demonstrated that the effective material response obtained through homogenization of high-resolution RVEs with a large number of grains can be approximated well by averaging through multiple realizations of RVEs with lower mesoscale simulation and fewer grains. The key novelties here are the unprecedented high-fidelity models that account for intricate slip-twinning interactions, the numerical methods capable of handling non-(quasi)convex energetic loading paths, and the understanding they bring regarding the homogenized inelastic response and micro-mechanical stress patterns in magnesium polycrystals.

Chapter 5 discussed a very different non-convex problem – anisotropic spinodal decomposition, modeled using a conservative phase field model with gradient-flow kinetics. It has been shown that the kinetics of this process, as well as tunable anisotropic parameters, have a strong influence on the patterns that form. In addition to the insight that has been gained into naturally occurring anisotropic phase separation, as discussed at the end of this chapter, producing bi-continuous networks has implications on the design of scalable metamaterials. Preliminary experimental and theoretical results show that the smooth topology of resulting metamaterials reduces stress concentrations and hence exceptional toughness and strength are achieved relative to traditional truss- and plate-based architected metamaterials.

In Chapter 6, the kinetics of phase transitions in ferroelectrics have been studied using a non-conservative phase-field model. As a novelty, numerical homogenization of high-resolution polycrystalline RVEs has produced strain and polarization hysteresis curves which, when renormalized, have shown convincing qualitative agreement with in-house experiments. Polycrystalline simulations have predicted striped domain pattern formation within grains, again reproducing in-house experiments. This approach has demonstrated promise in predicting the electromechanical response in realistic polycrystalline ferroelectrics. Additionally, these models have been shown to bridge the gap between numerical results obtained using first-principles-informed material models and experiments. Overall, as compared to previous approaches, the spectral homogenization techniques presented have expanded the range of time-scales and numerical fidelity for modeling the domain pattern formation process and electromechanical coupling.

7.2 Outlook & Future Directions

This thesis has presented a number of original contributions; however, a series of unanswered questions still remain, pointing towards potential research directions.

The numerical methods presented in Chapter 2 leave room for improvement in several aspects. The Richardson (fixed-point iteration) scheme does not have guaranteed convergence, and even the Newton-Raphson techniques outlined in Sec. 2.3 require fixed-point iterations to compute the

increments (Kabel et al., 2014). Developing or adopting convergent, contrast-independent schemes, such as outlined by Zeman et al. (2017) could be beneficial for solving non-convex minimization problems – albeit at increased computational cost. Additionally, several scientific libraries such as TAO (Munson et al., 2015) have implemented advanced numerical optimization procedures and line search algorithms, which could be incorporated into the present approach.

In the discussion of crystal plasticity, moving beyond pure magnesium to understand alloying through inclusions and multi-phase mixtures would be of physical relevance (Lun Sin et al., 2013). As opposed to using polycrystals with predetermined grain distributions, solving the non-convex problem of dynamic recrystallization could add a greater level of fidelity to the simulations. Additionally, non-constant hardening laws and improved flow rules would better reproduce the kinetics of deformation patterns, such as propagation of twin boundaries, which are observed in experiments (Kannan et al., 2018). Deriving the constants used in the phenomenological model using lower scale approaches (Sun et al., 2018) instead of fitting to arbitrary experiments would also be ideal. Additionally, understanding how the slip pattern formation process is influenced through non-monotonic loading paths due to cross-hardening and dissipation merits numerical investigation. Finally, incorporating and modeling inertial effects and wave propagation in polycrystalline RVEs would yield deeper insight into mechanical response during high-rate loading for magnesium and other hcp metals.

In terms of anisotropic spinodal decomposition, experimental validation of the energy landscapes and kinetic laws, particularly for crystal growth, polymer blend demixing and dealloying, would be beneficial. The addition of thermal transport, elasticity, and flow through the solution of auxiliary governing equations would give deeper insight of into influencing natural patterns to achieve desired properties. These numerical methods provide smooth architectures at the micro- and nano-scale scale which compete with current lattice-based metamaterials, and a performance comparison would be of interest. Utilizing natural anisotropic phase separation to create architected materials would revolutionize metamaterial fabrication by introducing scalability and tunability.

In the study of ferroelectrics, developing and validating improved kinetic laws would allow for a better match between experimentally observed domain wall velocity scaling and numerical results. Stochastic temperature-based approaches would improve the model calibrated with first-principles-informed constants since the DFT calculations have been performed at 0 K and gaussian noise would introduce an effective *thermalization*. Furthermore, modeling fatigue in ferroelectrics, by including failure and void growth, together with surface charge collection, would be of great interest since many applications involve cyclic loading over large time scales (Wojnar et al., 2014). In reality, commercially available ferroelectric samples consist of multiple phases and including these into the modeling strategies could be fruitful. Additionally, composites with ferroelectric

inclusions have shown extreme dynamic stiffness behavior ([Jaglinski et al., 2007](#)), and numerical predictions of the electromechanical response of such composites using presented methods would guide future experiments.

Overall, the methods of spectral homogenization presented are fast and accurate at predicting effective microscale response of a multitude of systems exhibiting instabilities. This would be crucial in the framework of multi-scale models; recent efforts on this front include FE-FFT coupling for polycrystal plasticity ([Kochmann et al., 2016](#)). Additionally, using fast spectral homogenization strategies to produce envelopes of homogenized responses for ensembles with different micromechanical geometries result in large data output. Dimension reduction and big data analysis performed on these results, using machine learning tools, could yield valuable insight into the underlying physics of various phenomena. This would also support recent efforts at data-driven computational models in mechanics ([Kirchdoerfer and Ortiz, 2016](#)).

As concluding remarks, the methods and findings presented in this thesis on predicting autonomous pattern formation and solving non-convex problems have broad applications in other fields of science. They serve to guide both analytical theory development and explain experimental observations. From an engineering perspective, being able to predict phenomena associated with non-(quasi)convex energy landscapes paves the way forward for designing novel tunable metamaterials which take advantage of these phenomena.

BIBLIOGRAPHY

- Abeyaratne, R., Chu, C., James, R. D., 1996. Kinetics of materials with wiggly energies: Theory and application to the evolution of twinning microstructures in a cu-al-ni shape memory alloy. *Philosophical Magazine A* 73 (2), 457–497.
URL <https://doi.org/10.1080/01418619608244394>
- Agnew, S. R., Duygulu, Ö., 2005. Plastic anisotropy and the role of non-basal slip in magnesium alloy AZ31B. *International Journal of Plasticity* 21 (6), 1161–1193.
- Ahzi, S., Asaro, R. J., Parks, D. M., 1993. Application of crystal plasticity theory for mechanically processed {BSCCO} superconductors. *Mechanics of Materials* 15 (3), 201 – 222.
URL <http://www.sciencedirect.com/science/article/pii/016766369390018M>
- Albin, N., Conti, S., Dolzmann, G., 2009. Infinite-order laminates in a model in crystal plasticity. *Proceedings of the Royal Society of Edinburgh Section A: Mathematics* 139 (4), 685–708.
- Allaire, G., Francfort, G., 1998. Existence of minimizers for non-quasiconvex functionals arising in optimal design. *Annales de l'Institut Henri Poincaré (C) Non Linear Analysis* 15 (3), 301 – 339.
URL <http://www.sciencedirect.com/science/article/pii/S0294144998801200>
- Allen, S. M., Cahn, J. W., 1979. A microscopic theory for antiphase boundary motion and its application to antiphase domain coarsening. *Acta Metallurgica* 27 (6), 1085–1095.
- Anguige, K., Dondl, P. W., 2014. Relaxation of the single-slip condition in strain-gradient plasticity. *Proceedings of the Royal Society of London A: Mathematical, Physical and Engineering Sciences* 470 (2169).
URL <http://rspa.royalsocietypublishing.org/content/470/2169/20140098>
- Arlt, G., Dederichs, H., 1980. Complex elastic, dielectric and piezoelectric constants by domain wall damping in ferroelectric ceramics. *Ferroelectrics* 29 (1), 47–50.
URL <http://www.tandfonline.com/doi/abs/10.1080/00150198008009006>
- Arockiarajan, A., Menzel, A., Delibas, B., Seemann, W., 2006. Computational modeling of rate-dependent domain switching in piezoelectric materials. *European Journal of Mechanics - A/Solids* 25 (6), 950–964.
URL <http://www.sciencedirect.com/science/article/pii/S0997753806000076>
- Aubry, S., Fago, M., Ortiz, M., 2003. A constrained sequential-lamination algorithm for the simulation of sub-grid microstructure in martensitic materials. *Computer Methods in Applied Mechanics and Engineering* 192 (26), 2823 – 2843.
URL <http://www.sciencedirect.com/science/article/pii/S0045782503002603>
- Badalassi, V., Ceniceros, H., Banerjee, S., 2003. Computation of multiphase systems with phase field models. *Journal of Computational Physics* 190 (2), 371–397.

- Ball, J. M., 1976. Convexity conditions and existence theorems in nonlinear elasticity. *Archive for Rational Mechanics and Analysis* 63, 337–403, 10.1007/BF00279992.
URL <http://dx.doi.org/10.1007/BF00279992>
- Ball, J. M., 1977. Convexity Conditions and Existence Theorems in Nonlinear Elasticity. *Archive of Rational Mechanics and Analysis* 63, 337–403.
- Ball, J. M., James, R. D., 1987. Fine phase mixtures as minimizers of energy. *Archive for Rational Mechanics and Analysis* 100 (1), 13–52.
- Ball, J. M., Murat, F., 1984. $W^{1,p}$ -quasiconvexity and variational problems for multiple integrals. *Journal of Functional Analysis* 58 (3), 225 – 253.
URL <http://www.sciencedirect.com/science/article/pii/0022123684900417>
- Bartels, S., Carstensen, C., Conti, S., Hackl, K., Hoppe, U., Orlando, A., 2006. *Relaxation and the Computation of Effective Energies and Microstructures in Solid Mechanics*. Springer Berlin Heidelberg, Berlin, Heidelberg, pp. 197–224.
URL https://doi.org/10.1007/3-540-35657-6_8
- Bartels, S., Carstensen, C., Hackl, K., Hoppe, U., 2004. Effective relaxation for microstructure simulations: Algorithms and applications. *Computer Methods in Applied Mechanics and Engineering* 193 (48-51), 5143–5175.
- Bartels, S., Prohl, A., 2004. Multiscale resolution in the computation of crystalline microstructure. *Numerische Mathematik* 96 (4), 641–660.
- Bassiouny, E., Ghaleb, A. F., Maugin, G. A., 1988. Thermodynamical formulation for coupled electromechanical hysteresis effects - II. Poling of ceramics. *International Journal of Engineering Science* 26 (12), 1297–1306.
URL <http://www.sciencedirect.com/science/article/pii/0020722588900481>
- Bates, P. W., Fife, P. C., 1990. Spectral comparison principles for the cahn-hilliard and phase-field equations, and time scales for coarsening. *Physica D: Nonlinear Phenomena* 43 (2-3), 335–348.
- Bauer, J., Meza, L. R., Schaedler, T. A., Schwaiger, R., Zheng, X., Valdevit, L., 2017. Nanolattices: An Emerging Class of Mechanical Metamaterials. *Advanced Materials* 29 (40), 1–26.
- Becker, R., Lloyd, J. T., 2016. A reduced-order crystal model for HCP metals: Application to Mg. *Mechanics of Materials* 98, 98–110.
- Berbenni, S., Taupin, V., Djaka, K. S., Fressengeas, C., 2014. A numerical spectral approach for solving elasto-static field dislocation and g-disclination mechanics. *International Journal of Solids and Structures* 51 (23-24), 4157–4175.
- Bergamaschini, R., Salvalaglio, M., Backofen, R., Voigt, A., Montalenti, F., 2016. Continuum modelling of semiconductor heteroepitaxy: an applied perspective. *Advances in Physics: X* 1 (3), 331–367.
URL <https://www.tandfonline.com/doi/full/10.1080/23746149.2016.1181986>

- Berger, J. B., Wadley, H. N., McMeeking, R. M., 2017. Mechanical metamaterials at the theoretical limit of isotropic elastic stiffness. *Nature* 543 (7646), 533–537.
URL <http://dx.doi.org/10.1038/nature21075>
- Bhattacharya, K., 2003. *Microstructure of Martensite*. Oxford University Press, Oxford, UK.
URL <https://global.oup.com/academic/product/microstructure-of-martensite-9780198509349?cc=ch&lang=en&>
- Bhattacharya, K., Friesecke, G., James, R. D., 1999. The mathematics of microstructure and the design of new materials. *Proceedings of the National Academy of Sciences* 96 (15), 8332–8333.
URL <http://www.pnas.org/content/96/15/8332.short>
- Bhattacharya, K., James, R. D., 2005. The material is the machine. *Science* 307 (5706), 53–54.
- Bhattacharya, K., Ravichandran, G., 2003. Ferroelectric perovskites for electromechanical actuation. *Acta Materialia* 51 (19), 5941 – 5960, the Golden Jubilee Issue. *Selected topics in Materials Science and Engineering: Past, Present and Future*.
URL <http://www.sciencedirect.com/science/article/pii/S1359645403004671>
- Bhattacharya, K., Suquet, P., 2005. A model problem concerning recoverable strains of shape-memory polycrystals. *Proceedings of the Royal Society of London A: Mathematical, Physical and Engineering Sciences* 461 (2061), 2797–2816.
URL <http://rspa.royalsocietypublishing.org/content/461/2061/2797>
- Biener, J., Hodge, A. M., Hamza, A. V., 2005. Microscopic failure behavior of nanoporous gold. *Applied Physics Letters* 87 (12), 121908.
- Bluestein, L., 1970. A linear filtering approach to the computation of discrete fourier transform. *IEEE Transactions on Audio and Electroacoustics* 18 (4), 451–455.
- Böhlke, T., Brüggemann, C., 2001. Graphical Representation of the Generalized Hooke's Law. *Technische Mechanik* 21 (2), 145–158.
- Brenner, R., 2009. Numerical computation of the response of piezoelectric composites using Fourier transform. *Physical Review B* 79 (March), 184106.
- Brisard, S., 2017. Reconstructing displacements from the solution to the periodic lippmann–schwinger equation discretized on a uniform grid. *International Journal for Numerical Methods in Engineering* 109 (4), 459–486.
- Brisard, S., Dormieux, L., 2010. FFT-based methods for the mechanics of composites: A general variational framework. *Computational Materials Science* 49 (3), 663–671.
- Brisard, S., Legoll, F., 2014. Periodic homogenization using the lippmann–schwinger formalism. *arXiv preprint arXiv:1411.0330*.
- Bruder, F., Brenn, R., Jul 1992. Spinodal decomposition in thin films of a polymer blend. *Phys. Rev. Lett.* 69, 624–627.
URL <https://link.aps.org/doi/10.1103/PhysRevLett.69.624>

- Burcsu, E., Ravichandran, G., Bhattacharya, K., 2000. Large strain electrostrictive actuation in barium titanate. *Applied Physics Letters* 77 (11), 1698.
URL <http://scitation.aip.org/content/aip/journal/apl/77/11/10.1063/1.1308533>
- Cahn, J. W., Hilliard, J. E., 1958. Free energy of a nonuniform system. i. interfacial free energy. *The Journal of Chemical Physics* 28 (2), 258–267.
URL <https://doi.org/10.1063/1.1744102>
- Carstensen, C., 2005. Ten remarks on nonconvex minimisation for phase transition simulations. *Computer Methods in Applied Mechanics and Engineering* 194 (2-5 SPEC. ISS.), 169–193.
- Carstensen, C., Hackl, K., Mielke, A., 2002. Non-convex potentials and microstructures in finite-strain plasticity. *Proceedings of the Royal Society of London A: Mathematical, Physical and Engineering Sciences* 458 (2018), 299–317.
URL <http://rspa.royalsocietypublishing.org/content/458/2018/299>
- Carstensen, C., Plecháč, P., 1997. Numerical solution of the scalar double-well problem allowing microstructure. *Mathematics of Computation* 66 (219), 997–1026.
URL <http://www.ams.org/mcom/1997-66-219/S0025-5718-97-00849-1/>
- Chang, Y., Kochmann, D. M., 2015. A variational constitutive model for slip-twinning interactions in hcp metals : Application to single- and polycrystalline magnesium. *International Journal of Plasticity*, 1–23.
URL <http://dx.doi.org/10.1016/j.ijplas.2015.03.008>
- Chang, Y., Lloyd, J. T., Becker, R., Kochmann, D. M., 2017. Modeling microstructure evolution in magnesium: Comparison of detailed and reduced-order kinematic models. *Mechanics of Materials* 108, 40–57.
URL <http://dx.doi.org/10.1016/j.mechmat.2017.02.007>
- Chaplya, P. M., Carman, G. P., 2001. Dielectric and piezoelectric response of lead zirconate–lead titanate at high electric and mechanical loads in terms of non-180° domain wall motion. *Journal Applied Physics* 90 (10), 5278–5286.
URL <http://link.aip.org/link/JAPIAU/v90/i10/p5278/s1&Agg=doi>
- Chaplya, P. M., Carman, G. P., 2002a. Compression of piezoelectric ceramic at constant electric field: Energy absorption through non-180° domain-wall motion. *Journal Applied Physics* 92 (3), 1504.
URL <http://link.aip.org/link/JAPIAU/v92/i3/p1504/s1&Agg=doi>
- Chaplya, P. M., Carman, G. P., 2002b. Compression of piezoelectric ceramic at constant electric field: Energy absorption through non-180° domain-wall motion. *Journal of Applied Physics* 92 (3), 1504–1510.
URL <http://dx.doi.org/10.1063/1.1489498>
- Chen, L., Shen, J., 1998. Applications of semi-implicit fourier-spectral method to phase field equations. *Computer Physics Communications* 108 (2–3), 147 – 158.
URL <http://www.sciencedirect.com/science/article/pii/S001046559700115X>

- Chen, L.-Q., 2002. Phase-field models for microstructure evolution. *Annual review of materials research* 32 (1), 113–140.
- Chen, L. Q., 2008. Phase-field method of phase transitions/domain structures in ferroelectric thin films: A review. *Journal of the American Ceramic Society* 91 (6), 1835–1844.
- Cheng, J., Ghosh, S., 2017. Crystal plasticity finite element modeling of discrete twin evolution in polycrystalline magnesium. *Journal of Mechanics and Physics of Solids* 99 (July 2016), 512–538.
- Chipot, M., Kinderlehrer, D., Sep 1988. Equilibrium configurations of crystals. *Archive for Rational Mechanics and Analysis* 103 (3), 237–277.
URL <https://doi.org/10.1007/BF00251759>
- Choudhury, S., Li, Y. L., Krill, C., Chen, L. Q., 2007. Effect of grain orientation and grain size on ferroelectric domain switching and evolution: Phase field simulations. *Acta Materialia* 55 (4), 1415–1426.
- Choudhury, S., Li, Y. L., Krill, C. E., Chen, L. Q., 2005. Phase-field simulation of polarization switching and domain evolution in ferroelectric polycrystals. *Acta Materialia* 53 (20), 5313–5321.
- Christian, J. W., Mahajan, S., 1995. Deformation twinning. *Progress in Materials Science* 39 (1-2), 1–157.
- Chu, C., James, R. D., 1995. Analysis of microstructures in Cu-14.0%A1-3.9%Ni by energy minimization. *Journal de Physique IV, Colloque C8* 5, 143.
- Chu, P., Chen, D. P., Wang, Y. L., Xie, Y. L., Yan, Z. B., Wan, J. G., Liu, J.-M., Li, J. Y., 2014. Kinetics of 90° domain wall motions and high frequency mesoscopic dielectric response in strained ferroelectrics: a phase-field simulation. *Scientific reports* 4, 5007.
URL <http://www.pubmedcentral.nih.gov/articlerender.fcgi?artid=4028899&tool=pmcentrez&rendertype=abstract>
- Chung, D. H., Buessem, W. R., 1967. The elastic anisotropy of crystals. *Journal of Applied Physics* 38 (5), 2010–2012.
- Clarke, F. H., Vinter, R. B., 1985. Regularity properties of solutions to the basic problem in the calculus of variations. *Transactions of the American Mathematical Society* 289 (1), 73–98.
URL <http://www.jstor.org/stable/1999689>
- Clayton, J. D., Knap, J., 2011. A phase field model of deformation twinning: Nonlinear theory and numerical simulations. *Physica D: Nonlinear Phenomena* 240 (9-10), 841–858.
URL <http://dx.doi.org/10.1016/j.physd.2010.12.012>
- Cocks, A. C. F., McMeeking, R. M., 1999. A phenomenological constitutive law for the behaviour of ferroelectric ceramics. *Ferroelectrics* 228 (1), 219–228.
URL <http://dx.doi.org/10.1080/00150199908226136>

- Conti, S., Dolzmann, G., Klust, C., 2009. Relaxation of a class of variational models in crystal plasticity. *Proceedings of the Royal Society A: Mathematical, Physical and Engineering Sciences* 465 (2106), 1735–1742.
URL <http://rspa.royalsocietypublishing.org/cgi/doi/10.1098/rspa.2008.0390>
- Conti, S., Dolzmann, G., Kreisbeck, C., 2015. *Variational Modeling of Slip: From Crystal Plasticity to Geological Strata*. Springer International Publishing, Cham, pp. 31–62.
URL https://doi.org/10.1007/978-3-319-18242-1_2
- Conti, S., Ortiz, M., 2005. Dislocation microstructures and the effective behavior of single crystals. *Archive for Rational Mechanics and Analysis* 176 (1), 103–147.
- Conti, S., Ortiz, M., 2008. Minimum principles for the trajectories of systems governed by rate problems. *Journal of the Mechanics and Physics of Solids* 56 (5), 1885–1904.
- Conti, S., Theil, F., Oct 2005. Single-slip elastoplastic microstructures. *Archive for Rational Mechanics and Analysis* 178 (1), 125–148.
URL <https://doi.org/10.1007/s00205-005-0371-8>
- Cooley, J. W., Tukey, J. W., 1965. An algorithm for the machine calculation of complex fourier series. *Mathematics of computation* 19 (90), 297–301.
- Dacorogna, B., 1989. *Direct methods in the calculus of variations*.
URL <http://www.springer.com/gb/book/9783642514401>
- Dayal, K., Bhattacharya, K., 2007. A real-space non-local phase-field model of ferroelectric domain patterns in complex geometries. *Acta Materialia* 55 (6), 1907–1917.
- Demange, G., Zapolsky, H., Patte, R., Brunel, M., 2017. A phase field model for snow crystal growth in three dimensions. *npj Computational Materials* 3 (1), 15.
- Deshpande, V. S., Fleck, N. A., Ashby, M. F., 2001. Effective properties of the octet-truss lattice material. *Journal of the Mechanics and Physics of Solids* 49 (8), 1747–1769.
- Dixit, N., Xie, K. Y., Hemker, K. J., Ramesh, K. T., 2015. Microstructural evolution of pure magnesium under high strain rate loading. *Acta Materialia* 87, 56–67.
URL <http://dx.doi.org/10.1016/j.actamat.2014.12.030>
- Dmitrieva, O., Dondl, P. W., Müller, S., Raabe, D., 2009. Lamination microstructure in shear deformed copper single crystals. *Acta Materialia* 57 (12), 3439 – 3449.
URL <http://www.sciencedirect.com/science/article/pii/S1359645409001943>
- Dmitrieva, O., Raabe, D., Müller, S., Dondl, P. W., 2015. Analysis and Computation of Microstructure in Finite Plasticity. *Lecture Notes in Applied and Computational Mechanics* 78, 205–218.
URL <http://www.scopus.com/inward/record.url?eid=2-s2.0-84928671115&partnerID=tZ0tx3y1>

- Dufresne, E. R., Noh, H., Saranathan, V., Mochrie, S. G., Cao, H., Prum, R. O., 2009. Self-assembly of amorphous biophotonic nanostructures by phase separation. *Soft Matter* 5 (9), 1792–1795.
- Eggleston, J. J., McFadden, G. B., Voorhees, P. W., 2001. A phase-field model for highly anisotropic interfacial energy. *Physica D: Nonlinear Phenomena* 150 (1-2), 91–103.
- Eisenlohr, P., Diehl, M., Lebensohn, R. A., Roters, F., 2013. A spectral method solution to crystal elasto-viscoplasticity at finite strains. *International Journal of Plasticity* 46, 37–53.
URL <http://linkinghub.elsevier.com/retrieve/pii/S0749641912001428>
- Elliott, C. M., 1989. The cahn-hilliard model for the kinetics of phase separation. In: *Mathematical models for phase change problems*. Springer, pp. 35–73.
- Ericksen, J. L., Nov 1975. Equilibrium of bars. *Journal of Elasticity* 5 (3), 191–201.
URL <https://doi.org/10.1007/BF00126984>
- Erlebacher, J., Aziz, M. J., Karma, A., Dimitrov, N., Sieradzki, K., 2001. Evolution of nanoporosity in dealloying. *Nature* 410 (6827), 450–453.
- Fonseca, I., Leoni, G., 2001. On lower semicontinuity and relaxation. *Proceedings of the Royal Society of Edinburgh Section A: Mathematics* 131 (3), 519–565.
- Fourier, J.-B.-J., 1822. *Mémoire sur la propagation de la chaleur dans les corps solides*. Paris F. Didot.
- Frazier, M. J., Kochmann, D. M., 2017. Atomimetic mechanical structures with nonlinear topological domain evolution kinetics. *Advanced Materials* 29 (19), 1605800–n/a, 1605800.
URL <http://dx.doi.org/10.1002/adma.201605800>
- Frigo, M., Johnson, S. G., 1998. Fftw: An adaptive software architecture for the fft. In: *Acoustics, Speech and Signal Processing, 1998. Proceedings of the 1998 IEEE International Conference on*. Vol. 3. IEEE, pp. 1381–1384.
- Fultz, B., 2014. *Phase transitions in materials*. Cambridge University Press.
- Gao, P., Britson, J., Jokisaari, J. R., Nelson, C. T., Baek, S.-H., Wang, Y., Eom, C.-B., Chen, L.-Q., Pan, X., 2013. Atomic-scale mechanisms of ferroelastic domain-wall-mediated ferroelectric switching. *Nature communications* 4 (2791), 2791.
URL <http://www.ncbi.nlm.nih.gov/pubmed/24256974>
- Gao, P., Britson, J., Nelson, C. T., Jokisaari, J. R., Duan, C., Trassin, M., Baek, S.-H., Guo, H., Li, L., Wang, Y., Chu, Y.-H., Minor, A. M., Eom, C.-B., Ramesh, R., Chen, L.-Q., Pan, X., 2014. Ferroelastic domain switching dynamics under electrical and mechanical excitations. *Nature communications* 5 (May), 3801.
URL <http://www.ncbi.nlm.nih.gov/pubmed/24787035>
- Gauss, C. F., 1866. *Nachlass: Theoria interpolationis methodo nova tractata*. Carl Friedrich Gauss, Werke, Analysis; Band 3, 265–303.

- Gelb, A., Gottlieb, S., 2007. The resolution of the gibbs phenomenon for fourier spectral methods. *Advances in The Gibbs Phenomenon*. Sampling Publishing, Potsdam, New York.
- Geslin, P. A., McCue, I., Gaskey, B., Erlebacher, J., Karma, A., 2015. Topology-generating interfacial pattern formation during liquid metal dealloying. *Nature Communications* 6, 1–8.
- Gibbs, J. W., 1898. Fourier's series. *Nature* 59, 200.
URL <http://www.nature.com/nature/journal/v59/n1522/abs/059200b0.html>
- Gibbs, J. W., 1899. Fourier's series. *Nature* 59, 606.
URL <http://www.nature.com/nature/journal/v59/n1539/pdf/059606a0.html>
- Giorgi, C., 2009. Continuum thermodynamics and phase-field models. *Milan journal of mathematics* 77 (1), 67.
- Giraldo, M., Stavenga, D., 2016. Brilliant iridescence of morpho butterfly wing scales is due to both a thin film lower lamina and a multilayered upper lamina. *Journal of Comparative Physiology A* 202 (5), 381–388.
- Goncu, F., Willshaw, S., Shim, J., Cusack, J., Luding, S., Mullin, T., Bertoldi, K., 2011. Deformation induced pattern transformation in a soft granular crystal. *Soft Matter* 7, 2321–2324.
URL <http://dx.doi.org/10.1039/C0SM01408G>
- Govindjee, S., Mielke, A., Hall, G. J., 2003. The free energy of mixing for n -variant martensitic phase transformations using quasi-convex analysis 51, 1897–1922.
- Graff, S., Brocks, W., Steglich, D., 2007. Yielding of magnesium: From single crystal to polycrystalline aggregates. *International Journal of Plasticity* 23 (12), 1957–1978.
- Gurtin, M. E., 1987. *Some Results and Conjectures in the Gradient Theory of Phase Transitions*. Springer New York, New York, NY, pp. 135–146.
URL https://doi.org/10.1007/978-1-4613-8704-6_9
- Hackl, K., Fischer, F. D., 2008. On the relation between the principle of maximum dissipation and inelastic evolution given by dissipation potentials. *Proceedings of the Royal Society A: Mathematical, Physical and Engineering Sciences* 464 (2089), 117–132.
URL <http://rspa.royalsocietypublishing.org/cgi/doi/10.1098/rspa.2007.0086>
- Hackl, K., Hoppe, U., Kochmann, D. M., 2014. *Variational modeling of microstructures in plasticity*. Springer Vienna, Vienna, pp. 65–129.
URL https://doi.org/10.1007/978-3-7091-1625-8_2
- Hackl, K., Kochmann, D., 2008. Relaxed potentials and evolution equations for inelastic microstructures. In: Reddy, B. (Ed.), *IUTAM Symposium on Theoretical, Computational and Modelling Aspects of Inelastic Media*. Vol. 11 of IUTAM Bookseries. pp. 27–39.
- Hadamard, J., 1923. *Lectures on Cauchy's problem in linear partial differential equations*. Courier Corporation.

- Hamming, R. W., 1986. Numerical Methods for Scientists and Engineers. Dover, New York.
- Hewitt, E., Hewitt, R. E., 1979. The gibbs-wilbraham phenomenon: An episode in fourier analysis. *Archive for History of Exact Sciences* 21 (2), 129–160.
URL <http://dx.doi.org/10.1007/BF00330404>
- Higgins, A. M., Jones, R. A., 2000. Anisotropic spinodal dewetting as a route to self-assembly of patterned surfaces. *Nature* 404 (6777), 476–478.
- Hill, R., 1952. The elastic behaviour of a crystalline aggregate. *Proceedings of the Physical Society. Section A* 65 (5), 349.
URL <http://stacks.iop.org/0370-1298/65/i=5/a=307>
- Hill, R., 1972. On constitutive macro-variables for heterogeneous solids at finite strain. *Proceedings of the Royal Society of London A: Mathematical, Physical and Engineering Sciences* 326 (1565), 131–147.
URL <http://rspa.royalsocietypublishing.org/content/326/1565/131>
- Homayonifar, M., Mosler, J., 2011. On the coupling of plastic slip and deformation-induced twinning in magnesium: A variationally consistent approach based on energy minimization. *International Journal of Plasticity* 27 (7), 983–1003.
URL <http://dx.doi.org/10.1016/j.ijplas.2010.10.009>
- Homayonifar, M., Mosler, J., 2012. Efficient modeling of microstructure evolution in magnesium by energy minimization. *International Journal of Plasticity* 28 (1), 1–20.
URL <http://dx.doi.org/10.1016/j.ijplas.2011.05.011>
- Huang, J., Wang, X., Wang, Z. L., 2006. Controlled replication of butterfly wings for achieving tunable photonic properties. *Nano letters* 6 (10), 2325–2331.
- Huber, J., Fleck, N., 2004. Ferroelectric switching: a micromechanics model versus measured behaviour. *European Journal of Mechanics - A/Solids* 23 (2), 203 – 217.
URL <http://www.sciencedirect.com/science/article/pii/S0997753803001335>
- Huber, J., Fleck, N., Landis, C., McMeeking, R., 1999. A constitutive model for ferroelectric polycrystals. *Journal of the Mechanics and Physics of Solids* 47 (8), 1663 – 1697.
URL <http://www.sciencedirect.com/science/article/pii/S0022509698001227>
- Idiart, M. I., 2014. Modeling two-phase ferroelectric composites by sequential laminates. *Modelling and Simulation in Materials Science and Engineering* 22 (2), 025010.
URL <http://stacks.iop.org/0965-0393/22/i=2/a=025010>
- Izadbakhsh, A., Inal, K., Mishra, R. K., Niewczas, M., 2011. New crystal plasticity constitutive model for large strain deformation in single crystals of magnesium. *Computational Materials Science* 50 (7), 2185–2202.
- Jaglinski, T., Kochmann, D., Stone, D., Lakes, R. S., 2007. Composite materials with viscoelastic stiffness greater than diamond. *Science* 315 (5812), 620–622.
URL <http://www.sciencemag.org/content/315/5812/620.abstract>

- Javili, A., Dortdivanlioglu, B., Kuhl, E., Linder, C., 2015. Computational aspects of growth-induced instabilities through eigenvalue analysis. *Computational Mechanics* 56 (3), 405–420.
- Jin, N., Winter, A., 1984. Dislocation structures in cyclically deformed [001] copper crystals. *Acta Metallurgica* 32 (8), 1173–1176.
- Kabel, M., Boehlke, T., Schneider, M., 2014. Efficient fixed point and Newton-Krylov solvers for FFT-based homogenization of elasticity at large deformations. *Computational Mechanics* 54 (6), 1497–1514.
- Kalidindi, S. R., 2001. Modeling anisotropic strain hardening and deformation textures in low stacking fault energy fcc metals. *International Journal of Plasticity* 17 (6), 837–860.
- Kalinin, S. V., Rodriguez, B. J., Jesse, S., Chu, Y. H., Zhao, T., Ramesh, R., Choudhury, S., Chen, L. Q., Eliseev, E. A., Morozovska, A. N., 2007. Intrinsic single-domain switching in ferroelectric materials on a nearly ideal surface. *Proceedings of the National Academy of Sciences of the United States of America* 104 (51), 20204–20209.
URL <http://www.pubmedcentral.nih.gov/articlerender.fcgi?artid=2154409&tool=pmcentrez&rendertype=abstract>
- Kannan, V., Hazeli, K., Ramesh, K., 2018. The mechanics of dynamic twinning in single crystal magnesium. *Journal of the Mechanics and Physics of Solids*.
- Kelley, E. W., Hosford, W. F., 1968. The Deformation Characteristics of Textured Magnesium. *Transactions Of The Metallurgical Society Of AIME* 242 (April), 654 – 661.
- Kinderlehrer, D., Pedregal, P., 1991. Characterizations of young measures generated by gradients. *Archive for rational mechanics and analysis* 115 (4), 329–365.
- Kinoshita, S., 2013. *Pattern Formations and Oscillatory Phenomena*. Newnes.
- Kirchdoerfer, T., Ortiz, M., 2016. Data-driven computational mechanics. *Computer Methods in Applied Mechanics and Engineering* 304, 81–101.
- Klusemann, B., Kochmann, D. M., 2014. Microstructural pattern formation in finite-deformation single-slip crystal plasticity under cyclic loading: Relaxation vs. gradient plasticity. *Computer Methods in Applied Mechanics and Engineering* 278, 765–793.
URL <http://dx.doi.org/10.1016/j.cma.2014.05.015>
- Kochmann, D., Hackl, K., 2011. The evolution of laminates in finite crystal plasticity: a variational approach. *Continuum Mechanics and Thermodynamics* 23 (1), 63–85.
URL <http://www.springerlink.com/content/b02h60851620u737/?MUD=MP>
- Kochmann, D. M., 2009. Mechanical modeling of microstructures in elastoplastically deformed crystalline solids. Ph.D. thesis, Inst. für Mechanik, Ruhr-Universität Bochum.
- Kochmann, D. M., Hackl, K., 2010. Influence of hardening on the cyclic behavior of laminate microstructures in finite crystal plasticity. *Techn. Mech.* 30, 387–400.
URL http://www.uni-magdeburg.de/ifme/zeitschrift_tm/2010_Heft4/08_Kochmann_Hackl.pdf

- Kochmann, J., Wulfinghoff, S., Ehle, L., Mayer, J., Svendsen, B., Reese, S., Sep 2017. Efficient and accurate two-scale fe-fft-based prediction of the effective material behavior of elasto-viscoplastic polycrystals. *Computational Mechanics*.
URL <https://doi.org/10.1007/s00466-017-1476-2>
- Kochmann, J., Wulfinghoff, S., Reese, S., Mianroodi, J. R., Svendsen, B., 2016. Two-scale FE-FFT- and phase-field-based computational modeling of bulk microstructural evolution and macroscopic material behavior. *Computer Methods in Applied Mechanics and Engineering* 305, 89–110.
URL <http://dx.doi.org/10.1016/j.cma.2016.03.001>
- Koiter, W., 1965. Energy criterion of stability for continuous elastic bodies. *Proceedings of the Koninklijke Nederlandse Academie van Wetenschappen B* 868, 178–202.
- Kouznetsova, V., Brekelmans, W. A. M., Baaijens, F. P. T., Jan 2001. An approach to micro-macro modeling of heterogeneous materials. *Computational Mechanics* 27 (1), 37–48.
URL <https://doi.org/10.1007/s004660000212>
- Kuo, J.-C., Zaefferer, S., Zhao, Z., Winning, M., Raabe, D., 2003. Deformation behavior of aluminum bicrystals. *Advanced Engineering Materials* 5 (8), 563–566.
- Kurukuri, S., Worswick, M. J., Tari, D. G., Mishra, R. K., Carter, J. T., 2014. Rate sensitivity and tension – compression asymmetry in AZ31B magnesium alloy sheet. *Phil. Trans. R. Soc. A* 372, 1–16.
- Kwon, Y., Thornton, K., Voorhees, P. W., 2010. Morphology and topology in coarsening of domains via non-conserved and conserved dynamics. *Philosophical Magazine* 90 (1-4), 317–335.
- Lambeck, P. V., Jonker, G. H., 1986. The nature of domain stabilization in ferroelectric perovskites. *Journal of Physics and Chemistry of Solids* 47 (5), 453 – 461.
URL <http://www.sciencedirect.com/science/article/pii/0022369786900429>
- Lanczos, C., 1956. *Applied Analysis*. Van Nostrand, Princeton, NJ.
- Landis, C. M., 2002. Fully coupled, multi-axial, symmetric constitutive laws for polycrystalline ferroelectric ceramics. *Journal of the Mechanics and Physics of Solids* 50 (1), 127–152.
URL <http://www.sciencedirect.com/science/article/pii/S0022509601000217>
- Lang, X. Y., Guan, P. F., Fujita, T., Chen, M. W., 2011. Tailored nanoporous gold for ultrahigh fluorescence enhancement. *Physical Chemistry Chemical Physics* 13 (9), 3795.
URL <http://xlink.rsc.org/?DOI=c0cp01571g>
- Le Dret, H., Raoult, A., 1995. The quasiconvex envelope of the saint venant–kirchhoff stored energy function. *Proceedings of the Royal Society of Edinburgh: Section A Mathematics* 125 (6), 1179–1192.
- le Graverend, J.-B., Wojnar, C. S., Kochmann, D. M., 2015. Broadband electromechanical spectroscopy: characterizing the dynamic mechanical response of viscoelastic materials under temperature and electric field control in a vacuum environment. *Journal of Materials Science* 50 (10),

3656–3685.

URL <http://dx.doi.org/10.1007/s10853-015-8928-x>

Lebensohn, R. A., Kanjarla, A. K., Eisenlohr, P., 2012. An elasto-viscoplastic formulation based on fast Fourier transforms for the prediction of micromechanical fields in polycrystalline materials. *International Journal of Plasticity* 32-33, 59–69.

URL <http://dx.doi.org/10.1016/j.ijplas.2011.12.005>

Lebensohn, R. A., Needleman, A., 2016. Numerical implementation of non-local polycrystal plasticity using fast fourier transforms. *Journal of the Mechanics and Physics of Solids* 97, 333 – 351, sI: Pierre Suquet Symposium.

URL <http://www.sciencedirect.com/science/article/pii/S0022509616301958>

Lee, C., Duggan, B., 1991. A simple theory for the development of inhomogeneous rolling textures. *Metallurgical Transactions A* 22 (11), 2637–2643.

URL <http://dx.doi.org/10.1007/BF02851357>

Levitas, V. I., Levin, V. A., Zingerman, K. M., Freiman, E. I., 2009. Displacive phase transitions at large strains: Phase-field theory and simulations. *Physical Review Letters* 103 (2), 1–4.

Li, D., Zhu, Y., Wang, H., Ding, Y., 2013. Nanoporous gold as an active low temperature catalyst toward CO oxidation in hydrogen-rich stream. *Scientific Reports* 3, 1–7.

Li, Y., Hu, S. Y., Liu, Z. K., Chen, L. Q., 2002. Effect of electrical boundary conditions on ferroelectric domain structures in thin films. *Applied Physics Letters* 81 (3), 427–429.

Lu, X., Balk, T. J., Spolenak, R., Arzt, E., 2007. Dealloying of Au-Ag thin films with a composition gradient: Influence on morphology of nanoporous Au. *Thin Solid Films* 515 (18), 7122–7126.

Lun Sin, S., Elsayed, A., Ravindran, C., 2013. Inclusions in magnesium and its alloys: a review. *International Materials Reviews* 58 (7), 419–436.

Mandel, J., 1966. Contribution théorique à l'étude de l'érouissage et des lois de l'écoulement plastique. In: *Applied Mechanics*. Springer, pp. 502–509.

Mandel, J., 1983. Sur la définition de la vitesse de déformation élastique en grande transformation élastoplastique. *International Journal of Solids and Structures* 19 (7), 573–578.

Marincel, D. M., Zhang, H., Jesse, S., Belianinov, A., Okatan, M. B., Kalinin, S. V., Rainforth, W. M., Reaney, I. M., Randall, C. A., Trolier-McKinstry, S., 2015. Domain wall motion across various grain boundaries in ferroelectric thin films. *Journal of the American Ceramic Society* 98 (6), 1848–1857.

URL <http://dx.doi.org/10.1111/jace.13535>

Máthis, K., Čapek, J., Zdražilová, Z., Trojanová, Z., 2011. Investigation of tension-compression asymmetry of magnesium by use of the acoustic emission technique. *Materials Science and Engineering A* 528 (18), 5904–5907.

- Merz, W. J., 1956. Switching time in ferroelectric BaTiO_3 and its dependence on crystal thickness. *Journal Applied Physics* 27 (8), 938–943.
URL <http://dx.doi.org/10.1063/1.1722518>
- Michel, J. C., Moulinec, H., Suquet, P., 2001. A computational scheme for linear and non-linear composites with arbitrary phase contrast. *International Journal for Numerical Methods in Engineering* 52 (12), 139–160.
URL <http://doi.wiley.com/10.1002/nme.275>
- Miehe, C., 2003. Computational micro-to-macro transitions for discretized micro-structures of heterogeneous materials at finite strains based on the minimization of averaged incremental energy. *Computer Methods in Applied Mechanics and Engineering* 192 (5-6), 559–591.
- Miehe, C., Koch, A., Jul 2002. Computational micro-to-macro transitions of discretized microstructures undergoing small strains. *Archive of Applied Mechanics* 72 (4), 300–317.
URL <https://doi.org/10.1007/s00419-002-0212-2>
- Miehe, C., Lambrecht, M., Gürses, E., 2004. Analysis of material instabilities in inelastic solids by incremental energy minimization and relaxation methods: Evolving deformation microstructures in finite plasticity. *Journal of the Mechanics and Physics of Solids* 52 (12), 2725–2769.
- Miehe, C., Rosato, D., 2011. A rate-dependent incremental variational formulation of ferroelectricity. *International Journal of Engineering Science* 49 (6), 466–496, theoretical-Read 05/14/13.
URL <http://www.sciencedirect.com/science/article/pii/S0020722510002466>
- Miehe, C., Schröder, J., Becker, M., 2002. Computational homogenization analysis in finite elasticity: material and structural instabilities on the micro- and macro-scales of periodic composites and their interaction. *Computer Methods in Applied Mechanics and Engineering* 191 (44), 4971–5005.
URL <http://www.sciencedirect.com/science/article/pii/S0045782502003912>
- Miller, R., Savage, A., 1958. Velocity of Sidewise 180° Domain-Wall Motion in BaTiO_3 as a Function of the Applied Electric Field. *Physical Review* 112 (3), 755–762.
URL http://prola.aps.org/abstract/PR/v112/i3/p755_1
- Mishra, N., Vondrejč, J., Zeman, J., 2015. A comparative study on low-memory iterative solvers for FFT-based homogenization of periodic media. arXiv:1508.02045, 21.
URL <http://arxiv.org/abs/1508.02045>
- Modica, L., 1987. The gradient theory of phase transitions and the minimal interface criterion. *Archive for Rational Mechanics and Analysis* 98 (2), 123–142.
- Morrey, C. B., 1952. Quasi-convexity and the lower semicontinuity of multiple integrals. *Pacific J. Math.* 2, 25–53.
- Moulinec, H., Silva, F., 2014. Comparison of three accelerated FFT-based schemes for computing the mechanical response of composite materials. *International Journal for Numerical Methods in Engineering* 97 (13), 960–985.

- Moulinec, H., Suquet, P., 1998. A numerical method for computing the overall response of non-linear composites with complex microstructure. *Computer Methods in Applied Mechanics and Engineering* 157 (1-2), 69–94.
- Moulinec, H., Suquet, P., 2003. Comparison of FFT-based methods for computing the response of composites with highly contrasted mechanical properties. *Physica B: Condensed Matter* 338 (1-4), 58–60.
- Mueller, W., 1998. Fourier Transforms and their application to the formation of textures and changes of morphology in solids. In: *IUTAM Symposium on Transformation Problems in Composite and Active Materials*. Kluwer Academic Publishers, pp. 61–72.
- Munson, T., Sarich, J., Wild, S., Benson, S., McInnes, L. C., 2015. *Tao 3.6 users manual*. Argonne National Laboratory, Mathematics and Computer Science Division.
- Nishikawa, Y., Jinnai, H., Koga, T., Hashimoto, T., Hyde, S. T., 1998. Measurements of interfacial curvatures of bicontinuous structure from three-dimensional digital images. 1. a parallel surface method. *Langmuir* 14 (5), 1242–1249.
URL <http://dx.doi.org/10.1021/la970868b>
- Oppedal, A., El Kadiri, H., Tomé, C., Vogel, S. C., Horstemeyer, M., 2013. Anisotropy in hexagonal close-packed structures: improvements to crystal plasticity approaches applied to magnesium alloy. *Philosophical Magazine* 93 (35), 4311–4330.
URL <http://www.tandfonline.com/doi/abs/10.1080/14786435.2013.827802>
- Ortiz, M., Repetto, E. A., 1999. Nonconvex energy minimization and dislocation structures in ductile single crystals. *Journal of the Mechanics and Physics of Solids* 47, 397–462.
- Ortiz, M., Stainier, L., 1999. The variational formulation of viscoplastic constitutive updates. *Computer Methods in Applied Mechanics and Engineering* 171 (3-4), 419 – 444.
URL <http://www.sciencedirect.com/science/article/pii/S0045782598002199>
- Overvelde, J. T. B., Shan, S., Bertoldi, K., 2012. Compaction through buckling in 2d periodic, soft and porous structures: Effect of pore shape. *Advanced Materials* 24 (17), 2337–2342.
URL <http://dx.doi.org/10.1002/adma.201104395>
- Park, C. L., Gibbs, J. W., Voorhees, P. W., Thornton, K., 2017. Coarsening of complex microstructures following spinodal decomposition. *Acta Materialia* 132, 13–24.
URL <http://dx.doi.org/10.1016/j.actamat.2017.03.020>
- Park, S. H., Lee, J. H., Moon, B. G., You, B. S., 2014. Tension-compression yield asymmetry in as-cast magnesium alloy. *Journal of Alloys and Compounds* 617, 277–280.
URL <http://dx.doi.org/10.1016/j.jallcom.2014.07.164>
- Paul, B., 1960. Prediction of elastic constants of multiphase materials. *Trans. Metall. Soc. AIME* 218, 36–41.
- Plucinsky, P., Bhattacharya, K., 2017. Microstructure-enabled control of wrinkling in nematic elastomer sheets. *Journal of the Mechanics and Physics of Solids* 102, 125 – 150.
URL <http://www.sciencedirect.com/science/article/pii/S0022509616308572>

- Pollock, T. M., 2010. Weight Loss with Magnesium Alloys. *Science* 328 (5981), 986–987.
URL <http://www.sciencemag.org/cgi/doi/10.1126/science.1182848>
- Pruchnicki, E., 1998. Homogenized nonlinear constitutive law using fourier series expansion. *International journal of solids and structures* 35 (16), 1895–1913.
- Quey, R., Dawson, P., Barbe, F., 2011. Large-scale 3d random polycrystals for the finite element method: Generation, meshing and remeshing. *Computer Methods in Applied Mechanics and Engineering* 200 (17), 1729 – 1745.
URL <http://www.sciencedirect.com/science/article/pii/S004578251100003X>
- Rader, C. M., 1968. Discrete fourier transforms when the number of data samples is prime. *Proceedings of the IEEE* 56 (6), 1107–1108.
- Rockafellar, R. T., 1970. *Convex analysis*. Princeton university press.
- Rodriguez, B. J., Chu, Y. H., Ramesh, R., Kalinin, S. V., 2008. Ferroelectric domain wall pinning at a bicrystal grain boundary in bismuth ferrite. *Applied Physics Letters* 93 (14).
URL <http://scitation.aip.org/content/aip/journal/apl/93/14/10.1063/1.2993327>
- Salvalaglio, M., Backofen, R., Bergamaschini, R., Montalenti, F., Voigt, A., 2015. Faceting of equilibrium and metastable nanostructures: A phase-field model of surface diffusion tackling realistic shapes. *Crystal Growth and Design* 15 (6), 2787–2794.
- Savage, a., Miller, R. C., 1960. Temperature Dependence of the Velocity of Sidewise 180° Domain-Wall Motion in BaTiO₃. *Journal of Applied Physics* 31 (9), 1546.
URL <http://link.aip.org/link/JAPIAU/v31/i9/p1546/s1&Agg=doi>
- Sawyer, C. B., Tower, C. H., Feb 1930. Rochelle salt as a dielectric. *Physical Review* 35, 269–273.
URL <http://link.aps.org/doi/10.1103/PhysRev.35.269>
- Schaedler, T. A., Carter, W. B., 2016. Architected Cellular Materials. *Annual Review of Materials Research* 46 (1), 187–210.
URL <http://www.annualreviews.org/doi/10.1146/annurev-matsci-070115-031624>
- Schneider, M., Merkert, D., Kabel, M., 2017. FFT-based homogenization for microstructures discretized by linear hexahedral elements. *International Journal for Numerical Methods in Engineering* 109 (10), 1461–1489, nme.5336.
URL <http://dx.doi.org/10.1002/nme.5336>
- Schrade, D., Mueller, R., Xu, B. X., Gross, D., 2007. Domain evolution in ferroelectric materials: A continuum phase field model and finite element implementation. *Computer Methods in Applied Mechanics and Engineering* 196 (41-44), 4365–4374.
- Schrade, D., Müller, R., Gross, D., Keip, M. A., Thai, H., Schröder, J., 2014. An invariant formulation for phase field models in ferroelectrics. *International Journal of Solids and Structures* 51 (11-12), 2144–2156.
URL <http://dx.doi.org/10.1016/j.ijsolstr.2014.02.021>

- Schröder, J., 2009. Derivation of the localization and homogenization conditions for electro-mechanically coupled problems. *Computational Materials Science* 46 (3), 595–599, proceedings of the 18th International Workshop on Computational Mechanics of Materials IWCMM-18.
URL <http://www.sciencedirect.com/science/article/pii/S0927025609001566>
- Sellers, S. R., Man, W., Sahba, S., Florescu, M., 2017. Local self-uniformity in photonic networks. *Nature Communications* 8, 14439.
- Shanthraj, P., Eisenlohr, P., Diehl, M., Roters, F., 2015. Numerically robust spectral methods for crystal plasticity simulations of heterogeneous materials. *International Journal of Plasticity* 66, 31–45.
URL <http://dx.doi.org/10.1016/j.ijplas.2014.02.006>
- Simo, J., 1988. A framework for finite strain elastoplasticity based on maximum dissipation and the multiplicative decomposition: Part II. Computational aspects. *Computer Methods in Applied Mechanics and Engineering* 66, 1–31.
- Stanford, N., Sotoudeh, K., Bate, P. S., 2011. Deformation mechanisms and plastic anisotropy in magnesium alloy AZ31. *Acta Materialia* 59 (12), 4866–4874.
URL <http://dx.doi.org/10.1016/j.actamat.2011.04.028>
- Stanich, C. A., Honerkamp-Smith, A. R., Putzel, G. G., Warth, C. S., Lamprecht, A. K., Mandal, P., Mann, E., Hua, T. A. D., Keller, S. L., 2013. Coarsening dynamics of domains in lipid membranes. *Biophysical Journal* 105 (2), 444–454.
- Steinbach, I., Pezzolla, F., Nestler, B., Seeßelberg, M., Prieler, R., Schmitz, G., Rezende, J., 1996. A phase field concept for multiphase systems. *Physica D: Nonlinear Phenomena* 94 (3), 135–147.
URL <http://linkinghub.elsevier.com/retrieve/pii/0167278995002987>
- Stolz, C., 2010. On micro-macro transition in non-linear mechanics. *Materials* 3 (1), 296–317.
- Su, Y., Landis, C. M., 2007a. Continuum thermodynamics of ferroelectric domain evolution: Theory, finite element implementation, and application to domain wall pinning. *J. Mech. Phys. Solids* 55, 280–305.
- Su, Y., Landis, C. M., 2007b. Continuum thermodynamics of ferroelectric domain evolution: Theory, finite element implementation, and application to domain wall pinning. *Journal of the Mechanics and Physics of Solids* 55 (2), 280–305.
- Sun, D., Ponga, M., Bhattacharya, K., Ortiz, M., 2018. Proliferation of twinning in hexagonal close-packed metals: Application to magnesium. *Journal of the Mechanics and Physics of Solids* 112, 368–384.
- Sun, S., Chen, X., Badwe, N., Sieradzki, K., 2015. Potential-dependent dynamic fracture of nanoporous gold. *Nature Materials* 14 (9), 894–898.
- Suquet, P. M., 1987. Introduction. In: Sanchez-Palencia, E., Zaoui, A. (Eds.), *Homogenization Techniques for Composite Media*. Springer Berlin Heidelberg, Berlin, Heidelberg, pp. 193–198.

- Šverák, V., 1992. Rank-one convexity does not imply quasiconvexity. *Proceedings of the Royal Society of Edinburgh Section A: Mathematics* 120 (1-2), 185–189.
- Tan, W. L., Kochmann, D. M., 2017. An effective constitutive model for polycrystalline ferroelectric ceramics: Theoretical framework and numerical examples. *Computational Materials Science* 136, 223 – 237.
URL <http://www.sciencedirect.com/science/article/pii/S0927025617302240>
- Taylor, G., 1985. *Piezoelectricity. Ferroelectricity and related phenomena.* Gordon and Breach Science Publishers.
URL <https://books.google.com/books?id=7b00AAAAQAAJ>
- Thomé, M., Nicole, L., Berthier, S., 2014. Multiscale replication of iridescent butterfly wings. *Materials Today: Proceedings* 1, 221 – 224, *living Light: Uniting biology and photonics – A memorial meeting in honour of Prof Jean-Pol Vigneron.*
URL <http://www.sciencedirect.com/science/article/pii/S2214785314000273>
- Tomé, C. N., Beyerlein, I. J., Wang, J., McCabe, R. J., 2011. A multi-scale statistical study of twinning in magnesium. *Jom* 63 (3), 19–23.
- Torabi, S., Lowengrub, J., Voigt, A., Wise, S., 2009. A new phase-field model for strongly anisotropic systems. *Proceedings of the Royal Society A: Mathematical, Physical and Engineering Sciences* 465 (2105), 1337–1359.
URL <http://rspa.royalsocietypublishing.org/cgi/doi/10.1098/rspa.2008.0385>
- Truesdell, C., Noll, W., 1965. The nonlinear field theories of mechanics. In: Flügge, S. (Ed.), *Encyclopedia of Physics* III/3. Springer, Berlin.
- Vidyasagar, A., Tan, W. L., Kochmann, D. M., 2017. Predicting the effective response of bulk polycrystalline ferroelectric ceramics via improved spectral phase field methods. *Journal of the Mechanics and Physics of Solids* 106, 133–151.
- Vidyasagar, A., Tutcuoglu, A. D., Kochmann, D. M., 2018. Deformation patterning in finite-strain crystal plasticity by spectral homogenization with application to magnesium. *Computer Methods in Applied Mechanics and Engineering* 335, 584–609.
- Völker, B., Marton, P., Elsässer, C., Kamlah, M., 2011. Multiscale modeling for ferroelectric materials: A transition from the atomic level to phase-field modeling. *Continuum Mechanics and Thermodynamics* 23 (5), 435–451.
- Volkert, C., Lilleodden, E., Kramer, D., Weissmüller, J., 2006. Approaching the theoretical strength in nanoporous Au. *Applied Physics Letters* 89 (6), 061920.
- von Schwerin, E., Szepessy, A., 2010. A stochastic phase-field model determined from molecular dynamics. *ESAIM: Mathematical Modelling and Numerical Analysis* 44 (4), 627–646.

- Wang, J., Beyerlein, I. J., Hirth, J. P., 2012. Nucleation of elementary $\bar{1}011$ and $\bar{1}013$ twinning dislocations at a twin boundary in hexagonal close-packed crystals. *Modelling and Simulation in Materials Science and Engineering* 20 (2), 024001.
URL <http://stacks.iop.org/0965-0393/20/i=2/a=024001?key=crossref.fb2b9a486c4b093d046f5abc11fb2e98>
- Wang, J., Shi, S. Q., Chen, L. Q., Li, Y., Zhang, T. Y., 2004. Phase-field simulations of ferroelectric/ferroelastic polarization switching. *Acta Materialia* 52 (3), 749–764.
- Willot, F., 2015. Fourier-based schemes for computing the mechanical response of composites with accurate local fields. *Comptes Rendus Mécanique* 343 (3), 232 – 245.
URL <http://www.sciencedirect.com/science/article/pii/S1631072114002149>
- Willot, F., Abdallah, B., Pellegrini, Y. P., 2014. Fourier-based schemes with modified Green operator for computing the electrical response of heterogeneous media with accurate local fields. *International Journal for Numerical Methods in Engineering* 98 (7), 518–533.
- Winograd, S., 1978. On computing the discrete fourier transform. *Mathematics of computation* 32 (141), 175–199.
- Wise, S., Kim, J., Lowengrub, J., 2007. Solving the regularized, strongly anisotropic Cahn-Hilliard equation by an adaptive nonlinear multigrid method. *Journal of Computational Physics* 226 (1), 414–446.
- Wojnar, C. S., Le Graverend, J. B., Kochmann, D. M., 2014. Broadband control of the viscoelasticity of ferroelectrics via domain switching. *Applied Physics Letters* 105 (16), 1–5.
- Xiao, Y., Bhattacharya, K., 2008. A continuum theory of deformable, semiconducting ferroelectrics. *Archive for Rational Mechanics and Analysis* 189 (1), 59–95.
URL <http://dx.doi.org/10.1007/s00205-007-0096-y>
- Yang, J., 2006. *An Introduction to the Theory of Piezoelectricity*. Advances in Mechanics and Mathematics. Springer US.
URL https://books.google.com/books?id=pt7A_4CKpTEC
- Yaraghi, N. A., Guarín-Zapata, N., Grunenfelder, L. K., Hintsala, E., Bhowmick, S., Hiller, J. M., Betts, M., Principe, E. L., Jung, J.-Y., Sheppard, L., et al., 2016. A sinusoidally architected helicoidal biocomposite. *Advanced Materials* 28 (32), 6835–6844.
- Zachariah, Z., Tatiparti, S. S. V., Mishra, S. K., Ramakrishnan, N., Ramamurty, U., 2013. Tension-compression asymmetry in an extruded Mg alloy AM30: Temperature and strain rate effects. *Materials Science and Engineering A* 572, 8–18.
URL <http://dx.doi.org/10.1016/j.msea.2013.02.023>
- Zeman, J., de Geus, T. W., Vondřejc, J., Peerlings, R. H., Geers, M. G., 2017. A finite element perspective on nonlinear fft-based micromechanical simulations. *International Journal for Numerical Methods in Engineering* 111 (10), 903–926.

- Zhang, J., Joshi, S. P., 2012. Phenomenological crystal plasticity modeling and detailed micromechanical investigations of pure magnesium. *Journal of the Mechanics and Physics of Solids* 60 (5), 945–972.
URL <http://dx.doi.org/10.1016/j.jmps.2012.01.005>
- Zhang, Q., Goddard, W. A., 2006. Charge and polarization distributions at the 90-degree domain wall in barium titanate ferroelectric. *Applied Physics Letters* 89 (18), 3–5.
- Zhang, W., Bhattacharya, K., 2005a. A computational model of ferroelectric domains. Part I: Model formulation and domain switching. *Acta Materialia* 53 (1), 185–198.
- Zhang, W., Bhattacharya, K., 2005b. A computational model of ferroelectric domains. Part II: Grain boundaries and defect pinning. *Acta Materialia* 53 (1), 199–209.
- Zhang, Y., Dong, B., Liu, X., Zi, J., 2013. Replication of spinodally decomposed structures with structural coloration from scales of the longhorn beetle *sphingnotus mirabilis*. *Bioinspiration & biomimetics* 8 (4), 045003.
- Zheng, X., Lee, H., Weisgraber, T. H., Shusteff, M., DeOtte, J., Duoss, E. B., Kuntz, J. D., Biener, M. M., Ge, Q., Jackson, J. A., Kucheyev, S. O., Fang, N. X., Spadaccini, C. M., jun 2014. Ultralight, ultrastiff mechanical metamaterials. *Science* 344 (6190), 1373–1377.
URL <http://www.sciencemag.org/cgi/doi/10.1126/science.1252291>
- Zhou, D., Kamlah, M., Munz, D., 2001. Rate dependence of soft pzt ceramics under electric field loading. *Proc. SPIE* 4333, 64–70.
URL <http://dx.doi.org/10.1117/12.432740>
- Zhu, J., Chen, L.-Q., Shen, J., Tikare, V., 1999. Coarsening kinetics from a variable-mobility cahn-hilliard equation: Application of a semi-implicit fourier spectral method. *Physical Review E* 60 (4), 3564.
- Ziehmer, M., Hu, K., Wang, K., Lilleodden, E. T., 2016. A principle curvatures analysis of the isothermal evolution of nanoporous gold: Quantifying the characteristic length-scales. *Acta Materialia* 120, 24–31.
URL <http://dx.doi.org/10.1016/j.actamat.2016.08.028>